

Aus dem Institut für Zytobiologie
Zentrum für Synthetische Mikrobiologie
Geschäftsführender Direktor: Prof. Dr. Roland Lill
des Fachbereichs Medizin der Philipps-Universität Marburg

**Molecular mechanisms of mitochondrial
de novo [2Fe-2S] cluster formation
and lipoyl biosynthesis**

Inaugural-Dissertation zur Erlangung des Doktorgrades
der Naturwissenschaften
(Dr. rer. nat.)

Dem Fachbereich Medizin der Philipps-Universität Marburg
vorgelegt von

Vinzent Schulz

aus Hamburg

Marburg, 2022

Angenommen vom Fachbereich Medizin der Philipps-Universität Marburg am: 7.9.2022

Gedruckt mit Genehmigung des Fachbereichs.

Dekanin: Prof. Dr. Denise Hilfiker-Kleiner

Referent: Prof. Dr. Roland Lill

Korreferent: Prof. Dr. Uwe Maier

Parts of this work can be found in the following publications:

Freibert, S.-A.[#], Boniecki, M.T.[#], Stümpfig, C., Schulz, V., Krapoth, N., Winge, D.R., Mühlenhoff, U., Stehling, O., Cygler, M.* and Lill, R.* (2021). **N-terminal tyrosine of ISCU2 triggers [2Fe-2S] cluster synthesis by ISCU2 dimerization.** *Nat. Comm.* 12: 6902

Schulz, V., Basu, S., Freibert, S.-A., Webert, H., Boß, L., Mühlenhoff, U., Pierrel, F., Essen, L.-O., Warui, D.M., Booker, S., Stehling, O.* and Lill, R.* (2022). **Functional spectrum and structural specificity of mitochondrial ferredoxins FDX1 and FDX2.** *Manuscript under revision (Nat. Chem. Biol.)*

Schulz, V., Freibert, S.-A., Lill, R. (2022). **Molecular mechanism of physiological ISCU2 persulfidation.** *Manuscript in preparation.*

[#]*these authors contributed equally*

^{*}*corresponding authors*

Grants:

European Cooperation in Science & Technology – Trainee Grant, September 2018, Université Grenoble Alpes

Conference contributions:

Human mitochondrial ferredoxins 1 and 2 perform different biosynthetic functions. (Talk), Young Mito Investigator Symposium “Mitochondria in life, death and disease”, 15.09.2021, online

Functions of human BOLA3 and FDX1 in lipoyl biosynthesis. (Talk), SPP1927 Meeting “FeS for Life”, 03.12.2020, online

Schulz, V., Freibert, S.-A., Linne, U. and Lill, R. **Quantitative analysis of dynamic thiol modifications.** (Poster), 3rd Spotlight Microbiology Meeting, 12.-13.11.2019, Marburg

Schulz, V., Basu, S., Stehling, O., Mühlenhoff, U., Webert, H., Freibert, S.-A. and Lill, R. **The different functions of the human ferredoxins 1 and 2.** (Poster), 4th FeSBioNet Meeting, 16.-19.09.2019, Gdansk

Biochemical examination of ISC (targeting) factors. (Workshop supervision), Workshop at the 8th Congress of the International Biolron Society, 03.05.2019, EMBL Heidelberg

Schulz, V., Freibert, S.-A., Boniecki, M.T., Gallo, A., Basu, S., Cygler, M., Banci, L. and Lill, R. **Structural and functional insights into mitochondrial Fe/S cluster synthesis.** (Poster), FeSBioNet Training School, 10.-14.09.2018, Grenoble

Contents

Summary	xi
Zusammenfassung	xiii
1 Introduction.....	1
1.1 Iron-sulfur proteins	1
1.1.1 The different Fe/S cluster types	1
1.1.2 Diverse functions of Fe/S proteins	3
1.2 Fe/S protein biogenesis systems	4
1.3 Mitochondrial Fe/S protein biogenesis	6
1.3.1 <i>De novo</i> [2Fe-2S] cluster formation in mitochondria	7
1.3.1.1 Structure and function of the core ISC complex	7
1.3.1.2 Persulfide formation on ISCU2	9
1.3.1.3 The function of FXN in the core ISC complex	11
1.3.1.4 FDX2-mediated [2Fe-2S] cluster maturation	12
1.3.1.5 The function of ISD11-ACP in the core ISC complex	13
1.3.2 [2Fe-2S] cluster trafficking	14
1.3.3 [4Fe-4S] cluster formation and trafficking	15
1.3.3.1 Assembly of [4Fe-4S] clusters	15
1.3.3.2 Targeting factors for [4Fe-4S] cluster insertion into mitochondrial recipients	16
1.4 Function and LIAS-dependent biosynthesis of the lipoyl cofactor	17
1.4.1 Lipoyl-dependent enzymes and their function.....	17
1.4.2 Biosynthesis of the lipoyl cofactor	19
1.4.3 Function and catalytic mechanism of lipoyl synthase (LIAS)	20
1.5 Ferredoxins	23
1.5.1 Ferredoxin functions in human mitochondria	24
1.6 Aims of this work	26
1.6.1 The molecular mechanism of <i>de novo</i> [2Fe-2S] cluster formation.....	26
1.6.2 The physiological electron donor for lipoyl cofactor biosynthesis	27
2 Materials	29
2.1 Devices	29
2.2 Chemicals, enzymes and markers	30
2.3 Oligonucleotides	30
2.4 Plasmids	30
2.5 Bacterial strains	32

2.5.1	<i>E. coli</i> DH5 α	32
2.5.2	<i>E. coli</i> BL21(DE3).....	32
2.6	Media	32
3	Methods.....	33
3.1	Microbiological and molecular biology methods	33
3.1.1	Preparation and transformation of chemically competent <i>E. coli</i> cells	33
3.1.2	Isolation of plasmid DNA from <i>E. coli</i>	33
3.1.3	Mutagenesis of plasmid DNA.....	33
3.1.3.1	Mutagenesis PCR	34
3.1.3.2	Restriction enzyme digest.....	34
3.2	Protein expression and purification	35
3.2.1	Recombinant protein expression in <i>E. coli</i>	35
3.2.2	Cell lysis	35
3.2.3	Chromatographic methods	36
3.2.3.1	Immobilized metal affinity chromatography (IMAC)	36
3.2.3.2	Anion exchange chromatography (AEC)	36
3.2.3.3	Size exclusion chromatography (SEC)	37
3.2.4	TEV cleavage of FXN.....	37
3.2.5	Buffer exchange of protein samples.....	38
3.2.6	Concentration of proteins	38
3.3	Protein biochemical methods	38
3.3.1	Sodium dodecyl sulfate polyacrylamide gel electrophoresis (SDS-PAGE).	38
3.3.2	Determination of protein concentration	39
3.3.3	Determination of Fe and sulfide concentration.....	39
3.3.4	Mass spectrometric analyses	39
3.3.5	Chemical reconstitution of Fe/S proteins	39
3.3.6	Immunoblotting.....	40
3.4	Enzymatic assays and other analyses	41
3.4.1	Fe binding of ISCU2.....	41
3.4.2	Analytical SEC and SEC-MALS	41
3.4.3	Persulfide transfer assay with maleimide polyethylenglycol ₁₁ biotin (MPB)	41
3.4.3.1	Persulfide reduction assay	42
3.4.4	Persulfide transfer assay with iodoacetyl tandem mass tag (iodoTMT) ..	42

3.4.5	Enzymatic reconstitution of <i>de novo</i> Fe/S cluster synthesis	43
3.4.6	Lipoylation assay.....	43
3.4.7	Cytochrome <i>c</i> reduction assay.....	44
3.4.8	Analysis of Fe/S cluster stability upon Cu titration	44
3.5	Spectroscopic methods.....	44
3.5.1	UV/Vis spectroscopy.....	44
3.5.2	CD spectroscopy.....	44
3.5.3	Preparation of Mössbauer and X-ray absorption spectroscopy samples	44
3.5.4	Mössbauer spectroscopy	45
3.5.5	X-ray absorption spectroscopy.....	46
3.6	Structural biology methods.....	46
3.6.1	Electron cryo-microscopy (cryo-EM).....	46
3.6.1.1	Sample preparation and vitrification.....	46
3.6.1.2	Data acquisition, processing and model building and refinement....	47
4	Results.....	48
4.1	Mechanism of <i>de novo</i> [2Fe-2S] cluster formation on ISCU2	48
4.1.1	Purification and characterization of ISCU2 variants	48
4.1.1.1	Purification of ISCU2 D71A.....	49
4.1.2	Cys69, Asp71 and Cys95 are essential for Fe(II) coordination by free ISCU2	50
4.1.3	Residues Asp71, Cys95 and Cys138 are essential for persulfide formation on ISCU2	52
4.1.4	ISCU2 Cys138 receives a persulfide from NFS1 Cys381 without a detectable intermediate	54
4.1.5	The persulfidated (Fe-NIAUX) ₂ complex exhibits Fe(II) coordination by an ISCU2 Cys138-bound persulfide.....	57
4.1.6	FXN modulates the ISCU2 assembly site to facilitate persulfide transfer	59
4.1.7	Specific molecular interactions between FXN and ISCU2 are critical for ISCU2 persulfidation and [2Fe-2S] cluster formation	62
4.1.8	Mössbauer spectroscopic analyses of intermediates of [2Fe-2S] cluster formation reveal a dynamic equilibrium between distinct Fe ligation modes.....	64
4.1.9	X-ray absorption spectroscopy of intermediates of [2Fe-2S] cluster formation.....	69
4.1.10	ISCU2 Cys69, Asp71, Cys95, His137 and Cys138 are required for enzymatic [2Fe-2S] cluster formation	70
4.1.11	ISCU2 Cys69, Cys95 and Cys138 are essential for [2Fe-2S] cluster coordination.....	71
4.2	<i>In vitro</i> reconstitution of human lipoyl biosynthesis identifies FDX1 as electron donor for LIAS	75

4.2.1	Purification and reconstitution of LIAS yields a functional holo-protein...	75
4.2.1.1	Purification and reconstitution of LIAS	75
4.2.1.2	Biochemical reconstitution of the lipoylation activity of LIAS identifies FDX1 as an efficient radical chain starter	77
4.2.2	Optimisation of lipoylation reaction conditions	79
4.2.3	Investigation of possible factors regenerating the auxiliary Fe/S cluster of LIAS	81
4.2.4	FDX1 but not FDX2 is required for lipoylation <i>in vitro</i>	83
4.2.5	C-terminal truncation of FDX2 enables lipoylation	84
4.2.6	Investigation of inhibitory effects of elesclomol and copper on FDXs and lipoyl synthesis	86
4.2.6.1	Cu but not Ele inhibits lipoylation <i>in vitro</i>	87
4.2.6.2	The Ele:Cu complex inhibits lipoylation <i>in vitro</i>	88
4.2.6.3	Chelation of Cu by Ele protects Fe/S clusters from destruction.....	90
5	Discussion	93
5.1	<i>De novo</i> [2Fe-2S] cluster formation on ISCU2.....	93
5.1.1	The order of assembly of the (Fe-NIAUX) ₂ complex	93
5.1.2	Fe coordination by ISCU2 at different stages of [2Fe-2S] cluster formation	94
5.1.2.1	Free ISCU2 coordinates Fe via residues Cys69, Asp71, Cys95 and His137	94
5.1.2.2	An equilibrium between distinct Fe coordination states present in the core ISC complex is modulated by FXN binding.....	95
5.1.3	The molecular mechanism of Fe-dependent persulfidation of ISCU2 Cys138	98
5.1.3.1	Conformational states of the persulfide-transferring NFS1 Cys381-loop are modulated by its interaction with Fe-ISCU2 and FXN.....	98
5.1.4	The mechanism of persulfide transfer from NFS1 Cys381 to ISCU2 Cys138	98
5.1.5	A proposed molecular mechanism of persulfide reduction	101
5.1.6	Assembly of a [2Fe-2S] cluster from persulfidated Fe-ISCU2 <i>in vivo</i> ...	102
5.1.7	Asymmetric [2Fe-2S] cluster ligation by ISCU2	105
5.1.8	Outlook.....	107
5.2	FDX1-dependent function of LIAS in human lipoyl biosynthesis.....	108
5.2.1	<i>In vitro</i> reconstitution of human lipoyl synthesis reveals similarities to bacterial catalysis	108
5.2.2	Potential Fe/S cluster donors for LIAS	109
5.2.3	Lipoyl biosynthesis is inhibited by Cu and the Ele:Cu complex	111

5.2.4	Structure prediction of a catalytically active LIAS-GCSH-FDX1 complex ...	113
5.3	Functions and specificity of the human ferredoxins	115
5.3.1	FDX1 and FDX2 support different mitochondrial pathways	115
5.3.2	Electrostatic and specific intermolecular interactions are key determinants of human FDX specificity	118
5.3.3	Outlook	121
6	Literature	122
7	Appendix	139
7.1	Figures	139
7.2	Abbreviations	160
8	Verzeichnis der akademischen Lehrenden	163
9	Danksagung	164

Summary

Iron-sulfur (Fe/S) clusters are small inorganic protein cofactors found in almost all known organisms. They enable various protein functions including electron transfer and catalysis and are integral to numerous essential biological processes like cellular respiration, translation, and DNA synthesis and repair. Fe/S clusters typically exhibit simple structures, with the rhombic [2Fe-2S]- and cubic [4Fe-4S]-types being the most common. Nevertheless, complex protein machineries are required for their biosynthesis and insertion into target apo-proteins. Mitochondrial Fe/S protein biogenesis requires the Fe/S cluster assembly (ISC) machinery consisting of up to 18 different proteins. The early ISC machinery assembles the [2Fe-2S] clusters *de novo*, and the late ISC machinery uses these clusters to produce and insert [4Fe-4S] clusters.

Despite the functions of many proteins of the ISC machinery being well characterized, the molecular mechanisms underlying mitochondrial Fe/S protein biogenesis, in particular *de novo* [2Fe-2S] cluster assembly, are not fully understood. The overarching aim of the first of the two projects in this work was to decipher at the molecular level how Fe and S are assembled on the scaffold protein ISCU2 to form [2Fe-2S] clusters *de novo*. In this process, one Fe ion and one persulfide moiety are delivered in a stepwise manner to the ISCU2 assembly site, which exhibits five conserved residues (Cys69, Asp71, Cys95, His137 and Cys138) believed to be critical for assembly. Efficient persulfidation of one of the three conserved ISCU2 Cys residues requires the heterodimeric cysteine desulfurase complex NFS1-ISD11-ACP (termed (NIA)₂) to bind to both ISCU2 (U) and FXN (X), forming (NIAUX)₂. The ISCU2-bound persulfide is reduced to sulfide via electron flow from the ferredoxin FDX2, and finally dimerization of two [1Fe-1S] ISCU2 units enables [2Fe-2S] cluster formation. It was shown in this work that NFS1 persulfidates ISCU2 Cys138 efficiently and with high specificity, and no detectable sulfur relay via other ISCU2 Cys residues was observed. Importantly, ISCU2 had to be preloaded with one Fe(II) ion to enable physiologically relevant persulfidation. Furthermore, the ISCU2 residues Cys69, Cys95, Cys138 and likely Asp71 were identified as ligands of the mature [2Fe-2S] cluster.

A combined structural, spectroscopic and biochemical approach revealed the hitherto ill-defined Fe coordination by ISCU2 at various intermediate stages of [2Fe-2S] cluster synthesis. Initially, Fe(II) is coordinated by free ISCU2 in a tetrahedral fashion (via Cys69, Asp71, Cys95 and His137). Binding of ISCU2 to (NIA)₂ was found to induce an equilibrium between the tetrahedral and a distinct octahedral coordination (via Asp71, Cys95, Cys138 and water ligands). The tetrahedral coordination was favored in (Fe-NIAU)₂, but the binding of FXN, leading to the formation of (Fe-NIAUX)₂, shifted the equilibrium towards the octahedral species. Specific intermolecular interactions between FXN and

ISCU2 assembly site residues support the formation of the octahedral species and are required for efficient [2Fe-2S] cluster synthesis. Furthermore, the 3D structure of the (Fe-NIAUX)₂ complex with persulfidated ISCU2 Cys138 was obtained by electron cryo-microscopy at 2.4 Å resolution, which is the first (NIAUX)₂ structure resolved below 3 Å. The Cys138 persulfide moiety participated in an octahedral Fe coordination similar to that in non-persulfidated complexes. Together, the aforementioned studies enabled the delineation of a detailed mechanistic route to physiological ISCU2 persulfidation as a decisive intermediate of [2Fe-2S] cluster synthesis.

The second project of this work focused on the function of human lipoyl synthase (LIAS), a mitochondrial radical S-adenosyl methionine (SAM) [4Fe-4S] enzyme. Lipoyl is a co-factor of α -ketoacid dehydrogenases as well as the glycine cleavage system and thus integral to mitochondrial carbon metabolism. LIAS possesses a catalytic and an auxiliary [4Fe-4S] cluster. The catalytic cluster receives electrons to initiate a radical SAM-based reaction mechanism in which two sulfur atoms from the auxiliary cluster are incorporated into an octanoyl substrate. Despite extensive characterisation of the molecular mechanism of lipoylation, the physiological electron donor for the catalytic cluster of human LIAS has remained unknown. To address this issue, an *in vitro* assay closely mimicking human lipoyl biosynthesis was developed. It was found that only the mitochondrial ferredoxin FDX1, but not the structurally similar FDX2, serves as an efficient electron donor for LIAS catalysis. This finding was corroborated by AlphaFold-based *in silico* analyses of LIAS-FDX interactions. FDX1 supported *in vitro* lipoylation much more efficiently than the commonly employed artificial reductant dithionite. The high specificity of lipoylation for FDX1 was found to be connected to the C-terminus, because removal of the conserved FDX2 C-terminus largely enhanced residual FDX2 function in lipoylation. The *in vitro* lipoylation assay was also employed to investigate the toxic effect of elesclomol (Ele), an anticancer agent and copper ionophore. It was shown that both Cu and the Ele:Cu complex, but not Ele alone, inhibit lipoylation, thus identifying the major cellular target of Ele toxicity.

In summary, this work structurally defined the cooperative action of five ISCU2 residues critical for consecutive states of *de novo* [2Fe-2S] cluster synthesis, and thereby provides valuable insights into the molecular dynamics of this process. Furthermore, the work contributes towards a better understanding of human lipoyl biosynthesis and the highly distinct functions of the two human FDXs. FDX1, in addition to its long-known role in steroidogenesis, was revealed as the physiological electron donor for LIAS catalysis.

Zusammenfassung

Eisen-Schwefel (Fe/S)-Cluster sind kleine anorganische Protein-Cofaktoren, die in fast allen bekannten Organismen vorkommen. Sie ermöglichen verschiedene Proteinfunktionen wie Elektronentransfer und Katalyse und werden für zahlreiche essentielle biologische Prozesse wie Zellatmung, Translation sowie DNA-Synthese und -Reparatur benötigt. Fe/S-Cluster weisen zumeist einfache Strukturen auf, wobei der rhombische [2Fe-2S]- und der kubische [4Fe-4S]-Typ am häufigsten sind. Für ihre Biosynthese und den Einbau in Zielproteine sind jedoch komplexe Proteinmaschinerien erforderlich. Die mitochondriale Fe/S-Protein-Biogenese erfordert bis zu 18 verschiedene Proteine der Fe/S-Cluster-Assemblierungs (ISC)-Maschinerie. Die frühe ISC-Maschinerie assembliert [2Fe-2S]-Cluster *de novo*, welche von der späten ISC-Maschinerie zu [4Fe-4S]-Clustern fusioniert und in Zielproteine eingebaut werden.

Obwohl die Funktionen vieler Proteine der ISC-Maschinerie eingehend charakterisiert wurden, sind die molekularen Mechanismen der mitochondrialen Fe/S-Protein-Biogenese und insbesondere der *de novo* Clustersynthese nicht vollständig verstanden. Im ersten der beiden Projekte dieser Arbeit sollte die Assemblierung von Fe und S auf dem Gerüstprotein ISCU2 bei der [2Fe-2S]-Clustersynthese untersucht werden. Hierbei werden ein Fe-Ion und ein Persulfidrest auf das ISCU2-Assemblierungszentrum übertragen, welches fünf konservierte Aminosäuren mit vermutlich funktionaler Bedeutung aufweist (Cys69, Asp71, Cys95, His137 und Cys138). Effiziente Persulfurierung von einem der drei konservierten ISCU2-Cysteine durch den heterodimeren Cystein-Desulfurasekomplex NFS1-ISD11-ACP ((NIA)₂) setzt die Bindung von ISCU2 (U) und FXN (X) voraus, wobei (NIAUX)₂ entsteht. Das Persulfid wird durch Elektronentransfer vom Ferredoxin FDX2 zu Sulfid reduziert. Schließlich führt die Dimerisierung von zwei [1Fe-1S]-ISCU2-Einheiten zur Bildung eines [2Fe-2S]-Clusters. In dieser Arbeit wurde gezeigt, dass NFS1 mit hoher Spezifität und Effizienz ISCU2 Cys138 persulfuriert, wobei kein intermediärer Schwefeltransfer über andere ISCU2-Cysteinreste beobachtet wurde. Die physiologisch relevante Persulfurierung erforderte voriges Binden eines Fe(II)-Ions an ISCU2. Weiterhin wurden die ISCU2-Reste Cys69, Cys95, Cys138 und wahrscheinlich Asp71 als Liganden des maturierten [2Fe-2S]-Clusters identifiziert.

Die Kombination struktureller, spektroskopischer und biochemischer Analysen erlaubte die Bestimmung der bisher weitestgehend unbekannten Fe-Koordination durch ISCU2 in aufeinanderfolgenden Zwischenschritten der [2Fe-2S]-Clustersynthese. Fe(II) wurde von freiem ISCU2 tetraedrisch koordiniert (über Cys69, Asp71, Cys95 und His137), während die ISCU2 Bindung an (NIA)₂ ein Gleichgewicht zwischen einer favorisierten tetraedrischen und einer oktaedrischen Koordination (über Asp71, Cys95, Cys138 und Wasserliganden) hervorrief. Bindung von FXN an (Fe-NIAU)₂ verschob das Gleichgewicht in

Richtung der oktaedrischen Spezies. Es wurden spezifische intermolekulare Wechselwirkungen zwischen FXN und ISCU2 identifiziert, die die Bildung der oktaedrischen Spezies unterstützen und eine effiziente [2Fe-2S]-Clustersynthese ermöglichen. Darüber hinaus wurde die Struktur von (Fe-NIAUX)₂ mit persulfuriertem ISCU2 Cys138 durch Elektronenkryomikroskopie mit einer Auflösung von 2.4 Å bestimmt, die erste Struktur eines (NIAUX)₂ Komplexes mit einer Auflösung unter 3 Å. Der Cys138-Persulfidrest war an einer oktaedrischen Fe-Koordination ähnlich der von nicht persulfurierten Komplexen beteiligt. Zusammengefasst ermöglichten die Studien die Beschreibung eines detaillierten molekularen Mechanismus der physiologischen ISCU2-Persulfurierung.

Das zweite Projekt dieser Arbeit befasste sich mit der Funktion humaner Lipoylsynthase (LIAS), einem mitochondrialen [4Fe-4S]-Enzym. Lipoyl ist Cofaktor von α -Ketosäure-Dehydrogenasen sowie des Glycin-spaltenden Systems und somit essentiell für den mitochondrialen Kohlenstoffmetabolismus. LIAS besitzt zwei [4Fe-4S]-Cluster, einen katalytischen und einen Hilfscluster. Der katalytische Cluster leitet durch Elektronentransfer eine Radikalreaktion ein, bei der zwei Schwefelatome aus dem Hilfscluster in ein Octanoylsubstrat inkorporiert werden. In dieser Arbeit sollte der unbekannte physiologische Elektronendonator des katalytischen Clusters humaner LIAS identifiziert werden. Dafür wurde ein *in vitro* Assay entwickelt, der die humane Lipoylsynthese nachstellt. Nur FDX1 und nicht das strukturell ähnliche FDX2 fungierte als effizienter Elektronendonator für die LIAS-Katalyse *in vitro*, in Übereinstimmung mit AlphaFold-basierten *in silico* Analysen von LIAS-FDX-Interaktionen. Die *in vitro* Lipoylsynthese war mit FDX1 sogar deutlich effizienter als mit dem üblicherweise verwendeten artifiziellen Reduktionsmittel Dithionit. Die hohe FDX1-Spezifität bei der Lipoylsynthese wurde auf den C-terminus zurückgeführt, da das Entfernen des konservierten C-Terminus von FDX2 dessen geringe Funktion *in vitro* erheblich verbesserte. Weiterhin wurde die Wirkung des Antikarzinogens und Kupferionophors Elesclomol (Ele) auf die Lipoylsynthese *in vitro* untersucht. Es zeigte sich, dass sowohl Cu als auch der Ele:Cu-Komplex, aber nicht Ele allein, die Lipoylsynthese hemmen, wodurch ein wesentliches Ziel der Ele-Toxizität identifiziert wurde.

Zusammenfassend ermöglichte diese Arbeit die strukturelle Bestimmung der kooperativen Funktion von fünf ISCU2-Resten, die von essentieller Bedeutung für aufeinanderfolgende Stadien der *de novo* [2Fe-2S]-Clustersynthese sind, und bietet dadurch wertvolle Einblicke in die molekulare Dynamik dieses Prozesses. Darüber hinaus trägt die Arbeit zu einem besseren Verständnis der humanen Lipoylsynthese und der unterschiedlichen Funktionen der beiden menschlichen Ferredoxine bei. FDX1 wurde als physiologischer Elektronendonator für die LIAS-Katalyse identifiziert, zusätzlich zu seiner seit langem bekannten Rolle in der Steroidsynthese.

1 Introduction

1.1 Iron-sulfur proteins

Iron-sulfur (Fe/S) clusters represent a group of ancient inorganic protein cofactors that likely already existed before the first lifeform emerged on earth (Goldman & Kacar, 2021). Fe/S proteins are integral to many highly conserved processes and metabolic pathways essential to the viability of almost all known organisms (Braymer *et al.*, 2020). The most common Fe/S clusters are of the [2Fe-2S]- and [4Fe-4S]-type, composed of ferric (Fe^{3+} or Fe(III)) or ferrous (Fe^{2+} or Fe(II)) Fe and sulfide (S^{2-}) ions. Whilst Fe/S proteins commonly facilitate electron transfer by switching between the 2+ and 3+ oxidation state of their Fe ions, several additional functions in a variety of proteins are known that have been acquired during evolution. Some Fe/S clusters are merely necessary for stabilizing a protein fold required for function, e.g., the interaction with partner proteins, as shown for DNA polymerases (Netz *et al.*, 2012). Furthermore, some Fe/S proteins function as transcriptional or translational regulators, using specific Fe/S cluster-dependent sensing mechanisms. These include the assembly or conversion of Fe/S clusters in response to environmental stimuli, like Fe or oxygen concentrations (Anderson *et al.*, 2012; Johnson *et al.*, 2005; Mettert & Kiley, 2015). Finally, Fe/S clusters are required for the catalytic function of certain enzymes, e.g., the aconitase-catalysed isomerization of citrate to isocitrate (Lloyd *et al.*, 1999). A particularly remarkable example of Fe/S cluster function(s) is found in the biosyntheses of the lipoyl and biotin cofactor. Both lipoyl and biotin synthase bind two Fe/S clusters. One cluster is employed to initiate a radical-based reaction mechanism in which sulfur atoms from the second cluster are incorporated into the nascent cofactor (Fugate & Jarrett, 2012; McCarthy & Booker, 2017; Tao *et al.*, 2018).

1.1.1 The different Fe/S cluster types

The presence of multiple distinct Fe/S cluster types (Figure 1) contributes to the functional diversity of Fe/S proteins. Of the [2Fe-2S]-, [3Fe-4S]- and [4Fe-4S]-type, [4Fe-4S] clusters are the most abundant, followed by [2Fe-2S] clusters. The most complex clusters contain 7 – 8 Fe and 7 – 9 sulfide ions and perform specialized functions, e.g., in nitrogenases and hydrogenases (Jeoung *et al.*, 2020). $\text{Fe}^{2+/3+}$ redox transitions of Fe/S clusters are the basis for their most widespread function as one-electron carriers. Depending on cluster type and protein environment, redox potentials range from -700 mV to +400 mV (Meyer, 2008). Among others, cluster stability, redox potential and spin state are affected by the protein ligands of the cluster's Fe ions (Beinert *et al.*, 1997; Johnson

et al., 2005). Whereas clusters are typically coordinated via protein Cys residues, alternative coordination modes include His, Asp, Ser or Arg residues, as well as non-protein organic (e.g., glutathione) or inorganic ligands (e.g., CO or CN⁻) (Johnson *et al.*, 2005; Lill, 2009; Meyer, 2008).

Fe/S cluster-related mononuclear [1Fe-0S] centres exhibiting a single Fe^{2+/3+} ion tetrahedrally coordinated by four Cys ligands are found in rubredoxins, small (often only 6 kDa) proteins functioning as electron carriers in numerous biological processes (Li *et al.*, 2019). Prominent modes of [2Fe-2S] cluster binding are the classic four Cys ligation of [2Fe-2S]-ferredoxins (FDXs) and the two Cys, two His coordination present in Rieske proteins. The ligation of one of the Fe ions with two His residues induces an elevated redox potential (Bian & Cowan, 1999; Brown *et al.*, 2008; Meyer, 2008). The rhombic [2Fe-2S] cluster can switch between an oxidised [2Fe-2S]²⁺ ground state and a reduced [2Fe-2S]¹⁺ paramagnetic state (Johnson *et al.*, 2005). Whereas [2Fe-2S]¹⁺ clusters usually exhibit localized electrons in a Fe²⁺/Fe³⁺ pair, clusters of higher complexity possess delocalized Fe^{2.5+}/Fe^{2.5+} pairs (Beinert *et al.*, 1997). The cubic [4Fe-4S] clusters include [4Fe-4S]^{1+/2+} FDX-type and [4Fe-4S]^{2+/3+} high potential Fe/S protein (HiPIP)-type redox couples (Rupnik *et al.*, 2011). Some [4Fe-4S] clusters exhibit a free (non-ligated) Fe site, enabling substrate binding and activation for enzymatic turnover, as in aconitase and lipoyl synthase (LIAS) (Johnson *et al.*, 2005; McCarthy & Booker, 2017).

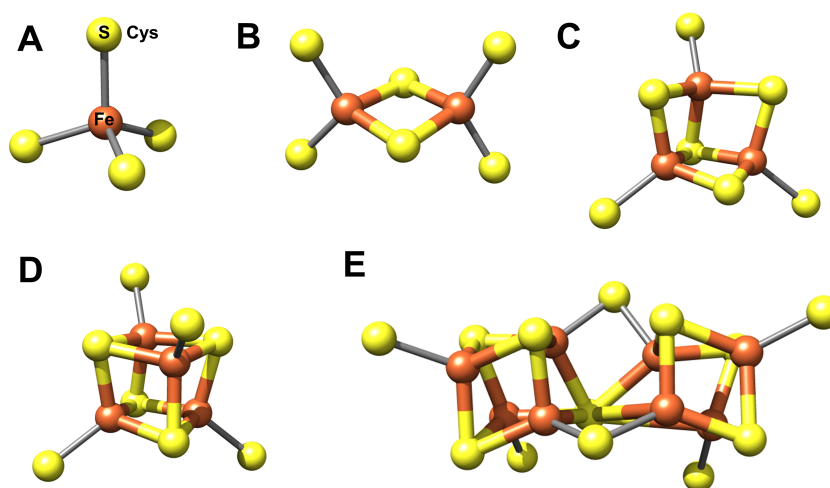


Figure 1: 3D structures of common Fe/S cluster types. Fe^{2+/3+} is coordinated by protein ligands (most often Cys residues) and inorganic sulfide (S²⁻). Fe/S clusters are indicated by colored sticks and Cys ligands by grey sticks. **A)** A rubredoxin [1Fe-0S] site constitutes a single Fe (orange) ion coordinated by four Cys sulfur (yellow) ligands. **B-E)** [2Fe-2S] (**B**), [3Fe-4S] (**C**) and [4Fe-4S] clusters (**D**) as well as the more complex nitrogenase [8Fe-7S] cluster (**E**). Adapted from Beinert *et al.*, 1997.

1.1.2 Diverse functions of Fe/S proteins

Cells possess around 50 – 70 different Fe/S proteins in eukaryotes, whereas the number is generally even higher in prokaryotes (Andreini *et al.*, 2016; Andreini *et al.*, 2017; Lill & Freibert, 2020). Eukaryotic Fe/S proteins are found in mitochondria, plastids, cytosol, nucleus and the outer endoplasmic reticulum. Fe/S proteins are required for essential mitochondrial functions, including oxidative phosphorylation by the respiratory chain (complexes I – III), the tricarboxylic acid (TCA) cycle (aconitase and complex II) and lipid β -oxidation as well as heme, biotin (only in plants and fungi (Marquet *et al.*, 2001)) and molybdenum cofactor (MoCo) biosyntheses (Figure 2) (Lill & Freibert, 2020). Respiratory chain complex I is a particularly remarkable example, the human complex containing eight Fe/S clusters as part of an electron transfer chain (ETC) (Wirth *et al.*, 2016). Plastidial Fe/S protein functions include photosynthetic electron transport (e.g., the cytochrome b_6f complex), chlorophyll metabolism, nitrogen as well as sulfur assimilation and carbon fixation (Przybyla-Toscano *et al.*, 2018). The lipoyl cofactor required, e.g., for formation of acetyl-CoA, substrate of the TCA cycle, is generated by LIAS, an Fe/S enzyme present in both mitochondria and plastids (Lill & Freibert, 2020; Przybyla-Toscano *et al.*, 2018). In addition, numerous Fe/S proteins involved in DNA replication and repair as well as chromosome segregation are crucial for maintenance of the nuclear genome (Fuss *et al.*, 2015; Lill & Freibert, 2020). Involvement of Fe/S proteins further extends to transcription and translation, including modifications of transfer RNAs and the ribosomal elongation factor 2 (Kimura & Suzuki, 2015; Tsuda-Sakurai & Miura, 2019). The cytosolic iron regulatory protein 1 (IRP1) regulates in an Fe/S cluster-dependent fashion the expression of proteins involved in Fe homeostasis. Additional functions of Fe/S proteins are found in nucleotide metabolism, antiviral response and mitosis (Lill & Freibert, 2020). The essential metabolic functions of Fe/S proteins underline the necessity of a regulated way to biosynthesize Fe/S cofactors and insert them into apo-proteins. The *in vivo* biogenesis of Fe/S proteins is performed by complex machineries, which in humans count at least 29 proteins in total (Lill & Freibert, 2020). Impairment of these biosynthetic pathways affects multiple cellular processes and can cause metabolic, neurological and haematological dysfunctions potentially fatal in early childhood (Beilschmidt & Puccio, 2014; Frazier *et al.*, 2019; Lill & Freibert, 2020; Stehling *et al.*, 2014).

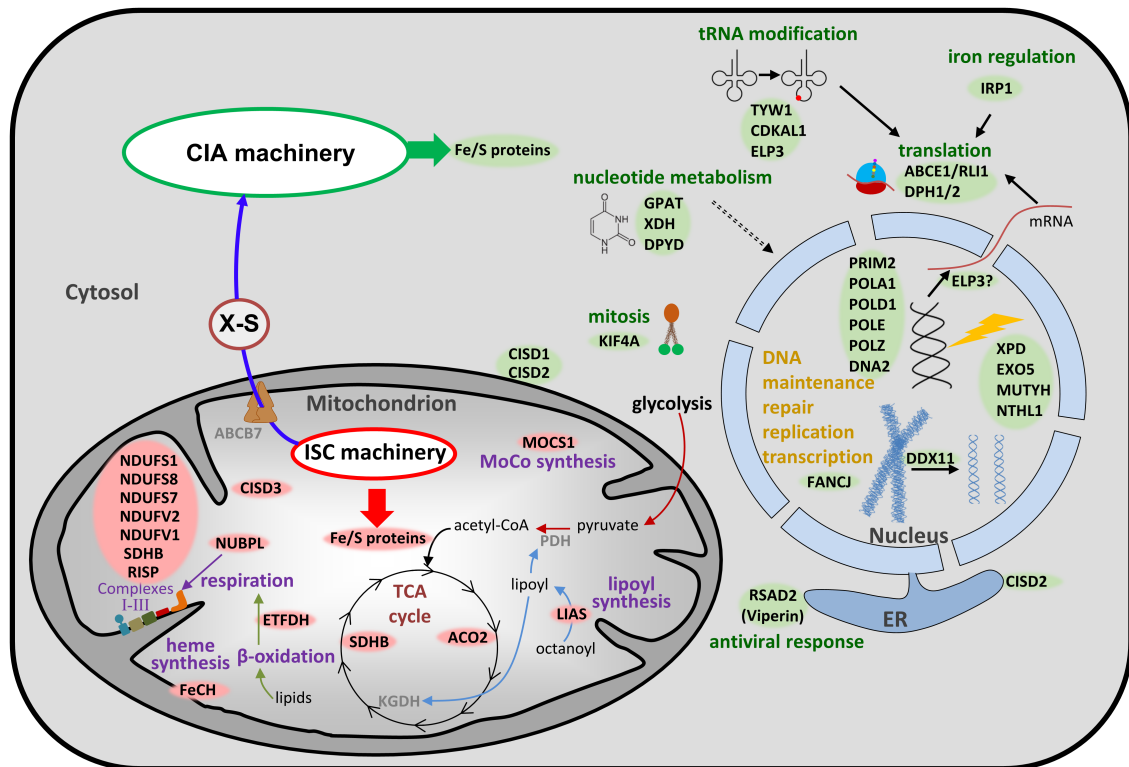


Figure 2: Functions of Fe/S proteins in non-green eukaryotic cells. The ISC (Fe/S cluster assembly) machinery supplies Fe/S clusters to the numerous mitochondrial Fe/S proteins (highlighted in red). These participate in a number of vital pathways including cellular respiration, the TCA cycle and biosynthesis of lipoyl, heme and molybdenum (MoCo) cofactors. The CIA (cytosolic Fe/S assembly) machinery depends on an unknown compound (X-S) formed by the ISC machinery and matures extra-mitochondrial Fe/S proteins (highlighted in green). These fulfill dedicated functions, e.g., in nucleotide metabolism, transfer RNA (tRNA) modification, Fe regulation, translation and DNA replication and maintenance. ER: endoplasmic reticulum. Adapted from Lill & Freibert, 2020.

1.2 Fe/S protein biogenesis systems

Whereas the individual factors involved in Fe/S protein assembly are often highly distinct between different organisms and organelles, common principles underlie the complex pathways of Fe/S protein biogenesis (Figure 3) (Braymer *et al.*, 2020). These include the *de novo* biosynthesis of an Fe/S cluster on a protein scaffold, followed by insertion into recipient apo-proteins with the help of dedicated transfer proteins. *De novo* formation of an Fe/S cluster is realised by the sequential assembly of inorganic sulfide and Fe ions on the scaffold, which exhibits an assembly site suitable for coordination of an Fe/S cluster and its synthesis intermediates. A key feature of the scaffold protein is that the assembled cofactor is bound with a certain degree of lability, allowing its transfer to downstream acceptor proteins. Fe/S cluster delivery to specific targets typically is a multi-step process involving transient binding by transfer proteins.

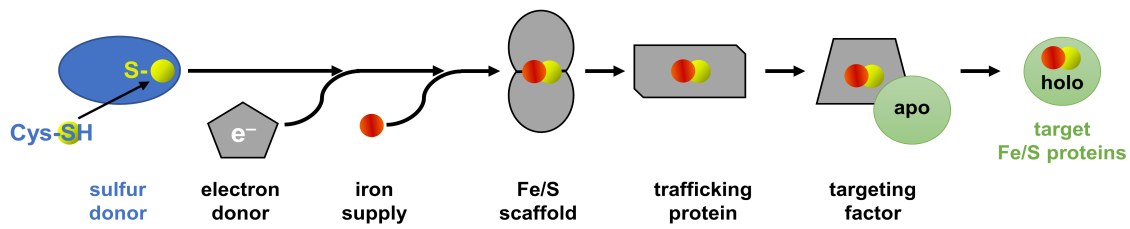


Figure 3: General principle of Fe/S protein biogenesis. *De novo* Fe/S cluster formation on a dedicated scaffold protein requires sulfur, electrons and Fe. A cysteine desulfurase converts free cysteine to alanine, forming a persulfide on a catalytic protein-bound Cys residue. The persulfide sulfur (S^0) is then transferred to a conserved Cys of the scaffold protein. Reduction of sulfur (S^0) to sulfide (S^{2-}) requires electron flow to the scaffold. In mitochondria of eukaryotes and bacteria, electrons are supplied by FDXs. Whether delivery of Fe to the scaffold requires additional proteins or other chelating factors is not clear to date. The synthesized Fe/S cluster is bound to the scaffold in a labile fashion. Trafficking proteins either transfer the Fe/S cluster directly to apo-proteins or via an additional step employing targeting factors, which often exhibit high specificity to certain Fe/S protein targets. Adapted from Braymer *et al.*, 2020.

Depending on the organism, one or more of four distinct machineries is performing Fe/S protein biogenesis. Prokaryotes rely either on the Fe/S cluster assembly (ISC) or sulfur mobilization (SUF) system for general Fe/S protein biogenesis. In some organisms like *Escherichia coli*, both systems are present but differentially regulated, depending on environmental conditions (Blahut *et al.*, 2020). The nitrogen fixation (NIF) machinery is specifically required for the maturation of nitrogenase, an enzyme complex binding multiple and complex Fe/S clusters and catalysing the ATP-dependent conversion of molecular nitrogen to ammonia (Einsle & Rees, 2020). Due to its specialised function, the NIF system is mainly found in nitrogen-fixing bacteria, with few exceptions (Braymer *et al.*, 2020). ISC, SUF and NIF machineries generally include a cysteine desulfurase providing persulfide sulfur to a scaffold protein for *de novo* Fe/S cluster formation.

Eukaryotes possess organelle-specific Fe/S protein biogenesis machineries. Whilst mitochondria rely on the ISC system, the SUF system is found in plastids. The mitochondrial ISC system is highly conserved in eukaryotes and also shows a marked similarity to the bacterial counterpart, owed to the fact that the evolutionary ancestor of mitochondria is an α -proteobacterium (Braymer *et al.*, 2020; Zimorski *et al.*, 2014). Similarly, the plastidial and bacterial SUF system show a close resemblance of core components related to the evolutionary origin of plastids from a cyanobacterium. Maturation of cytosolic and nuclear Fe/S proteins is performed by the cytosolic Fe/S cluster assembly (CIA) machinery, which in contrast to all other systems does not form Fe/S clusters *de novo* from Fe and sulfide. Instead, it relies on a yet unknown sulfur-containing compound produced by the mitochondrial ISC system and exported to the cytosol (Ellinghaus *et al.*,

2021). Since in this work functions of human mitochondrial Fe/S proteins were investigated, Fe/S protein biogenesis by the mitochondrial ISC system will be described in detail hereinafter, using the nomenclature of the human proteins.

1.3 Mitochondrial Fe/S protein biogenesis

The human mitochondrial ISC system encompasses up to 18 different proteins and its function can formally be divided into three steps: (1) *De novo* [2Fe-2S] cluster synthesis performed by the core ISC complex, (2) [2Fe-2S] cluster trafficking and insertion, and (3) [4Fe-4S] cluster synthesis and insertion (Figure 4).

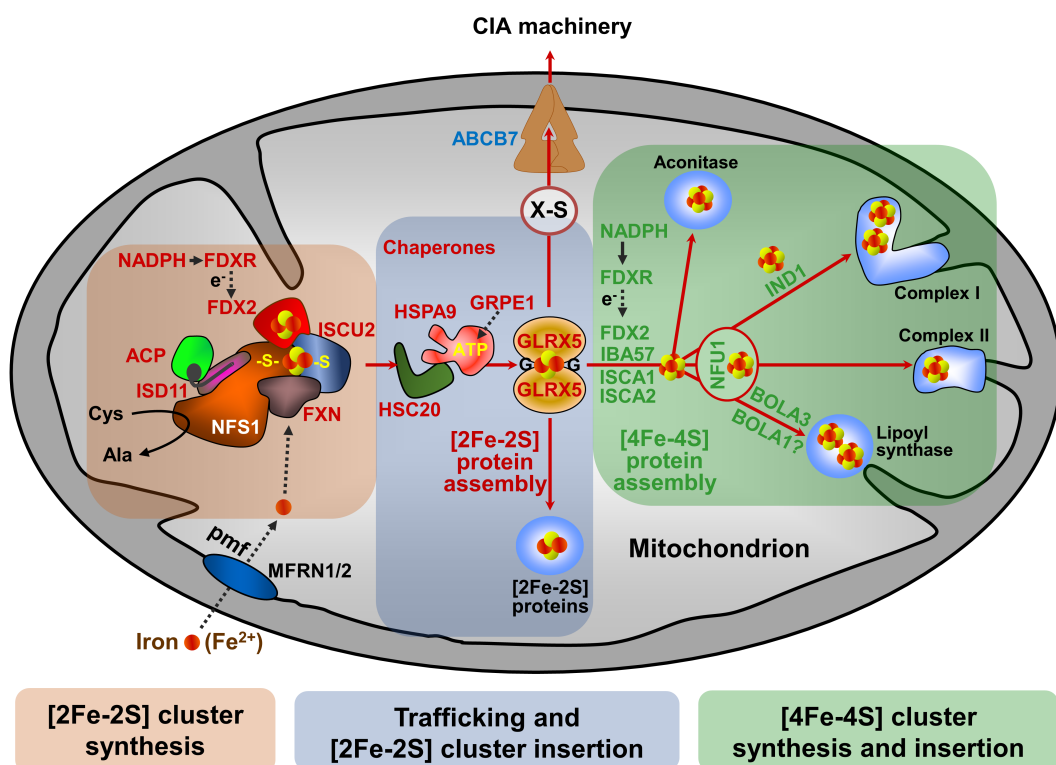


Figure 4: Mitochondrial Fe/S protein biogenesis by the ISC machinery. The pathway is formally divided into three steps, indicated by colored boxes. **1)** (red box): *De novo* [2Fe-2S] cluster synthesis requires the core ISC complex constituted of the sulfur-supplying cysteine desulfurase complex (NFS1-ACP-ISD11), Fe/S assembly scaffold ISC2, frataxin (FXN) and electron donor FDX2. FDX2 receives electrons via ferredoxin reductase (FDXR) and NADPH. Only one half of the dimeric heterocomplex is shown. The Fe importers MFRN1/2 supply the required Fe(II), dependent on a proton motif force (pmf). **2)** (blue box): An ATP-dependent chaperone system comprising HSPA9, HSC20 and GRPE1 transfers the [2Fe2S] cluster to glutaredoxin 5 (GLRX5). The cluster is coordinated in a GLRX5 homodimer via one Cys residue of each monomer and furthermore two non-covalently bound molecules glutathione (G). [2Fe-2S]-GLRX5 acts as donor for [2Fe-2S] proteins and [4Fe-4S] cluster assembly as well as ABCB7, which exports a yet unknown compound (X-S) needed for cytosolic Fe/S cluster assembly by the CIA machinery. **3)** (green box): The assembly of [4Fe-4S] clusters is performed by the proteins IBA57, ISCA1 and ISCA2, with electrons supplied via NADPH, FDXR and FDX2. Subsequent insertion into specific apo-proteins requires the targeting factors NFU1, IND1, BOLA1 and BOLA3. Adapted from Lill & Freibert, 2020.

1.3.1 *De novo* [2Fe-2S] cluster formation in mitochondria

1.3.1.1 Structure and function of the core ISC complex

[2Fe-2S] clusters are assembled in mitochondria in a complex process requiring seven different proteins. Six of these form the so-called core ISC complex with the pyridoxal-phosphate (PLP)-dependent cysteine desulfurase NFS1 at its centre (Figure 5A). The dimeric structure of NFS1 with the PLP binding site at its centre close to the interface of both units is conserved among cysteine desulfurases, which belong to the fold type I subfamily of PLP-dependent enzymes (Percudani & Peracchi, 2009; Schneider *et al.*, 2000). The NFS1 dimer binds the 11 kDa desulfurase-interacting protein 11 (ISD11) and the acyl carrier protein (ACP) on each unit, forming a NFS1-ISD11-ACP ((NIA)₂) heterodimer, with the two ISD11 units making contact to each other on the surface of NFS1. ACP of the mitochondrial fatty acid synthesis system II (mtFAS II) inserts a phosphopantetheine-bound acyl moiety into a cavity of ISD11. The described arrangement has been supported by a number of studies (Boniecki *et al.*, 2017; Cai *et al.*, 2018a; Fox *et al.*, 2019; Freibert *et al.*, 2021). A (NIA)₂ complex in which the NFS1 units are dramatically rotated, leading to surface exposure of the PLP sites, has been reported based on X-ray crystallography (Cory *et al.*, 2017). Since this conformation was not reported for any other PLP-dependent enzyme, its physiological relevance is not clear.

(NIA)₂ serves as a platform for the dynamic binding of the other core ISC components ISCU2 (U), frataxin (FXN or X) and FDX2 (F) throughout the biosynthetic process of [2Fe-2S] cluster formation on ISCU2 (Figure 5B). The underlying mechanism includes FXN-facilitated persulfide transfer from NFS1 to ISCU2 and subsequent FDX2-mediated reduction of the persulfide (S⁰) to sulfide (S²⁻) and is discussed in detail in the following chapters. Binding of ISCU2 at opposing tips of (NIA)₂ with its Fe/S cluster assembly site facing NFS1 forms a stable (NIAU)₂ complex. So far, crystal structures could be obtained for the (NIAU)₂ complex but not (sub-)complexes including FXN or FDX2, in line with a less stable interaction of these two proteins with the other core ISC components. Small-angle X-ray scattering (SAXS) experiments with *Chaetomium thermophilum* core ISC components indicated binding of FXN in a cleft between NFS1 and ISCU2 (Boniecki *et al.*, 2017). A cryo-EM structure obtained for the human (NIAUX)₂ complex showed a similar location, with FXN making contacts to ISCU2 and both NFS1 units (Fox *et al.*, 2019). A high resolution structure showing FDX2 binding to the human core ISC complex has not yet been published. However, based on SAXS and nuclear magnetic resonance (NMR) analyses of *C. thermophilum* and yeast proteins (Boniecki *et al.*, 2017; Webert *et al.*, 2014), FDX2 binding to ISCU2 and NFS1 was shown, with FXN and FDX2 binding to opposite sides of ISCU2.

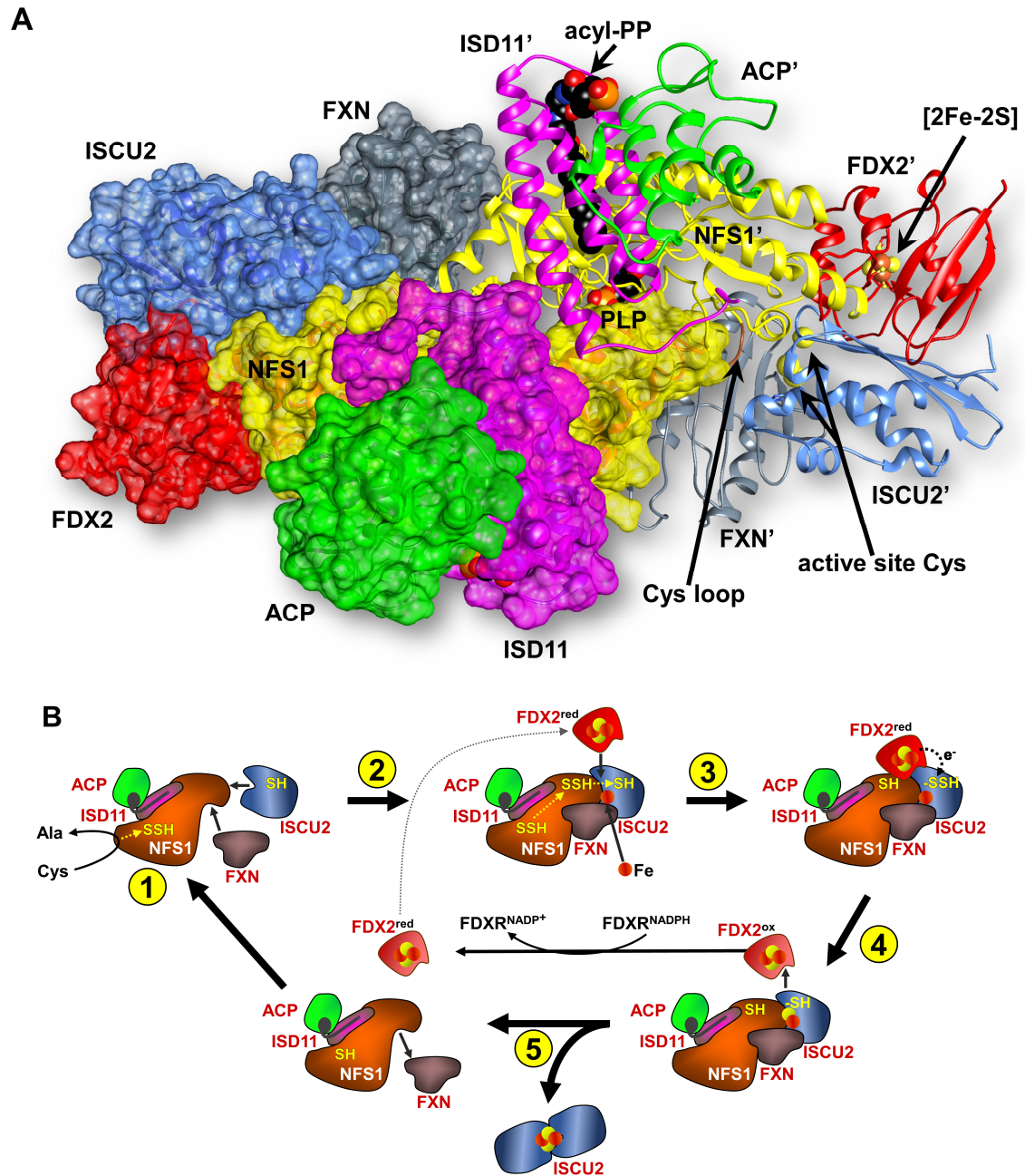


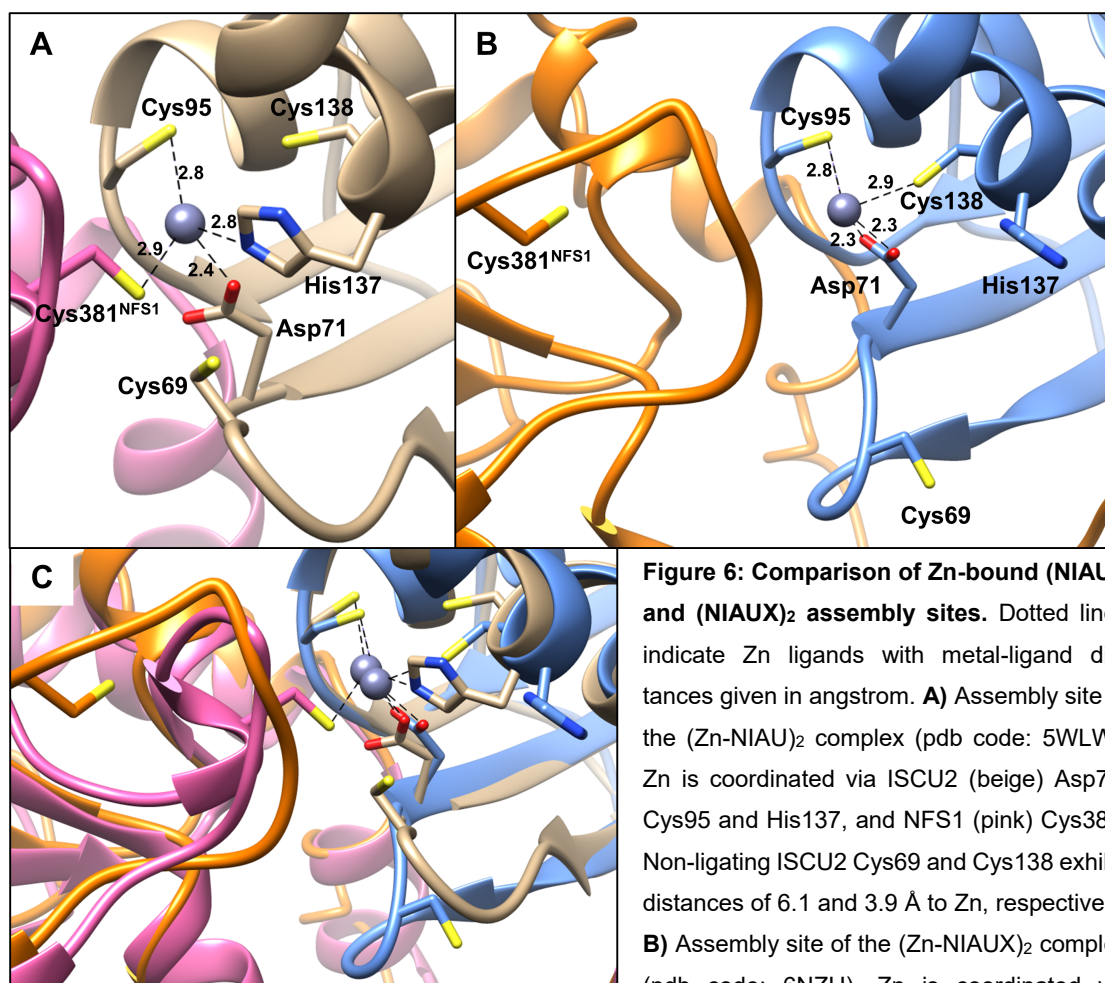
Figure 5: Structure and function of the core ISC complex. **A)** Structure of the core ISC complex based on X-ray crystallography, cryo-EM, SAXS and NMR. The left half of the heterodimer shows individual proteins in surface representation and the right half as ribbon model. NFS1-bound PLP is depicted by spheres and the flexible catalytic loop is colored brown. Cys residues of the ISCU2 Fe/S cluster assembly site, the ACP-bound acyl phosphopantetheinyl (PP) moiety and the FDX2-bound [2Fe-2S] cluster are depicted as spheres. Colors: NFS1 (yellow), ISD11 (magenta), ACP (green), ISCU2 (blue), FXN (grey), FDX2 (red). **B)** Model of the catalytic cycle of the core ISC complex. For reasons of simplification, only one half of the heterodimeric complex (**A**) is shown. **1)** NFS1 abstracts sulfur from free cysteine, forming a persulfide ($-SSH$) on the conserved Cys381 located on a flexible loop of NFS1. **2)** The persulfide is transferred to a Cys residue of ISCU2. The transfer is facilitated by FXN. It is not clear to date if FXN may fulfill an additional function in the delivery of Fe to ISCU2. **3)** Electron transfer from reduced FDX2 enables the reduction of the persulfide (S^0) to sulfide (S^{2-}). **4)** FDX2 dissociates from the biosynthetic complex and is re-reduced by FDXR in an NADPH-dependent manner. **5)** Interaction of the N-terminal Tyr35 residues of two ISCU2 monomers enables their dimerization, forming [2Fe-2S]-ISCU2 (Freibert *et al.*, 2021). Taken from Lill & Freibert, 2020.

1.3.1.2 Persulfide formation on ISCU2

ISCU2 receives persulfide sulfur required for cluster assembly via the PLP-dependent function of the cysteine desulfurase NFS1. The internal aldimine formed by PLP and the ϵ -amino moiety of Lys258 is positioned at the core of the NFS1 dimer. Cysteine can access the PLP site via a cavity located close to the ISCU2 binding site and reacts with PLP in a mechanism involving 13 intermediates (Behshad & Bollinger, 2009; Zheng & Dean, 1994), including the formation of an external cysteine aldimine in which covalent bonding of Lys258 and PLP is broken. The sulfur of a subsequently formed ketimine intermediate is transferred onto the side chain of the conserved catalytic Cys381 of NFS1, forming a persulfide, and the reaction proceeds with release of alanine and re-formation of the internal aldimine. Cys381 is located on a flexible loop of NFS1. Swinging of the loop from the NFS1 PLP site to ISCU2 enables persulfide transfer to one of the Cys residues of the ISCU2 Fe/S cluster assembly site. Even though its flexibility has rendered structural resolution of the catalytic loop challenging (Blahut *et al.*, 2019; Boniecki *et al.*, 2017; Freibert *et al.*, 2021; Kaiser *et al.*, 2000), variable positioning of Cys381^{NFS1} closer to either the PLP or ISCU2 assembly site has been observed. A crystal structure of (NIAU)₂ shows an outwards extended catalytic loop, Cys381^{NFS1} coordinating a Zn ion bound to the ISCU2 assembly site (Figure 6A) (Boniecki *et al.*, 2017). Another conformation with Cys381^{NFS1} positioned halfway between ISCU2 and PLP site, the catalytic loop making direct contact to FXN, was found in a (NIAUX)₂ cryo-EM structure containing Zn-bound ISCU2. Since FXN has been found to accelerate persulfide transfer from NFS1 to ISCU2 (Gervason *et al.*, 2019; Parent *et al.*, 2015), it has been speculated that FXN-induced rearrangement of the catalytic loop might be important for efficient Fe/S cluster synthesis (Fox *et al.*, 2019; Patra & Barondeau, 2019).

ISCU2 possesses five assembly site residues that may participate in coordination of a [2Fe-2S] cluster and its potential biosynthetic intermediates: Three strictly conserved Cys residues (Cys69, Cys95 and Cys138) as well as Asp71 and His137. Mass spectrometric analysis of *in vitro* persulfidation reactions suggested Cys138 to be the persulfide acceptor of human ISCU2 (Parent *et al.*, 2015). In the (Zn-NIAU)₂ crystal structure showing the catalytic NFS1 loop in a putative persulfide-donating-like conformation, a Zn ion is coordinated by Asp71, Cys95 and His137 of ISCU2 as well as Cys381^{NFS1} (Figure 6A). Remarkably, Cys138^{ISCU2} exhibits the farthest distance (6.5 Å) from Cys381^{NFS1} among all ISCU2 Cys residues (Boniecki *et al.*, 2017). Furthermore, His137 blocks direct access to Cys138. It is therefore conceivable that persulfide transfer to Cys138^{ISCU2} might proceed via intermediate persulfidation of either Cys69^{ISCU2} located on a flexible loop, or Cys95^{ISCU2}. The latter exhibits distances of 3.8 Å and 4.8 Å to Cys138^{ISCU2} and Cys381^{NFS1}, respectively. However, the cryo-EM structure of (Zn-NIAUX)₂ exhibits a

changed conformation with Cys69 and His137 folded away from the ISCU2 assembly site and interacting with FXN (discussed in chapter 1.3.1.3), whereas Zn is coordinated by Asp71, Cys95 and Cys138 (Figure 6B). Displacement of His137 might enable direct persulfide transfer from Cys381^{NFS1} to Cys138^{ISCU2}. Nevertheless, also in this structure Cys95^{ISCU2} is more accessible to Cys381^{NFS1}, making it a viable candidate as an intermediate persulfide acceptor.



Even though Zn-bound ISCU2 has been subject of many structural and biochemical studies that employ proteins recombinantly expressed in *E. coli* (Boniecki *et al.*, 2017; Fox *et al.*, 2018; Iannuzzi *et al.*, 2014; Liu *et al.*, 2005; Ramelot *et al.*, 2004), Zn is most likely not physiologically relevant for Fe/S cluster synthesis (Gervason *et al.*, 2019). Nevertheless, due to similar physical properties of Zn(II) and Fe(II), it seems likely that the ISCU2

assembly site conformations shown in Figure 6 would be similar if Zn(II) was substituted with Fe(II). *In vitro* persulfidation of ISCU2 by NFS1 was shown to be efficient in presence of either Zn or Fe (Gervason *et al.*, 2019). However, detailed structural insights into the Fe and/or persulfide-bound state of ISCU2 are lacking.

1.3.1.3 The function of FXN in the core ISC complex

FXN is crucial for efficient *de novo* Fe/S cluster synthesis, and impaired function of the protein causes the rare but fatal neurodegenerative disease Friedreich's Ataxia (FRDA) (Cook & Giunti, 2017; Santos *et al.*, 2010; Vaubel & Isaya, 2013). FXN has been proposed as an Fe donor for Fe/S cluster synthesis. Negatively charged residues of surface-exposed α -helices of this acidic protein (pI 4.7) have been suggested to be involved in Fe-delivery to the ISCU2 assembly site (Stemmler *et al.*, 2010). However, the published (NIAUX)₂ cryo-EM structure shows these residues most likely not being suitably positioned for Fe-delivery (Fox *et al.*, 2019). Since ISCU2 could potentially enter the ISC complex preloaded with Fe, an additional Fe-supplying factor may not be required, or needs to function in loading ISCU2.

Multiple studies support human FXN to function as an allosteric activator of Fe/S cluster biosynthesis. *In vitro* sulfide production mediated by NFS1 is accelerated in presence of both FXN and ISCU2 (Bridwell-Rabb *et al.*, 2011; Freibert *et al.*, 2021; Tsai & Barondeau, 2010). Most importantly, persulfide transfer from NFS1 to ISCU2 as well as [2Fe-2S] cluster formation on ISCU2 are dramatically accelerated in presence of FXN (Bridwell-Rabb *et al.*, 2014; Bridwell-Rabb *et al.*, 2011; Fox *et al.*, 2015; Freibert *et al.*, 2021; Gervason *et al.*, 2019; Parent *et al.*, 2015; Patra & Barondeau, 2019). Notably, persulfide formation on ISCU2 has been indicated to be the rate-limiting step of Fe/S cluster synthesis (Gervason *et al.*, 2019). Despite the proposed function of FXN in modulating the conformation of the catalytic NFS1 loop (see chapter 1.3.1.2), the molecular mechanism(s) underlying FXN function are not well understood.

As mentioned in the previous chapter, comparison of (NIAU)₂ and (NIAUX)₂ structures indicates a FXN-induced rearrangement of ISCU2, folding residues Cys69^{ISCU2} and His137^{ISCU2} away from the ISCU2 assembly site (Figure 6). The His137^{ISCU2} side chain is inserted into a hydrophobic pocket formed by FXN residues Trp155, Ser157, Pro163 and Arg165 (Figure 7), the arrangement apparently being stabilized by His137^{ISCU2}–Trp155^{FXN} π -stacking. Gln148^{FXN} and Asn151^{FXN} are in close proximity to Cys69^{ISCU2}, potentially allowing for H-bonding. The FXN-induced “opening” of the ISCU2 assembly site might be an important step in Fe/S cluster synthesis. This is in line with exchanges of FXN Gln148, Trp155 and Arg165 being found in FRDA patients (Santos *et al.*, 2010). However, the function of the discussed FXN residues has not been investigated in detail.

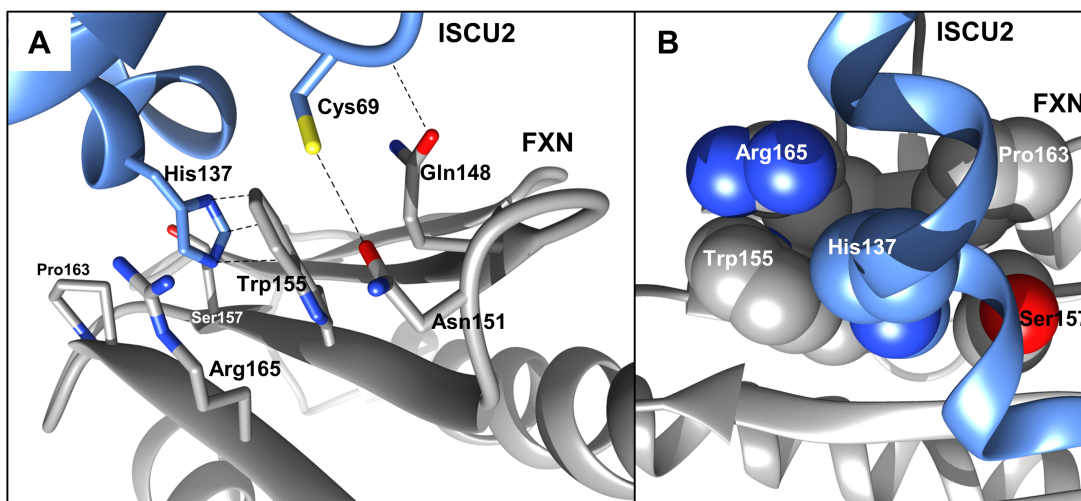


Figure 7: Interaction of ISCU2 and FXN in the (NIAUX)₂ complex. ISCU2, blue; FXN, grey; pdb code: 6NZU. **A)** The His137^{ISCU2} side chain is inserted into a pocket formed by FXN residues Trp155, Ser157, Pro163 and Arg165, with major hydrophobic interactions between His137^{ISCU2} and Trp155^{FXN}. Gln148^{FXN} and Asn151^{FXN} may form H-bonds with the Cys69^{ISCU2} backbone amide and thiol moiety, respectively. **B)** The hydrophobic pocket viewed from top, with respective FXN residues and His137^{ISCU2} shown as spheres.

1.3.1.4 FDX2-mediated [2Fe-2S] cluster maturation

After Fe- and persulfide-binding of ISCU2, the persulfide sulfur (S^0) needs to be reduced to sulfide (S^{2-}) to allow formation of a mature [2Fe-2S] cluster. Whilst under *in vitro* conditions the artificial reductant dithiothreitol (DTT) can facilitate cluster formation (Adinolfi *et al.*, 2009; Fox *et al.*, 2015; Tsai & Barondeau, 2010; Yoon & Cowan, 2003), FDX2 is the physiological electron donor in Fe/S protein biogenesis (Freibert *et al.*, 2018; Gervason *et al.*, 2019; Sheftel *et al.*, 2010; Webert *et al.*, 2014). Compared with the initial formation of a persulfide on ISCU2, the following FDX2-dependent maturation of the cluster has been indicated to proceed around 2-fold faster (Gervason *et al.*, 2019). However, this step is mechanistically not well understood. A recent study revealed the N-terminal Tyr35 of ISCU2 to be essential for [2Fe-2S] cluster formation by facilitating dimerization of two ISCU2 molecules via hydrophobic Tyr-Tyr interaction (Freibert *et al.*, 2021). The final [2Fe-2S] ISCU2 homodimer might hence be formed from two [1Fe1S]-bound ISCU2 monomers. This notion is also supported by the fact that sequential formation of a complete [2Fe-2S] unit on one ISCU2 monomer would in all likelihood require more metal ligands than available. Since ISCU2 molecules are placed on opposite ends of the core ISC complex at great distance from each other (Figure 5A), dimerization can only be achieved if ISCU2 monomers from two individual core ISC complexes interact, as supported by *in vitro* experiments (Freibert *et al.*, 2021).

The exact coordination mode of the mature [2Fe-2S] cluster in human ISCU2 is not clear to date. The general lability of ISCU2-bound Fe/S clusters has hindered structural elucidation so far, and high resolution structures of [2Fe-2S]-IscU have only been reported using homologs from thermophilic archaea or bacteria (Kunichika *et al.*, 2021; Marinoni *et al.*, 2012; Shimomura *et al.*, 2008). In all published structures, all three assembly site Cys residues of one IscU monomer are participating in [2Fe-2S] cluster ligation. The fourth ligand is either Asp or His of the same IscU molecule, or a Cys ligand from a second IscU molecule or NFS1. In most structures, the IscU assembly site Asp is exchanged to Ala, which was reported to increase stability of the bound Fe/S cluster (Mansy *et al.*, 2002; Marinoni *et al.*, 2012; Shimomura *et al.*, 2007; Wu *et al.*, 2002a). Replacement of Asp interferes with the physiologically essential ability of IscU to transfer its cluster to acceptor proteins (Wu *et al.*, 2002b). The only published structure of WT [2Fe-2S]-IscU (from *Methanothrix thermoacetophila*) shows Asp as the fourth ligand (Kunichika *et al.*, 2021).

1.3.1.5 The function of ISD11-ACP in the core ISC complex

ISD11-ACP is part of the eukaryotic, but not bacterial core ISC complex (Lill & Freibert, 2020). Being located at great distance from the Fe/S cluster assembly site of ISCU2, ISD11 is not directly involved in the catalytic mechanism but important for NFS1 stability (Adam *et al.*, 2006; Wiedemann *et al.*, 2006) by binding to a hydrophobic patch (Boniecki *et al.*, 2017) on the desulfurase surface. ISD11 exhibits a Leu-Tyr-Arg motif (LYRM) participating in ACP binding. ACP also binds to other members of the LYRM family, including subunits of the mitochondrial ribosome and respiratory complex I (Brown *et al.*, 2017; Zhu *et al.*, 2016). ISD11-ACP binding is further stabilised by insertion of the ACP acylphosphopantetheine cofactor into a cavity of ISD11. Yeast studies showed ACP exerting a stabilising effect on the NFS1-ISD11 complex, however, ACP is not essential for Fe/S protein biogenesis (Boniecki *et al.*, 2017; Kastaniotis *et al.*, 2017; Masud *et al.*, 2019; Van Vranken *et al.*, 2016). Since the ISD11-ACP interaction is likely influenced by the chain length of the ACP-bound acyl moiety, the protein has been proposed to regulate Fe/S protein biogenesis depending on the energy level of the cell (Lill & Freibert, 2020). Higher carbon source supply leading to longer acyl chain length would possibly increase stability of the NIA complex and hence accelerate Fe/S protein biogenesis, whilst shortage of carbon sources would have the opposite effect. Fe/S cluster synthesis is additionally linked to energy metabolism via lipoyl cofactor formation, which depends on the Fe/S cluster enzyme LIAS (see chapter 1.4).

1.3.2 [2Fe-2S] cluster trafficking

After formation of homodimeric holo-ISCU2, its [2Fe-2S] cluster is transferred to glutaredoxin 5 (GLRX5) for insertion into apo-proteins and formation of [4Fe-4S] clusters (see Figure 4). The transfer is assisted by two chaperones, the Hsp40 cochaperone HSC20, exclusively participating in Fe/S protein biogenesis, and the ATP-binding Hsp70 chaperone HSPA9, which is also involved in mitochondrial protein import and folding (Dutkiewicz & Nowak, 2018; Lill & Freibert, 2020). HSC20 binds to a conserved hydrophobic patch of holo-ISCU2 (Figure 8, step 1) and subsequently recruits HSPA9, which binds to a conserved hydrophobic LPPVK motif of ISCU2 (step 2) (Ciesielski *et al.*, 2012; Dutkiewicz *et al.*, 2004). Since the chaperone interaction sites of ISCU2 are obstructed in the core ISC complex by NFS1 and FXN, it seems likely that holo-ISCU2 has to be released from the biosynthetic complex before chaperone binding. After formation of the ternary complex, HSPA9-bound ATP is hydrolysed and HSC20 released from the complex, allowing binding of GLRX5 (step 3). ATP-hydrolysis leads to a tighter binding of HSPA9 to ISCU2 and likely destabilizes Fe/S cluster coordination by ISCU2, thereby facilitating its transfer to GLRX5. In the last step of the reaction cycle, ADP is replaced with ATP via action of the nucleotide exchange factor GRPE1, loosening the binding of HSPA9 to ISCU2 (step 4). The formed [2Fe-2S]-GLRX5 homodimer and apo-ISCU2 are then released from the protein complex, and the [2Fe-2S] cluster is transferred from GLRX5 to recipient proteins. Due to the high efficiency of [2Fe-2S] cluster transfer from holo-GLRX5 to apo-FDX1 *in vitro*, it can be assumed that this reaction requires no further ISC factors *in vivo* (Weiler *et al.*, 2020). The efficiency of transfer to other [2Fe-2S] targets under physiologically relevant conditions has yet to be assessed.

Remarkably, even though GLRX5 takes a central position in the mitochondrial Fe/S protein biogenesis pathway (Figure 4), it is not essential for yeast viability as opposed to NFS1, ISD11, ISCU2, FDX2, FDXR, HSC20 and GRPE1 (Lill & Freibert, 2020). This indicates direct [2Fe-2S] cluster transfer from ISCU2 also being possible (albeit less efficient), potentially with the help of chaperones.

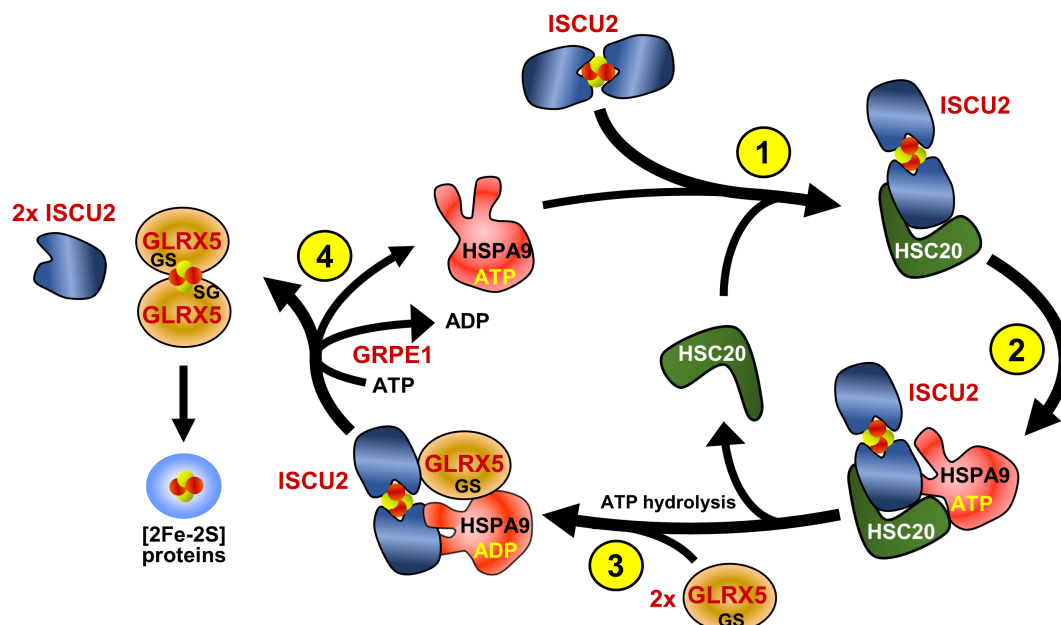


Figure 8: Mechanism of [2Fe-2S] cluster transfer from ISCU2 to GLRX5. The chaperone-dependent reaction cycle comprises four reaction steps (see main text for details). **1)** Complex formation between holo-ISCU2 and HSC20. **2)** Formation of a ternary complex with HSPA9. **3)** Formation of a ternary complex with GLRX5, and ATP hydrolysis of HSPA9. **4)** Cluster transfer and subsequent release of dimeric holo-GLRX5 and apo-ISCU2. GLRX5 coordinates the [2Fe-2S] cluster via one conserved Cys of each monomer and two non-covalently attached molecules of glutathione (GS). Taken from Lill & Freibert, 2020.

1.3.3 [4Fe-4S] cluster formation and trafficking

1.3.3.1 Assembly of [4Fe-4S] clusters

Maturation of the numerous mitochondrial [4Fe-4S] proteins requires the action of a dedicated set of protein factors responsible for formation of [4Fe-4S] clusters and their targeted insertion into apo-proteins. A number of studies indicated the proteins ISCA1, ISCA2 and IBA57 to be essential for the formation of [4Fe-4S] clusters. In human patients, mutations of the *ISCA1*, *ISCA2* and *IBA57* genes all lead to similar disease phenotypes (Al-Hassnan *et al.*, 2015; Alaimo *et al.*, 2018; Alfadhel *et al.*, 2018; Lossos *et al.*, 2015; Toldo *et al.*, 2018; Torraco *et al.*, 2018), in line with yeast studies showing deletion of the respective genes all causing the same general defect in mitochondrial [4Fe-4S] protein maturation (Gelling *et al.*, 2008; Mühlenhoff *et al.*, 2011). *In vitro* studies showed GLRX5 to interact with and transfer [2Fe-2S] clusters to the ISCA proteins. However, formation of [4Fe-4S] clusters was typically achieved only in presence of the non-physiological and cytotoxic reductant DTT (Banci *et al.*, 2014; Brancaccio *et al.*, 2014; Gourdoups *et al.*, 2018). A recent study reported formation of [4Fe-4S] cluster-bound and enzymatically active mitochondrial aconitase in presence of ISCA1, ISCA2 and

IBA57, using GLRX5 as [2Fe-2S] cluster donor (Weiler *et al.*, 2020). The reducing equivalents required for cluster fusion were supplied by an ETC consisting of NADPH, FDXR and FDX2. This surprisingly shows FDX2 being required for [4Fe-4S] cluster synthesis in addition to its already established function in *de novo* [2Fe-2S] cluster formation (Sheftel *et al.*, 2010; Webert *et al.*, 2014). Despite the recent advances, the molecular mechanism of [4Fe-4S] cluster formation and the exact interplay of all components involved is not clear to date.

1.3.3.2 Targeting factors for [4Fe-4S] cluster insertion into mitochondrial recipients

The insertion of [4Fe-4S] clusters formed by the ISCA1-ISCA2-IBA57 system into mitochondrial recipients commonly requires the help of one or more of the targeting factors NFU1, BOLA1, BOLA3 and IND1. The P-loop ATPase IND1 is specifically required for the assembly of complex I and is absent in *S. cerevisiae*, which lacks this component of the respiratory chain (Bych *et al.*, 2008; Calvo *et al.*, 2010; Sheftel *et al.*, 2009). Human NFU1 targets complex I and II of the respiratory chain as well as lipoyl synthase (LIAS) (Cameron *et al.*, 2011; Navarro-Sastre *et al.*, 2011). LIAS requires the differential function of two [4Fe-4S] clusters for the synthesis of the lipoyl cofactor from an octanoyl substrate: The catalytic cluster, needed for initiating the radical SAM (S-adenosyl methionine)-based reaction mechanism and the auxiliary cluster, supplying two of its sulfur atoms for formation of the lipoyl product. The auxiliary cluster is degraded during LIAS-catalysed lipoyl formation, therefore LIAS requires Fe/S clusters both for initial maturation and catalytic turnover. Experiments using *E. coli* homologs of NFU1 and LIAS showed [4Fe-4S]-NfuA enabling multiple turnovers of LipA by replacing its degraded auxiliary cluster (McCarthy & Booker, 2017).

Genetic studies of the yeast BOLA1/3 homologs Bol1/3 showed an impaired function of the LIAS homolog Lip5 and complex II in Bol1/3 Δ double knockout cells (Melber *et al.*, 2016; Uzarska *et al.*, 2016). In contrast, no and little effect was observed in Bol1 Δ and Bol3 Δ cells, respectively, indicating at least partially redundant functions of the two proteins. However, Bol1/3 could not replace Nfu1 in Lip5 as well as complex II maturation and vice versa, indicating distinct functions of the Bol proteins and Nfu1. Whilst in humans *BOLA3* mutation impairs function of complex I and II as well as LIAS (Baker *et al.*, 2014; Cameron *et al.*, 2011), the exact function of *BOLA1* in [4Fe-4S] protein maturation remains to be identified (Willems *et al.*, 2013). *BOLA1* and *BOLA3* both interact with apo- and holo-GLRX5 *in vitro* and enable formation of heterodimeric bridged [2Fe-2S] cluster complexes (Melber *et al.*, 2016; Nasta *et al.*, 2017; Uzarska *et al.*, 2016). The *in vivo* function of these complexes, also in respect to LIAS assembly/regeneration, remains to

be identified (see also chapter 1.4.3). The vital functions of the lipoyl cofactor in mitochondrial metabolism as well as its LIAS-dependent biosynthesis will be discussed in the following chapters.

1.4 Function and LIAS-dependent biosynthesis of the lipoyl cofactor

1.4.1 Lipoyl-dependent enzymes and their function

The lipoyl cofactor consists of an octanoyl chain substituted with sulfhydryl moieties at the C6 and C8 positions. These undergo reversible disulfide formation in the course of lipoyl-dependent catalysis (Figure 9). The cofactor is covalently attached to the ϵ -amino group of conserved Lys residues (Cronan, 2016). In addition to the glycine cleavage system (GCS), four α -ketoacid dehydrogenase complexes depend on the cofactor for their catalytic function in human mitochondria (Solmonson & DeBerardinis, 2018). These are the pyruvate dehydrogenase (PDH), α -ketoglutarate dehydrogenase (KGDH), branched-chain α -ketoacid dehydrogenase (BCKDH) and α -ketoadipate dehydrogenase (KADH) multienzyme complexes, which are all constituted of three independent subunits termed E1, E2 and E3. An assembly of multiple E2 subunits forms the core of these dehydrogenase complexes, to which the E1 and E3 components are binding (Cronan, 2016; Reed, 2001). The thiamine pyrophosphate (TPP)-binding E1 subunit catalyses decarboxylation of the respective α -ketoacid substrate, forming an acyl-TPP intermediate (exemplified by PDH function in Figure 9, reaction 1). Subsequently, the acyl-moiety is transferred to coenzyme A (CoA) via the lipoyllysyl arm of the E2 subunit (reactions 2 and 3). This involves reductive opening of the lipoyl disulfide-bond. Subunit E3 (or dihydrolipoamide dehydrogenase, DLD) re-oxidises lipoyl using FAD, and the generated FADH₂ is re-oxidised by NAD⁺ (reaction 4). Whereas the E1 and E2 subunits are specific to the PDH, KGDH and BCKDH complexes, the same E3 subunit is shared between them. For the less well studied KADH, an analogous behaviour seems likely (Shaag *et al.*, 1999; Solmonson & DeBerardinis, 2018).

The discussed dehydrogenases are essential for the mitochondrial carbon metabolism. Their dysfunction, despite being rare, can severely affect the health of individuals (Mayr *et al.*, 2014; Solmonson & DeBerardinis, 2018). PDH and KGDH are vital to the function of the TCA cycle, as they synthesize its substrates acetyl- and succinyl-CoA, respectively. Dysfunction of their respective E1 subunits exerts similar symptoms in patients, including developmental delay, ataxia and hypotonia, among others (Rahman & Mayr, 2016; Solmonson & DeBerardinis, 2018). BCKDH catalyses the decarboxylation of Ile-, Val- and Leu-derived α -ketoacid products formed by the upstream branched chain amino acid transferase. BCKDH E1 or E2 subunit deficiency leads to the so-called maple syrup

urine disease characterised by increased amounts of sweet-smelling BCAAs and α -ketoacids in urine, but also more severe symptoms are known. The substrate of KADH, α -ketoacidipate, is formed in tryptophan and lysine catabolism. KADH-associated diseases are very rare and in half of the cases asymptomatic. KGDH, converting a similar substrate, might be able to partially replace the function of KADH. Dysfunction of the E3 subunit shared between the discussed hydrogenases, as well as impaired biosynthesis of the lipoyl cofactor itself, leads to generally impaired dehydrogenase functions and can exert severe medical conditions (Mayr *et al.*, 2014; Rahman & Mayr, 2016). Since LIAS requires two [4Fe-4S] clusters for its function in lipoyl synthesis, both mutation of *LIAS* and impaired assembly/regeneration of its Fe/S cofactors leads to decreased lipoylation of α -ketoacid dehydrogenases and GCS.

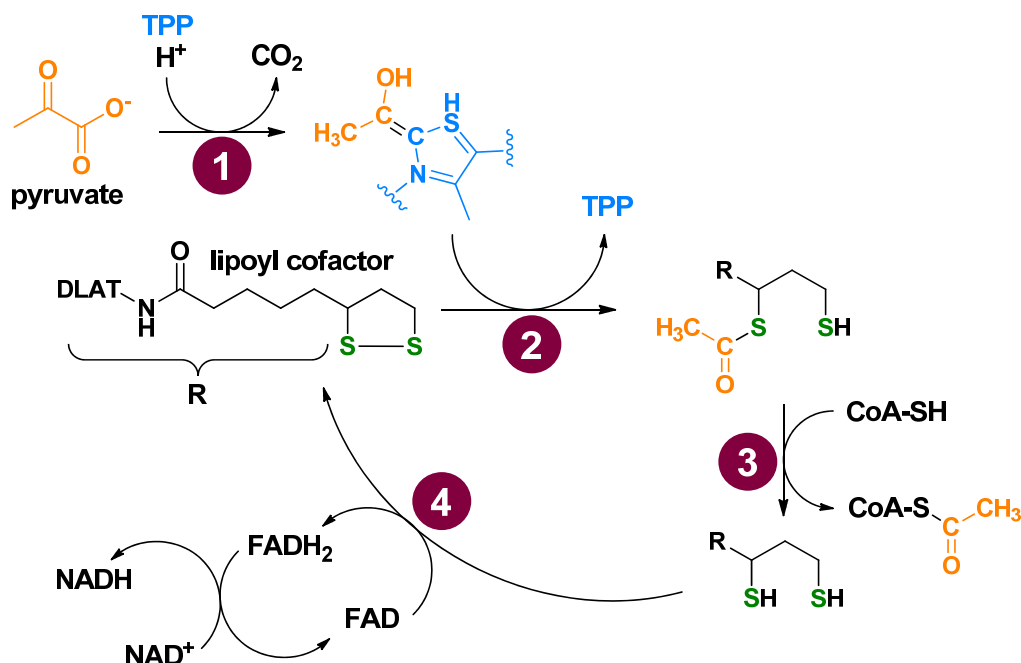


Figure 9: Lipoyl-dependent mechanism of acetyl-CoA formation by the PDH complex. 1) TPP bound to the E1 (PDH) subunit catalyzes the decarboxylation of pyruvate. 2) An oxidized lipoyl cofactor bound to subunit E2 (dihydrolipoamide acetyltransferase, DLAT) undergoes nucleophilic attack of the acetyl moiety, resulting in a ring opening. 3) The lipoyl-bound acetyl moiety is transferred to coenzyme A, forming acetyl-CoA. 4) The disulfide bond of the lipoyl cofactor is reestablished via reduction of FAD bound to the E3 subunit (DLD). The generated FADH_2 is converted back to FAD via reduction of NAD^+ . Reaction mechanisms of the KGDH, BCKDH and KADH complexes are analogous, with the E1 and E2 subunits processing their respective substrates. Adapted from Cronan, 2016.

Lipoyl is also cofactor of the H protein (GCSH), one of four components of GCS, which performs a reversible reaction mechanism. Here, the cofactor is required for shuttling of an aminomethyl moiety generated from P protein-catalysed glycine decarboxylation to the T protein (Fujiwara & Motokawa, 1983; Kikuchi *et al.*, 2008). The T protein forms

5,10-methylenetetrahydrofolate (MTHF) and ammonia from the lipoyl-bound aminomethyl moiety and tetrahydrofolate. The lipoyl disulfide bond reductively opened throughout the reaction mechanism is re-oxidised by the L protein under NAD⁺ consumption. GCS represents the major pathway for serine and glycine degradation in mammals, its dysfunction leading to nonketotic hyperglycinemia characterized by extremely high glycine levels in blood and urine (Kikuchi *et al.*, 2008; Tada & Kure, 2005; Yoshida & Kikuchi, 1972, 1973). The reaction product of GCS, MTHF, is needed as one-carbon donor in purine, thymidine and methionine biosynthesis but is also formed by the enzyme serine hydroxymethyl transferase, which converts serine to glycine (Ducker & Rabinowitz, 2017).

1.4.2 Biosynthesis of the lipoyl cofactor

Biosynthesis of the lipoyl cofactor attached to E2-subunits of α -ketoacid dehydrogenases involves three enzymes in humans (Mayr *et al.*, 2014; Solmonson & DeBerardinis, 2018). Octanoyl-ACP produced by the mitochondrial fatty acid synthesis system II (mtFAS II) is substrate of the octanoyltransferase LIPT2, which transfers the octanoyl moiety to GCSH (Schonauer *et al.*, 2009). Subsequently, LIAS forms the mature lipoyl cofactor in a mechanism that supplies sulfur atoms from one of its [4Fe-4S] clusters and depends on SAM and electrons (Douglas *et al.*, 2006; McCarthy & Booker, 2017; Morikawa *et al.*, 2001). The GCSH-bound lipoyl residue is then transferred to the E2-subunits of α -ketoacid dehydrogenases by the putative lipoyltransferase LIPT1 (Hermes & Cronan, 2013; Schonauer *et al.*, 2009). This is in line with dysfunction of LIPT1 affecting the function of α -ketoacid dehydrogenases, but not GCS (Mayr *et al.*, 2014; Soreze *et al.*, 2013; Tort *et al.*, 2014). The current understanding of the sequence of events has, to a large extent, been derived from studies in yeast, which possesses orthologs of the respective human enzymes. Yeast and humans lack the ability to use exogenously supplied lipoic acid for protein lipoylation. Consequently, human lipoyl deficiencies associated with often severe medical conditions (see chapter 1.4.1) cannot be treated by dietary lipoic acid supplementation (Hiltunen *et al.*, 2010; Mayr *et al.*, 2014). In contrast, *E. coli* can perform lipoylation from both octanoyl-ACP and lipoic acid via separate pathways, the latter relying on the function of a single enzyme termed lipoyl-protein ligase (LplA) (Cronan, 2016; Solmonson & DeBerardinis, 2018). A more detailed understanding of lipoyl biosynthesis would likely facilitate the development of treatment strategies for various lipoyl deficiencies. The function of LIAS, linking lipoyl biosynthesis to Fe/S protein biogenesis, is described in detail below.

1.4.3 Function and catalytic mechanism of lipoyl synthase (LIAS)

LIAS belongs to the superfamily of radical SAM enzymes that employ a [4Fe-4S] cluster to form a catalytically active 5'-deoxyadenosyl radical (5'-dA \cdot) (Figure 10) (Frey *et al.*, 2008). This catalytic [4Fe-4S] cluster is coordinated via a conserved CX₃CX₂C motif, SAM constituting the fourth Fe ligand (McLaughlin *et al.*, 2016). Formation of the 5'-dA \cdot radical via electron transfer from the catalytic cluster to SAM enables LIAS to perform the kinetically challenging C–H bond activation of its octanoyl substrate (reaction mechanism in Figure 11) (Lanz *et al.*, 2014). LIAS possesses a second, auxiliary [4Fe-4S] cluster supplying the two sulfur atoms sequentially inserted to the octanoyl C6 and C8 carbons (Cicchillo *et al.*, 2004; Douglas *et al.*, 2006). Consequently, the auxiliary cluster is degraded throughout lipoyl formation and has to be regenerated to allow additional turnovers of the enzyme (Lanz *et al.*, 2014; McCarthy & Booker, 2017). An analogous sulfur-donating Fe/S cluster function is also found in, e.g., biotin synthase, yet here of the [2Fe-2S]-type (Booker *et al.*, 2007; Frey *et al.*, 2008). The auxiliary cluster is ligated via a lipoyl synthase-specific CX₄CX₅C motif, and in absence of the octanoyl substrate, a Ser residue likely functions as fourth ligand, supported by crystallographic snapshots of lipoyl synthesis by *Mycobacterium tuberculosis* LipA (Figure 10) (McLaughlin *et al.*, 2016). Both SAM and the GCSH-bound octanoyl substrate are accommodated in proximity by a protein cavity in which the two Fe/S clusters are located.

Generally, *in vitro* studies of sulfur-donating radical SAM enzymes like lipoyl synthase have shown low enzymatic turnover (Booker *et al.*, 2007). In line with the destruction of the auxiliary cluster during lipoyl synthesis, bacterial LipA catalysed no more than one turnover in multiple studies (Bryant *et al.*, 2006; Cicchillo *et al.*, 2004; Lanz *et al.*, 2014). This significantly changed in reactions containing the *E. coli* Fe/S cluster donor NfuA, where multiple turnovers were achieved, albeit with an arguably slow time course (~12 turnovers in 150 min with excess of [4Fe-4S]-NfuA) (McCarthy & Booker, 2017). In these *in vitro* studies, higher amounts of SAM were consumed than formally required by radical SAM enzymes LIAS and biotin synthase, indicating the occurrence of radical-induced side reactions (Booker *et al.*, 2007; Frey *et al.*, 2008).

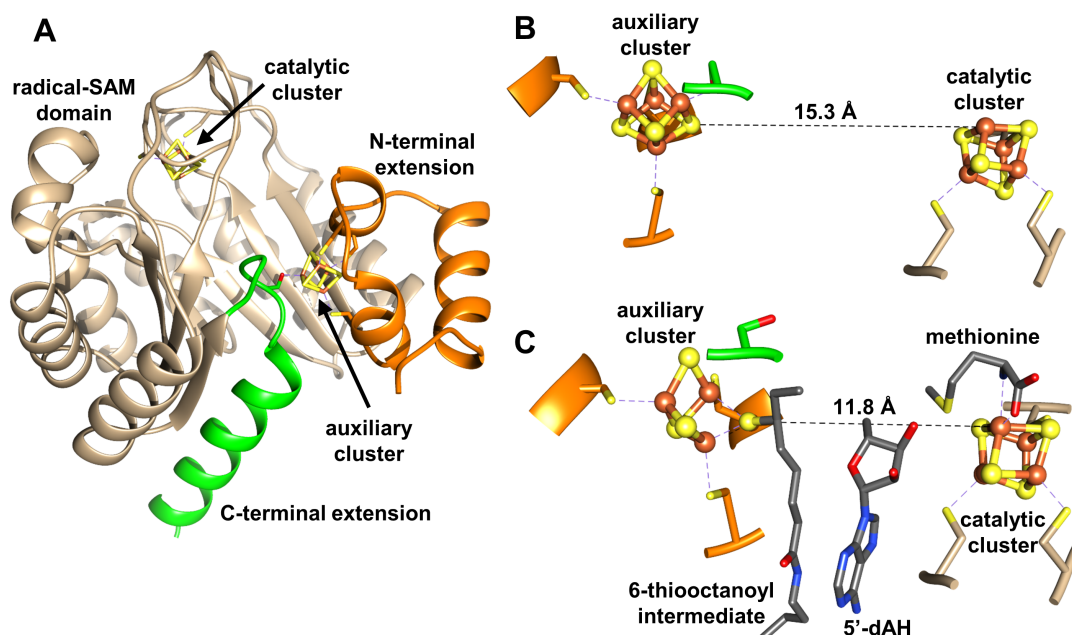


Figure 10: *M. tuberculosis* LipA in presence and absence of reaction intermediates. **A)** Overall structure of substrate-free LipA (pdb code: 5EXJ). The catalytic cluster is bound by the radical SAM domain (beige), whereas the auxiliary cluster is coordinated by N- (orange) and C-terminal (green) extensions of LipA. **B)** The substrate-free active site (pdb code: 5EXJ). Both Fe/S clusters are coordinated by three Cys residues (coloring as in **A**). The auxiliary cluster is additionally coordinated by Ser292 (green), whereas in the catalytic cluster one Fe ion is solvent-exposed. **C)** The intermediate-binding active site (pdb code: 5EXK). One of the auxiliary cluster's sulfur atoms is covalently attached to an octanoyl substrate, constituting the 6-thiooctanoyl intermediate of lipoyl synthesis. The Fe ion previously coordinated by Ser292 (**B**) is lost. The catalytic cluster still binds methionine that is reductively cleaved from SAM, also generating 5'-deoxyadenosine (5'-dAH). Conformational changes in the enzyme lead to closer proximity of the two Fe/S clusters compared to the substrate-free state. Adapted from McLaughlin *et al.*, 2016.

There are two major questions regarding the mechanism of lipoyl biosynthesis: What factors are involved in Fe/S cluster assembly/regeneration of human LIAS and what is the physiological electron donor? The auxiliary cluster of *E. coli* LipA can be regenerated by [4Fe-4S]-reconstituted NfuA or IscU (homologs of human NFU1 and ISCU2) *in vitro*, enabling multiple turnovers of the enzyme (McCarthy & Booker, 2017; McCarthy *et al.*, 2019). In humans, both NFU1 and BOLA3 appear to fulfil essential and non-overlapping functions in LIAS assembly/regeneration (Cameron *et al.*, 2011; Navarro-Sastre *et al.*, 2011), whilst human ISCU2 does not directly participate in [4Fe-4S] protein assembly (Lill & Freibert, 2020). Whereas human NFU1 coordinates a [4Fe-4S] cluster in a homodimeric fashion (Tong *et al.*, 2003), the BOLA proteins form [2Fe-2S]-bridged heterodimeric complexes with GLRX5 according to *in vitro* studies (Melber *et al.*, 2016; Uzarska *et al.*, 2016), raising the question of how these complexes might contribute as cluster donors for an enzyme binding exclusively [4Fe-4S] clusters. Since only two sulfur atoms

of the auxiliary [4Fe-4S] cluster of LIAS are required for lipoyl formation, it might be possible that a [2Fe-2S]-GLRX5-BOLA complex can function in replenishing the remaining [2Fe-2S] unit, forming a new functional [4Fe-4S] cluster.

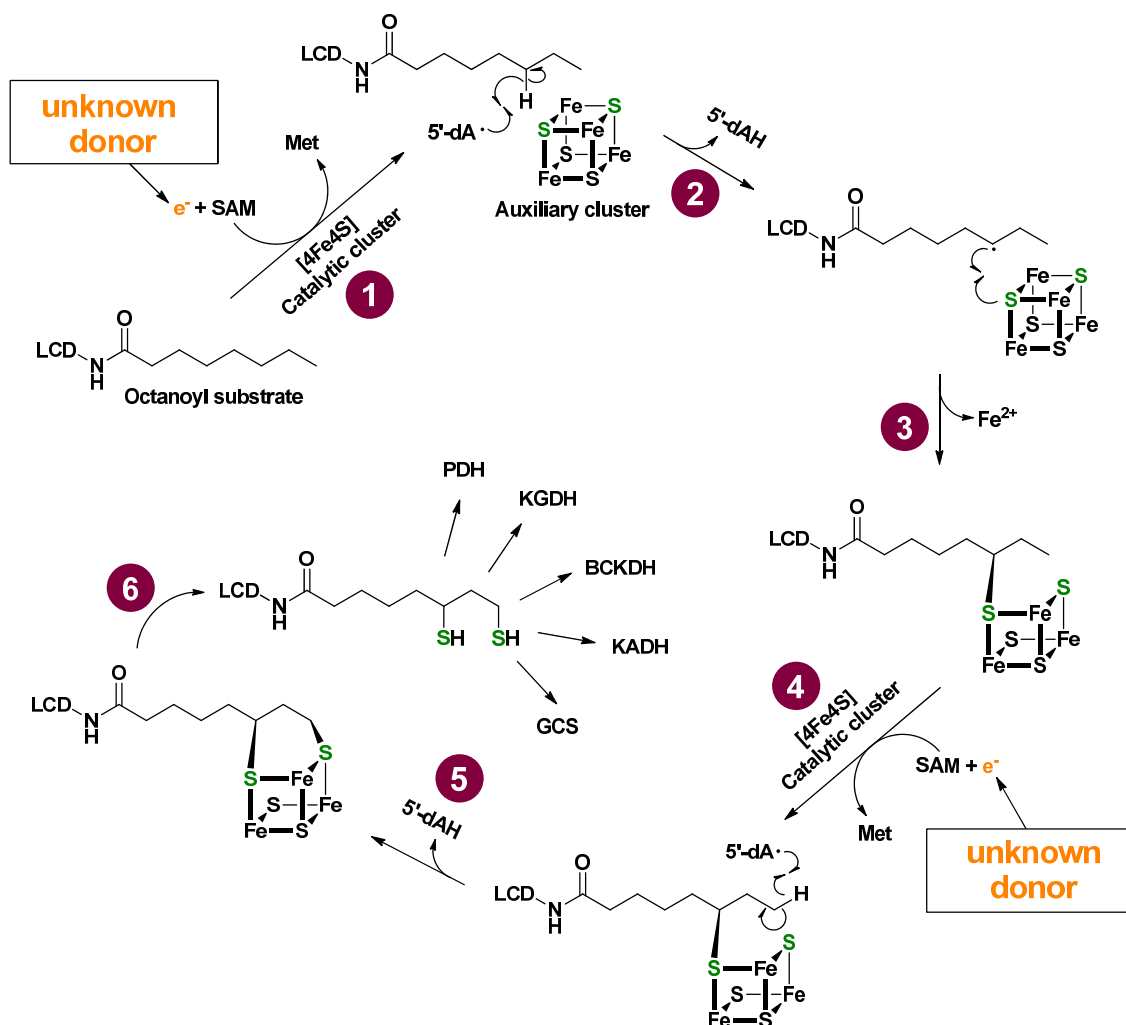


Figure 11: The reaction mechanism of lipoyl formation by lipoyl synthase. 1) The reaction starts with the binding of SAM and the octanoyl substrate. The latter is covalently attached to a lysinyl residue of a lipoyl carrier domain (LCD), in humans the H protein of the glycine cleavage system (GCS). A yet unknown electron donor (orange) transfers a single electron to the catalytic cluster which mediates reductive cleavage of SAM, forming methionine (Met) and a 5'-deoxyadenosyl radical ($5'\text{-dA}^\bullet$). 2) The radical abstracts a hydrogen atom from the octanoyl C6 carbon, forming 5'-deoxyadenosine ($5'\text{-dAH}$). 3) The octanoyl C6 carbon in turn forms a covalent bond with a sulfur atom of the auxiliary cluster (6-thiooctanoyl intermediate), concomitant with degradation of the cluster. 4) A second SAM molecule binds to LIAS and is reductively cleaved by the catalytic cluster as before. 5) $5'\text{-dA}^\bullet$ abstracts a hydrogen atom from the terminal C8 carbon of the 6-thiooctanoyl moiety, forming $5'\text{-dAH}$. 6) A second sulfur atom is covalently attached to the 6-thiooctanoyl molecule, forming the mature lipoyl cofactor. Overall, two electrons, two molecules SAM and two sulfur atoms are required for synthesis of one lipoyl molecule. To enable multiple reaction cycles, the auxiliary cluster must be regenerated, yet this is poorly defined hitherto. The lipoyl cofactor is integral to the function of pyruvate, α -ketoglutarate, branched-chain α -ketoacid and α -ketoadipate dehydrogenase (PDH, KGDH, BCKDH and KADH) complexes as well as GCS in humans (Solomonson & DeBerardinis, 2018). Adapted from Dong *et al.*, 2018.

Since the electron donor for LIAS is unknown, the inorganic artificial reductant dithionite (DT) is typically used in *in vitro* experiments (McCarthy & Booker, 2017, 2018). Remarkably, CRISPR-Cas9-mediated knockouts of FDX1 in human cell culture (Schulz *et al.* 2022, submitted manuscript) led to a severe depletion of lipoylation of the PDH and KGDH E2 subunits (Appendix Figure 48). This might indicate a previously unknown function of FDX1 in lipoyl biosynthesis. Whether LIAS depends on reducing equivalents supplied by FDX for biosynthetic function has not yet been assessed by a suitable *in vitro* assay. The known functions of the two human FDXs, FDX1 and FDX2, will be discussed in the following chapters.

1.5 Ferredoxins

FDXs comprise a large family of redox proteins found in all kingdoms of life. Their bound Fe/S clusters allow single electron transfer to numerous targets in diverse biological pathways. [4Fe-4S] FDXs have been proposed as the potentially most ancient low potential electron carriers based on phylogenetic analyses, *in vitro* studies and the often times short and primitive FDX sequences (Bertini *et al.*, 1995; Campbell *et al.*, 2019; Eck & Dayhoff, 1966; Sousa *et al.*, 2013; Venkateswara Rao & Holm, 2004). The later emergence of [2Fe-2S]-FDXs in bacteria coincided with the advent of oxygenic photosynthesis (Campbell *et al.*, 2019). [2Fe-2S]-containing FDXs usually comprise 75 to 200 amino acids and coordinate their cluster via four conserved Cys ligands. FDXs often exhibit a hydrophobic patch that is surrounded by multiple acidic residues and covers the Fe/S cofactor. [2Fe-2S]-FDXs are generally more oxygen tolerant than [4Fe-4S]-FDXs (Pierella Karlusich *et al.*, 2014) and maintain a low redox potential (Atkinson *et al.*, 2016). Binding of FDXs to cognate redox partners involves electrostatic interactions of charged surface patches establishing a transient encounter state, followed by entropy-driven water repulsion at the (often) hydrophobic interface, concomitant with conformational rearrangements of the binding partners (Lee *et al.*, 2011; Martinez-Julvez *et al.*, 2009). The final complex is stabilized by specific intermolecular interactions (Hiruma *et al.*, 2013; Muller *et al.*, 2001; Strushkevich *et al.*, 2011). However, particularly in weak complexes, electron transfer has been suggested to occur already in the encounter state, mainly relying on electrostatic attraction (Long *et al.*, 2008; Xu *et al.*, 2008).

[2Fe-2S]-FDXs constitute the most abundant FDX type in eukaryotes (Campbell *et al.*, 2019). Whereas mitochondrial members show sequence similarity to bacterial ones, plastids of algae and plants harbor a variety of FDXs distinct in sequence and function. Plastidial FDXs accept electrons from photosystem I and transfer them to a wide variety of acceptors participating in chlorophyll, phytochrome and fatty acid biosynthesis, redox

metabolism, assimilation of nitrogen and sulfur, as well as NADP⁺ reduction to NADPH (Hanke & Mulo, 2013). In mitochondria, reductive power is transmitted via a redox chain from NADPH via FDXR to FDX and then to the final electron acceptor.

1.5.1 Ferredoxin functions in human mitochondria

Humans possess two FDXs located in the mitochondrion, the [2Fe-2S] cluster-binding FDX1 and FDX2, which exhibit highly similar 3D structures (Figure 12). Nevertheless, they exhibit a pronounced specificity for their respective electron acceptors. Whereas mammalian FDX1-type FDXs are known as redox partners of multiple cytochrome P450 enzymes (Ewen *et al.*, 2012; Johnson *et al.*, 2017), FDX2 is recognized for its role in Fe/S protein biogenesis (Lill & Freibert, 2020) (overview in Figure 13). Furthermore, human FDX2 has been implicated in heme *a* formation (Sheftel *et al.*, 2010). The most abundant type of heme and in mitochondria relevant for example for the function of respiratory chain complexes II and III is heme *b* (Hildenbeutel *et al.*, 2014; Kim *et al.*, 2012; Tran *et al.*, 2006; Yun *et al.*, 1991). Farnesylation of heme *b* by heme *o* synthase (COX10) and subsequent oxidation by heme *a* synthase (COX15) yields heme *a*, the cofactor of respiratory chain complex IV (also named cytochrome *c* oxidase, COX) (Swenson *et al.*, 2020). COX15 is highly conserved from bacteria to humans and was shown in *S. cerevisiae* to depend on yeast adrenodoxin homolog 1 (Yah1) and adrenodoxin reductase homolog (Arh1), the counterparts of mammalian FDXs and FDXR (Barros *et al.*, 2001; Barros *et al.*, 2002). In contrast to humans, Yah1 is the sole FDX in *S. cerevisiae* and functions additionally in Fe/S protein biogenesis and coenzyme Q (CoQ or ubiquinone) biosynthesis (Li *et al.*, 2001; Ozeir *et al.*, 2011; Pierrel *et al.*, 2010).

The most prominent function of FDX2 is its role in human Fe/S protein biogenesis. The core ISC machinery forming [2Fe-2S] clusters *de novo* as well as the late ISC machinery synthesizing [4Fe-4S] clusters from [2Fe-2S] units both require reducing equivalents (see also chapter 1.3). *In vivo* complementation experiments with human FDX variants indicated the FDX2 C-terminus, which is conserved in FDX2-type but not FDX1-type FDXs, to fulfill a crucial function in Fe/S protein biogenesis (Webert, 2011). Accordingly, FDX1 did not enable Fe/S protein biogenesis in these experiments. In contrast, two studies proposed a redundant additional function of FDX1 in Fe/S protein biogenesis based on RNAi experiments (Shi *et al.*, 2012) and *in vitro* reconstitution of ISC U2 using FDX pre-incubated with the artificial reductant DT (FDX1 yielding approximately half the rate of FDX2 reactions in the latter study) (Cai *et al.*, 2017). However, *in vivo* RNAi and complementation experiments in human and yeast cell culture, respectively, showed only FDX2 to function in Fe/S protein biogenesis (Sheftel *et al.*, 2010), a finding supported later by FDX1 knockouts in human cells (Schulz *et al.*, submitted manuscript).

A biochemical assay reconstituting *de novo* [2Fe-2S] cluster formation *in vitro* using ISC machinery components including the physiological ETC comprising NADPH, FDXR and FDX supported that human FDX2 and yeast Yah1, but not human FDX1, can efficiently facilitate cluster synthesis (Webert *et al.*, 2014).

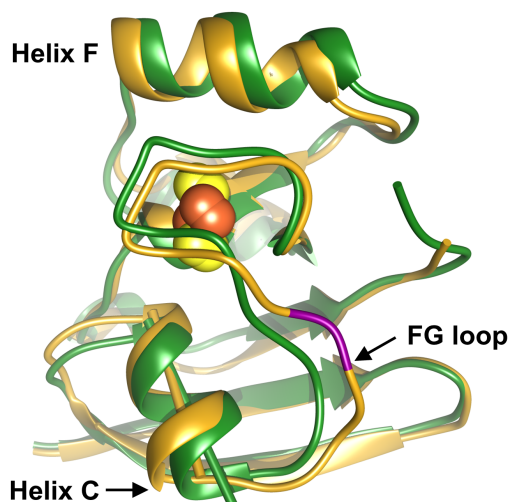


Figure 12: Comparison of 3D structures of the human FDXs. FDX1 (gold, PDB code: 3P1M, residues 65–170) and FDX2 (green, PDB code: 2Y5C, residues 69–174) are superimposed. Both proteins display a compact ($\alpha+\beta$) fold typical for vertebrate-type mitochondrial FDXs. FDX1 exhibits a Phe-Gly insertion (FG loop, shown in magenta), and the differential orientation of both FDXs in helix C is indicated by rods. Apart from these differences, the structures are highly similar. The flexible C-terminus is not resolved in the FDX2 structure and corresponding FDX1 residues are not shown.

FDX1 (also termed adrenodoxin) participates not only in steroid hormone biosynthesis but also in bile acid and vitamin A and D metabolism by transferring electrons from FDXR to all seven class I cytochrome P450 (CYP) enzymes present in human mitochondria (Ewen *et al.*, 2012; Johnson *et al.*, 2017). This class of monooxygenases is capable of mediating the chemically challenging oxidation of hydrocarbons, catalyzed by an active site heme *b* cofactor. For example, 11 α -hydroxylase (CYP11A1) converts cholesterol to pregnenolone, the precursor of steroid hormones. Further processing requires 11 β -hydroxylase (CYP11B1) for cortisol formation, a reaction supported by FDX1 but not its counterpart FDX2 (Sheftel *et al.*, 2010). In line with its specific function, FDX1 protein levels in the steroid-producing adrenal gland by far surpass those of FDX1 or FDX2 in any other tested tissue (Sheftel *et al.*, 2010).

Studies of human FDX1 knockout cells have revealed lipoylation deficiency of the PDH and KGDH complexes (Schulz *et al.*, submitted manuscript; see also chapter 1.4.3). This might indicate FDX1 serving as an electron donor for lipoyl formation, in addition to its function in steroid, bile acid and vitamin A and D metabolism. Since the electron donor

for the radical SAM enzyme LIAS is yet unknown, involvement of FDX appears to be a viable and intriguing hypothesis.

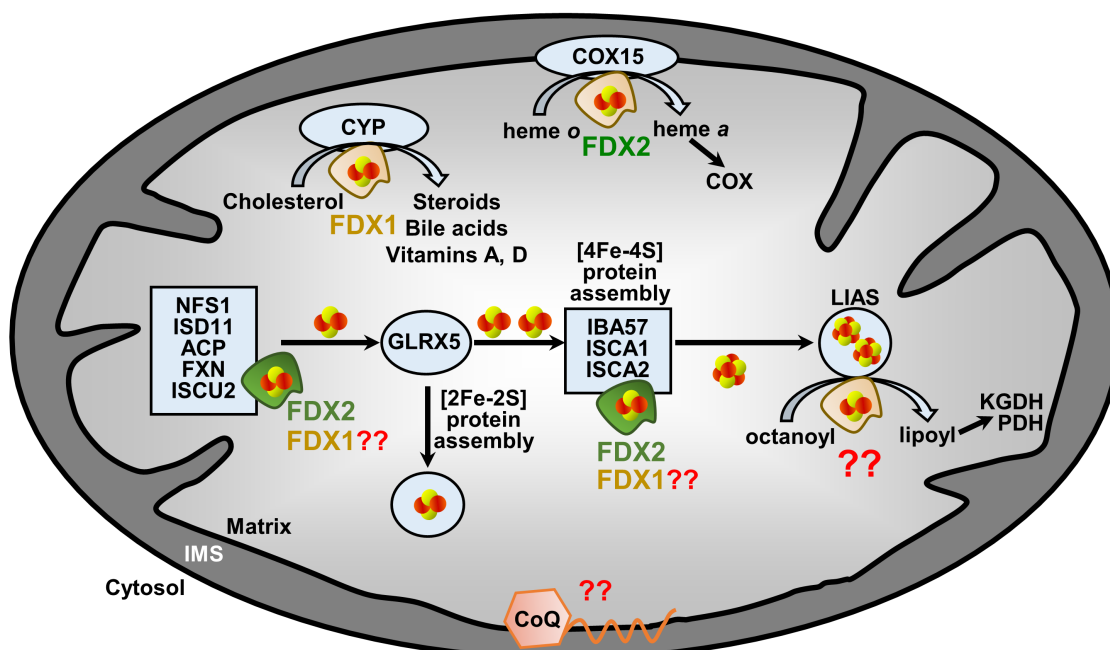


Figure 13: Known functions of human mitochondrial FDXs. FDX2 is an electron donor for the assembly of both [2Fe-2S] and [4Fe-4S] clusters in Fe/S protein biogenesis and was furthermore proposed as electron donor for COX15 in heme a biosynthesis. FDX1 is redox partner of seven cytochrome P450 (CYP) enzymes involved in steroid biosynthesis (CYP11A1, CYP11B1, CYP11B2) as well as in the metabolism of vitamins A and D and bile acids (CYP24A1, CYP27A1, CYP27B1, CYP27C1). A redundant function of FDX1 in Fe/S protein biogenesis has been proposed but requires further elucidation. Lipoyl biosynthesis by LIAS may also require FDX function. In contrast to humans, yeast possesses only one ferredoxin (Yah1), which functions in Fe/S protein biogenesis as well as heme a and coenzyme Q (CoQ) biosynthesis. The electron donor for CoQ biosynthesis in humans is presently unknown.

1.6 Aims of this work

1.6.1 The molecular mechanism of *de novo* [2Fe-2S] cluster formation

The biosynthesis of Fe/S cluster cofactors and their insertion into recipient proteins is a complex process requiring a machinery of at least 29 proteins in humans, 18 thereof located in mitochondria (Braymer *et al.*, 2020; Lill & Freibert, 2020). In eukaryotes, mitochondrial Fe/S protein biogenesis is of particular importance, as it not only enables mitochondrial Fe/S protein assembly, but also produces a precursor essential for the assembly of cytosolic and nuclear Fe/S proteins. Since Fe/S proteins are integral to numerous vital biological processes including cellular respiration, the TCA cycle and DNA replication and maintenance, deficiencies in Fe/S protein biogenesis can lead to severe and potentially fatal medical conditions in humans (Beilschmidt & Puccio, 2014; Lill &

Freibert, 2020). The prominent example Friedreich's ataxia, linked to impaired *de novo* synthesis of [2Fe-2S] clusters, is only one of many associated diseases. Consequently, research in the field of Fe/S protein biogenesis is highly valuable not only to gain a deeper mechanistic understanding of mitochondrial and cellular metabolism, but also to enable improved diagnosis and treatment of Fe/S diseases. Furthermore, engineering of organisms for biotechnological purposes may require intimate knowledge of their Fe/S metabolism.

The mechanism of mitochondrial *de novo* [2Fe-2S] cluster synthesis by the core ISC complex, which comprises six different proteins, is only partially understood despite recent advances. An overarching aim of this work was therefore to achieve a molecular understanding of this vital but complex process, which provides the Fe/S units required for maturation of all Fe/S proteins of non-green eukaryotes. Particular emphasis was on ISCU2, the scaffold for [2Fe-2S] cluster assembly. A previous study indicated that a persulfide is formed on one of the three assembly site Cys residues (Cys138) of this Fe-binding protein as an intermediate of [2Fe-2S] cluster formation (Parent *et al.*, 2015). However, whether Cys138 received the persulfide directly from the cysteine desulfurase NFS1 or via sulfur relay at the ISCU2 assembly site was not clear and subject of this work. Apart from three conserved Cys residues, ISCU2 possesses two more assembly site residues (Asp71 and His137) potentially involved in Fe and/or Fe/S cluster coordination. The individual roles of these five key residues throughout [2Fe-2S] cluster assembly were to be identified using biochemical, spectroscopic and structural methods. This goal included if and how Fe coordination at the ISCU2 assembly site would change at different stages of cluster formation. Ultimately, a characterisation of the ISCU2 assembly site at the various steps of cluster synthesis was intended, with focus on the persulfide-bound intermediate of ISCU2. A cryo-EM structure of the core ISC complex previously had shown an interaction of the ISCU2 assembly site with FXN (Fox *et al.*, 2019), a protein crucial for efficient ISCU2 persulfidation and [2Fe-2S] cluster formation. The molecular interactions of the two proteins and their relevance for Fe/S protein biogenesis were aimed to be characterised in more detail as part of this work.

1.6.2 The physiological electron donor for lipoyl cofactor biosynthesis

The lipoyl cofactor is essential to the function of the human α -ketoacid dehydrogenase complexes, namely PDH, KGDH, BCKDH and KADH. These multienzyme complexes transfer acyl-units derived from α -ketoacid substrate decarboxylation to coenzyme A using a lipoyllysyl "swinging arm". PDH and KGDH synthesize the TCA cycle substrates acetyl- and succinyl-CoA, respectively, whereas BCKDH and KADH are involved in

amino acid catabolism. The lipoyl cofactor is additionally employed by GCS, which constitutes the major pathway for serine and glycine degradation and is involved in purine, thymidine and methionine biosynthesis. Due to the fundamental functions of the lipoyl cofactor in mitochondrial carbon metabolism, dysfunction of individual lipoyl-dependent enzymes and particularly lipoyl biosynthesis itself causes severe diseases (Mayr *et al.*, 2014; Rahman & Mayr, 2016).

Lipoyl formation from an octanoyl precursor is catalysed by the [4Fe-4S] cluster enzyme LIAS. Consequently, impaired mitochondrial [4Fe-4S] cluster assembly severely affects lipoylation efficiency. Whereas the radical SAM-based reaction mechanism of LIAS is understood to some extent, important questions remain unsolved. Most importantly, the physiological electron donor for the catalytic [4Fe-4S] cluster facilitating reductive SAM cleavage to form a catalytically active 5'-deoxyadenosyl radical is unknown for human LIAS. Intriguingly, *FDX1* knockouts indicated lipoylation deficiency of the PDH and KGDH complexes (Schulz *et al.*, submitted manuscript), making an involvement of FDX1 in lipoyl biosynthesis conceivable. The primary goal of the second project in this work was hence to examine the relative contribution of the two human FDXs to electron transfer to LIAS. In previous works, *in vitro* studies had employed bacterial but not human LIAS using an inorganic artificial electron donor, with radical SAM enzymes that generally exhibited low turnover. To allow for a reliable investigation of human LIAS, a suitable *in vitro* assay closely reflecting physiological conditions using exclusively human proteins had to be established. This included purification and reconstitution of catalytically active human LIAS binding two [4Fe-4S] clusters, and furthermore the use of a physiological ETC comprising NADPH, FDXR and FDXs. Regarding the structurally highly similar FDX1 and FDX2, analysis of FDX variants in the *in vitro* assay was necessary to reveal the specificity of FDXs.

The auxiliary [4Fe-4S] cluster donating the two sulfur atoms incorporated into the nascent lipoyl cofactor is degraded during turnover and has to be regenerated to allow for a true catalytic function of LIAS. Since the [4Fe-4S] targeting factors NFU1 and BOLA3 had been implicated in LIAS assembly/regeneration in human cells *in vivo*, their potential role in regeneration of the auxiliary cluster should be tested in the *in vitro* assay. Lastly, the toxic anticancer agent and mitochondria-targeting copper ionophore elesclomol (Ele) had been suggested as an inhibitor of FDX1, based on genetic screens and *in vitro* experiments (Tsvetkov *et al.*, 2019). The proposed inhibitory function of Ele should be addressed by the *in vitro* LIAS assay to reveal the potential toxicity of Ele and its Cu complex.

Both projects from this work served the overarching goal to gain a deeper understanding of the biosynthesis and function of mitochondrial Fe/S proteins.

2 Materials

2.1 Devices

Table 1: Devices used in this work.

Device	Model	Manufacturer
AEC column	HiTrap ANX FF (HS) 5 mL	Cytiva Lifesciences
AEC column	XK16/20 column packed with 25 mL Source 30Q resin	Cytiva Lifesciences
anaerobic chamber	AC12-110	COY laboratory products
anaerobic chamber	AALC	COY laboratory products
autoclave	Systec V-150	Systec GmbH
autoclave	Tuttnauer 2540 EL	Tuttnauer Europe B.V.
balance	PT 1500	Sartorius
balance	SBC22	Scaltec
balance	PCB	Kern
blotting apparatus	Semidry-Blotter Sedec M	Peqlab Mini Trans-Blot®
CD spectrometer	J-850	Jasco
centrifuge	Biofuge pico	Heraeus
centrifuge	Avanti J20 XP	Beckmann
centrifuge	5810 R	Eppendorf
centrifuge	Megafuge 1.OR	Heraeus
centrifuge	Microstar 17R	VWR
chemiluminescence documentation	Chemostar Professional	Intas
clean bench	Labgard Class II	IBS Integra Biosciences
FPLC system	ÄKTA purifier 10 with monitor UV-900 and fraction collector Frac-950	GE Healthcare
FPLC system	ÄKTA pure 25 with monitor U9-M and fraction collector F9-R	GE Healthcare
FPLC system	ÄKTA start	GE Healthcare
homogeniser	generator GM 3100, ultrasonic converter UW 3100, booster horn SH 70 G, tip VS 70 T	Bandelin
HPLC system	SRD-3200 solvent rack with 2 degasser channels, HPG-3200SD pump, DAD-3000 detector with 13 µL analytical flow cell and VF-F11-A-01 fraction collector	Thermo Fisher
IMAC column	HisTrap FF crude 5 mL	Cytiva Lifesciences
incubator	B6	Heraeus instruments
pH meter	Sevencompact S210	Mettler Toledo
plate reader	Infinite R M200	Tecan
SDS-PAGE documentation	ILCE-6100	Sony
SDS-PAGE system	Mini Protean Tetra	BioRad
SEC column	HiLoad 26/600 Superdex 200 pg	GE Healthcare
SEC column	HiLoad 16/600 Superdex 200 pg	GE Healthcare
SEC column	HiLoad 16/600 Superdex 75 pg	GE Healthcare
SEC column	Superdex 200 10/300 GL	GE Healthcare
SEC column	Superdex 200 increase 10/300 GL	GE Healthcare
SEC column	Superdex 75 increase 10/300 GL	GE Healthcare
shaker	Multitron	Infors HT
rocking shaker	ST5	Ingenieurbüro CAT
spectrophotometer	Genesys 20	Thermo Scientific

Device	Model	Manufacturer
spectrophotometer	U-550	Jasco
sterilizer	Modell 700	Memmert
thermal cycler	Advanced primus 25	Peqlab
thermomixer	5436	Eppendorf
transformer	EPS 600	Pharmacia Biotech
vortex	Genie 2	Scientific Industries
water purification system	Ultra clear	Evoqua

2.2 Chemicals, enzymes and markers

Chemicals were bought from Aesar Alfar, Abcam, AppliChem, BioRad, Biozym, Merck, Roche, Roth, Sigma Aldrich, TargetMol and Thermo Fisher in the highest available purity. Restriction enzymes from New England Biolabs or Thermo Fisher and Phusion® DNA polymerase from Thermo Fisher were used for cloning. S-adenosyl homocysteine nucleosidase (SAHN) was obtained from ProSpec-Tany Technogene Ltd. and cytochrome c from Sigma Aldrich. PageRuler™ Prestained Protein Ladder, 10 to 180 kDa (Thermo Fisher) was used as marker for SDS-PAGE and low molecular weight (LMW) calibration kits from Cytiva Lifesciences and Amersham Biosciences were used for analytical size-exclusion chromatography (aSEC).

2.3 Oligonucleotides

Table 2: Oligonucleotides used for mutagenesis of pET24b(+)_*ISCU2*. Mutation sites are underlined. Residues are numbered according to the respective amino acid sequence in the UniProt database (<https://www.uniprot.org/>).

Name	Sequence (5' to 3')
<i>ISCU2_C69S_fwd</i>	AGCA <u>AGC</u> GGTGACGTAATGAAATTACAGATTCAAG
<i>ISCU2_C69S_rev</i>	GGAGCCCCCACCAGTCCAGTTC
<i>ISCU2_D71A_fwd</i>	TGAAATTACAGATTCAAGTGGATGAAAAGGG
<i>ISCU2_D71A_rev</i>	TTACT <u>GC</u> ACCACATGCTGGAGCC
<i>ISCU2_C95S_fwd</i>	TGGC <u>AGC</u> GGTTCCGCAATTGCCT
<i>ISCU2_C95S_rev</i>	AATGTTTTAAACCTAGCATCCACAATCTTCC
<i>ISCU2_C130S_fwd</i>	CTCCCGTGAACTGCACTGC
<i>ISCU2_C130S_rev</i>	GAAGGCTGAGCTCCTTGGCGATATCTG
<i>ISCU2_H137A_fwd</i>	ACTG <u>GC</u> ATGCTCCATGCTGGCTGAAGATGC
<i>ISCU2_H137A_rev</i>	TTACGGGAGGAAGGCAGAG
<i>ISCU2_C138S_fwd</i>	GCAC <u>AGC</u> TCCATGCTGGCTGAAGAT
<i>ISCU2_C138S_rev</i>	AGTTTCACGGGAGGAAGGCAGAGCT

2.4 Plasmids

All plasmids and mutant constructs were sequenced by Microsynth Seqlab (Göttingen) for sequence verification.

Table 3: Plasmid constructs used for protein overexpression. Numbering is according to respective amino acid sequences in the UniProt database.

Plasmid	ORF	Backbone	Source/reference
pETDuet1-FDX1	<i>His₆-FDX1 (1-60Δ)</i>	pETDuet1	(Sheftel <i>et al.</i> , 2010)
pETDuet1-FDX2	<i>His₆-FDX2 (1-68Δ)</i>	pETDuet1	(Sheftel <i>et al.</i> , 2010)
pASK-IBA43(+)-FDX1	<i>FDX1 (1-62Δ)</i>	pASK-IBA43(+)	(Webert, 2011)
pASK-IBA43(+)-FDX2	<i>FDX2 (1-68Δ)</i>	pASK-IBA43(+)	(Webert, 2011)
pET15b-Yah1	<i>S.c. Yah1 (1-57Δ)</i>	pET15b	U. Mühlenhoff ^a
pET28a(+)-LIAS	<i>His₆-Thr-LIAS (1-35Δ)</i>	pET28a(+)	S. Booker ^b
pETDuet1_NFU1	<i>His₆-NFU1 (1-56Δ)</i>	pETDuet1	(Uzarska <i>et al.</i> , 2016)
pETDuet1_NFU1	<i>NFU1 (1-44Δ)</i>	pETDuet1	obtained from Synbio
pETDuet1_NFU1	<i>NFU1 (1-58Δ)</i>	pETDuet1	obtained from Synbio
BOLA1	<i>His₆-BOLA1 (1-29Δ)</i>	pETDuet1	(Uzarska <i>et al.</i> , 2016)
BOLA3	<i>His₆-BOLA3 (1-24Δ)</i>	pETDuet1	(Uzarska <i>et al.</i> , 2016)
GLRX5	<i>His₆-GLRX5 (1-31Δ)</i>	pETDuet1	(Uzarska <i>et al.</i> , 2016)
pET24b(+)-ISCU2	<i>ISCU2-His₆ (1-34Δ)</i>	pET24b(+)	(Freibert <i>et al.</i> , 2021)
pETDuet1-NFS1-ISD11	<i>NFS1 (1-55Δ), His₆-Tev-ISD11</i>	pETDuet1	(Freibert <i>et al.</i> , 2021)
pRSFDuet1-ACP	<i>ACP (1-68Δ)</i>	pRSFDuet1	(Freibert <i>et al.</i> , 2021)
pMCSG7-FXN	<i>His₆-Tev-FXN (1-80Δ)</i>	pMCSG7	(Freibert <i>et al.</i> , 2021)
pETDuet1-FDXR	<i>His₆-FDXR (1-32Δ)</i>	pETDuet1	(Sheftel <i>et al.</i> , 2010)

^a Institut für Zytobiologie, Philipps-Universität Marburg, Karl-von-Frisch-Str. 14, 35032 Marburg, Germany

^b Department of Biochemistry and Molecular Biology, Pennsylvania State University, University Park, PA 16802, USA

Table 4: Mutant constructs used for protein overexpression based on plasmids listed in Table 3. FDX2 variants are further described in Table 5.

Plasmid	Exchanges	Source/reference
pET24b(+)-ISCU2	Y35A	obtained from Synbio
pET24b(+)-ISCU2	C69S	this work
pET24b(+)-ISCU2	D71A	this work
pET24b(+)-ISCU2	C95S	this work
pET24b(+)-ISCU2	C130S	this work
pET24b(+)-ISCU2	K135A	obtained from Synbio
pET24b(+)-ISCU2	H137A	this work
pET24b(+)-ISCU2	C138S	this work
pET24b(+)-ISCU2	C69/95S	this work
pET24b(+)-ISCU2	C69/138S	this work
pET24b(+)-ISCU2	C95/138S	this work
pMCSG7-FXN	Q148A	obtained from Synbio
pMCSG7-FXN	N151A	obtained from Synbio
pMCSG7-FXN	W155A	obtained from Synbio
pMCSG7-FXN	W155F	obtained from Synbio
pMCSG7-FXN	N151A/R165A	obtained from Synbio
pASK-IBA43(+)-FDX2	M5	(Webert, 2011)
pASK-IBA43(+)-FDX2	R135E	(Webert, 2011)
pASK-IBA43(+)-FDX2	ΔC12	(Webert, 2011)
pASK-IBA43(+)-FDX2	M5 ΔC12	(Webert, 2011)
pASK-IBA43(+)-FDX2	M3 M5 ΔC12	(Webert, 2011)
pASK-IBA43(+)-FDX2	M5 R135E ΔC12	(Webert, 2011)

Table 5: Interconversion variants of FDX2. Listed FDX2 sequences were replaced with the respective FDX1 sequences.

Variant	Residues (FDX2)	Sequence (FDX2)	Residues (FDX1)	Sequence (FDX1)
M3	95 – 101	HLAQRH	91 – 97	DVVVEN
M5	--	--	103 – 104	FG
R135E	135	R	133	E
ΔC12	163 – 174	NFYVDGHVPKPH	173 – 184	DARQSIDVGKTS

2.5 Bacterial strains

2.5.1 E. coli DH5α

This strain obtained from Invitrogen was used for cloning purposes. Deletion of endonuclease A and DNA repair enzyme RecA in this strain enables high plasmid stability.

Genotype: *F*⁻φ80/*lacZ*ΔM15 Δ(*lacZYA-argF*)U169 *recA1 endA1 hsdR17*(*r*_K⁻ *m*_K⁺) *phoA supE44 thi-1gyrA96 relA1 λ*⁻

2.5.2 E. coli BL21(DE3)

This strain obtained from Invitrogen was used for recombinant protein expression. OmpT and Lon protease are deleted, and the strain contains the λ prophage DE3 encoding T7 RNA polymerase under control of the *lacUV5* promoter and *laqlq*. This allows for IPTG-induced protein expression using plasmids with T7 promoter (Studier *et al.*, 1990).

Genotype: *F*⁻ *ompT*, *hsdS_B* (*r*_B⁻ *m*_B⁻), *dcm*⁺ *Tet*^r *galλ*(DE3) *endA Hte*

2.6 Media

E. coli cells were cultivated in liquid lysogeny broth (LB). Terrific broth (TB) and super optimal broth (SOB) were used for recombinant protein expression and generation of chemically competent cells, respectively. Media components listed in Table 6 were dissolved in dH₂O and autoclaved for 20 min at 121 °C and 1.5 bar. Solid media additionally contained 20 g/L agar. SOB medium was adjusted to pH 7.0. To 1 L autoclaved SOB medium, 2.5 mL of 1 M KCl, 10 mL of 1 M MgCl₂ and 10 mL of 1 M MgSO₄ from separately autoclaved solutions were added. Autoclaved TB medium was pH-adjusted using a separately autoclaved 10x stock of potassium phosphate (125.4 g/L K₂HPO₄, 23.12 g/L KH₂PO₄).

Table 6: Composition of 1 L of LB, TB and SOB media.

Component	LB	TB	SOB
tryptone	10 g	12 g	20 g
yeast extract	5 g	24 g	5 g
NaCl	10 g	-	2 mL of 5 M stock
glycerol	-	4 mL	-

3 Methods

3.1 Microbiological and molecular biology methods

3.1.1 Preparation and transformation of chemically competent *E. coli* cells

5 mL liquid SOB medium were inoculated with one colony of *E. coli* DH5 α or BL21 cells and shaken overnight at 30 °C. 100 mL SOB medium in a 1 L flask were inoculated with 1 mL overnight culture, 7.2 mL of a 5 M NaCl solution added and the culture grown to OD₆₀₀ ~0.5. The cells were collected by centrifugation (3220 x g, 5 min) and remaining liquid removed thoroughly with a pipette. Cells were resuspended in 10 mL cold filter sterilized TFB buffer (10 mM MES pH 6.2 with KOH, 100 mM RbCl, 45 mM MnCl₂, 10 mM CaCl₂, 3 mM [Co(NH₃)₆]Cl₃) and incubated 10 min on ice. After addition of 350 μ L DMSO whilst swirling, the cells were incubated for 10 min, and subsequently 100 μ L aliquots were flash-frozen in liquid nitrogen using Eppendorf tubes pre-cooled on ice. Cells were stored at -80 °C and used for up to one year.

For transformation, cell aliquots were thawed on ice and incubated for 15 – 30 min with 10 – 100 ng of plasmid DNA before a heat shock of 42 °C for exactly 90 s was applied. After incubation on ice for 1 – 2 min, 1 mL LB medium was added and the transformants shaken for 1 h (37 °C, 1000 rpm). Cells were pelleted (rt, 1 min, 4000 x g) and the majority of supernatant discarded, leaving 100 – 150 μ L. After resuspension, cells were streaked on an LB agar plate with appropriate antibiotics and incubated overnight at 37 °C.

3.1.2 Isolation of plasmid DNA from *E. coli*

Plasmid DNA was extracted from *E. coli* overnight cultures using the NucleoSpin® Plasmid Kit from Machery-Nagel according to the manufacturer's protocol.

3.1.3 Mutagenesis of plasmid DNA

Point mutated plasmid DNA was either ordered from Synbio Technologies or introduced by site-directed mutagenesis similar to the QuikChange® protocol from Stratagene but with different primer design. Mutagenesis PCR was done with a pair of non-overlapping primers, their 5'-ends being directly adjacent when bound to the plasmid and one primer

encoding the desired mutation. Subsequently, methylated parent DNA was selectively removed using the restriction enzyme *DpnI* (target sequence: 5'-Gm⁶ATC-3') and DH5 α cells were directly transformed with the mixture.

3.1.3.1 Mutagenesis PCR

The standard reaction composition and program of polymerase chain reactions (PCRs) for site-directed mutagenesis are given below. The annealing temperature was based on the melting temperature (T_m) of the primers as calculated by the OligoAnalyzer™ Tool. PCR optimization included altering concentrations of primers or template DNA as well as annealing temperature, elongation time, the number of amplification cycles or addition of up to 3 μ L DMSO.

Table 7: Standard PCR composition.

Volume (μ L)	Component
10	10x HF-buffer
1.0	10 mM dNTPs
2.5	10 μ M forward primer
2.5	10 μ M reverse primer
1.0	15 ng/ μ L DNA template
1.0	1M MgCl ₂
1.0	Phusion polymerase
ad 50	ddH ₂ O

Table 8: Standard PCR program.

Step	Temperature (°C)	Time
initial denaturation	98	90 s
denaturation (35x)	98	15 s
annealing (35x)	T_m	35 s
elongation (35x)	72	30 s/kb
final elongation	72	10 min
hold	8	-

3.1.3.2 Restriction enzyme digest

1 μ L *DpnI* (Thermo Fisher) was added to 50 μ L PCR product and incubated for 40 min at 37 °C. Transformation was done directly afterwards adding 25 μ L pre-cooled digestion product to 100 μ L chemically competent DH5 α cells, incubating for 30 min and proceeding as described in chapter 3.1.1.

3.2 Protein expression and purification

3.2.1 Recombinant protein expression in *E. coli*

E. coli BL21(DE3) cells containing the required expression plasmid(s) were grown in LB medium with appropriate antibiotics (100 mg/L carbenicillin and/or 30 mg/L kanamycin) overnight at 37 °C. For (NIA)₂ production, cells co-transformed with two plasmids encoding NFS1-ISD11 and ACP were grown. 2 L TB medium in 5 L flasks was inoculated with 25 – 50 mL of the starter culture, appropriate antibiotics (100 mg/L ampicillin and/or 30 mg/L kanamycin) added and the culture shaken at 37 °C and 160 rpm for ~7 h. pASK-IBA43(+) constructs were induced with 0.2 mg/L anhydrotetracycline and pET-vectors with 1 mM isopropyl β-D-thiogalactopyranoside (IPTG). Additional supplements were added after induction if required ((NIA)₂: 2 mM pyridoxine hydrochloride, FDXs: 250 μM Fe(NH₄)₂(SO₄)₂, FDXR: 5 μM riboflavin). Subsequently, cultures were shaken at 22 °C overnight and cell pellets harvested by centrifugation (7548 x *g*, 10 min, 4 °C). LIAS expression was done based on a published protocol (McCarthy & Booker, 2018). BL21 cells harbouring two plasmids (encoding human LIAS and the *ISC* operon from *Azotobacter vinelandii*) were induced with 0.2% (w/v) L-arabinose at OD₆₀₀ ~0.3 (expression of ISC factors) and grown to OD₆₀₀ ~0.8. Temperature was lowered from 37 to 18 °C and LIAS overexpression induced with 200 μM IPTG. The culture was supplemented with 250 μM Fe(NH₄)₂(SO₄)₂ and 250 μM cysteine and grown overnight. The LIAS expression strain was kindly supplied by Dr. S. Booker and Dr. D. Warui.

3.2.2 Cell lysis

Around 15 mL of cell pellet were resuspended in buffer compatible with the subsequent purification (Table 9) to a final volume of ~80 mL. A spatula's tip of lysozyme and DNaseI and a tablet proteinase inhibitor cocktail (cOmplete™) were added together with optional supplements (ISCU2 D71A and (NIA)₂: spatula's tip of ATP and 100 μL of 1 M MgCl₂, (NIA)₂: PLP) and the suspension mixed for ~15 min. Cells were cooled in a water-ice bath and lysed using a homogeniser with an ultrasonic probe (Bandelin) for 20 min (95% amplitude, 1 s on, 1 s off). The lysate was cleared by centrifugation (55,914 x *g*, 40 min, 4 °C) and the supernatant used for chromatographic protein purification. Only for LIAS, cell lysis and protein purification were done anaerobically.

Table 9: Buffers used for resuspension of cell pellets.

IMAC buffer	AEC buffer	(NIA) ₂	ISCU2 D71A	LIAS
50 mM Tris	35 mM Tris	50 mM Tris	50 mM HEPES	100 mM HEPES
300 mM NaCl	50 mM NaCl	300 mM NaCl	500 mM KCl	300 mM KCl
5% (w/v) glycerol	5% (w/v) glycerol	5% (w/v) glycerol	10% (w/v) glycerol	5 mM TCEP
pH 7.4 with HCl	pH 7.5 with HCl	pH 8.0 with HCl	5 mM TCEP	20 mM imidazole
			pH 7.5 with KOH	pH 7.5 with KOH

3.2.3 Chromatographic methods

After cell lysis, His-tagged constructs were purified aerobically by immobilised metal affinity chromatography (IMAC) and non-His-tagged constructs by anion exchange chromatography (AEC; compare Table 3). All proteins were subsequently purified anaerobically by size exclusion chromatography (SEC). All purifications were done at 0 – 4 °C. For LIAS, the whole purification procedure was done anaerobically. Since the anaerobic chamber could not be cooled, the used buffers and collected eluate were cooled in ice water and the purification procedure performed as fast as possible. All buffers were filtered using a 0.22 µm filter and gas exchanged for at least 48 h if used anaerobically.

3.2.3.1 Immobilized metal affinity chromatography (IMAC)

All steps were done at 5 mL/min flow rate. A 5 mL HisTrap FF crude column (Cytiva) pre-packed with Nickel Sepharose™ and equilibrated with resuspension buffer (Table 9) was loaded with cleared lysate and washed with ~10 column volumes (CV) wash buffer. Wash buffers were equal to resuspension buffers but additionally contained 10 mM imidazole in standard purifications. Imidazole concentration was different for ISCU2 and FXN (70 mM imidazole) and (NIA)₂ (5 mM imidazole). The washing step during LIAS purification was performed with a different buffer containing 100 mM HEPES, 300 mM KCl, 2 mM TCEP, 20 mM imidazole and 10% (w/v) glycerol, pH 7.5. Proteins were eluted with buffer containing 250 mM imidazole (LIAS: 100 mM HEPES, 300 mM KCl, 2 mM TCEP, 250 mM imidazole, 20% (w/v) glycerol, pH 7.5), and fractions containing the desired protein were concentrated as described in chapter 3.2.6. If proteins were not further purified on the same day, the buffer was exchanged to the respective resuspension buffer, and samples were flash-frozen in liquid nitrogen and stored at -80 °C.

3.2.3.2 Anion exchange chromatography (AEC)

All AEC steps were done at 2.5 mL/min flow rate. Cleared lysate was loaded onto a 25 mL column packed with Source™ 30Q resin (Cytiva Lifesciences) and equilibrated

with AEC buffer using a 50 mL superloop. After washing with 4 CV of AEC buffer, proteins were eluted with a gradient from 0 to 100% elution buffer (35 mM Tris, 1 M NaCl, 5% (w/v) glycerol, pH 7.5) over 6 CV. Desired protein fractions were pooled based on the AU_{410 nm} (FDXs) or SDS-PAGE (NFU1) and concentrated.

For cryo-EM and spectroscopic experiments, (NIA)₂ purification included an additional AEC step. A pre-packed HiTrap ANX FF (HS) 5 mL column (Cytiva Lifesciences) equilibrated in buffer A (17 mM Tris, 100 mM NaCl, 1.7% w/v glycerol, pH 8.0) was loaded with IMAC eluate diluted 1:4 in 50 mM Tris pH 8.0. After washing with 2 CV of buffer A, (NIA)₂ was eluted using a gradient to 100% buffer B (35 mM Tris, 1 M NaCl, 5% w/v glycerol, pH 8.0) over 15 CV. Desired protein fractions were combined and concentrated to <2 mL.

3.2.3.3 Size exclusion chromatography (SEC)

Proteins given in Table 10 were incubated anaerobically on ice for 40 – 60 min with the stated compounds. Samples were cleared using a 0.22 µm filter and loaded onto a Hi-Load 16/600 Superdex 200 pg ((NIA)₂ and FDXR) or 75 pg (all other proteins) equilibrated with the appropriate SEC buffer (Table 11). Proteins were purified with 1.2 CV SEC buffer at a flow rate of 1 mL/min, and desired fractions were concentrated.

Table 10: Pre-incubation of protein samples.

ISCU2, FXN, NFU1, GLRX5, BOLA3	ISCU2 D71A	(NIA) ₂
10 mM TCEP	10 mM TCEP	10 mM TCEP
10 mM DTPA	10 mM DTPA	10 mM DTPA
25 mM KCN	25 mM KCN	0.5 mM PLP
	10 mM DT	
	40 mM MgCl ₂	
	10 mM ATP	

Table 11: SEC buffers

standard	(NIA) ₂	LIAS
50 mM Tris	50 mM Tris	50 mM HEPES
150 mM NaCl	150 mM NaCl	300 mM KCl
5% (w/v) glycerol	10% (w/v) glycerol	10% (w/v) glycerol
pH 7.4 with HCl	pH 8.0 with HCl	pH 7.5 with KOH

3.2.4 TEV cleavage of FXN

The N-terminal His-tag of IMAC-purified FXN was removed by TEV cleavage, since it inhibits *de novo* Fe/S cluster biogenesis (Freibert *et al.*, 2021). Cleavage was done according to a published protocol (Raran-Kurussi *et al.*, 2017). 831 µM FXN and self-made

recombinant TEV protease at an AU₂₈₀ ratio of 60:1 were incubated with 0.1% v/v β -mercaptoethanol (ME) and 0.5 mM EDTA and incubated overnight at 10 °C. The digested product was loaded onto a HisTrap FF crude column and the flow-through collected. SDS-PAGE indicated completely cleaved FXN. The TEV protease bound to the column and was not detected in the flow through. Cleaved FXN was further purified by SEC.

3.2.5 Buffer exchange of protein samples

Buffer exchange was done with PD-10 desalting columns (Cytiva) according to the manufacturer's instructions.

3.2.6 Concentration of proteins

Proteins were concentrated using Amicon centrifugal filters of appropriate MW cut-off (100 kDa: (NIA)₂; 30 kDa: FDXR, LIAS; 10 kDa: all other proteins) at 3,220 x *g* and 4 °C in 10 min intervals. The solution was mixed by gentle inversion between each interval to avoid protein precipitation at the filter membrane.

3.3 Protein biochemical methods

3.3.1 Sodium dodecyl sulfate polyacrylamide gel electrophoresis (SDS-PAGE)

Standard SDS-PAGE analysis of protein samples was done using the Laemmli system (Laemmli, 1970) and gels casted according to Table 12. Acrylamide content of the resolving gel varied from 10 – 15% w/v, depending on protein size. A stock of 30% w/v acrylamide (Biorad) was used. Protein samples were mixed with an equivalent volume of 2x sample buffer, incubated 5 min at 95 °C or 15 min at room temperature and centrifuged (13,000 x *g*, 1 min) before loading onto the gel. Electrophoresis was done in SDS running buffer (50 mM Tris, 200 mM glycerol, 0.1% w/v SDS, not pH adjusted) at 10 mA until the samples left the stacking gel (~1 h) and subsequently at 15 – 30 mA until the desired separation was reached (2 – 4 h). For staining, gels were shaken for 1 h in 5 – 10 mL of InstantBlue™ (Abcam) and incubated in water overnight.

When separation of low molecular weight proteins (10 – 20 kDa) was not sufficient with the Laemmli system, tricine SDS-PAGE (Schagger, 2006) was performed instead. A stock of 40% w/v acrylamide (AppliChem) was used. Electrophoresis was performed at 15 mA (stacking gel, ~1 h) and subsequently 40 mA (resolving gel, ~6 h), using different buffers in the anode (100 mM Tris, pH 8.9) and cathode (100 mM Tris, 100 mM tricine, 0.1% w/v SDS, pH 8.25) compartments.

Table 12: Composition of gels and sample buffer for SDS-PAGE.

stacking gel (Laemmli)	resolving gel (Laemmli)	stacking gel (tricine)	resolving gel (tricine)	2x sample buffer
126 mM Tris pH 6.8	378 mM Tris pH 8.8	1 M Tris pH 8.45	1 M Tris pH 8.45	120 mM Tris pH 6.8
0.1% w/v SDS	0.1% w/v SDS	0.1% w/v SDS	0.1% w/v SDS	20% w/v glycerol
4% w/v acrylamide	15% w/v acrylamide	5% w/v acrylamide	10% w/v glycerol	4% w/v SDS
0.1% w/v APS	0.1% w/v APS	0.05% w/v APS	16% w/v acrylamide	0.02% w/v bromophenol blue
0.1% v/v TEMED	0.032% v/v TEMED	0.083% v/v TEMED	0.033% w/v APS	100 mM TCEP
			0.033% w/v TEMED	

3.3.2 Determination of protein concentration

Protein concentration was determined using Bradford reagent (BioRad) according to the manufacturer's instructions. Bovine serum albumin was used for generation of a calibration curve. Concentrations of NIA, ISCU2, FXN, FDX1, FDX2, LIAS and NFU1 Δ N58 were additionally determined by amino acid analysis (service provided by Leibniz-Institut für Analytische Wissenschaften, Dortmund). Proteins were buffer-exchanged to 50 mM HEPES, 150 mM NaCl, pH 7.5 to avoid interference from Tris or glycerol. Protein concentrations were determined by both Bradford assay ($n = 4$) and amino acid analysis ($n = 2$). A correction factor compensating for the systematic error of the Bradford assay was calculated and subsequently applied to Bradford concentration determinations of the stated proteins.

3.3.3 Determination of Fe and sulfide concentration

The content of Fe and acid labile sulfide of protein samples was determined using colorimetric assays as described previously (Miethke *et al.*, 2011).

3.3.4 Mass spectrometric analyses

Mass spectrometric (MS) analyses were performed by the Mass Spectrometry facility of the department of Chemistry, University of Marburg.

3.3.5 Chemical reconstitution of Fe/S proteins

All reconstitutions were done at 0 – 8 °C under strictly anaerobic conditions (Coy anaerobic chamber). For ISCU2 and BOLA3-GLRX5 reconstitutions, non-diluted protein stocks were pre-incubated with thiol reductant (ISCU2: 1% v/v ME or 5 mM DTT, BOLA3-

GLRX5: 10 mM GSH). Proteins were diluted in reconstitution buffer (Table 13) to a final volume of 0.5 – 2.5 mL, and the solution was incubated for at least 1 h. Ferric ammonium citrate was added whilst mixing gently, and the solution was incubated for 20 min. Depending on the sample, appearance of orange colour of varying intensity could be observed. Lithium sulfide was added slowly and stepwise under constant mixing to avoid formation of sulfide precipitates, and the solution incubated for at least 30 min, concomitant with appearance of a reddish or brown colour. Remaining Fe and sulfide contaminants of the reconstituted sample were removed by buffer exchange or SEC, and the sample was concentrated if necessary. Since desalting of ISCU2 reconstitutions led to significant sample loss, it was omitted in several experiments. Reconstituted samples were characterised spectroscopically, and optionally Fe and sulfide content were determined.

Table 13: Conditions for chemical reconstitution of protein samples.

protein	buffer	FAC (μ M)	Li ₂ S (μ M)
100 μ M ISCU2 (WT or variants)	50 mM Tris, 150 mM NaCl, 5% w/v glycerol, 0.2% v/v ME or 0.5 – 1.0 mM DTT, pH 8.0	300	300
100 μ M BOLA3, 100 μ M GLRX5	50 mM Tris, 150 mM NaCl, 5% w/v glycerol, 2 mM GSH, pH 8.0	400	400
150 μ M NFU1	50 mM HEPES, 300 mM KCl, 20% w/v glycerol, 5 mM DTT, pH 7.5	600	600
100 μ M LIAS		800	800

3.3.6 Immunoblotting

Samples were separated by SDS-PAGE and transferred to a nitrocellulose membrane. The membrane and four Whatman papers were soaked in transfer buffer (25 mM Tris, 200 mM glycine, 20% v/v ethanol, 0.02% w/v SDS, not pH adjusted) and everything stacked in a blotting apparatus in the order 2x Whatman paper, membrane, gel, 2x Whatman paper from anode to cathode. Blotting was done for 130 min at 250 mA. The membrane was rinsed with water, stained with 0.2% w/v Ponceau S, 3% w/v trichloroacetic acid and 3% w/v sulfosalicylic acid, and dried overnight. Membranes were shaken in ddH₂O for 15 min and in TBST buffer (20 mM Tris, 150 mM NaCl, 0.05% v/v Tween 20, pH 7.4) for 15 min. Blocking was done in TBST with 5% milk powder overnight at 4 °C and subsequently the membrane was incubated in primary antibody (rabbit anti-NFU1 (Navarro-Sastre *et al.*, 2011)) diluted in TBST + 5% milk powder for 2 h at room temperature. After washing in TBST and storage overnight, the membrane was shaken in a peroxidase-coupled secondary antibody (anti-rabbit, BioRad) diluted in TBST + 5% w/v milk powder for 1 h. After washing in TBST, proteins were detected by chemiluminescence using Pierce ECL western blotting substrate (Thermo Fisher) according to the manufacturer's instructions.

3.4 Enzymatic assays and other analyses

All analyses except the cytochrome c reduction assay were performed under strictly anaerobic conditions in an anaerobic chamber with anaerobic buffers.

3.4.1 Fe binding of ISCU2

50 μ M ISCU2 in 35 mM Tris, 150 mM NaCl, 5% w/v glycerol, pH 8.0 was incubated with 2 mM TCEP for 5 min at room temperature. A CD spectrum (250 – 350 nm) was recorded in a cuvette tightly sealed with a rubber plug. Subsequently, another spectrum with anaerobically added 2 – 5 eq. FeCl_2 over ISCU2, inducing formation of Fe-ISCU2 was recorded. The apo-ISCU2 spectrum was subtracted from the Fe-ISCU2 spectrum to remove signal contributions from aromatic amino acids (Kelly & Price, 2000).

3.4.2 Analytical SEC and SEC-MALS

Analytical SEC (aSEC) was performed to determine the oligomeric state and cofactor binding of proteins. Columns were equilibrated in SEC buffer (0.5 – 1 mL/min) and approximately 100 μ L of 1 mg/mL protein samples were loaded for analysis. The molecular weight (MW) of sample signals was calculated based on calibration curves generated for the employed SuperdexTM 75 (aprotinin, 6.5 kDa; ribonuclease A, 13.7 kDa; carbonic anhydrase, 29 kDa; ovalbumin, 44 kDa; conalbumin, 75 kDa; Cytiva Lifesciences) and SuperdexTM 200 (ribonuclease A, 13.7 kDa; chymotrypsinogen A, 25 kDa; ovalbumin, 43 kDa; albumin, 67 kDa; Amersham Biosciences) increase 10/300 GL columns using low MW (LMW) calibration kits according to the manufacturer's instructions. aSEC in combination with multi-angle light scattering (MALS) was performed at 0.5 mL/min flow rate using a PN3150 refractive index detector coupled with a PN3609 MALS detector (both Postnova Analytics), measuring at five angles (60°, 76°, 90°, 108° and 124°). Data analysis was performed using NovaMALS version 1.5.0.8 with data fitting via Debye's model.

3.4.3 Persulfide transfer assay with maleimide polyethyleneglycol₁₁ biotin (MPB)

Persulfide transfer from NFS1 to ISCU2 was analysed based on Cys alkylation and adapted from a previously described method (Parent *et al.*, 2015). Standard reactions contained 100 μ M FeCl_2 , 100 μ M Na-ascorbate, 20 μ M ISCU2, 40 μ M FXN and 40 μ M NIA in assay buffer (35 mM Tris, 150 mM NaCl, 5% w/v glycerol, pH 7.4). After incubation for 3 min at room temperature, 200 μ M cysteine was added to initiate persulfide formation, and the reaction was quenched after 10 s by mixing with 2 eq. (over total thiol concentration) of maleimide-polyethyleneglycol₁₁-biotin (MPB) dissolved in DMSO. After

additional 20 s, 1% w/v SDS was added, and samples were mixed vigorously and incubated for 10 min. Two aliquots of each sample containing 1 µg of ISCU2 were mixed with SDS-PAGE sample buffer with and without TCEP, respectively. After incubation at room temperature for 15 min, reduced and optionally non-reduced samples were analysed by electrophoresis using separate gels. Reduced samples allowed the quantification of persulfide species based on the mass shift of MPB-labelled ISCU2 (schematic outline in Appendix Figure 49). Non-reduced samples were used as a control for completeness of labelling. For ISCU2 WT and variants with at least three Cys residues remaining, standard 15% w/v acrylamide resolving gels were employed. Variants with less than three Cys residues were analysed by tricine SDS-PAGE using 16% w/v acrylamide resolving gels to achieve better separation. ISCU2 bands of the gels were quantified by densitometry using Image Studio Lite version 5.2 to calculate the percentage of persulfidated ISCU2.

3.4.3.1 Persulfide reduction assay

Samples for persulfide reduction by FDX2 were treated as for MPB-based persulfide transfer, except that 10 s after cysteine addition, 200 µM NADPH, 1 mM MgCl₂, 0.4 µM FDXR and 20 µM FDX2 were added simultaneously. The solution was incubated for 3 min before quenching with MPB11 and further analysed as described above.

3.4.4 Persulfide transfer assay with iodoacetyl tandem mass tag (iodoTMT)

Using iodoTMTsixplex™ isobaric labels (Thermo Fisher) in persulfide transfer reactions allowed for quantification of persulfide content of each individual Cys residue of ISCU2 and NFS1 by MS² analysis (schematic outline in Appendix Figure 50). Stocks of 30 mM iodoTMT dissolved in 50% v/v methanol, 5% w/v SDS, 5 mM Na-EDTA and 100 mM Tris pH 8.0 were made directly before the experiment. Standard reactions contained 100 µM FeCl₂, 20 µM ISCU2, 20 µM FXN and 20 µM NIA in assay buffer (35 mM Tris, 150 mM NaCl, 5% w/v glycerol, pH 8.0). Following incubation for 3 min at room temperature, 100 µM cysteine was added to initiate persulfide formation. After 10 – 320 s, reactions were quenched with 15 mM iodoTMT, incubating for 10 min. Samples were incubated with 22 mM cysteine for 10 min to quench remaining iodoTMT and persulfides were cleaved by incubation with 5 mM TCEP for 10 min. Cys residues were subsequently labelled using a second iodoTMT reagent of different reporter fragment mass (15 mM, 10 min) and remaining label quenched with cysteine (15 mM, 10 min). Samples were subjected to trypsin digestion and enriched via immobilization on anti-TMT resin. IodoTMT labels were quantified based on their collision-induced dissociation (CID) monoi-

sotopic reporter masses by nanoHPLC-MS² by the Mass Spectrometry core facility Marburg, according to the manufacturer's instructions. Reporter fragments were extracted from MS² data with 5 ppm mass accuracy, and the signals were integrated. For each protein Cys residue, the percentage of persulfidation was calculated from the detected amounts of both iodoTMT labels.

3.4.5 Enzymatic reconstitution of *de novo* Fe/S cluster synthesis

In vitro enzymatic reconstitutions were performed similarly to previous experiments (Freibert *et al.*, 2017; Webert *et al.*, 2014). Standard reactions contained 0.5 mM NADPH, 0.8 mM Na-ascorbate, 0.3 mM FeCl₂, 0.2 mM MgCl₂, 5 mM GSH, 40 µM ISCU₂, 5 µM NIA, 5 µM FXN, 5 µM FDX₂ and 0.5 µM FDXR in a final volume of 300 µL in reconstitution buffer (50 mM Tris, 150 mM NaCl, 5% w/v glycerol, pH 8.0). Reactions were transferred to a CD spectrometer in a cuvette tightly sealed with a rubber plug and containing a magnetic stirring bar, and the CD signal at 431 nm was monitored at 20 °C. A time course was recorded for 12 – 20 min. After 30 s, Fe/S cluster synthesis was initiated by injecting 0.5 mM cysteine into the sealed cuvette. Optionally, CD spectra (300 – 650 nm) were recorded before and after the time course.

3.4.6 Lipoylation assay

The lipoylation assay developed in this work using human proteins was based on an assay established for bacterial lipoyl synthase (McCarthy & Booker, 2018). Reaction buffer (50 mM HEPES, 300 mM KCl, 10% w/v glycerol, pH 7.5) was supplied with 10 mM MgCl₂, 2 mM NADPH and 0.5 mM octanoyl peptide (Glu-Ser-Val-[N⁶-octanoyl]Lys-Ala-Ala-Ser-Asp). The peptide sequence resembles the *E. coli* H protein (gcvH). The corresponding sequence of the human homolog GCSH is almost identical, with only the C-terminal Asp being replaced with Glu. Optionally, up to 4 mM CuCl₂ and/or Ele (from a stock solution in DMSO) were added. Ele/Cu reactions contained up to 2% v/v DMSO. Control reactions showed that LIAS activity was not altered up to the highest tested concentration of 4% v/v DMSO. 20 µM FDXR, 140 µM FDX and 1 mM SAM were added, and reactions were started by adding 35 µM reconstituted LIAS to a final volume of 25 µL. After incubation at 23 °C for 6 – 150 min, reactions were quenched by adding 100 mM H₂SO₄ and 4 mM TCEP and subjected to HPLC-MS as described previously (McCarthy & Booker, 2018). Product formation was quantified by determining the mass areas (MA) of the respective ion traces. Peptide substrate and standards were kindly supplied by Dr. S. Booker and Dr. D. Warui.

3.4.7 Cytochrome c reduction assay

In vitro cytochrome c reduction by FDXs was performed as described previously (Weiler *et al.*, 2020).

3.4.8 Analysis of Fe/S cluster stability upon Cu titration

In an anaerobic chamber, FDX1, FDX2 or LIAS were diluted to a final volume of 300 μ L in buffer (50 mM Tris, 150 mM NaCl, 5% w/v glycerol, pH 7.5) in a CD cuvette which was sealed tightly. CD spectra (300 – 650 nm) were recorded at 20 °C and the proteins subsequently titrated with Ele and/or CuCl₂. For each addition of the reagents, the cuvette was transferred back to the anaerobic chamber to retain anaerobicity.

3.5 Spectroscopic methods

3.5.1 UV/Vis spectroscopy

Fe/S proteins were analysed by UV/Vis spectroscopy based on the different characteristic signals of [2Fe-2S] and [4Fe-4S] clusters in the range of ~300 – 650 nm (Freibert *et al.*, 2018). Samples were diluted in an appropriate buffer under anaerobic conditions to an AU_{280 nm} of 0.5 – 1.0, and spectra (260 – 900 nm) were recorded at 200 nm/min scan rate. A buffer spectrum was recorded and subtracted to yield the final protein spectrum.

3.5.2 CD spectroscopy

Circular dichroism (CD) spectroscopy was employed to investigate the Fe and Fe/S cluster binding of proteins. Spectra of Fe (250 – 350 nm, 200 nm scanning speed, 4 accumulations) and Fe/S cluster (350 – 650 nm, 200 nm scanning speed, 2 accumulations) binding protein samples (300 μ L of typically 50 – 100 μ M concentration) were recorded in a 4 mm wide quartz cuvette. All data were collected at the following settings: Sensitivity: low; data integration time: 2 s; band width: 1.71 nm; data pitch: 0.1 nm; scanning mode: continuous.

3.5.3 Preparation of Mössbauer and X-ray absorption spectroscopy samples

To achieve maximum comparability between Mössbauer and X-ray absorption spectroscopy (XAS), aliquots taken from the same sample preparations were analysed by the respective methods. Ferrous ammonium sulfate (Mohr's salt, (NH₄)₂⁵⁷Fe(SO₄)₂) was employed as ⁵⁷Fe source, enabling low levels of Fe(III) impurities. (NH₄)₂⁵⁷Fe(SO₄)₂ was

synthesized from elemental ^{57}Fe as well as $(\text{NH}_4)_2\text{SO}_4$ and H_2SO_4 , according to a previously described method (Konz *et al.*, 2014).

Samples were prepared under strictly anaerobic conditions in an anaerobic chamber. Chemicals were dissolved in buffer 1 (50 mM Tris, 150 mM NaCl, 5% w/v glycerol, pH 8.0), and all components listed in Table 14 were mixed with buffer 1 or buffer 2 (50 mM Tris, 150 mM NaCl, 70% w/v glycerol, pH 8.0) to achieve a final glycerol content of 30% w/v at a final volume of 360 μL . Buffers, ISCU2, $(\text{NH}_4)_2^{57}\text{FeSO}_4$ and Na-ascorbate were mixed first, and samples were incubated for 5 – 10 min. Cysteine was added last to samples to initiate persulfide formation. Directly afterwards, 120 μL were pipetted into XAS sample cells and 240 μL into Mössbauer cups. Samples were flash frozen in liquid nitrogen inside the anaerobic chamber. This resulted in an incubation time with cysteine of approximately 1 and 2 min for XAS and Mössbauer samples, respectively. The [2Fe-2S]-ISCU2 sample was incubated for 40 min before flash freezing, and the formation of [2Fe-2S]-loaded ISCU2 was confirmed by analysing an aliquot (50 μL) by CD spectroscopy.

Table 14: Final μM concentration of the components of standard samples.

Compound (μM)	Fe-U	(Fe-NIAU) ₂	(Fe-NIAUX) ₂	(Fe-NIAUX) ₂ + Cys	“reduced persulfide”	Fe + (NIAU) ₂	[2Fe-2S]-U
ISCU WT	900	300	300	300	-	-	450
ISCU Y35D	-	-	-	-	300	-	-
Na-ascorbate	2700	900	900	900	900	900	2700
$(\text{NH}_4)_2^{57}\text{FeSO}_4$	900	300	300	300	300	300	900
NIA	-	450	450	450	450	450	22.5
FXN	-	-	450	450	450	450	22.5
FDX2	-	-	-	-	15	-	22.5
FDXR	-	-	-	-	0.15	-	0.23
NADPH	-	-	-	-	1500	-	2250
MgCl ₂	-	-	-	-	1500	-	2250
cysteine	-	-	-	900	900	-	900

3.5.4 Mössbauer spectroscopy

Mössbauer transmission data of the prepared samples were recorded and processed by J. Oltmanns and Dr. V. Schünemann (TU Kaiserslautern) using a conventional Mössbauer spectrometer in constant acceleration mode. The setup included a 512-channel analyser (WissEl GmbH) in the time-scale mode. Calibration of spectra was performed at room temperature with $\alpha\text{-Fe}$ foil. Zero-field spectra were recorded upon sample cooling to 77 K via a continuous flow cryostat (Oxford Instruments) filled with liquid nitrogen. To record applied-field spectra at 0.1 and 5 T, samples were cooled to 4.2 K using a

helium closed-cycle cryostat (Cryo Industries of America). The closed-cycle cryostat contains a superconducting coil enabling application of a homogenous magnetic field parallel to the γ -ray beam. Data analysis was performed using the Microsoft Excel add-on VindaB (Gunnlaugsson, 2016), employing least-squares fits with Lorentzian line shapes. Simulation of applied-field spectra was done using the spin Hamilton formalism (Schünemann & Winkler, 2000). The standard deviation of the count rate of the background transmission was converted to relative transmission to determine the experimental error.

3.5.5 X-ray absorption spectroscopy

X-ray absorption data were recorded and processed by T. Hilton and Dr. T. Stemmler (Wayne State University, Michigan, USA) on beamline 9-3 at the Stanford Synchrotron Light Source (Menlo Park, California, USA). The beamline was equipped with a Si[220] high resolution monochromator and a continuous-flow liquid helium cryostat set to 10K. Fluorescence XAS data was collected on each sample via a Canberra 100-element germanium solid state detector. Data collection was performed in 5 eV increments for the pre-edge region and 0.25 eV increments for the edge region. Fe foil spectra were recorded simultaneously with each sample for calibration. Analysis of spectral data was performed using the EXAFSPAK program suite (Pritts *et al.*, 2020).

3.6 Structural biology methods

3.6.1 Electron cryo-microscopy (cryo-EM)

Cryo-EM experiments were performed in collaboration with R. Steinhilper and Dr. B. Murphy (Max Planck Institute of Biophysics, Frankfurt am Main).

3.6.1.1 Sample preparation and vitrification

To achieve the highest possible resolution in cryo-EM experiments, protein preparations of highest purity were used (85% purity of (NIA)₂ and 92 – 99% purity of all other proteins, based on densitometry of SDS-PAGE bands). (NIA)₂ purification included an additional AEC step after IMAC. Cryo-EM samples were prepared and vitrified in an anaerobic chamber. NIA and ISCU2 were mixed in a 1:2 molar ratio and incubated for 5 min. The formed (NIAU)₂ complex was purified by SEC using a Superdex™ 200 increase 10/300 GL column equilibrated with anaerobic cryo-EM buffer (35 mM Tris, 150 mM NaCl, pH 7.4) and concentrated using a 100 kDa centrifugal filter. 55 μ M NIA, 275 μ M Na-

ascorbate, 275 μM FeCl_2 and 55 μM FXN were mixed in cryo-EM buffer and the persulfidation reaction initiated by addition of 300 μM cysteine. Samples were mixed with 1.5 mM Fos-choline-8 and 3 μL applied to Quantifoil Au 0.6/1 300 mesh grids, blotted for 4 s and vitrified in liquid ethane using a Vitrobot Mark IV (Thermo Fisher) at 4°C and 100% humidity. The time from cysteine addition to vitrification was approximately 40 s.

3.6.1.2 Data acquisition, processing and model building and refinement

Data acquisition and processing was performed by R. Steinhilper. Electron micrographs were obtained using a Krios G3i with a bioquantum energy filter and a K3 detector exhibiting an image pixel size of 0.837 Å per pixel. 5410 dose-fractionated movies with a total dose of 60 $\text{e}^-/\text{Å}^2$ spread evenly over 60 fractions were automatically recorded via the software EPU (Thermo Fisher). MotionCor2 (Zheng *et al.*, 2017) was employed for whole-frame motion correction. Defocus parameters were calculated using CTFFind4.1 (Rohou & Grigorieff, 2015) and micrographs with a contrast transfer function (CTF) estimated better than 5 Å were selected for further processing. Particles were picked using the template picker implementation in cryoSPARC (Punjani *et al.*, 2017) and classified in 2D. The cleaned up particles were extracted in Relion 3 (Zivanov *et al.*, 2018) for *de novo* model generation and 3D classification. Particles from the predominant 3D class were subjected to 3D refinements applying C2 symmetry. After two rounds of CTF refinement and particle polishing, the final refinement gave a consensus map with a global resolution of 2.4 Å (Fourier shell correlation = 0.143 criterion). The dataset was C2 symmetry expanded and focused classification with a mask on the FXN region of the asymmetric unit of the map was performed, which separated the dataset into particles with FXN (74.5%) and particles without FXN (24.6%). Those classes were subjected to local 3D refinements, yielding resolutions of 2.4 Å (FXN-bound) and 2.7 Å (not FXN-bound), respectively.

The human FXN-bound cryo-EM structure ((NIAUX)₂, pdb code: 6NZU) was used as a template for model building and refinement in Coot (Emsley *et al.*, 2010). The models were real-space refined against the respective maps using the PHENIX software package (Afonine *et al.*, 2018).

4 Results

4.1 Mechanism of *de novo* [2Fe-2S] cluster formation on ISCU2

4.1.1 Purification and characterization of ISCU2 variants

To biochemically characterize the individual steps of *de novo* [2Fe-2S] cluster biosynthesis, variants of ISCU2, in particular with exchanges of the assembly site residues Cys69, Asp71, Cys95, His137 and Cys138, were essential tools. ISCU2 constructs containing a C-terminal His-tag and lacking the N-terminal presequence were overexpressed in *E. coli* and purified by IMAC (immobilized metal affinity chromatography). Incubation with TCEP, KCN and DTPA enabled reductive cleavage of disulfides and polysulfanes (Christ *et al.*, 2016; Kamyshny *et al.*, 2006) as well as removal of bound metals, in particular Zn (Gervason *et al.*, 2019). After anaerobic size-exclusion chromatography (SEC), ISCU2 and its variants were obtained in their apo-form, with all Cys residues in a reduced state. The proteins were obtained at a yield of 2 – 7 mg per litre cell culture at high purity (Figure 14A-B, Appendix Figure 51A). Purification of ISCU2 D71A led to formation of high MW (HMW) ISCU2 aggregates, hence the purification procedure was optimized until a species of similar MW to ISCU2 WT was obtained (see chapter 4.1.1.1). Intact protein mass spectrometry (MS) of ISCU2 WT (Appendix Figure 51B) indicated the presence of the full-length protein with the N-terminal Met cleaved (15.5 kDa). To assess the oligomeric state of the proteins, anaerobic analytical SEC (aSEC) using a Superdex 200 10/300 GL column calibrated with a low MW (LMW) protein kit was performed and confirmed the high purity of the protein samples. ISCU2 WT and variants D71A, C130S, H137A and C138S exhibited similar elution profiles corresponding to a MW of 16.5 – 17.7 kDa, indicating the presence of a monomer (Figure 14C,E). A MW of 20.1 kDa was determined for variant C69S, likely also corresponding to a monomer. Interaction of ISCU2 with the stationary phase of the column may be altered directly by exchange of this solvent-exposed residue and/or indirectly due to conformational changes, leading to an altered elution profile. ISCU2 C95S and furthermore Cys double variants exhibited elution profiles corresponding to a MW of 26.2 – 32.9 kDa (Figure 14D-E) which might indicate ISCU2 dimers (31.0 kDa). To assess whether dimerization might be induced by formation of disulfide bridges between two monomers, additional aSEC runs using a mobile phase with TCEP were done (Appendix Figure 52). No significant change in running behaviour was observed, indicating putative dimerization not being related to Cys oxidation. It is possible that exchange of the ISCU2 assembly site residues leads to a dramatically altered running behaviour, which would make the aSEC-based assignment of monomeric versus dimeric states challenging. In conclusion, all analysed

proteins could be obtained in high purity and good yield with aSEC indicating good solubility and no aggregation.

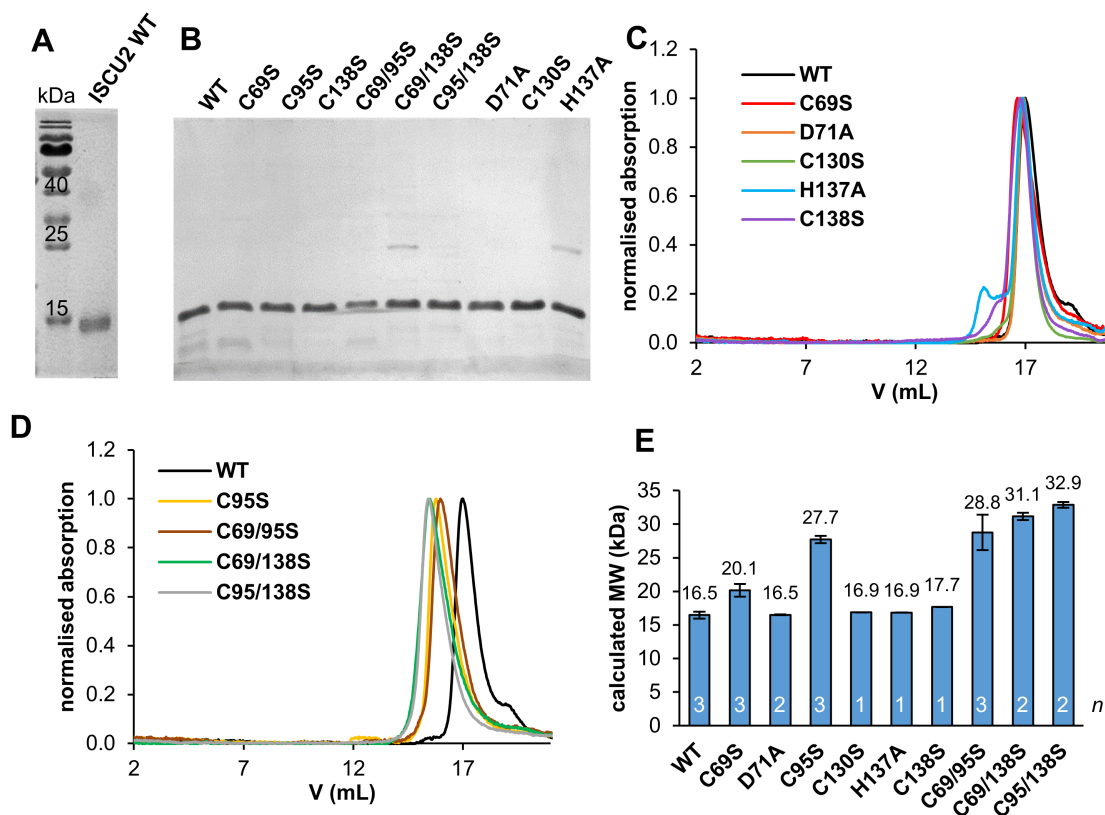


Figure 14: SDS-PAGE and aSEC analysis of anaerobically purified ISCU2 WT and variants. A) SDS-PAGE of anaerobically purified ISCU2 WT is in agreement with the presence of the full-length protein (MW 15.5 kDa). **B)** SDS-PAGE shows high purity of all ISCU2 variants and indicates the presence of the full-length proteins. **C-D)** aSEC analysis of the indicated purified ISCU2 (variant) proteins using a Superdex 200 10/300 GL column monitoring the absorption at 280 nm. Chromatograms were normalised to the major peak for each run. **E)** The apparent MW of ISCU2 WT and variants was calculated based on column calibration with a LMW kit. Error bars indicate the SEM (*n* as indicated).

4.1.1.1 Purification of ISCU2 D71A

Standard IMAC purification of ISCU2 D71A yielded a reddish-brown solution, in contrast to colourless preparations of the other variants and ISCU2 WT. No colour change was observed after 1 h treatment with 25 mM DTT, 25 mM KCN and 50 mM EDTA. Precipitates formed upon concentration of the sample and were removed by centrifugation and filtration. Anaerobic preparative SEC and subsequent SDS-PAGE indicated a major HMW fraction containing ISCU2 as well as ~30 and ~70 kDa proteins (possibly including chaperones) and a minor fraction containing ISCU2 in a LMW monomeric or dimeric state (Appendix Figure 53A-B). To minimize aggregation and precipitation of the mutant protein, cell lysis was repeated using a different buffer composition (50mM HEPES,

500 mM KCl, 10% w/v glycerol, 5 mM TCEP, pH 7.5) and ATP was added to release bound chaperones. A reddish-orange solution was obtained after IMAC purification with a CD spectrum likely related to the presence of an Fe/S cluster (Figure 15). However, spectral features were distinct from those of [2Fe-2S]-reconstituted ISCU2 WT, indicating a different cluster binding mode. Several publications suggest that exchanging the conserved assembly site Asp of ISCU with Ala stabilizes [2Fe-2S] cluster binding via altered coordination of the cofactor (Mansy *et al.*, 2002; Marinoni *et al.*, 2012; Shimomura *et al.*, 2007; Wu *et al.*, 2002a; Wu *et al.*, 2002b). To obtain the apo-protein required for biochemical assays, ISCU2 D71A was incubated for 1 h with DT, ATP and MgCl₂ plus TCEP, KCN and DTPA. Immediately after DT addition, sample colour changed from orange to a pale yellow, indicating Fe/S cluster destruction. No precipitates were observed. Anaerobic preparative SEC with standard buffer yielded a dramatically increased amount of colourless apo-ISCU2 D71A (Appendix Figure 53C-D) in a stable monomeric state as identified by aSEC (Figure 14C,E). This protein was used for subsequent experiments.

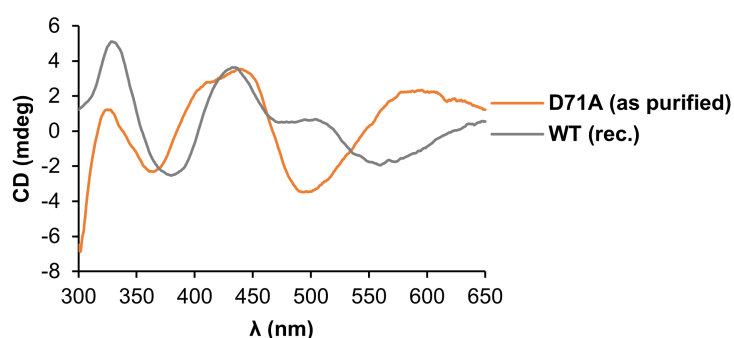


Figure 15: As-isolated ISCU2 D71A binds an Fe/S cluster. CD spectra of IMAC-purified ISCU2 D71A and of [2Fe-2S]-ISCU2 WT. Both proteins contain a [2Fe-2S] cluster, yet the different spectral features indicate distinct cluster binding modes of the two proteins. The WT spectrum obtained from enzymatic reconstitution was normalized for comparison.

4.1.2 Cys69, Asp71 and Cys95 are essential for Fe(II) coordination by free ISCU2

ISCU2 purified from *E. coli* cultures has frequently been observed to bind Zn (Boniecki *et al.*, 2017; Iannuzzi *et al.*, 2014; Liu *et al.*, 2005; Ramelot *et al.*, 2004). However, Zn was reported not to fulfil a physiological function in *de novo* Fe/S cluster formation (Gervason *et al.*, 2019). The source of Fe for cluster formation is likely Fe(II) that is bound by ISCU2 either before or after the protein forms a complex with (NIA)₂ (Gervason *et al.*, 2019). To identify which residues of free (not (NIA)₂-bound) ISCU2 are required for Fe(II) coordination, CD-spectroscopic features induced by Cys-Fe ligand-metal charge transfer interactions in the near-UV range (250 – 350 nm) were exploited (McLaughlin *et al.*, 2012; Tucker *et al.*, 2008). ISCU2 exhibited Fe(II)-dependent CD signals at 274 and

314 nm which could be quenched with an excess of the chelator DTPA (Figure 16A). In absence of Fe(II), ISCU2 featured a weak signal at 276 nm which can possibly be attributed to one or more ISCU2 Tyr residues. Aromatic side chains of Tyr, Phe and Trp as well as disulfide bonds can induce CD signals in the near-UV range (Kelly & Price, 2000). Despite anaerobic experimental conditions, the Fe-ISCU2 complex was labile in absence of reductants and slowly decomposed over time (Appendix Figure 54A), likely due to disulfide formation and/or Fe(II) oxidation to Fe(III). Since ascorbate showed a strong CD signal overlaying the Fe-ISCU2 features, the reductant could not be used to keep Fe in the Fe(II) state. However, addition of excess TCEP led to a stable Fe(II)-ISCU2 complex for prolonged time, therefore all Fe binding experiments were performed in presence of TCEP. Analysis of ISCU2 assembly site variants revealed that CD signals were quenched in variants C69S, D71A and C95S, suggesting that the respective residues are essential for Fe(II) coordination of free ISCU2 (Figure 16B). Variant C138S exhibited a spectrum similar to the positive controls ISCU2 WT and K135A, indicating residue Cys138 not being required for Fe coordination. Exchanging His137 to Ala led to a weaker signal with shifted maxima, indicating that Fe(II) binding might still be possible, but with altered coordination geometry. His137 might be part of the native coordination mode without being strictly essential. The data show that Cys69, Asp71, Cys95 and possibly His137 are ligating Fe(II) in free ISCU2.

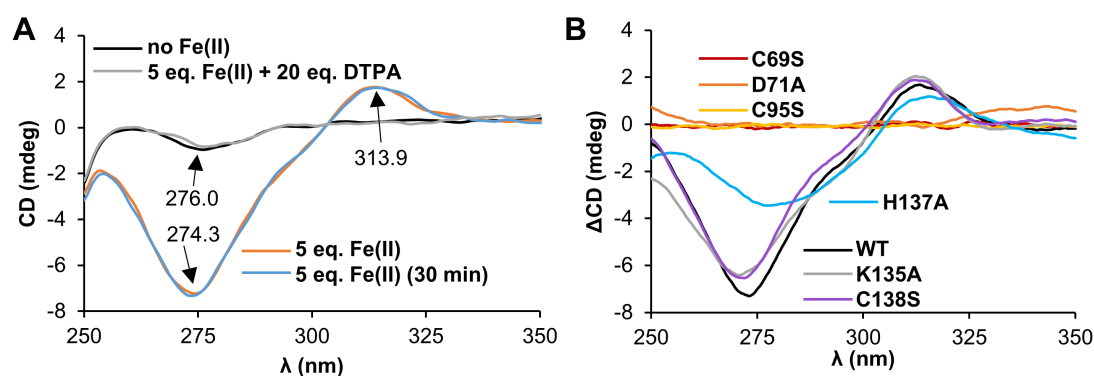


Figure 16: CD-spectroscopic analysis of ISCU2 mutant proteins reveals Fe ligation by Cys69, Asp71, Cys95 and potentially His137. All samples contained 100 μ M ISCU2 and 2 mM TCEP and were measured 2 min after mixing the components, if not noted otherwise. **A)** CD spectra of ISCU2 in presence of Fe(II) and/or DTPA. The wavelengths (in nm) of major signals are marked by arrows. A weak signal at 276 nm in absence of Fe(II) is likely related to aromatic amino acids of ISCU2. **B)** CD spectra of ISCU2 WT and mutant proteins were recorded before and after addition of 2 eq. Fe(II) (see Appendix Figure 54B-C), and corresponding difference spectra are shown.

4.1.3 Residues Asp71, Cys95 and Cys138 are essential for persulfide formation on ISCU2

De novo [2Fe-2S] cluster synthesis requires the cysteine desulfurase NFS1 to generate a Cys-bound persulfide which is subsequently transferred to ISCU2. Efficient persulfide transfer furthermore requires FXN (Parent *et al.*, 2015). To elucidate whether ISCU2-bound Fe(II) is required for persulfide transfer, and to find out which ISCU2 assembly site residues are required, an anaerobic Cys alkylation-based assay including ISCU2, FXN, (NIA)₂ and optionally Fe(II) was employed. FXN and NIA were added in a two-fold excess over ISCU2 to ensure the protein being complexed completely. Persulfide formation was initiated by addition of free cysteine and quenched by labelling native and persulfidated Cys residues with maleimide-polyethylene glycol₁₁-biotin (MPB) in presence of denaturing agent. Reductive cleavage of disulfides led to a protein mass shift between persulfidated and non-persulfidated ISCU2 that could be resolved by SDS-PAGE (see Appendix Figure 49 for a schematic outline of the MPB alkylation assay).

Initial experiments were performed to evaluate a possible role for Zn in *de novo* Fe/S cluster biosynthesis. After 2 min reaction time, ISCU2 was persulfidated to similar extents in presence of either Zn(II) or Fe(II) (Appendix Figure 55A). However, *in vitro* enzymatic reconstitution of [2Fe-2S]-ISCU2 via the core ISC machinery in presence of Fe(II) was abolished upon addition of Zn(II) (Appendix Figure 55B), showing Zn(II) to be an inhibitor rather than a facilitator of physiological cluster formation.

To assess efficiency and kinetics of ISCU2 persulfidation, reactions in presence of Fe(II) were quenched at different time points from 10 s to 10 min (Figure 17A). Quantification of bands from SDS-PAGE analysis showed that already after 10 s (the shortest reaction time that could be analysed) 75% of ISCU2 bound one persulfide (1x SSH, Figure 17B). At later time points, the amount of the species with one persulfide did not change dramatically. The non-persulfidated species was slowly diminished over time, concomitant with a steady increase in doubly persulfidated (2x SSH) ISCU2. Given the fast formation of the first persulfide, the slow formation of a second persulfide is likely a non-physiological side reaction. Therefore, the reaction period of 10 s was concluded to be optimal and used for all subsequent persulfidation assays. To investigate if Fe(II) is essential for persulfide formation, reactions in presence of the strong metal chelator DTPA were done. Quantification of SDS-PAGE bands showed reactions without Fe only yielding 14% persulfidated ISCU2 compared to reactions with Fe(II) (Figure 17C, Appendix Figure 56E,G), indicating that only metal-loaded ISCU2 allows for rapid persulfide formation. All subsequent reactions were therefore done in presence of Fe(II). Furthermore, reactions lacking FXN showed a significantly reduced persulfide yield (Figure 17C, Appendix Figure 56E), in line with FXN being required for efficient persulfide transfer to ISCU2.

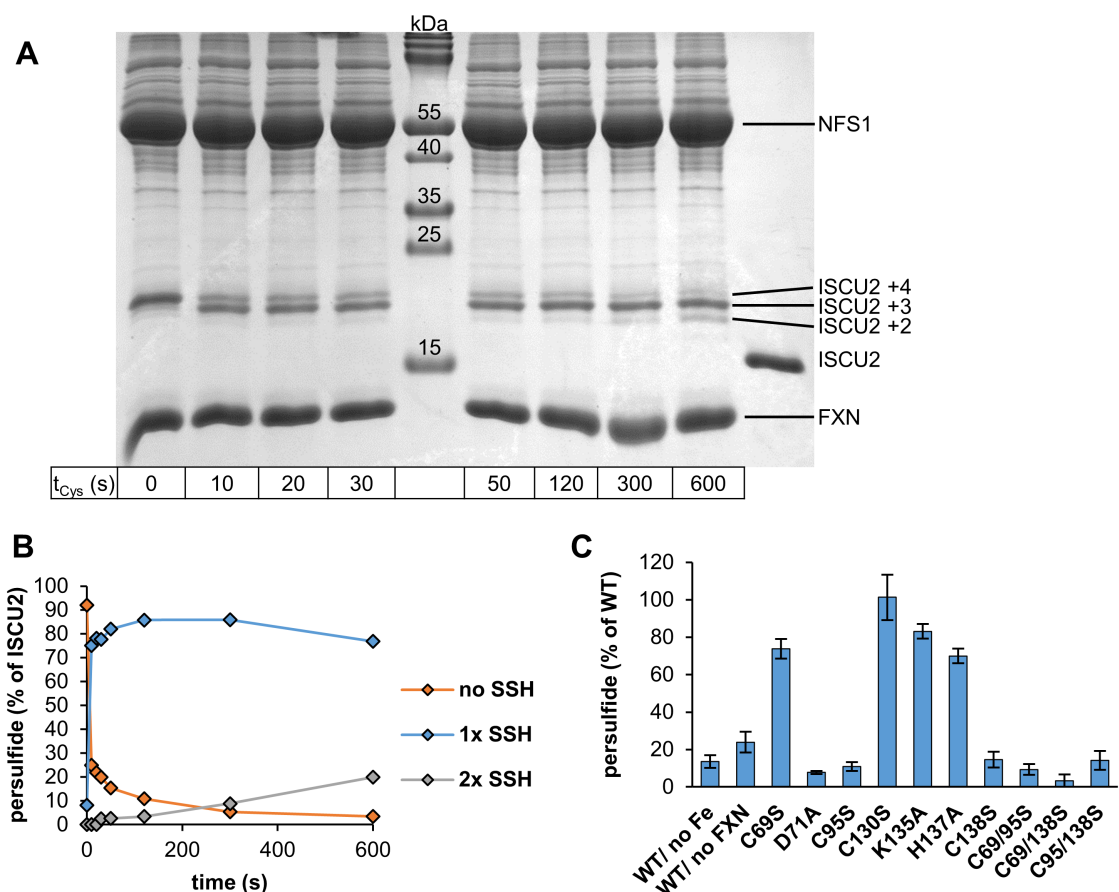


Figure 17: Residues Asp71, Cys95 and Cys138 are essential for the Fe-dependent persulfidation of ISCU2. *In vitro* persulfidation of ISCU2 by the cysteine desulfurase NFS1 was investigated via a MPB alkylation-based gel-shift assay (schematic outline in Appendix Figure 49). **A**) In reactions containing 20 μM ISCU2, 40 μM NIA, 40 μM FXN, as well as excess Fe(II) and ascorbate, persulfide formation was initiated by addition of excess cysteine, and after the indicated time periods quenched by addition of MPB and SDS. Persulfides were cleaved using TCEP, and persulfidation-induced mass shift of ISCU2 was analysed by SDS-PAGE. The outmost right lane shows non-labelled ISCU2 and the outmost left lane (reaction without cysteine) ISCU2 with all four protein Cys residues labelled with MPB (ISCU2 +4). ISCU2 +3 and +2 correspond to species with one and two persulfidated protein Cys residues, respectively. **B**) ISCU2 species with no, one or two persulfides (SSH) within the gel depicted in **(A)** were quantified by densitometry to obtain a time course of persulfidation. **C**) Persulfidation of ISCU2 mutant proteins and control reactions with ISCU2 WT lacking Fe or FXN were investigated using the MPB alkylation assay after a 10 s reaction with cysteine. The percentage of persulfidated ISCU2 was quantified by densitometry of the corresponding bands in SDS-PAGE gels and normalised to control reactions with ISCU2 WT. “WT/ no Fe” reactions contained no Fe(II) or ascorbate but an excess of 1 mM DTPA. Error bars indicate the SEM ($n \geq 3$).

To investigate which residues of ISCU2 are required for persulfide formation, ISCU2 variants were subjected to the persulfidation assay. Assembly site variants C69S, K135A and H137A and a variant of the only non-conserved ISCU2 cysteine (C130S) yielded 65 – 91% persulfide compared to ISCU2 WT (Figure 17C, Appendix Figure 56A-E), showing that these residues are not essential for persulfide formation. In pronounced contrast, ISCU2 mutant proteins D71A, C95S and C138S exhibited severely diminished persulfide

levels (8 – 15% of WT reactions). Since residues Asp71 and Cys95 had been found to be crucial for Fe(II) coordination of free ISCU2 (see Figure 3B), the severely impaired persulfide transfer to these mutant ISCU2 proteins may readily be explained by a lack of Fe ligation. Interestingly, ISCU2 C69S showed robust persulfide formation despite Cys69 being essential for Fe(II) coordination of free ISCU2 (compare Figure 16B), suggesting that Fe coordination is different in free ISCU2 versus the NIA-ISCU2-FXN (NIAUX)₂ complex containing persulfidated ISCU2. Residue Cys69 is apparently no longer required for Fe(II) binding within the (NIAUX)₂ complex. The results furthermore indicate that Cys95 or Cys138 could serve as a persulfide acceptor (see below).

4.1.4 ISCU2 Cys138 receives a persulfide from NFS1 Cys381 without a detectable intermediate

Experiments in the previous chapter showed ISCU2 Cys95 and Cys138 to be crucial for persulfide formation. However, MPB labelling did not allow for identification of an individual Cys residue that accepts the persulfide. A previous study (Parent *et al.*, 2015) reported Cys138 as persulfide acceptor, however reactions were done under aerobic conditions and at long reaction times (3 min) using an only semi-quantitative MS approach. In this work, anaerobic persulfidation assays with an isobaric iodoacetyl tandem mass tag (iodoTMT, Thermo Fisher) were performed to achieve a more reliable and accurate quantification of persulfide levels on the individual ISCU2 Cys residues (for details, see Appendix Figure 50). Cysteine-dependent persulfide formation on ISCU2 was quenched with iodoTMT reagent and SDS. Excess label was quenched with cysteine, and after reductive cleavage of persulfides, a second iodoTMT reagent was used to label cleavage products. MS² analysis of trypsin-digested samples allowed for accurate quantification of persulfide amounts for each Cys-containing peptide.

In initial experiments employing the one-pot isobaric labelling approach, reactions containing equimolar amounts of ISCU2, FXN and NIA were quenched at different time points using 2.2 eq. iodoTMT over total thiol concentration. In presence of Fe(II), Cys138 was persulfidated with high specificity already after 10 s reaction time (Appendix Figure 57A). Overall persulfide levels then slowly increased with progressing reaction time. The fast formation of one persulfide on Cys138 in combination with additional, most likely non-physiological persulfidation at longer reaction times is in good agreement with results obtained from the MPB-based persulfidation assay. The lower overall percentage of persulfide species in the iodoTMT assay might be related to the lower stoichiometry of NIA and FXN over ISCU2, which was chosen to minimize the amount of costly iodoTMT. Furthermore, ascorbate was not used in iodoTMT assays, possibly making the employed Fe(II) more susceptible to oxidation.

Reactions without Fe(II) (and also without metal chelator) showed a much decreased persulfidation rate where Cys138 persulfide levels increased from 9.2% before cysteine addition to only 12.5% after 10 s reaction time (Appendix Figure 57B). Whilst Cys138 was still the preferred target, relative persulfidation of other Cys residues at later time points was higher compared to the Fe(II)-containing reactions. The results support the requirement of Fe(II) for efficient persulfidation. The residual activity in samples without added Fe could be associated either with metal contamination (by, e.g., Zn or Fe) and/or a residual slow rate of the reaction in the absence of metal.

The different persulfidation assays identified Cys95 and Cys138 as essential for persulfide transfer to ISCU2, with Cys138 being the final acceptor. Cys95 may then be essential for Fe(II) ligation in the (NIAUX)₂ complex, the prerequisite for ISCU2 persulfidation. However, it would also be conceivable that Cys95 functions as an intermediate sulfur carrier, thus acting as a sulfur relay residue receiving sulfur from Cys381^{NFS1} and transferring it to Cys138^{ISCU2}. To adapt the iodoTMT assay for resolving fast sulfur transfer reactions, the composition of the iodoTMT stocks was optimized to enable fast quenching and labelling reactions. In contrast to previous reactions, stock solutions of the iodoTMT label did not only contain methanol, but also 5% SDS to denature proteins simultaneously to labelling, 5 mM EDTA to remove metals and 100 mM Tris pH 8.0 to adjust the optimal pH for labelling. Removal of Fe and dissociation/denaturation of the (NIAUX)₂ components stop the Fe-dependent persulfidation of ISCU2 rapidly. Addition of the quench mixture to Fe-ISCU2 led to quantitative liberation of Fe from ISCU2 within 10 s, the shortest time period that could be measured (Appendix Figure 58). To additionally improve the speed of thiol labelling, a much higher excess of 39.5 eq. label over total thiol concentration was used. Reactions in presence of Fe(II) (Figure 18A) confirmed Cys138 being the final sulfur acceptor but did not provide any evidence for an intermediate sulfur acceptor. From the experimental setup, a reaction intermediate transferring the sulfur in the 10 s range can be excluded. However, it cannot be ruled out that the shortest possible reaction time of 10 s is not sufficient to identify transient persulfidation of Cys95.

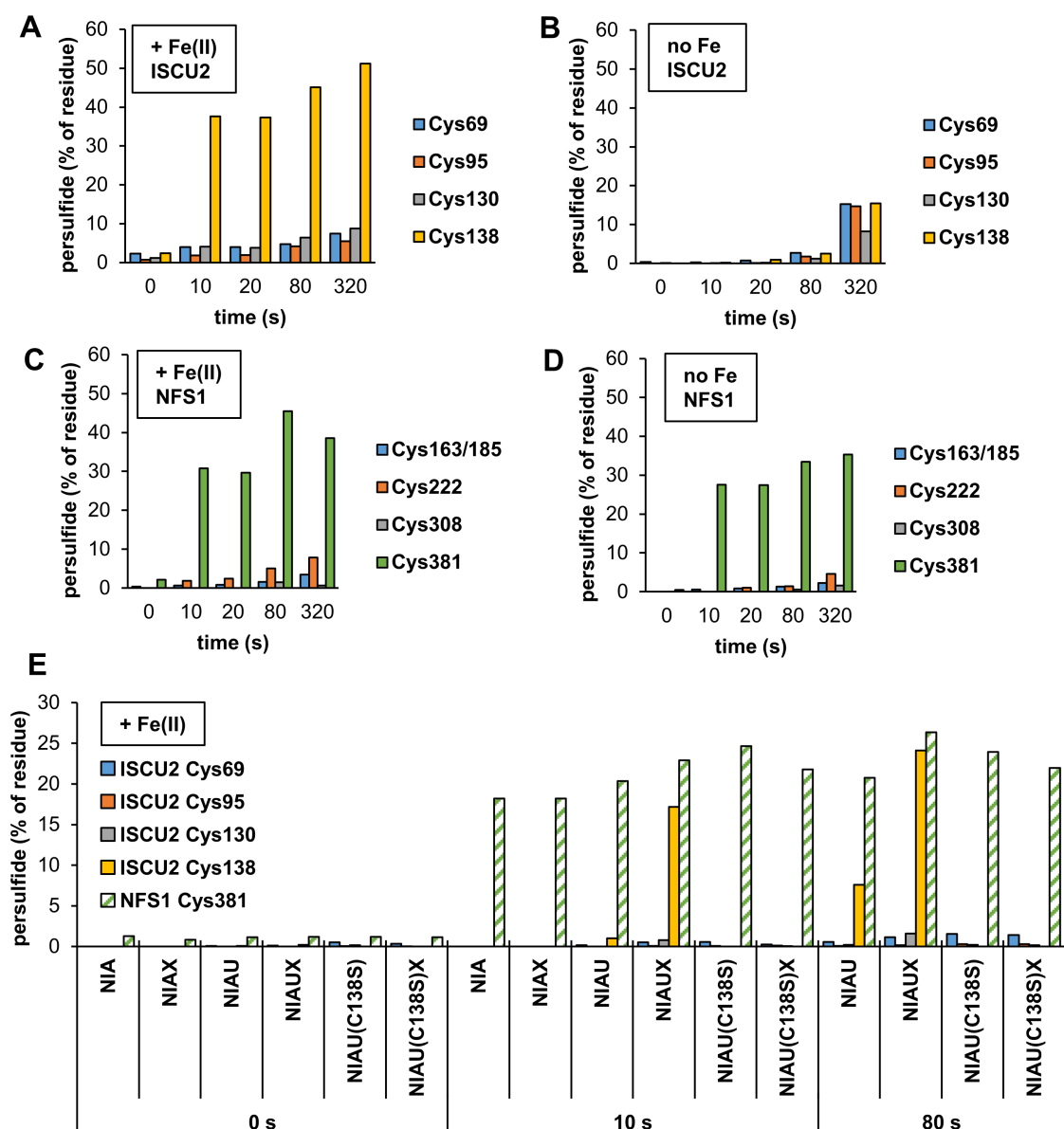


Figure 18: Quantification of *in vitro* persulfidation of individual Cys residues reveals specific persulfidation of ISC2 Cys138 and NFS1 Cys381. ISC2 and NFS1 persulfidation in presence of cysteine was investigated via a iodoTMT-based isobaric labelling approach (schematic outline in Appendix Figure 50). **A-D**) Reactions containing 20 μ M ISC2, NIA and FXN, and either 100 μ M FeCl₂ or 500 μ M DTPA (Fe-chelator) were quenched with 15 mM (39.5 eq. over initial total thiol concentration) iodoTMT (stocks dissolved in 50% v/v methanol, 5% w/v SDS, 5 mM EDTA, 100 mM Tris pH 8.0) at the indicated time points after addition of 100 μ M cysteine. Following TCEP-mediated persulfide cleavage, samples were labelled with a second iodoTMT reagent (15 mM). Trypsin-digested samples were analysed by nanoHPLC-MS² and iodoTMT reporter fragment signals of both labels integrated. Persulfidation levels of individual Cys residues are shown for ISC2 in presence of FeCl₂ (**A**) or DTPA (**B**), and for NFS1 in presence of FeCl₂ (**C**) or DTPA (**D**). Cys163^{NFS1} and Cys185^{NFS1} are located on the same peptide after trypsin digest, hence the persulfide content cannot be distinguished and represents the sum of both Cys residues. **E**) Persulfidation of ISC2 and NFS1 in (NIAUX)₂ and different sub-complexes. Reactions contained 30 μ M ISC2 WT or C138S, 15 μ M FXN and 15 μ M NIA as indicated, as well as 150 μ M FeCl₂ and 75 μ M cysteine. 4.4 mM (12.2 eq. over initial total thiol concentration) iodoTMT (stocks dissolved in 50% v/v methanol, 8% w/v SDS, 3 mM EDTA, 100 mM Tris pH 8.5) was used for labelling.

Reactions in absence of Fe and presence of the chelator DTPA showed virtually no persulfidation within 10 s reaction time (Figure 18B), supporting the physiological sulfur transfer reaction to be strictly metal-dependent.

Persulfide formation on NFS1 was additionally investigated in the same experiment. Quantification suggested rapid persulfide formation on Cys381^{NFS1} being independent of the presence of Fe(II) and the persulfide levels of ISCU2 (Figure 18C-D). In addition to the catalytic residue Cys381^{NFS1}, three other cysteine-containing peptides of NFS1 were probed as controls, and did not show any significant persulfide formation, in particular at short time periods. The results underline the high specificity of persulfidation of Cys381^{NFS1}.

To assess if persulfide formation on (NIA)₂ was dependent on ISCU2 and investigate the influence of FXN on persulfidation, (NIAUX)₂ and sub-complexes were subjected to the iodoTMT-based persulfidation assay. Persulfide formation was strictly cysteine-dependent and persulfidation of ISCU2 Cys138 was slowed down severely in absence of FXN (Figure 18E), in line with its previously suggested function of facilitating persulfide transfer (Parent *et al.*, 2015). Persulfide formation on (NIA)₂ was largely independent of ISCU2 and FXN, indicating that after persulfide transfer to ISCU2, NFS1 can quickly undergo another round of persulfidation. Replacement of ISCU2 WT with the C138S variant served as a control and abrogated ISCU2 persulfidation, in line with previous experiments (see Figure 17C).

4.1.5 The persulfidated (Fe-NIAUX)₂ complex exhibits Fe(II) coordination by an ISCU2 Cys138-bound persulfide

Biochemical analyses (chapters 4.1.3 and 4.1.4) showed that Fe and the ISCU2 residues Asp71, Cys95 and Cys138 are essential for a physiologically relevant persulfidation of ISCU2, and furthermore that the persulfide is bound specifically by Cys138. How the bound Fe is coordinated in a persulfidated intermediate and how a respective core ISC complex is structurally arranged nevertheless remained unknown. A previous cryo-EM study had reported the structure of non-persulfidated (NIAUX)₂ with Zn bound to ISCU2 (Fox *et al.*, 2019). To gain insight into the structural basis of the molecular mechanism of ISCU2 persulfidation, cryo-EM analysis of cysteine-treated (Fe-NIAUX)₂ was performed in this work, taking advantage of the relatively stable persulfidated ISCU2 species (Figure 18).

Preliminary experiments showed that by mixing purified core ISC proteins and subjecting them to aSEC, (NIAU)₂ could be obtained in an approximate 1:1 stoichiometry of ISCU2 and NIA (Appendix Figure 59). This was independent of the presence or absence of Fe(II). In contrast, most FXN was lost during aSEC, indicating FXN-binding to (NIAU)₂

being unstable. Consequently, (NIAU)₂ was prepared freshly by SEC for cryo-EM analysis to enhance the purity of the complex, and all other components including FXN were added afterwards without further SEC. Cysteine was added as the last component and subsequent vitrification done as fast as possible, resulting in persulfidation reaction times of approximately 40 s.

A structure of persulfidated (Fe-NIAUX)₂ could be obtained at a high resolution of 2.4 Å, significantly higher than the published structure of (Zn-NIAUX)₂ resolving at 3.2 Å (Fox *et al.*, 2019). Both structures exhibit a similar overall fold, with ISCU2 and FXN each binding to opposite sides of a (NIA)₂ heterodimer (Figure 19A and Appendix Figure 60A-B). The catalytic Cys381-loop of NFS1 was the only region that could not be fully resolved in the new structure, most likely due to its high flexibility. Intriguingly, additional electron density was observed at Cys138^{ISCU2}, indicating persulfidation of the residue (Figure 19B). The presence of a persulfide could be verified by difference mapping of the structure, comparing the fit of theoretical persulfide and non-persulfide-bound structures to the experimental electron density (Joseph *et al.*, 2020). Additional electron density at the ISCU2 assembly site showed coordination of a metal atom via ISCU2 Asp71, Cys95 and the terminal sulfur of Cys138-SSH (Figure 19B-C), similar to Zn coordination by the same residues reported for non-persulfidated (Zn-NIAUX)₂ (Fox *et al.*, 2019) (Appendix Figure 60C). Even though the type of metal present in persulfidated (NIAUX)₂ cannot be identified by cryo-EM, the experimental setup makes it likely that only Fe is bound to ISCU2. To remove metal contaminants, proteins had been treated with the strong metal chelator DTPA during purification. For cryo-EM sample preparation, metal-free (NIAUX)₂ was then treated with excess Fe(II). Therefore, the metal density observed in the 3D structure in all likelihood represents Fe(II).

In conclusion, the first 3D structure of (NIAUX)₂ resolving at below 3 Å could be obtained in this work. The structure was at the same time the first to show a persulfide-bound intermediate of *de novo* Fe/S cluster biosynthesis, and showed Fe coordination by ISCU2 Asp71, Cys95 and the terminal sulfur of Cys138-SSH. This result was well in line with *in vitro* assays showing the metal-dependent persulfidation of ISCU2 to require residues Asp71, Cys95 and Cys138.

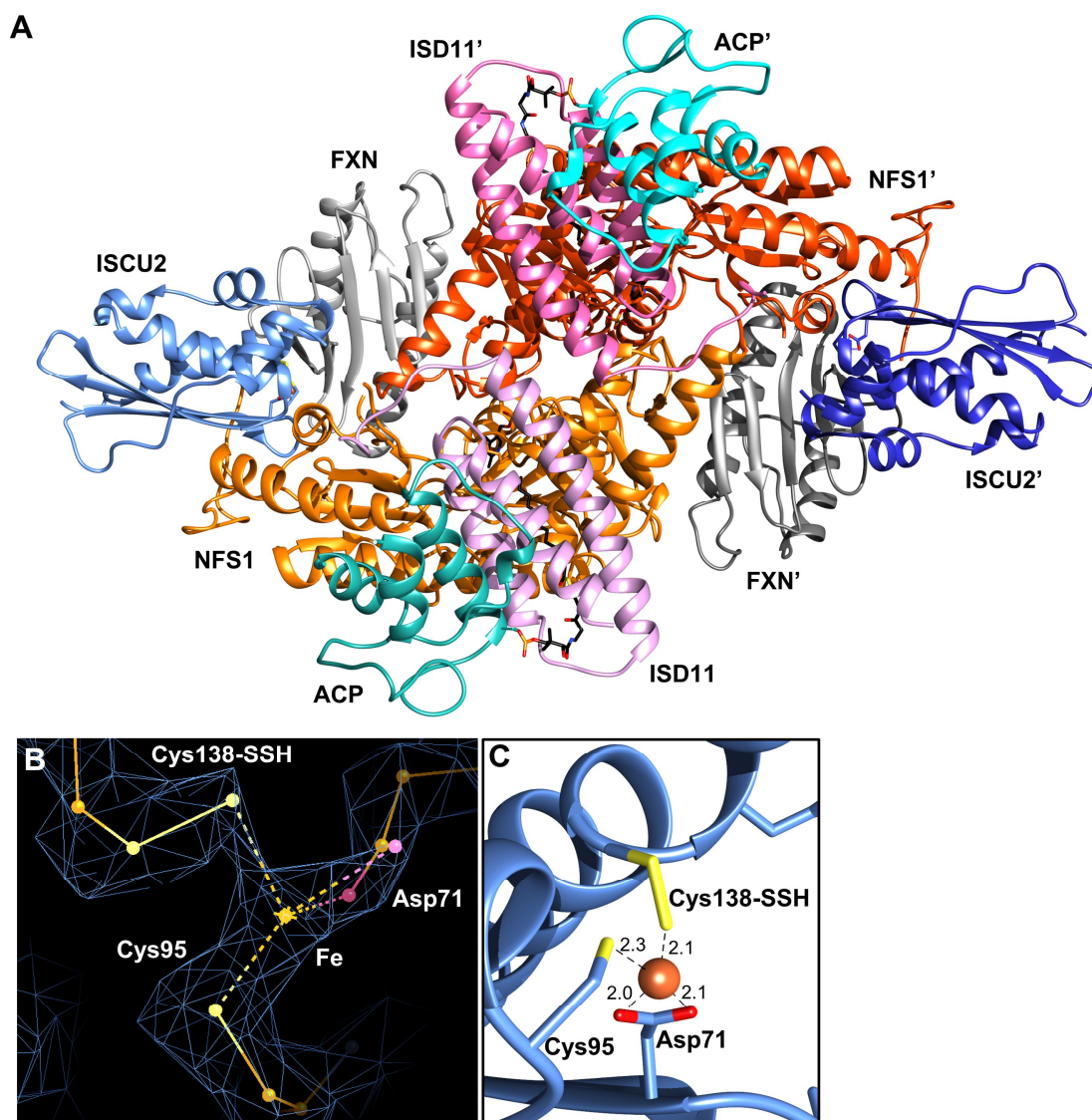


Figure 19: ISCU2 Cys138-SSH of persulfidated $(\text{Fe-NIAUX})_2$ participates in Fe coordination at the ISCU2 assembly site. A) Overall architecture of metal-bound and persulfidated $(\text{NIAUX})_2$ at 2.4 Å resolution, viewing the ISD11-ACP binding site from top. The structure is fully resolved except residues 378 – 386 of the flexible catalytic loop of NFS1. NFS1-bound PLP and the ACP-bound fatty acyl phosphopantetheinyl moiety are depicted as black sticks. **B-C)** Zoom into the ISCU2 assembly site. The electron density map (**B**) supports the presence of metal and persulfidation of Cys138^{ISCU2}. Metal-ligand distances are given in Å and Fe is represented as orange sphere (**C**). Done in collaboration with R. Steinhilper and Dr. B. Murphy.

4.1.6 FXN modulates the ISCU2 assembly site to facilitate persulfide transfer

Whilst around 75% of the particles from the prepared cryo-EM sample discussed in the previous chapter exhibited a full $(\text{Fe-NIAUX})_2$ complex, 25% of the particles lacked FXN. The lower affinity of FXN to the core ISC complex compared to ISCU2 may explain this observation (Appendix Figure 59) (Cai *et al.*, 2018b; Gervason *et al.*, 2019; Uzarska *et al.*, 2022). Consequently, the 3D structure of $(\text{Fe-NIAU})_2$ was also analysed (Figure 20A). Whilst a crystal structure of $(\text{Zn-NIAU})_2$ (Boniecki *et al.*, 2017) and a cryo-EM structure

of (Zn-NIAUX)₂ (Fox *et al.*, 2019) have been reported previously, the cryo-EM analyses from this work allowed for the first time the structural comparison of Fe-bound (NIAU)₂ and (NIAUX)₂ from the same sample.

The overall 3D fold of (Fe-NIAU)₂ is similar to the previously published structure of (Zn-NIAU)₂ (crystallized in absence of cysteine), with both structures exhibiting the catalytic Cys381-loop of NFS1 facing the ISCU2 assembly site. The average resolution of (Fe-NIAU)₂ is 2.7 Å, but local resolution is significantly lower in regions known to interact with FXN, including the NFS1 C-terminus as well as the Cys69^{ISCU2}-loop and His137^{ISCU2}. This may be explained by the absence of FXN leading to a higher structural flexibility of the respective regions. Additional electron density at the ISCU2 assembly site indicates that metal is bound (Figure 20B), despite a resolution below 2.7 Å in this area. The ISCU2 assembly site residues as well as Cys381^{NFS1} are positioned similarly to the published (Zn-NIAU)₂ structure (Boniecki *et al.*, 2017) (Figure 20C), with Asp71^{ISCU2}, Cys95^{ISCU2} and Cys381^{NFS1} participating in Fe ligation. Due to the weak electron density, it is not entirely clear whether His137^{ISCU2} may additionally participate in metal coordination as seen in (Zn-NIAU)₂. Furthermore, limited resolution at the ISCU2 assembly site precluded analysis for the presence of persulfides.

Cys69^{ISCU2}-loop and His137^{ISCU2} orientation towards the ISCU2 assembly site is in pronounced contrast to (Fe-NIAUX)₂, which shows interaction of these residues with FXN (Figure 20D). This supports a physiologically relevant reorientation of these residues induced by FXN binding. Both persulfidated (Fe-NIAUX)₂ and non-persulfidated (Zn-NIAUX)₂ (Fox *et al.*, 2019) show a strikingly similar interaction of FXN with the ISCU2 assembly site (Appendix Figure 60C). His137^{ISCU2} is inserted into a hydrophobic pocket formed by Trp155^{FXN} and other FXN residues, whereas Cys69^{ISCU2} may undergo hydrogen bonding with Gln148^{FXN} and/or Asn155^{FXN} (see also Figure 7). In line with these observations, *in vitro* persulfidation assays performed with ISCU2 variants (chapter 4.1.3) excluded an essential function of His137 and Cys69 in Fe ligation or sulfur relay in (Fe-NIAUX)₂. Interaction of these residues with FXN may rather have the function of providing access to ISCU2 Cys138^{ISCU2} for persulfide transfer from Cys381-SSH^{NFS1}. In particular His137^{ISCU2} likely obstructs access to Cys138^{ISCU2} in (M-NIAU)₂ structures (see also chapter 1.3.1.2).

In conclusion, the first 3D structure of (Fe-NIAU)₂, obtained from the same sample as persulfidated (Fe-NIAUX)₂, provides direct evidence for the FXN-induced rearrangement of the ISCU2 assembly site, most likely to facilitate persulfide transfer. Specific molecular ISCU2-FXN interactions were further investigated by biochemical assays (chapter 4.1.7). The spectroscopic, biochemical and structural data obtained in this and previous works indicate that Fe coordination at the ISCU2 assembly site is different for free Fe-ISCU2

(chapter 4.1.2), $(\text{Fe-NIAU})_2$, $(\text{Fe-NIAUX})_2$ and persulfidated $(\text{Fe-NIAUX})_2$. The differential Fe coordination of these species was further investigated by spectroscopic methods (chapters 4.1.8 and 4.1.9).

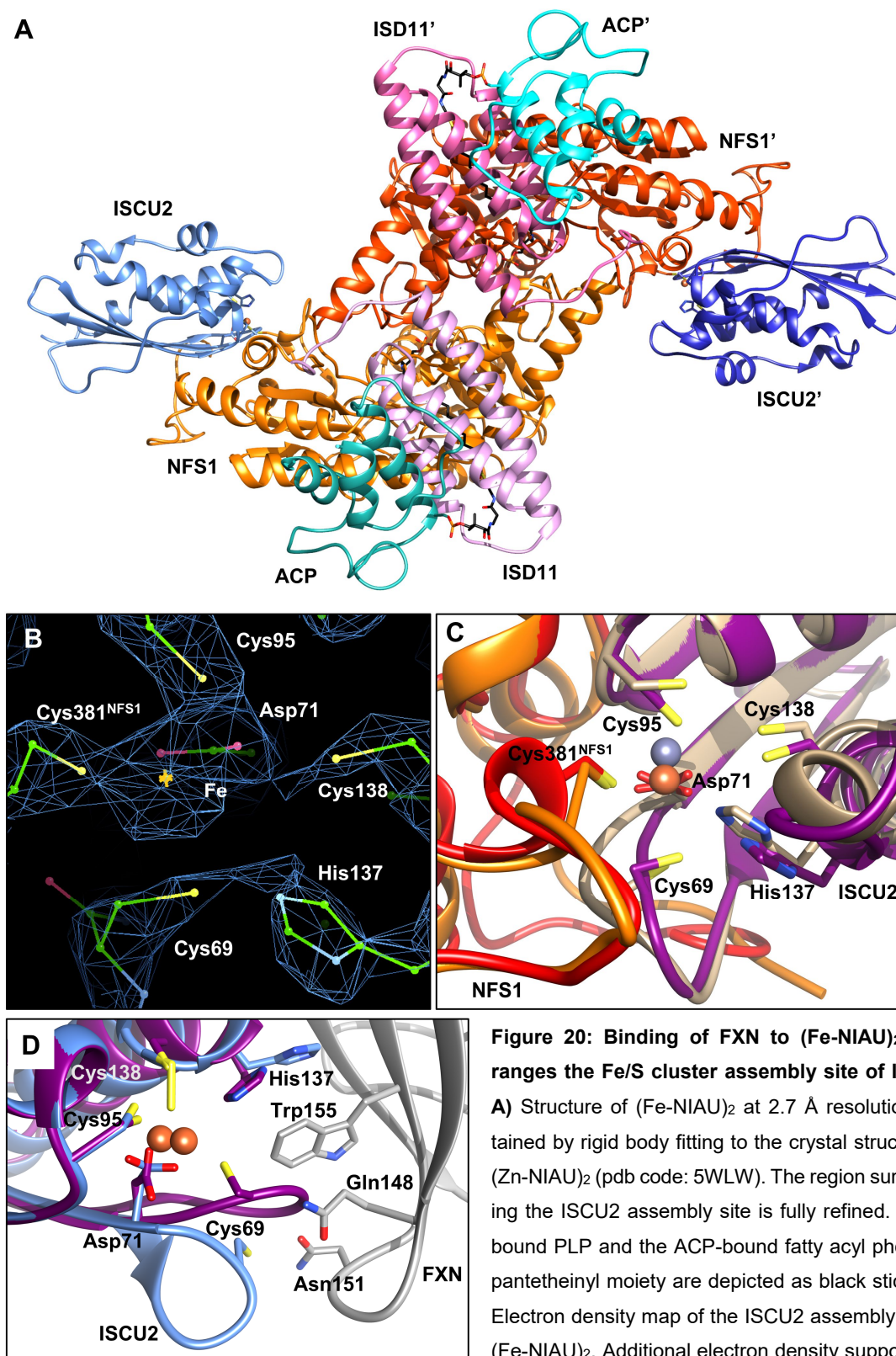


Figure 20: Binding of FXN to $(\text{Fe-NIAU})_2$ rearranges the Fe/S cluster assembly site of ISCU2.

A) Structure of $(\text{Fe-NIAU})_2$ at 2.7 Å resolution, obtained by rigid body fitting to the crystal structure of $(\text{Zn-NIAU})_2$ (pdb code: 5WLW). The region surrounding the ISCU2 assembly site is fully refined. NFS1-bound PLP and the ACP-bound fatty acyl phosphoantetheinyl moiety are depicted as black sticks. **B)** Electron density map of the ISCU2 assembly site of $(\text{Fe-NIAU})_2$. Additional electron density supports the presence of Fe, despite limited resolution around the metal density. Fe is coordinated by at least Asp71^{ISCU2}, Cys95^{ISCU2} and Cys381^{NFS1}. Cys69^{ISCU2} and His137^{ISCU2} exhibit significantly weaker electron densities than

other ISCU2 assembly site residues. **C)** Overlay of the ISCU2 assembly site from (Fe-NIAU)₂ with (Zn-NIAU)₂ (pdb code: 5WLW). Coloring: (Fe-NIAU)₂: ISCU2 (magenta), NFS1 (red); (Zn-NIAU)₂: ISCU2 (beige), NFS1 (orange). Both structures exhibit similar orientations of assembly site residues. **D)** Zoom into the interaction site of ISCU2 (blue) with FXN (grey) from persulfidated (Fe-NIAUX)₂, overlaid with ISCU2 (magenta) from (Fe-NIAU)₂. Both structures were obtained from the same sample, and made the FXN-dependent rearrangement of His137^{ISCU2} and the Cys69^{ISCU2}-loop evident. Zn is depicted as grey sphere, Fe as orange sphere. Done in collaboration with R. Steinhilper and Dr. B. Murphy.

4.1.7 Specific molecular interactions between FXN and ISCU2 are critical for ISCU2 persulfidation and [2Fe-2S] cluster formation

This and previous works showed FXN to be required for efficient persulfidation of ISCU2 Cys138 (chapters 4.1.3 and 4.1.4) (Parent *et al.*, 2015). Structural data support a rearrangement of the ISCU2 assembly site induced by FXN being crucial for persulfide transfer. Whereas His137^{ISCU2} is inserted into a hydrophobic pocket of FXN formed by Trp155, Arg165 and other residues (Figure 7), Cys69^{ISCU2} may undergo H-bonding with Gln148^{FXN} and/or Asn151^{FXN}. To verify the specific intermolecular interactions of FXN and ISCU2, persulfide and [2Fe-2S] cluster formation on ISCU2 were investigated using ISCU2 and FXN variants (SDS-PAGE of purified FXN variants in Appendix Figure 61).

De novo synthesis of [2Fe-2S]-ISCU2 in presence of FXN variants was reconstituted in an anaerobic enzymatic assay. Reaction mixtures contained ISCU2, Fe(II), NADPH and catalytic amounts of (NIA)₂, FXN, FDX2 and FDXR and cluster formation was initiated by the addition of cysteine. The time course of [2Fe-2S] cluster formation on ISCU2 was monitored via CD spectroscopy at 431 nm. FXN Q148A but not N151A led to a significantly reduced reconstitution rate compared to FXN WT (Figure 21A-B). This suggests Gln148^{FXN} but not Asn151^{FXN} interacting with Cys69^{ISCU2}, most likely via H-bonding. Exchanging the FXN hydrophobic pocket residues Trp155 and Arg165 decreased the reconstitution rate to varying degrees. A more severe defect upon Trp155 exchange is in line with the residue being the primary interactor of His137^{ISCU2}.

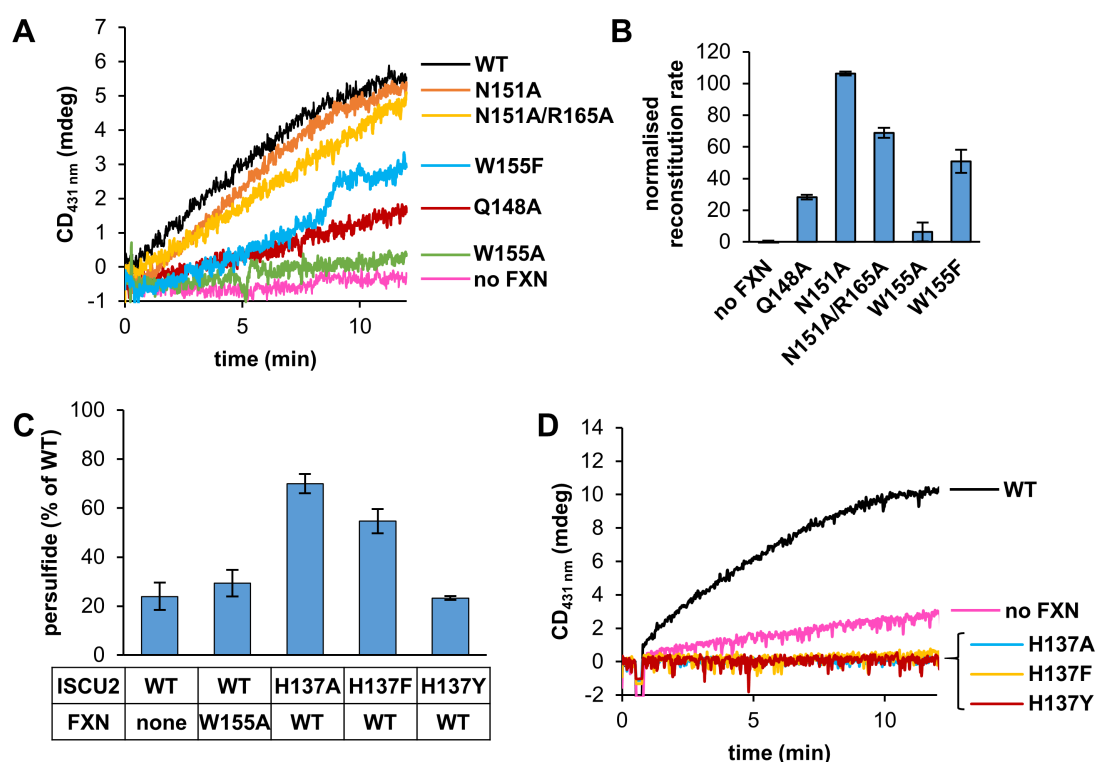


Figure 21: FXN residues Trp155 and Gln148, but not Asn151, are important for interaction with ISCU2.

A) Time course of enzymatic [2Fe-2S] cluster synthesis on ISCU2 in presence of the indicated FXN mutant proteins. Control reactions included WT ISCU2 and either WT FXN or no FXN. Components were mixed in an air-tight cuvette and the CD_{431 nm} signal set to zero upon starting time course measurements. After 30 s, cluster synthesis was initiated by injection of cysteine into the cuvette through a rubber plug, and the CD_{431 nm} signal was monitored for 12 min. **B)** Initial rates of enzymatic reconstitution reactions of the indicated FXN mutant proteins. Rates were determined by linear fitting of initial phases of the time course measurements and normalised to the ISCU2 WT rate. Error bars indicate the SEM ($n = 2$). **C)** ISCU2 persulfidation in presence of indicated ISCU2 and FXN proteins was measured via the MPB-alkylation assay (cf. Figure 17C), and data was normalised to reactions with the WT proteins. Error bars indicate the SEM ($n \geq 3$). **D)** Time course of enzymatic [2Fe-2S] cluster synthesis on ISCU2 in presence of the indicated ISCU2 mutant proteins. Control reactions included WT ISCU2 and either WT FXN or no FXN. Results shown in **A-B** were obtained in collaboration with N. Krapoth.

The His137^{ISCU2}-Trp155^{FXN} interaction was further characterised employing the MPB-based *in vitro* persulfidation assay. ISCU2 could still be persulfidated when His137^{ISCU2} was replaced with Ala or Phe, but significantly less efficiently if replaced by Tyr (Figure 21C, Appendix Figure 56D-E). Whereas Phe is likely able to insert into the FXN pocket, Tyr insertion is presumably (sterically) hindered and might consequently obstruct access of Cys381-SSH^{NFS1} to the ISCU2 assembly site. This obstruction is not present if His137^{ISCU2} is substituted by Ala. ISCU2 persulfidation was significantly decreased in presence of FXN W155A, which presumably exhibits a degenerated hydrophobic pocket, hampering FXN interaction with His137^{ISCU2}. Overall, these results support the hydro-

phobic His137^{ISCU2}–Trp155^{FXN} interaction to enable rearrangement of the ISCU2 assembly site for persulfidation by Cys381-SSH^{NFS1}. Despite enabling ISCU2 persulfidation, H137A and H137F did not allow for formation of a [2Fe-2S] cluster on ISCU2 in enzymatic reconstitution reactions (Figure 21D).

In conclusion, the data support His137^{ISCU2}–Trp155^{FXN} and Cys69^{ISCU2}–Gln148^{FXN} interactions triggering the FXN-induced conformational rearrangements observed in cryo-EM structures. Removal of His137^{ISCU2} from the ISCU2 Fe site under concomitant movement of Cys138^{ISCU2} by 1.0 Å towards the metal (Figure 6C) primes the latter residue for persulfidation by Cys381-SSH^{NFS1}.

4.1.8 Mössbauer spectroscopic analyses of intermediates of [2Fe-2S] cluster formation reveal a dynamic equilibrium between distinct Fe ligation modes

Studies from this and previous works imply different Fe coordination modes being present in free Fe-ISCU2 (Fe-U), (Fe-NIAU)₂, (Fe-NIAUX)₂ and persulfidated (Fe-NIAUX)₂ (Figure 22). All of these species may represent physiologically relevant stages of *de novo* Fe/S cluster biosynthesis.

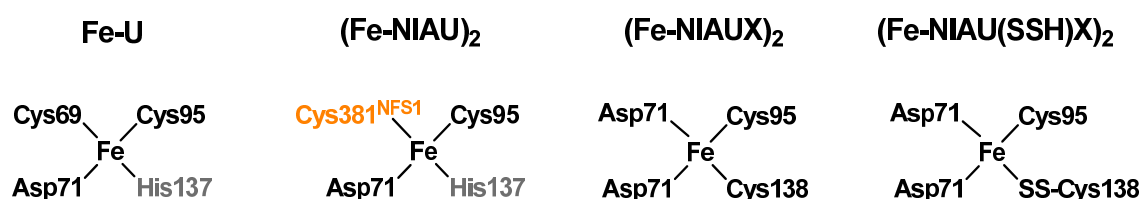


Figure 22: Fe coordination modes at the ISCU2 assembly site. Fe-ISCU2 (Fe-U) coordinates Fe via Cys69, Asp71, Cys95 and possibly His137 (chapter 4.1.2). 3D structures imply replacement of Cys69 by Cys381^{NFS1} (orange) in (Fe-NIAU)₂. Whereas the structure of (Zn-NIAU)₂ shows metal ligation via His137 (Boniecki *et al.*, 2017), weak electron density of His137 in (Fe-NIAU)₂ (Figure 20) precludes its definite assignment as a ligand. Structures of non-persulfidated (Zn-NIAUX)₂ (Fox *et al.*, 2019) and persulfidated (Fe-NIAUX)₂ both show metal coordination by Asp71, Cys95 and Cys138, with Asp71 acting as a bidentate ligand. Fe coordination in non-persulfidated and persulfidated (Fe-NIAUX)₂ may hence only differ in that Cys138 coordinates Fe via its persulfide rather than thiol moiety in the latter species.

To further characterise and investigate the different Fe coordination modes, Mössbauer spectroscopy was employed. This method provides information including the oxidation state of Fe as well as the number and type of its ligands (Garcia-Serres *et al.*, 2018). To enable identification of non-ISCU2-specific Fe-impurities, a sample containing (NIAUX)₂ but no ISCU2 served as a negative control. The physiological relevance of the experimental setup was verified by a positive control containing all core ISC components to

enable enzymatic [2Fe-2S] cluster synthesis on ISCU2. Furthermore, a “reduced persulfide” sample was prepared to investigate a potential intermediate present after ISCU2 persulfidation and before [2Fe-2S] cluster formation (described in detail below).

In initial experiments with five samples (Fe-U, (Fe-NIAU)₂, (Fe-NIAUX)₂, persulfidated (Fe-NIAUX)₂ and Fe+(NIAUX)₂), ⁵⁷Fe enriched ferric ammonium citrate (FAC) served as Fe source and was pre-reduced using excess ascorbate to obtain Fe(II). After sample preparation (see Appendix Table 18 for composition), excess Fe was removed by buffer exchange. Mössbauer analysis revealed two distinct ISCU2-specific Fe species (components 1 and 2, Appendix Figure 62 and Table 19). Additionally, significant amounts of Fe(III) and Fe(II) impurities (components 3 and 4, respectively) were present.

In subsequent experiments, NIA and FXN were added in a 1.5-fold excess over ISCU2 to ensure the scaffold protein being completely saturated with the proteins. Additionally, FAC was replaced by the Fe(II)-source (NH₄)₂⁵⁷Fe(SO₄)₂, which was added equimolar to ISCU2. Fe impurities in ISCU2-containing samples were thereby significantly reduced (from 45 – 79% to 0 – 8%), whereas the same ISCU2-specific components 1 and 2 were observed, underlining the reproducibility between the experimental setups.

The Mössbauer spectrum of free Fe-ISCU2 (Figure 23A) showed one ISCU2-dependent Fe(II) species (component 1), with parameters in line with tetrahedral coordination of Fe by 1 – 2 Cys residues and 2 – 3 N/O ligands (Table 15). Applied-field spectra of free Fe-ISCU2 (Figure 63B-C and Table 20) furthermore showed similarity to those of a previously reported Fe(II) species ligated by two Cys, one His and water (Bill *et al.*, 1989). Overall, this supports Fe(II) being coordinated by Cys69, Asp71, Cys95 and His137, as indicated by CD spectroscopy (chapter 4.1.2).

(Fe-NIAU)₂ (Figure 23B) exhibited the two ISCU2-specific components 1 and 2, representing 65% and 27%, respectively, of all Fe species. (Fe-NIAUX)₂ (Figure 23C) exhibited the same components as (Fe-NIAU)₂, but at a significantly shifted ratio with 36% component 1 and 61% component 2. It can be assumed that both components represent (NIA)₂-bound but not free Fe-ISCU2, since NIA had been added in 1.5-fold excess over ISCU2, and furthermore aSEC experiments had shown formation of a stable (NIAU)₂ complex (Appendix Figure 59).

Component 1 exhibited almost identical parameters in samples Fe-U and (Fe-NIAU)₂ (Table 15). In agreement, spectroscopic and structural data indicate similar Fe coordination, the only difference being that Cys69^{ISCU2} is replaced by Cys381^{NFS1} as a ligand upon (Fe-NIAU)₂ formation (Figure 22). Exchange of one Cys ligand by another cannot readily be detected by Mössbauer spectroscopy.

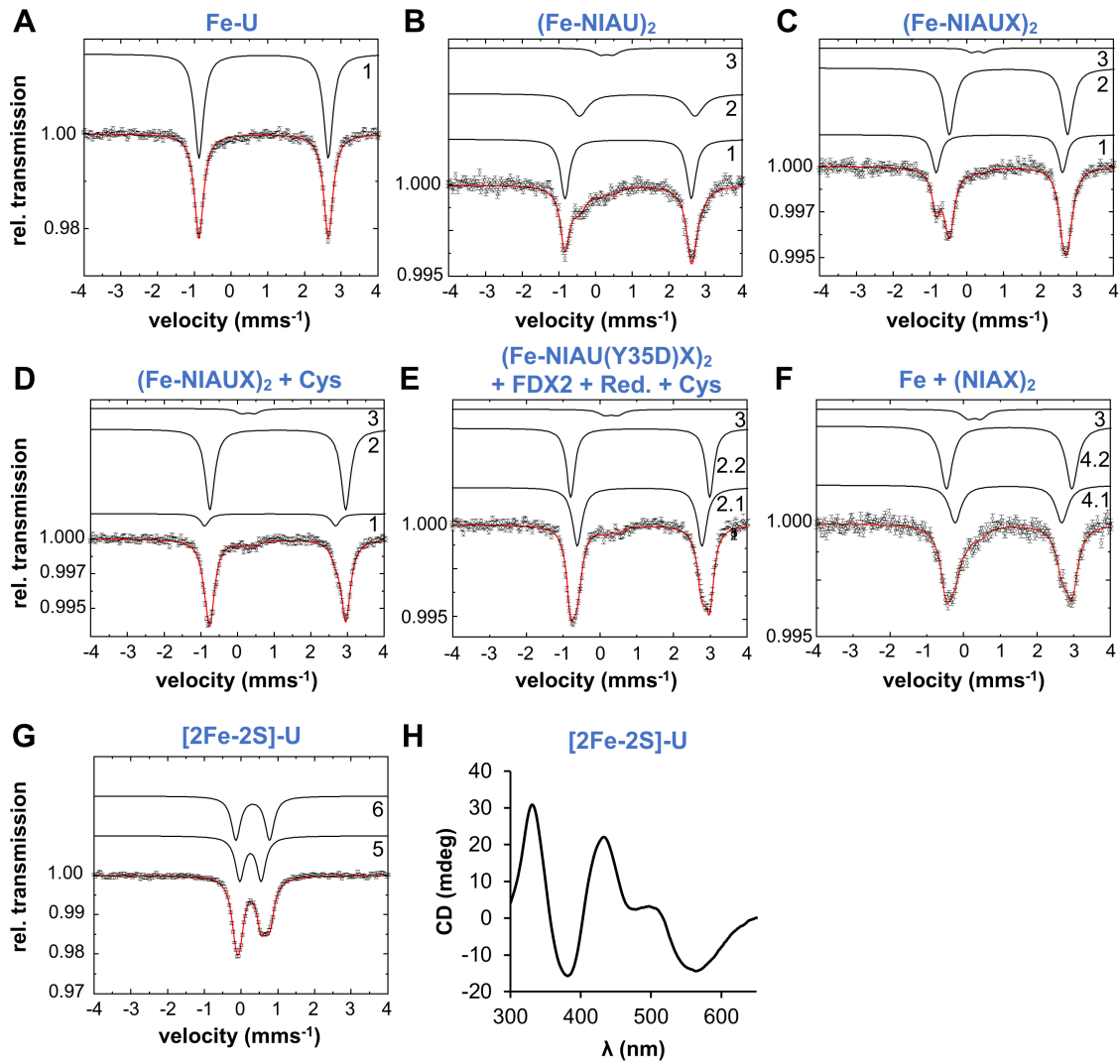


Figure 23: Mössbauer spectroscopy reveals an equilibrium of two distinct Fe coordination modes in biosynthetic intermediates of physiologically relevant [2Fe-2S]²⁺-ISCU2 synthesis. **A-G)** Mössbauer spectra of the indicated samples reconstituted with 1 eq. (NH₄)₂⁵⁷Fe(SO₄)₂ over ISCU2. For the detailed sample composition, see Table 14. U: ISCU2; X: FXN; F: FDX2. **A)** Spectrum recorded in presence of ISCU2. **B-E)** Spectra of samples including 1.5 eq. NIA and/or FXN over ISCU2. **Red.** indicates the presence of NADPH and FDXR. **Cys** indicates cysteine added as last component. The “reduced persulfide” sample (**E**) contained ISCU2 Y35D instead of ISCU2 WT and furthermore cysteine, NADPH and catalytic amounts of FDX2 and FDXR. **F)** Spectrum in presence of (NIAUX)₂, lacking ISCU2. **G)** Spectrum of enzymatically reconstituted [2Fe-2S]²⁺-ISCU2 containing all proteins except ISCU2 in catalytic amounts, as well as cysteine and NADPH. **H)** CD spectrum of the sample shown in (**G**), exhibiting the typical signature of [2Fe-2S]²⁺-ISCU2 (see chapter 4.1.11) (Freibert *et al.*, 2018). Each spectrum was recorded at 77 K and 0 T. The red line displays the best fit of the data using the components shown as black lines. Error bars indicate the SD. Mössbauer spectroscopic analyses were done in collaboration with J. Oltmanns and Dr. V. Schünemann.

Table 15: Mössbauer parameters of individual components as numbered in Figure 23A-G. Isomer shift (δ), quadrupole splitting (ΔE_Q) and line width (Γ) are given in mm s⁻¹. A², surface area. For the detailed sample composition, see Table 14.

	Component 1				Component 2				Component 3			
	δ	ΔE_Q	Γ	A ² (%)	δ	ΔE_Q	Γ	A ² (%)	δ	ΔE_Q	Γ	A ² (%)
Fe-U	0.89	3.52	0.30	100								
(Fe-NIAU)₂	0.89	3.42	0.31	65	1.15	3.15	0.40	27	0.30	0.35	0.39	8
(Fe-NIAUX)₂	0.89	3.40	0.28	36	1.15	3.23	0.32	61	0.30	0.35	0.38	3
(Fe-NIAUX)₂ + Cys	0.89	3.57	0.28	11	1.10	3.70	0.31	83	0.30	0.35	0.36	6
(Fe-NIAU(Y35D)X)₂ + FDX2 + Red. + Cys					1.08	3.39	0.31	47				
					1.09	3.78	0.27	47				
	Component 3				Component 4							
Fe + (NIAUX)₂					1.24	2.91	0.40	35				
					1.25	3.42	0.38	57				
	Component 5				Component 6							
[2Fe-2S]-U	0.26	0.58	0.29	50	0.32	0.92	0.30	50				

Mössbauer parameters of component 2 are in line with high-spin (HS) Fe(II) being octahedrally coordinated with 1 – 2 Cys residues and 4 – 5 N/O ligands. This fits to an Asp71, Cys95 and Cys138 ligated Fe of (Fe-NIAUX)₂ observed in cryo-EM experiments (Figure 19) (Fox *et al.*, 2019) and supported by ISCU2 persulfidation assays (Figure 17C). (M-NIAUX)₂ cryo-EM structures show Asp71 acting as a bidentate ligand, implying the coordination sphere of component 2 being completed by two water ligands.

The data support an equilibrium between two distinct ISCU2-specific Fe species in the (Fe-NIAU)₂ and (Fe-NIAUX)₂ samples, shifted by the addition of FXN. (Fe-NIAU)₂ exhibits its preferred Fe ligation probably by Cys381^{NFS1}, Asp71, Cys95 and His137 (component 1) and in (Fe-NIAUX)₂, Fe coordination by Asp71, Cys95 and Cys138 (component 2) is favoured. The equilibrium in (Fe-NIAU)₂ is in line with weak electron densities of His137^{ISCU2} and the Cys69^{ISCU2}-loop observed in the 3D structure of (Fe-NIAU)₂, indicating a certain plasticity of the assembly site in the absence of FXN. Furthermore, the line width of component 2 is significantly decreased in (Fe-NIAUX)₂ compared to (Fe-NIAU)₂ (Table 15), supporting that this Fe species is rigidified in presence of FXN. Plasticity of the ISCU2 assembly site has not been implied in 3D structures of (M-NIAUX)₂. However, this work (Appendix Figure 59) and previous studies (Gervason *et al.*, 2019; Uzarska *et al.*, 2022) support an unstable/dynamic binding of FXN to (Fe-NIAU)₂. The equilibrium observed in Mössbauer analysis of (Fe-NIAUX)₂ may hence reflect the association and dissociation of FXN.

To investigate Fe coordination of persulfidated ISCU2, (Fe-NIAUX)₂ in presence of cysteine was analysed (Figure 23D). The proportion of component 2 increased to 83%, whereas component 1 only represented 11% of Fe species. In good agreement, cryo-EM analysis had yielded 75% of particles representing persulfidated ISCU2 in (Fe-NIAU(SSH)X)₂ with an Fe coordination corresponding to component 2 (chapter 4.1.6). Whereas the isomer shift of component 2 is similar before and after (Fe-NIAUX)₂ persulfidation, the quadrupole splitting is significantly increased (by 0.47 mm s⁻¹, Table 15). The observed increase may be caused by Fe coordination via persulfidated Cys138-SSH leading to a slightly altered coordination geometry of the metal. Nevertheless, Mössbauer data support that the same protein ligands coordinate Fe in (Fe-NIAUX)₂ both before and after Cys138^{ISCU2} persulfidation.

After characterising Fe binding of persulfidated ISCU2, subsequent steps of *de novo* [2Fe-2S] formation were investigated. A recent study had shown that ISCU2 Tyr35 was required for ISCU2 dimerization to enable [2Fe-2S] cluster synthesis (Freibert *et al.*, 2021). *In vitro* assays had shown Tyr35 variants to still enable ISCU2 persulfidation and persulfide reduction, but abolish [2Fe-2S] cluster maturation (Appendix Figure 64). ISCU2 Y35D was employed instead of the WT protein in reactions containing all core ISC components to enable capture of a cluster synthesis intermediate potentially exhibiting a persulfide reduced by electron flow from FDX2. The species of interest is termed “reduced persulfide” intermediate hereinafter. Mössbauer analysis (Figure 23E) revealed two similar components (2.1 and 2.2) in an exact 1:1 ratio with distinct quadrupole splitting, whereas component 1 was absent. Component 2.2 exhibits parameters similar to component 2 of persulfidated (Fe-NIAUX)₂, suggesting the presence of persulfidated ISCU2. Component 2.1 exhibits a significantly decreased quadrupole splitting more similar to non-persulfidated (Fe-NIAUX)₂. However, no evidence for the presence of a distinct species was found. FDX2-mediated persulfide reduction might have led to liberation of the persulfide as hydrogen sulfide. Due to the exact 1:1 ratio of components 2.1 and 2.2, it is tempting to speculate that reduction of the persulfide might only be possible on one side of the dimeric (NIAUX)₂ complex in presence of ISCU2 Y35D. However, it is also possible that ISCU2 persulfidation was just less efficient in presence of ISCU2 Y35D.

To verify ISCU2-specificity of the different Mössbauer components, Fe+(NIAUX)₂ (Figure 23F) was analysed as a control. The two detected ISCU2-independent components 3 and 4 likely represent Fe(III) impurities and non-specifically bound HS Fe(II), respectively. The lack of components 1 and 2 in the sample supports their specificity to ISCU2. Finally, Fe coordination in [2Fe-2S] ISCU2 was analysed by subjecting fully reconstituted WT ISCU2 to Mössbauer spectroscopy. Two components (5 and 6, Figure 23G) at an

exact 1:1 ratio were detected, their parameters similar to those published for mouse [2Fe-2S]-ISCU (Gervason *et al.*, 2019). Applied-field spectra (Appendix Figure 63E-F) and CD spectroscopy (Figure 23H) provided further evidence for the presence of a [2Fe-2S]²⁺ cluster, highlighting the physiological relevance of the experimental setup. Component 5 likely represents four-fold S-ligated Fe(III), whereas component 6 indicates four-fold ligation of Fe(III) with 2 – 3 S-ligands and 1 – 2 N/O-ligands. This is in agreement with a [2Fe-2S]²⁺ cluster being coordinated by 2 – 3 Cys and 1 – 2 N/O ligands. Which ISCU2 residues are required for cluster coordination was investigated in detail by reconstitution experiments (chapter 4.1.11).

In summary, Mössbauer analyses support free Fe-U (Figure 9) to exclusively exhibit tetrahedral Fe ligation by Cys69, Asp71, Cys95 and His137 (component 1). Upon binding to (NIA)₂, Cys69 is likely exchanged with Cys381^{NFS1}. Whilst component 1 is the major species in (Fe-NIAU)₂, it is in equilibrium with component 2, exhibiting octahedral Fe coordination by Asp71, Cys95, Cys138 and water. Presence of FXN shifts the equilibrium towards component 2. ISCU2 persulfidation requires component 2, and Fe is coordinated via Asp71, Cys95, persulfidated Cys138-SSH and water. Full reconstitution of ISCU2 then yields a [2Fe-2S]²⁺ cluster. For a detailed model, see also chapter 5.1.2.2 (Figure 37) in the discussion.

4.1.9 X-ray absorption spectroscopy of intermediates of [2Fe-2S] cluster formation

To further characterize the different intermediate stages of [2Fe-2S] cluster synthesis, the same samples analysed in the Mössbauer experiment shown in Figure 23 (except fully reconstituted ISCU2) were also analysed by X-ray absorption spectroscopy (XAS). Unfortunately, ice crystals formed in the samples, making extended X-ray absorption fine structure (EXAFS) analysis impossible. This precluded a detailed analysis of the Fe coordination sphere. Nevertheless, X-ray absorption near edge structure (XANES) data were evaluated. Spectra of all samples except (NIAU)₂ looked overall similar, with the region of 7130 – 7150 eV exhibiting changes from Fe-U to (Fe-NIAU)₂ and again to (Fe-NIAUX)₂ (Figure 24). This may reflect the transition from component 1 to component 2 as observed by Mössbauer spectroscopy (Table 15). (Fe-NIAUX)₂ as well as the persulfide and “reduced persulfide” sample exhibited similar spectra, in line with only subtle changes in Fe coordination as observed by Mössbauer spectroscopy. Fe-U and Fe+(NIAU)₂ exhibited spectral features similar to previously published analyses of yeast Fe-Isu1 (Cook *et al.*, 2010) and human Fe-FXN (Bencze *et al.*, 2007). The latter had been reported to exhibit HS Fe(II) coordinated via 6 N/O-ligands, likely reflected by component 4 observed in Mössbauer analyses.

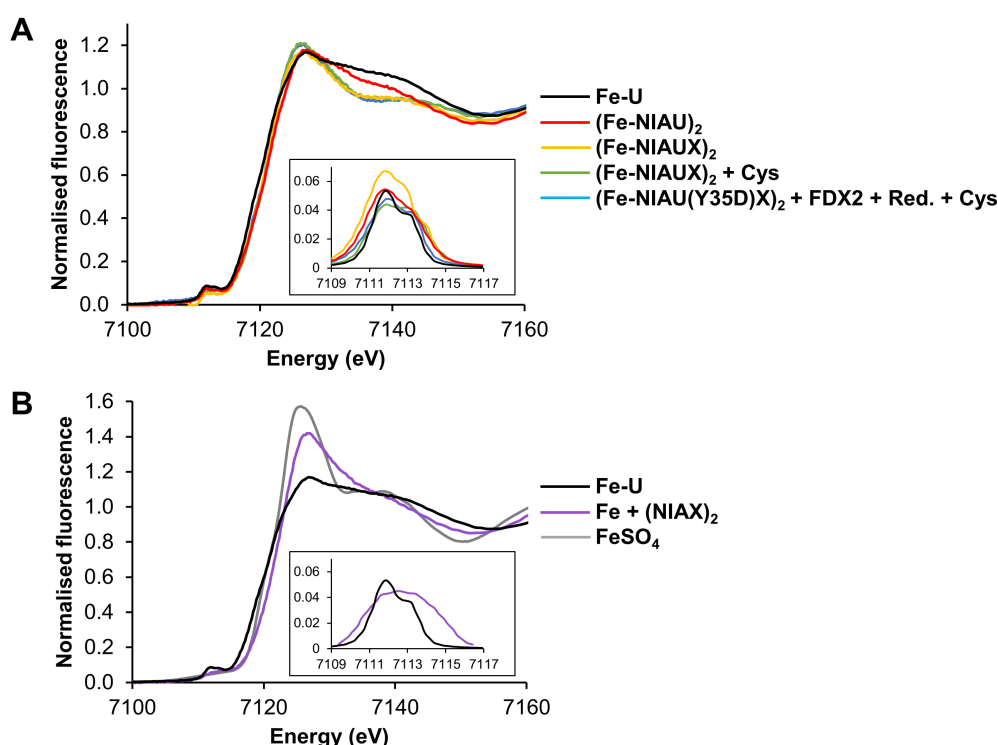


Figure 24: XAS analysis of [2Fe-2S] cluster synthesis intermediates. A-B) Normalized and smoothed Fe K-edge XANES spectra recorded at 10 K from the same samples analysed by Mössbauer spectroscopy (Figure 23). Spectra are shown in two panels for better visualization. A normalised Fe(II)SO₄ spectrum (grey) is shown for comparison in **(B)**. Insets depict an enlargement of the pre-edge region from 7109 – 7117 eV.

4.1.10 ISCU2 Cys69, Asp71, Cys95, His137 and Cys138 are required for enzymatic [2Fe-2S] cluster formation

To assess the overall functional importance of the individual assembly site ISCU2 residues, *de novo* synthesis of [2Fe-2S]-ISCU2 was reconstituted in an anaerobic enzymatic assay employing the respective variants. The time course of [2Fe-2S] cluster formation was monitored via CD spectroscopy at 431 nm. Additionally, spectra were recorded at the end of the reaction period. ISCU2 WT and C130S showed efficient cluster formation and virtually identical CD-spectral features (Figure 25), in line with the non-conserved Cys130 not being involved in Fe/S cluster biogenesis. Reactions including WT ISCU2 but no FXN still allowed for cluster formation, but at a much reduced reaction rate, in line with the observed reduced efficiency of ISCU2 persulfidation in absence of FXN (compare Figure 17C). Apart from minute cluster formation on ISCU2 H137A, mutant proteins C69S, D71A, C95S, H137A and C138S did not enable efficient [2Fe-2S] cluster formation, indicating crucial functions of these residues.

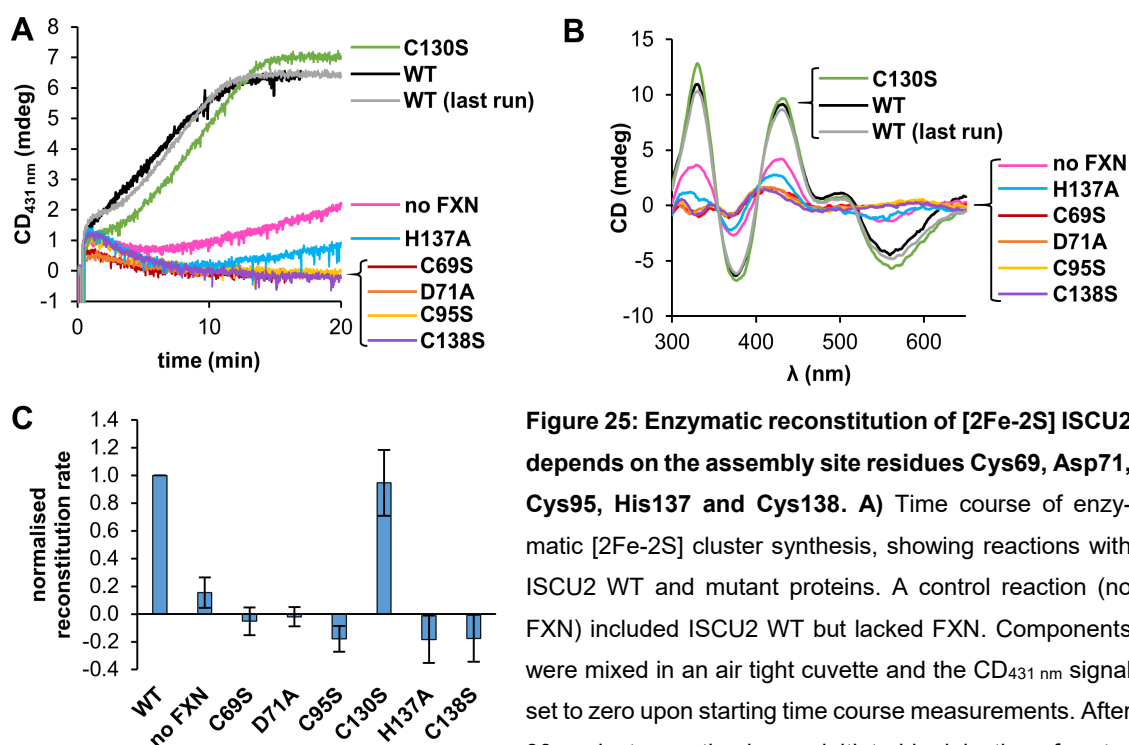


Figure 25: Enzymatic reconstitution of [2Fe-2S] ISCU2 depends on the assembly site residues Cys69, Asp71, Cys95, His137 and Cys138. **A)** Time course of enzymatic [2Fe-2S] cluster synthesis, showing reactions with ISCU2 WT and mutant proteins. A control reaction (no FXN) included ISCU2 WT but lacked FXN. Components were mixed in an air tight cuvette and the CD_{431 nm} signal set to zero upon starting time course measurements. After 30 s, cluster synthesis was initiated by injection of cysteine into the cuvette through a rubber plug and the monitoring of the CD_{431 nm} signal for 20 min. Immediately afterwards, a CD spectrum of the reconstitution mixture was recorded (**B**). To ensure none of the components are degrading throughout the time of the measurements, two ISCU2 WT samples were measured as the first and last reaction of the experiment. **C)** Initial reconstitution rates were determined by linear fitting of the time course measurements in **A** and normalised to the ISCU2 WT rate. Error bars indicate the SEM ($n \geq 3$).

4.1.11 ISCU2 Cys69, Cys95 and Cys138 are essential for [2Fe-2S] cluster coordination

The enzymatic reconstitution reactions performed above showed the ISCU2 assembly site Cys residues as well as His137 and Asp71 having an essential function in [2Fe-2S] cluster formation on the scaffold protein ISCU2. However, it was not clear from this approach, which of these residues were the ones required for coordination of the mature cluster. Asp71, Cys95 and Cys138 had been shown to be important for persulfide formation on ISCU2 (see chapter 4.1.3), hence removing these residues would necessarily disable all proceeding steps. To circumvent this issue, the variants were reconstituted chemically using inorganic Fe(III) and sulfide under anaerobic conditions in presence of a thiol reductant. The assumption of this approach is that chemical reconstitution artificially assembles the [2Fe-2S] cluster without the need of residues serving as persulfide acceptors or Fe binding sites in the physiological assembly pathway. Therefore, only residues directly involved in final Fe/S cluster coordination would be revealed. A fraction of these reconstituted samples was used for measurement of a CD spectrum, whereas

another fraction was analysed by aSEC coupled with a diode array detector (DAD). To improve separation of LMW species, a newly available analytical Superdex 75 pg column was used as opposed to the 200 pg column previously employed for characterization of as-purified ISCU2 WT and variants (chapter 4.1.1). Apo-ISCU2 WT exhibited an elution volume of 12.2 mL using the 75 pg column (Figure 26A), opposed to 17.0 mL using the 200 pg column (Figure 14C). Reconstituted ISCU2 WT exhibited a major peak of low MW (LMW) at 12.1 mL (corresponding to a calculated mass of 20.2 kDa based on column calibration) and a minor peak of high MW (HMW) at 9.6 mL (calculated mass 48.1 kDa) (Figure 26A).

The UV/Vis spectrum of the LMW species recorded by the DAD exhibited distinct peaks at 323, 404 and 455 nm and a shoulder at around 520 nm (Figure 26B), suggesting the presence of a [2Fe-2S] cluster (Freibert *et al.*, 2018). In contrast, the spectrum of the HMW species only showed a shoulder around 325 nm and a broad peak around 400 nm (Figure 26C), indicating the presence of a [4Fe-4S] cluster. Extended incubation of the reconstituted sample led to decreased amounts of the LMW species as detected by aSEC (Appendix Figure 65B), concomitant with decreased intensity of CD-spectral features (Appendix Figure 66A), supporting the LMW species representing [2Fe-2S] cluster-loaded ISCU2. CD-spectral features of ISCU2 WT and elution volume of the LMW species were similar to enzymatically reconstituted ISCU2 (Figure 26E, Appendix Figure 65C). Enzymatically reconstituted [2Fe-2S]-ISCU2 eluting at 11.7 mL (compared to 12.1 mL in chemical reconstitution) exhibited a mass of 15.6 kDa (Appendix Figure 65D) as determined by multiangle light scattering (MALS). This indicated the presence of a holo-monomer (theoretical mass [2Fe-2S]-ISCU2: 15.7 kDa). Altogether, the data support chemical reconstitution and subsequent aSEC to yield a [2Fe-2S]-loaded ISCU2 monomer with the same cluster binding mode as enzymatically synthesized ISCU2. In chemical reconstitution, this species represented 92% of Fe/S cluster-bound ISCU2, whilst the [4Fe-4S]-containing species (8%) constituted a minor fraction.

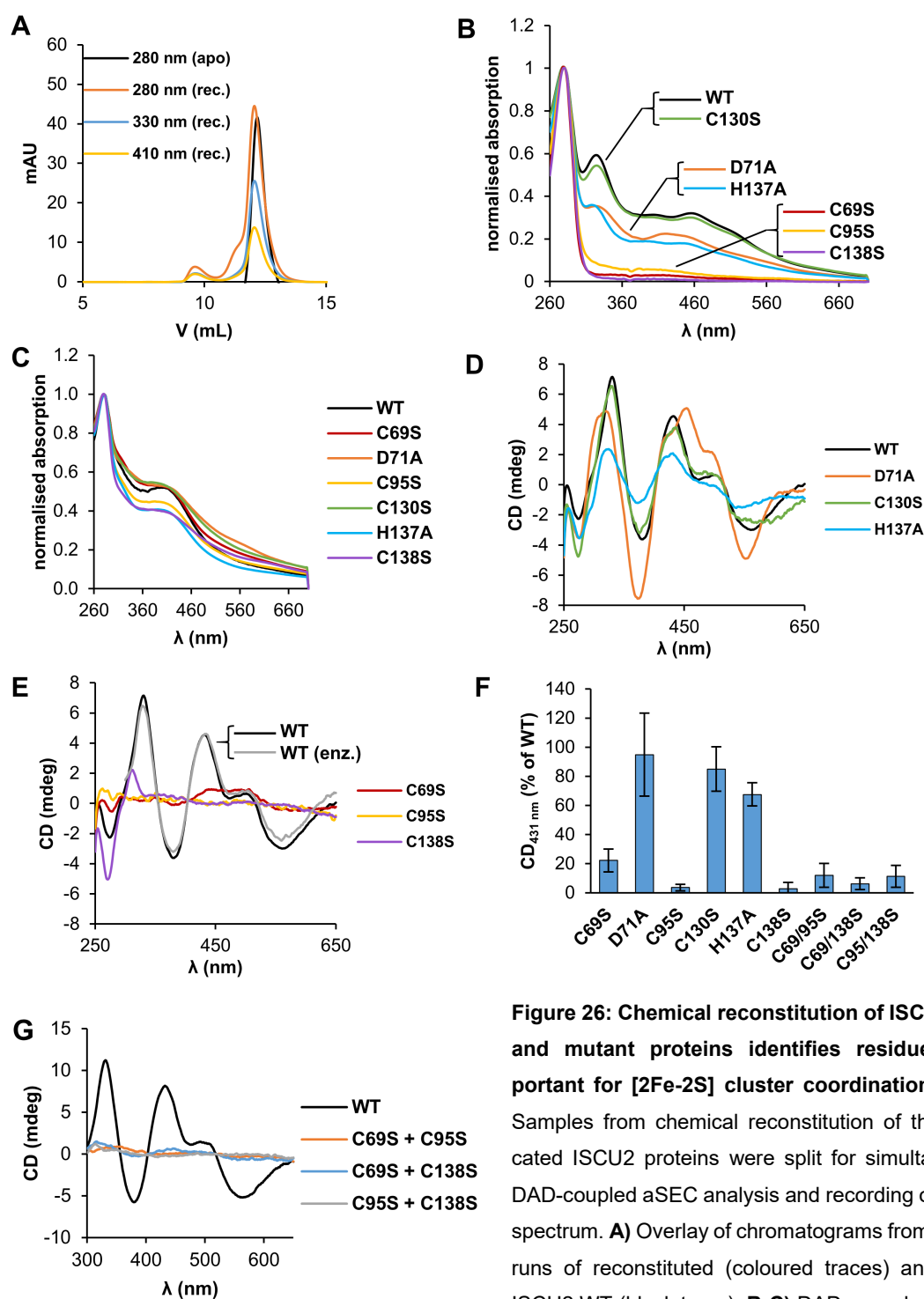


Figure 26: Chemical reconstitution of ISCU2 WT and mutant proteins identifies residues important for [2Fe-2S] cluster coordination. A-E)

Samples from chemical reconstitution of the indicated ISCU2 proteins were split for simultaneous DAD-coupled aSEC analysis and recording of a CD spectrum. **A)** Overlay of chromatograms from aSEC runs of reconstituted (coloured traces) and apo-ISCU2 WT (black trace). **B-C)** DAD-recorded spectra

from aSEC runs of chemically reconstituted ISCU2 WT and mutant proteins from peaks at elution volumes of 11.7 – 12.2 mL **(B)** and 9.4 – 9.8 mL **(C)** normalised to the absorption at 280 nm. **D-E)** CD spectra of the indicated, chemically reconstituted proteins (shown in two panels for better visualization). Enzymatically reconstituted ISCU2 WT (grey, 300 – 650 nm) is overlaid for comparison **(E)**, normalised to chemically reconstituted ISCU2 WT (black). **F)** The CD signal at 431 nm of chemically reconstituted ISCU2 mutant proteins was normalised to that of ISCU2 WT. Error bars indicate the SEM ($n \geq 3$). **G)** Two different ISCU2 Cys variants were combined (e.g., ISCU2 C69S + ISCU2 C95S) in a 1:1 ratio and CD spectra of chemical reconstitutions recorded. Reactions contained 50 μ M of each indicated variant. A control was performed using 100 μ M ISCU2 WT.

Chemically reconstituted ISCU2 variants showed varying amounts of Fe/S cluster-containing LMW and HMW species (Appendix Figure 65E-J) with elution volumes similar to those of the WT Fe/S species at 12.1 and 9.6 mL. Other peaks with high signal intensity at 280 nm but low intensity at 330 and 410 nm of most of the variants indicated additional protein species without any Fe/S cluster content. Comparing UV/Vis spectra of peaks at 11.7 – 12.2 mL elution volume, ISCU2 C130S showed a spectrum almost identical to [2Fe-2S]-ISCU2 WT (Figure 26B). Variants D71A and H137A showed spectra likely corresponding to [2Fe-2S] species but with somewhat decreased intensity compared to WT protein and with slightly altered spectral features, in particular for ISCU2 D71A. Replacing any of the three assembly site Cys residues with Ala abolished binding of a [2Fe-2S] cluster completely. Remarkably, all mutant proteins still allowed for formation Fe/S cluster-containing HMW species with elution volumes of 9.4 – 9.8 mL (Figure 26C). The spectral features of these reconstituted ISCU2 WT and mutant proteins were consistent with the presence of [4Fe-4S] clusters. Additional Fe/S cluster species present in variants C69S, D71A and C95S and eluting at 8.7, 9.1 and 11.3 mL, respectively, showed spectral features different from [2Fe-2S] ISCU2, rather indicating [4Fe-4S] clusters (Appendix Figure 66B).

The results suggest that [4Fe-4S] clusters can be coordinated by multimeric ISCU2 species, possibly with different combinations of residues from two or more monomers. However, CD- and Mössbauer-spectroscopic analyses of enzymatic reconstitutions done in this work strongly suggest only the [2Fe-2S] cluster species being physiologically relevant, in line with earlier studies (Gervason *et al.*, 2019; Webert *et al.*, 2014).

CD-spectroscopic analysis of chemically reconstituted ISCU2 revealed strong spectral features of ISCU2 WT and the variants D71A, C130S and (to a lesser extent) H137A (Figure 26D), fitting to the signals observed by UV/Vis spectroscopy of the LMW species, further supporting the presence of a [2Fe-2S] cluster in these proteins. Variant D71A exhibited a significantly altered spectrum, in support of a changed binding mode of the [2Fe-2S] cluster. ISCU2 C69S showed a broad signal at 400 – 550 nm (Figure 26E), however, no signal in this range could be observed in the UV/Vis spectrum of the monomeric species, indicating this signal being related to multimeric ISCU2. ISCU2 C95S and C138S being void of CD-spectral features in the 350 – 650 nm range indicated [4Fe-4S] ISCU2 species not being detectable by CD spectroscopy at the employed concentrations. ISCU2 C138S exhibited peaks at 271 and 312 nm, in line with the ability of this variant to coordinate Fe (compare Figure 16B). Additional reconstitution experiments further supported ISCU2 D71A, C130S and H137A to enable [2Fe-2S] cluster formation, whereas the three assembly site Cys residues were essential for coordination (Figure 26F). Since exchanging Asp71 apparently altered the cluster binding mode, the residue

might function as a fourth ligand enabling a certain lability of the cluster to facilitate its transfer to recipient proteins, as reported for other organisms (Marinoni *et al.*, 2012; Wu *et al.*, 2002b). Exchanging His137 led to a decreased yield of [2Fe-2S]-ISCU2 (Figure 26D,F), however, spectral properties were not significantly affected (compare Appendix Figure 66C).

Despite SEC-MALS analysis of reconstituted ISCU2 suggesting the presence of monomeric [2Fe-2S]-ISCU2, transient formation of a semi-stable holo-dimer that dissociates throughout SEC cannot be excluded. However, since all three assembly site Cys residues are essential for cluster coordination, the coordination mode of such a dimer would be asymmetric (meaning different Cys residues from each ISCU2 monomer coordinate the cluster). To address this possibility, different combinations of the three ISCU2 single mutant proteins C69S, C95S and C138S were chemically reconstituted. None of the combinations enabled [2Fe-2S] cluster formation (Figure 26G), indicating that the cluster is ligated by Cys69, Cys95 and Cys138 from one ISCU2 molecule.

4.2 *In vitro* reconstitution of human lipoyl biosynthesis identifies FDX1 as electron donor for LIAS

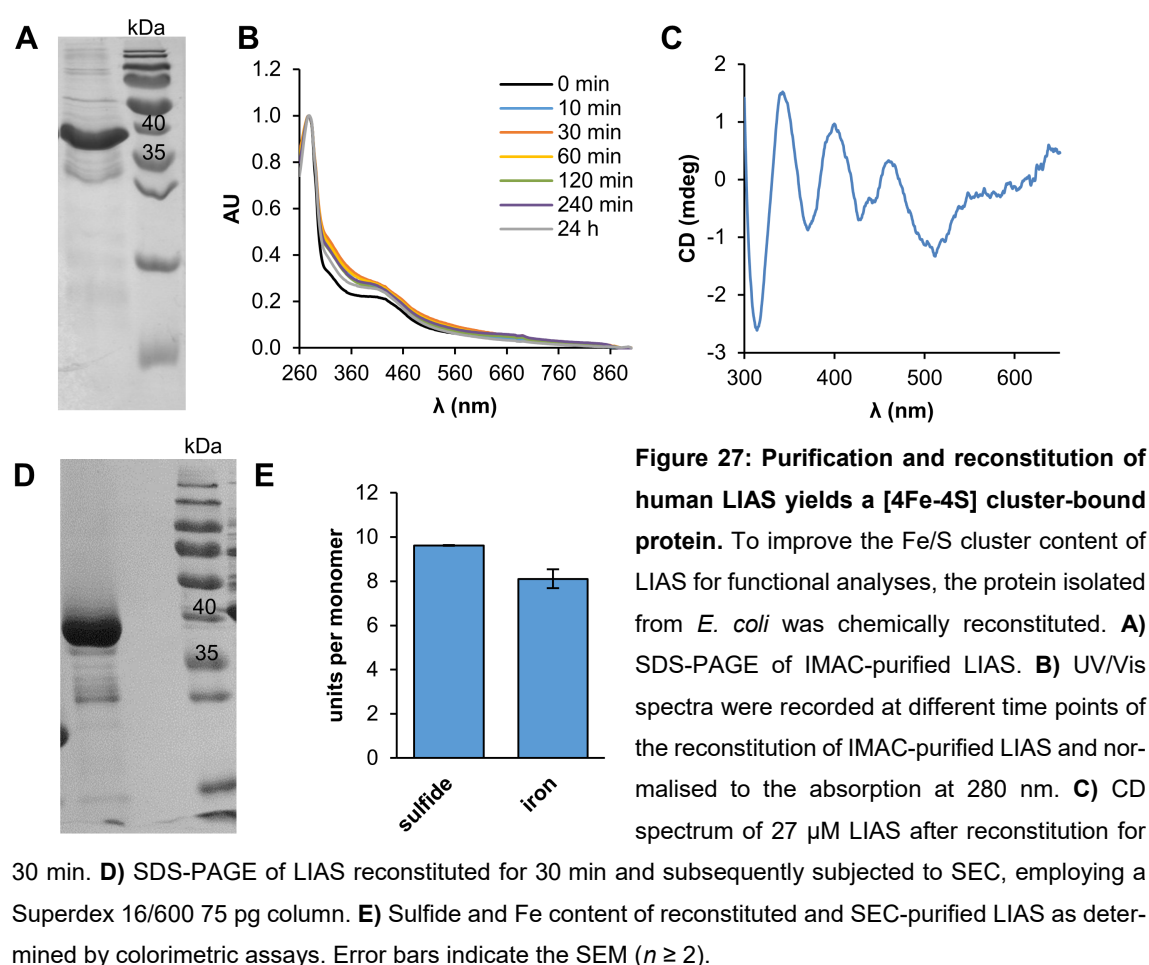
The lipoyl cofactor is essential for mitochondrial metabolism, for example due to its function in PDH and KGDH enzymes which synthesize TCA cycle substrates. The molecular mechanism of sulfur insertion into an octanoyl substrate by LIAS to form the lipoyl product has been extensively characterised (Lanz *et al.*, 2014; McCarthy & Booker, 2017; McLaughlin *et al.*, 2016). However, the electron donor for the LIAS-mediated radical SAM-based reaction mechanism has remained unknown. In this work, a possible function of FDX as electron donor for human LIAS should be investigated. Quantification of lipoyl formation had been previously performed via *in vitro* assays using bacterial proteins and the non-physiological inorganic electron donor dithionite (DT) (McCarthy & Booker, 2018). Here, an analogous *in vitro* assay using human proteins to identify the physiological electron donor for LIAS should be established.

4.2.1 Purification and reconstitution of LIAS yields a functional holo-protein

4.2.1.1 Purification and reconstitution of LIAS

Human LIAS was purified anaerobically according to a protocol received from Dr. S. Booker and Dr. D. Warui (Penn State University, PA, USA), with few adjustments. The protein could be obtained at high yield (17.6 mg/L cell culture) and good purity (Figure 27A) after IMAC. The presence of only two peaks at around 330 and 410 nm in the

UV/Vis spectrum of IMAC-purified LIAS was indicative of exclusive [4Fe-4S] cluster binding (Figure 27B) (Freibert *et al.*, 2018). Chemical reconstitution under anaerobic conditions with UV/Vis analysis at up to 24 h reconstitution time showed that maximum cluster loading was reached at 30 min. A merely 28% increase of the absorption at 410 nm after 30 min indicated that most of the protein had already at least one [4Fe-4S] cluster bound after purification. Weak CD-spectral features supported the presence of only [4Fe-4S] clusters (Figure 27C) (Freibert *et al.*, 2018). The sample reconstituted for 30 min was subjected to SEC (Figure 27D). Subsequently, Fe and sulfur content were determined via colorimetric assays to be 8.1 and 9.6 atoms per monomer, respectively (Figure 27E). This result was in line with LIAS binding two [4Fe-4S] clusters.



4.2.1.2 Biochemical reconstitution of the lipoylation activity of LIAS identifies FDX1 as an efficient radical chain starter

To address the question of the physiological electron donor for the lipoylation activity of human LIAS, an HPLC-MS-based assay previously established for bacterial lipoyl synthase LipA (McCarthy & Booker, 2018) was employed. A chemically synthesized octapeptide containing the required octanoyllysyl precursor was used as substrate analogue, and the SAM-dependent sequential formation of the 6-thiooctanoyl intermediate and lipoyl product (Figure 28A) under strictly anaerobic conditions was quantified by HPLC-MS. The LIAS enzymatic function involves the electron-requiring SAM cleavage to methionine and a 5'-deoxyadenosyl radical (5'-dA \cdot), which starts the synthesis reaction (for details regarding the mechanism see Figure 11). Previously, the artificial reductant DT had been commonly used *in vitro* to initiate the LIAS reaction, since the physiological electron donor was unknown. We suspected that an electron transfer chain (ETC) comprising NADPH, FDXR and either FDX1 or FDX2 could serve as a possible physiological electron donor for LIAS. *In vivo* studies performed by Dr. S. Basu and Dr. O. Stehling in fact showed that *in vivo* both FDX1 and FDX2 were required for lipoylation of the E2 subunits of PDH and KGDH (Figure 48). Since FDX2 was shown to be generally required for Fe/S cluster assembly and hence probably also matures LIAS, FDX1 might perform a specific function as a possible radical chain starter. Verification of this hypothesis cannot be obtained by *in vivo* studies, but requires biochemical reconstitution of the LIAS enzymatic function. The HPLC-MS analysis of LIAS function revealed ion traces that indicated the formation of both intermediate and lipoyl product in reactions containing the artificial reductant DT, establishing that the activity of human LIAS can be followed using a similar assay as developed for bacterial LipA (Figure 28B) (McCarthy & Booker, 2018). Remarkably, replacing DT by the mixture of NADPH, FDXR and FDX1 also supported intermediate and lipoyl product formation (Figure 28C). Compared to the reaction with DT, the FDX1-supported intermediate and product formation was even 2.4- and 2.1-fold more efficient, respectively, as evident from integrated mass areas of 6-thiooctanoyl and lipoyl ion traces (Figure 28E). This quantitation also showed that formation of the intermediate was much more efficient than that of the product, suggesting the latter step to be rate-limiting. Omitting FDX1 from the ETC abolished lipoyl formation completely, showing the essential role of this FDX (Figure 28D-E). Strikingly, this suggested FDX1 being a physiological electron donor for LIAS. Together, the findings showed reconstituted LIAS to be functional in enzymatic lipoylation reactions.

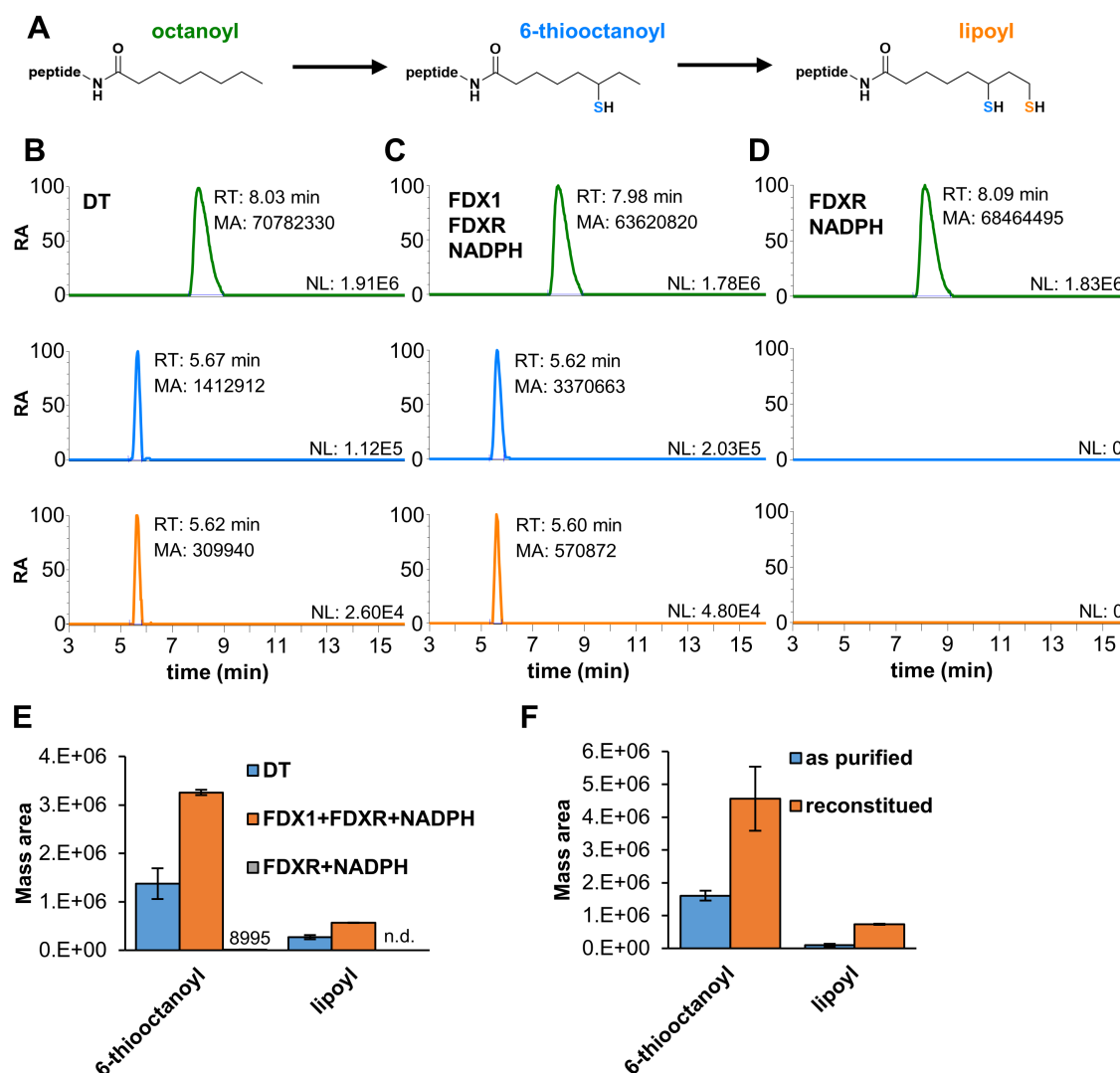


Figure 28: Both DT and FDX1 enable LIAS-mediated lipoyl formation *in vitro*. **A)** Scheme of lipoyl synthesis by LIAS as followed *in vitro* using an octanoyllysyl-octapeptide substrate. Depicting are the substrate, intermediate and product molecules quantified by HPLC-MS (octanoyl peptide: 932.49 Da; 6-thiooctanoyl peptide: 964.47 Da; lipoyl peptide: 996.44 Da). **B-D)** MS ion traces corresponding to octanoyl (green), 6-thiooctanoyl (blue) and lipoyl (orange) peptide from 150 min lipoylation reactions including reconstituted LIAS, octanoyl peptide and SAM. Electrons were provided by either DT (**B**), or a physiological ETC comprising FDX1, FDXR and NADPH (**C**). Reactions in presence of FDXR and NADPH but lacking FDX1 (**D**) served as negative control. Peaks are normalized to a relative abundance (RA) of 100. Retention time (RT), mass area (MA) and normalization level (NL) of the respective peaks are given inside the chromatograms. **E)** Quantitation of 6-thiooctanoyl and lipoyl yields as determined from ion traces of reactions shown in **B-D**. **F)** Mass area of HPLC-MS peaks corresponding to the 6-thiooctanoyl and lipoyl peptide from 150 min lipoylation reactions including 0.1 mM octanoyl peptide, 7 μ M FDX1, 1 μ M FDXR, 10 mM NADPH, 1 mM SAM and 100 μ M of either IMAC purified or reconstituted LIAS. Error bars indicate the SEM ($n \geq 2$). n.d., not detected.

Does LIAS also function enzymatically without prior reconstitution? To address this question, the lipoylation activity of reconstituted LIAS was compared to that of the non-reconstituted, IMAC-purified protein. Comparing the integrated mass areas of 6-thiooctanoyl and lipoyl ion traces, reconstitution of LIAS increased the yields 2.8- and 7.7-fold, respectively (Figure 28F). This shows reconstitution of LIAS to be beneficial for enzymatic functionality. The 6-thiooctanoyl to lipoyl ratio was 16.8 for as-purified and 6.2 for reconstituted LIAS, indicating the second sulfur insertion being considerably slower in non-reconstituted samples. It is possible that a portion of the as-purified LIAS might exhibit a partially degraded auxiliary cluster that can still provide one but not two sulfur atoms for lipoylation.

4.2.2 Optimisation of lipoylation reaction conditions

Achieving efficient turnover *in vitro* with radical SAM enzymes has often times been challenging (Booker *et al.*, 2007; Frey *et al.*, 2008; Lanz *et al.*, 2014). In order to establish a reliable biochemical assay for quantification of lipoyl formation by human LIAS, various reaction parameters were altered to find optimal conditions. Varying amounts of peptide substrate, SAM, FDXR and FDX1 were tested as well as a change of the reaction buffer (replacing HEPES with Tris) and addition of S-adenosyl homocysteine nucleosidase (SAHN) to cleave SAH, a potential inhibitor of LIAS catalysis. In lipoylation assays with bacterial proteins, SAHN had been added to avoid competitive binding of SAH to lipoyl synthase (Lanz *et al.*, 2014). However, test reactions did not indicate a significant effect of SAHN on the formation of 6-thiooctanoyl or lipoyl peptides (Figure 29A-B). The most pronounced improvement of lipoyl formation was achieved by increasing the peptide substrate and FDX1 concentrations. Based on these findings, subsequent assays were performed using a higher amount (0.5 mM) of the octanoyl peptide substrate. In addition, LIAS was purified with improved cooling throughout IMAC and an overall reduced processing time. Reconstituted protein from this batch was employed in follow-up experiments.

The effect of increasing the FDX1 concentration on enzyme turnover was addressed in a time-resolved manner. Generally, formation of the intermediate was significantly faster compared to formation of the final product (Figure 29C), as observed in previous experiments (chapter 4.2.1.2) and for bacterial LipA (Lanz *et al.*, 2014). Notably, the 6-thiooctanoyl concentration never exceeded approximately 35 μ M, which is in 1:1 stoichiometry to LIAS. This was also observed in subsequent experiments (see following chapters), supporting the view that the substrate stays bound to LIAS until the fully matured lipoyl moiety is formed. FDX1 concentration had a strong effect on the rate of both intermediate and product formation. Since 6-thiooctanoyl formation is relatively efficient compared to

lipoyl formation, insertion of the second sulfur atom appears to be the rate-limiting step under the *in vitro* conditions. The highest lipoyl yield at 150 min reaction time was reached using 560 μM FDX1. In this case, the generated 16.7 μM lipoyl peptide corresponds to 48% of LIAS concentration (0.48 turnovers). Since no factors for regenerating the auxiliary LIAS cluster were present, only one or two turnovers could theoretically be achieved, depending on whether one auxiliary cluster serves the formation of one or two lipoyl peptides.

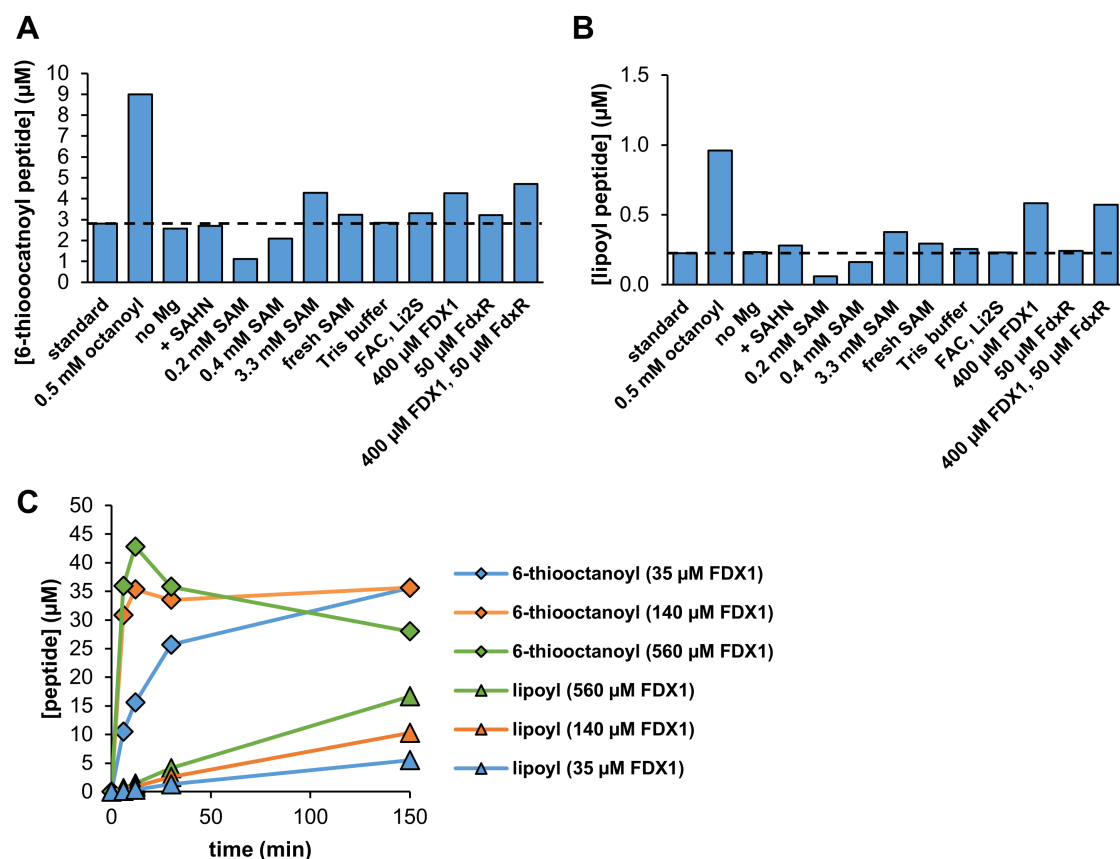


Figure 29: Increasing octanoyl substrate and FDX1 concentrations improves product yields in lipoylation assays. **A-B)** Standard lipoylation reactions included 0.1 mM octanoyl peptide, 2 mM MgCl_2 , 2 mM NADPH, 20 μM FDXR, 140 μM FDX1, 200 μM NFU1, 20 μM LIAS and 1 mM SAM. The reaction composition was altered as indicated, and 6-thiooctanoyl (**A**) and lipoyl (**B**) peptide concentrations were measured after incubation for 150 min. + SAHN: addition of 0.5 μM S-adenosyl homocysteine nucleosidase; fresh SAM: SAM was dissolved directly before the experiment instead of using solution aliquots stored at -80°C ; Tris buffer: 50 mM HEPES pH 7.5 was replaced by 50 mM Tris pH 7.5 as buffer component; FAC, Li₂S: 0.4 mM of each FAC and Li₂S was added to potentially enable *in situ* reconstitution of LIAS. The dashed lines indicate product concentrations of the standard reaction. **C)** Time course of lipoylation reactions including 10 mM MgCl_2 , 2 mM NADPH, 1 mM SAM, 0.5 mM octanoyl peptide, 5 μM FDXR, 35 μM LIAS, and the indicated concentrations of FDX1.

The rate of lipoyl formation under the experimental conditions in all likelihood does not match the corresponding rate *in vivo*. However, low rates of product formation have been generally observed for the sulfur-donating radical SAM enzymes biotin and lipoyl synthase *in vitro* (Booker *et al.*, 2007), and are therefore not an isolated problem of the experimental setup in this work. Radical-induced side reactions have been proposed to interfere with the complex reaction mechanism. Even in the well-established bacterial lipoylation assay employing *E. coli* LipA, maximum turnover (~0.8) was only reached at around 60 min (McCarthy & Booker, 2017). Addition of excess NfuA as an Fe/S cluster donor led to up to ~12 turnovers in 150 min. After optimizing concentrations of the individual LIAS assay components in this work, it was therefore addressed whether Fe/S cluster-donating factors could improve lipoylation efficiency.

4.2.3 Investigation of possible factors regenerating the auxiliary Fe/S cluster of LIAS

Since the auxiliary [4Fe-4S] cluster of lipoyl synthases is degraded upon lipoylation, it has to be regenerated to enable the enzyme working in a catalytic fashion. For *E. coli* LipA, the [4Fe-4S] cluster-coordinating NfuA had been identified as a cluster-regenerating donor, thereby enabling multiple turnovers of lipoylation (McCarthy & Booker, 2017; McCarthy *et al.*, 2019). No cluster-regenerating donor has been reported for human LIAS. However, several *in vivo* studies implied NFU1 and BOLA3 as likely candidates (Cameron *et al.*, 2011; Melber *et al.*, 2016; Navarro-Sastre *et al.*, 2011). In this work, human NFU1, coordinating a [4Fe-4S] cluster as a homodimer, and [2Fe-2S]-containing BOLA3-GLRX5 were tested for their ability to regenerate the auxiliary [4Fe-4S] cluster on LIAS. The purified apo-proteins were chemically reconstituted, and the assembly of the respective Fe/S clusters was verified by UV/Vis and CD spectroscopy (Appendix Figure 67). Using DT as electron donor for lipoylation, the presence of N-terminally His-tagged NFU1 increased the lipoyl yield 2.1-fold (Figure 30A). However, when using the physiological electron donor FDX1, His-tagged NFU1 decreased the lipoyl yield by 39% (Figure 30B). To eliminate the possibility of the His-tag to interfere with lipoylation, constructs without His-tag were generated. Since two different cleavage sites of the NFU1 presequence were conceivable, two constructs (NFU1 Δ N44 and NFU1 Δ N58) were cloned. As they exhibited a low pI of 4.31 and 4.21, respectively, the IMAC purification step could be readily replaced by anion exchange chromatography (AEC). Comparing the construct sizes with human HeLa cell extracts by immunoblotting (Appendix Figure 68) indicated NFU1 Δ N58 to be the physiologically relevant construct. However, no significant increase in lipoylation was observed for any NFU1 construct compared to reactions without Fe/S cluster donor (Figure 30B). Similarly, reactions including [2Fe-2S]

cluster-reconstituted BOLA3-GLRX5 did not increase product yield. Kinetic analyses revealed rates of 6-thiooctanoyl and lipoyl formation to be largely independent of the presence of these potential Fe/S cluster donors (Figure 30C-D).

What may explain the increased lipoyl formation with NFU1 observed in reactions employing DT as electron donor (Figure 30A)? A possible scenario might be that the strong reductant DT destroys a portion of Fe/S clusters on LIAS, which could subsequently be reloaded in presence of NFU1. Inactivation of LIAS by DT might also contribute to the decreased lipoyl formation compared to FDX1 reactions (see Figure 28E). Further experiments will be required to elucidate the potential function of NFU1 and other factors as Fe/S cluster donors for LIAS.

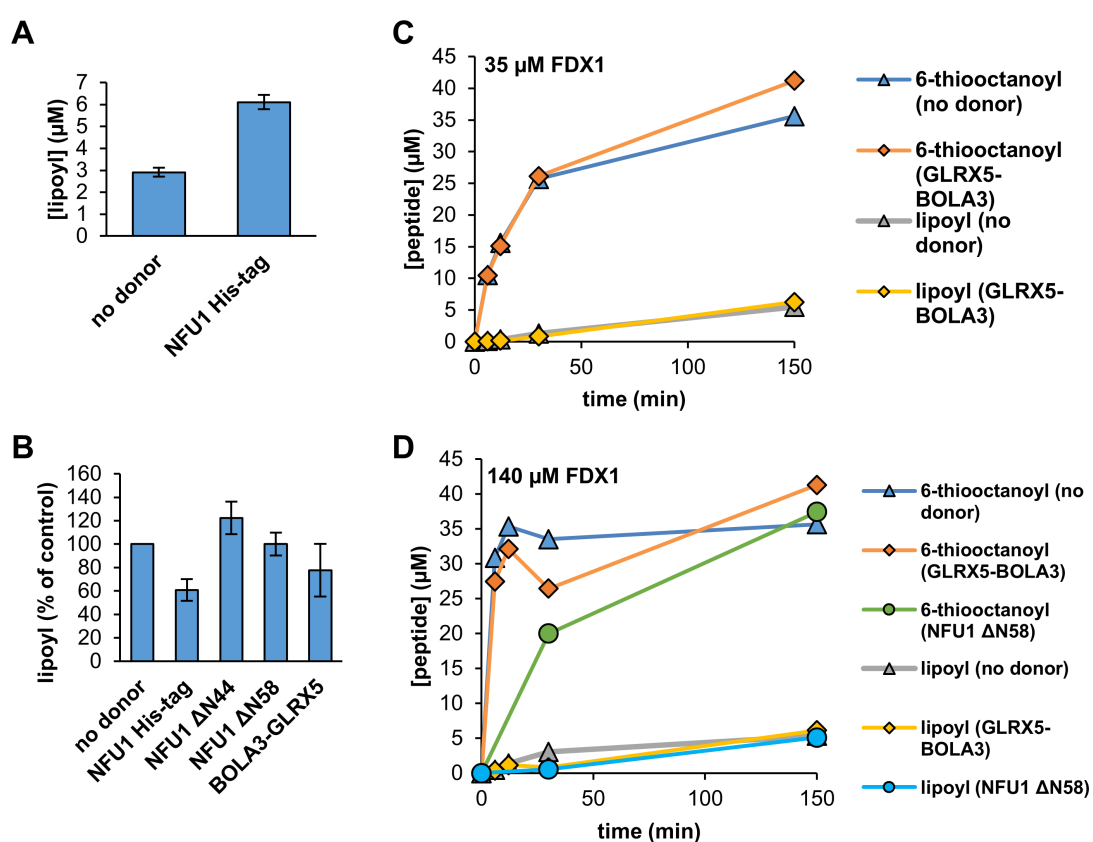


Figure 30: Lipoyl formation in presence of potential Fe/S cluster donors for LIAS. **A)** Lipoyl formation in reactions including 0.1 mM octanoyl peptide, 2 mM MgCl₂, 1 mM SAM, 20 μM LIAS, 2 mM DT and optionally 200 μM His-tagged [4Fe-4S]-NFU1. Error bars indicate the SEM ($n = 4$). **B)** Lipoyl formation in reactions including 0.5 mM octanoyl peptide, 10 mM MgCl₂, 1 mM SAM, 35 μM LIAS, 2 mM NADPH, 20 μM FDXR, 140 μM FDX1 and optionally 200 μM [4Fe-4S]-NFU1 or 100 μM [2Fe-2S]-BOLA3-GLRX5. Lipoyl concentrations are normalised to control reactions lacking an Fe/S cluster donor. Error bars indicate the SEM ($n \geq 2$). **C-D)** 6-thiooctanoyl and lipoyl peptide formation in reactions including 0.5 mM octanoyl peptide, 10 mM MgCl₂, 1 mM SAM, 35 μM LIAS, 2 mM NADPH, 20 μM FDXR and optionally 200 μM [4Fe-4S]-NFU1 ΔN58 or 100 μM [2Fe-2S]-BOLA3-GLRX5. FDX1 was supplied at the indicated concentrations.

4.2.4 FDX1 but not FDX2 is required for lipoylation *in vitro*

As described in chapter 4.2.1.2, initial lipoylation experiments remarkably had shown FDX1 to enable LIAS-mediated product formation. Humans also possess a second FDX, FDX2, which functions in Fe/S protein biogenesis and is therefore required for the formation of the [4F-4S] clusters enabling LIAS catalysis. However, whether FDX2 may additionally function as electron donor for reductive SAM cleavage has not been addressed so far. The function of both human FDXs in lipoylation was compared in a quantitative manner under the conditions developed above. Strikingly, FDX1 reactions generated 29- and 61-fold higher yields of 6-thiooctanoyl intermediate and lipoyl product, respectively, compared to FDX2 (Figure 31). Reactions containing both FDX1 and FDX2 did not lead to a pronounced increase in lipoylation compared to FDX1 alone, therefore a cooperative function of both FDXs in lipoylation seems unlikely. FDX1-enabled product formation was strictly dependent on the presence of LIAS, SAM and FDX1, highlighting the physiological relevance of the experimental setup. As observed before (compare Figure 28E), 6-thiooctanoyl and lipoyl yield were approximately 2-fold higher in FDX1 reactions compared to reactions with the artificial electron donor DT. Generally, reactions with FDX1 yielded more reproducible results compared to DT, possibly since DT might not be stable in solution over time and also due to its strong reductive power which might damage the Fe/S clusters of LIAS or lead to side reactions interfering with product formation. In conclusion, the experiment provides strong evidence for exclusively FDX1 delivering electrons to the catalytic Fe/S cluster of LIAS, thereby enabling reductive cleavage of SAM and initiating the radical-based reaction mechanism.

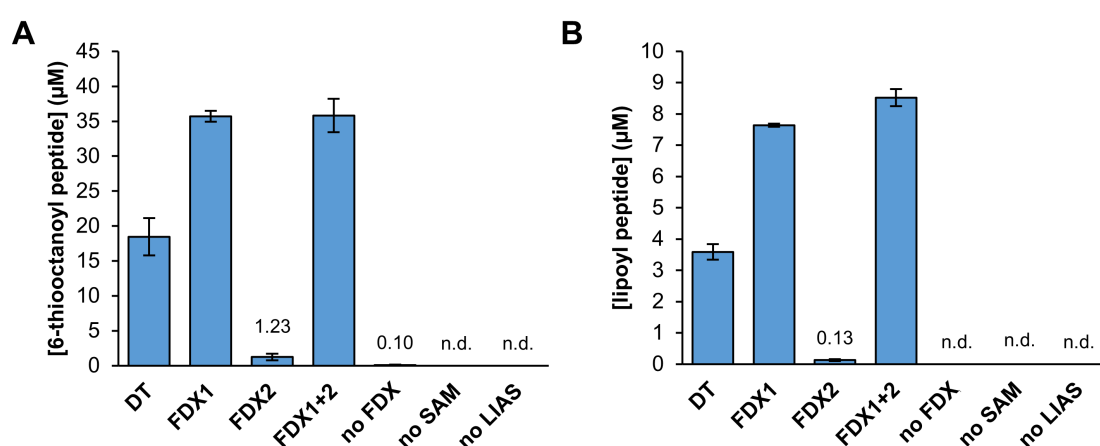


Figure 31: FDX1 but not FDX2 enables efficient products formation by LIAS *in vitro*. Formation of the 6-thiooctanoyl (**A**) and lipoyl (**B**) peptides by LIAS from an octanoyl substrate. Samples included 0.5 mM peptide substrate, 35 μM LIAS, 2 mM NADPH, 20 μM FDXR, 1 mM SAM, plus 140 μM FDX1 and/or FDX2 as indicated. DT samples included 2 mM DT and did not contain NADPH, FDXR, and FDX1. In control reactions, either FDX, SAM, or LIAS were omitted. Error bars indicate the SEM ($n \geq 3$). n.d., not detected.

4.2.5 C-terminal truncation of FDX2 enables lipoylation

FDX1 but not FDX2 enabled lipoylation despite both proteins exhibiting highly similar 3D folds, as evident from their crystal structures (Figure 12). Hence, the molecular reason(s) for the different specificities of the FDXs were aimed to be identified. Characterising the discriminating features of redox partner binding is often challenging, as electron transfer typically depends on a multitude of factors including redox potential, electrostatic interactions as well as 3D structure and specific intermolecular interactions. Electrostatic interactions are known to be crucial for formation of electron transfer complexes (Chiliza *et al.*, 2020; Xu *et al.*, 2008). Comparison of the electrostatic surface potential revealed FDX1 to be much more negatively charged than FDX2 in an area surrounding the [2Fe-2S] cluster binding site, including helix F, which is known to participate in protein partner recognition (Figure 32A, Appendix Figure 69) (Coghlan & Vickery, 1991; Muller *et al.*, 2001; Strushkevich *et al.*, 2011). The replacements of Asp91^{FDX1} by His95^{FDX2} and Glu133^{FDX1} by Arg135^{FDX2} likely contribute to the changed surface potential at the redox-active site.

In a previous work, several interconversion variants replacing residues/regions of FDX2 (Figure 32B) with the corresponding residues from CYP11B1 partner FDX1 had been tested for their ability to implement CYP11B1-dependent cortisol formation activity in FDX2 (Webert, 2011). In the mutant protein FDX2 R135E a 35-fold increased cortisol formation compared to FDX2 WT was observed (Figure 32C), indicating that the corresponding Glu133^{FDX1} residue conserved in FDX1-type FDXs is important for interaction with CYP11B1. In comparison, FDX2 variants M3, M5 and Δ C12 led to minor increases of cortisol levels. M3 represents exchange of a His95-containing motif in FDX2 helix C with the corresponding FDX1 sequence, which includes Asp91 conserved in FDX1-type FDXs. M5 refers to the introduction of a Phe-Gly sequence only found in FDX1-type FDXs into FDX2, and variant Δ C12 exhibits a truncation of the FDX2 C-terminus conserved only in FDX2-type FDXs (Webert, 2011).

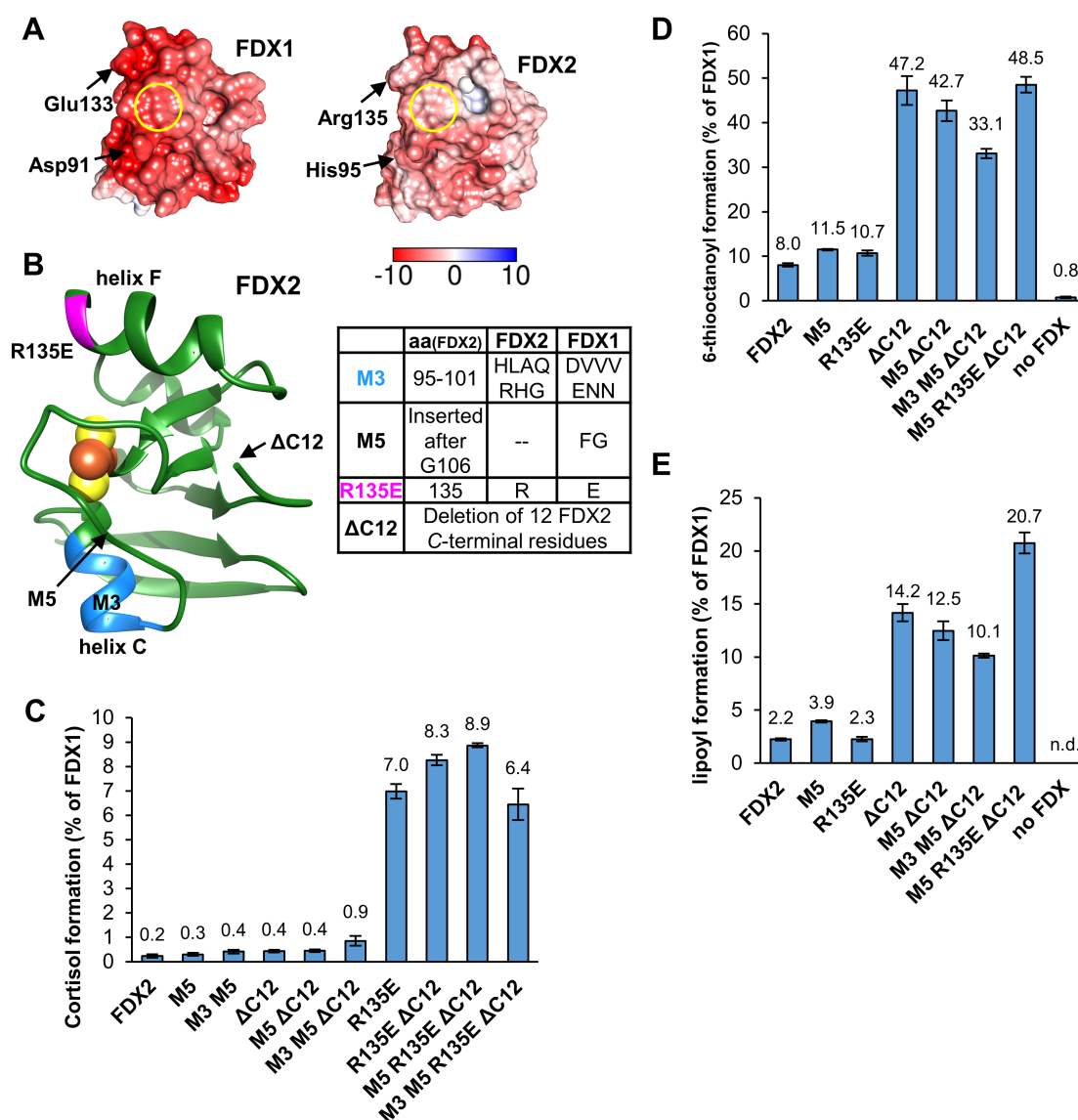


Figure 32: Removal of the FDX2 C-terminus largely increases catalytic function in lipoylation. A) Electrostatic surface potential calculated by the APBS server (<https://server.poissonboltzmann.org>) mapped to human FDX surfaces. The Fe/S cluster binding site is viewed from top and marked by yellow circles. Negative charges are indicated in red, positive charges in blue. The color bar covers the range from -10 kT/e to +10 kT/e. **B)** The ribbon model of the crystal structure of FDX2 (pdb code: 2Y5C, residues: 69 – 174) highlights the regions of FDX2 (see Table on the right) that were exchanged for the corresponding FDX1 sequence. The site of deletion in variant ΔC12 is marked by an arrow because the C-terminus is not resolved in the crystal structure. **C)** Cortisol formation by different FDX2 variants depicted in (B) after 10 min reaction time at 37°C. Reproduced from Webert, 2011 for comparison. Reactions included 11-deoxycortisol, human CYP11B1 and an ETC composed of NADPH, FDXR and FDX. NADPH was regenerated *in situ* using glucose-6-phosphate (G6P) and G6P dehydrogenase. Cortisol content was quantified by HPLC and normalized to FDX1 reactions. Error bars indicate the SEM ($n \geq 2$). **D-E)** The formation of 6-thiooctanoyl (D) and lipoyl (E) by LIAS in presence of FDX2 WT and variants depicted in (B). Reactions included 0.5 mM peptide substrate, 35 μM LIAS, 2 mM NADPH, 20 μM FDXR, 140 μM FDX and 1 mM SAM. Values are normalized to FDX1 reactions. Error bars indicate the SEM ($n = 3$). n.d., not detected.

In this work, the same FDX2 variants were subjected to the lipoylation assay. Remarkably, FDX2 R135E did not lead to a significant improvement of the LIAS products compared to FDX2 WT (Figure 32D-E). Of the various mutant proteins tested, the C-terminally truncated FDX2 Δ C12 variants (with or without additional exchanges) showed the strongest activity increase. FDX2 Δ C12 enabled 47% 6-thiooctanoyl and 14% lipoyl formation compared to FDX1, equivalent to a 6.5-fold increase over FDX2-catalyzed levels. Highest lipoyl formation was achieved with FDX2 M5 R135E Δ C12, yielding 21% of FDX1-catalyzed levels, corresponding to a 9.4-fold increase relative to FDX2 WT. The results indicate the C-terminus of FDX2 to negatively interfere with LIAS interaction, yet no other residue or region of FDX1 essential for LIAS interaction could be identified. Since the conserved FDX2 C-terminus has been suggested to be essential for Fe/S cluster biogenesis (Webert, 2011), it might be important for establishing specificity of FDX2. Interestingly, the regions of FDX1 with importance for cytochrome P450-dependent cortisol or LIAS-dependent lipoyl formation differ, raising the possibility that the FDX1 interaction modes with the two proteins are not identical.

To gain more insight into the interaction of FDX1 and LIAS on a molecular level, anaerobic crystallization of reconstituted LIAS alone and in complex with FDX1 was attempted. Unfortunately, no crystals diffracting to a resolution sufficient for structure modelling could be obtained.

4.2.6 Investigation of inhibitory effects of elesclomol and copper on FDXs and lipoyl synthesis

The small molecule elesclomol (Ele) has been tested as chemotherapeutic agent in clinical trials and proposed as an agent for the treatment of Menkes disease (Guthrie *et al.*, 2020). Ele forms a stable 1:1 complex with Cu(II) or Cu(I) (Ele:Cu) and has been shown to act as a mitochondria-targeting Cu ionophore (Hasinoff *et al.*, 2014; Kirshner *et al.*, 2008; Nagai *et al.*, 2012; Vo *et al.*, 2014; Yadav *et al.*, 2013). Tsvetkov *et al.* identified FDX1 as the only target of Ele-mediated toxicity based on whole genome CRISPR-Cas9 deletion screens (Tsvetkov *et al.*, 2019). However, the authors proposed Ele to induce a toxic gain of function of FDX1 in Fe/S protein biogenesis based on a most likely not physiologically relevant *in vitro* setup: Enzymatic reconstitution of a [2Fe-2S] cluster on ISCU2 was followed in presence of FDX1 and Ele. As discussed in chapter 1.5.1, several studies have reported that the reconstitution reaction requires FDX2 but not FDX1 both *in vivo* and *in vitro* (Appendix Figure 48) (Sheftel *et al.*, 2010; Webert, 2011; Webert *et al.*, 2014). This could be confirmed by the first concentration-dependent investigation of FDX1 and FDX2 function in enzymatic [2Fe-2S] reconstitutions *in vitro* (Figure 33). [2Fe-2S] cluster formation strictly depended on FDX2, whereas addition of FDX1 to up to 5 eq.

over NIA did not enable cluster synthesis. Hence, the reported toxic effect of Ele on FDX1 function is most likely not affecting Fe/S protein biogenesis.

Recently and in contrast to their previous publication, Tsvetkov *et al.* reported Ele not only targeting FDX1 *in vivo*, but also components of the lipoylation pathway, including LIAS. Ele was furthermore shown to interfere with protein lipoylation *in vivo* (Schulz *et al.*, submitted manuscript; Tsvetkov *et al.*, 2022). The *in vitro* lipoylation assay developed in this work provided a suitable tool to directly assess whether this observation is related to impaired LIAS catalysis. It was addressed whether Ele or Cu alone (chapter 4.2.6.1), or the Ele:Cu complex (chapter 4.2.6.2) may confer toxicity.

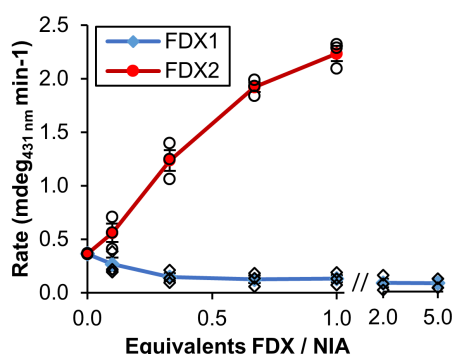


Figure 33: FDX2 but not FDX1 enables [2Fe-2S] cluster formation on ISCU2 *in vitro*. Enzymatic [2Fe-2S] cluster reconstitution on ISCU2 upon titration of FDX1 or FDX2 was monitored by CD spectroscopy (cf. Figure 21). Initial reaction rates were determined by linear fitting. Error bars indicate the SEM ($n = 3$ except 5 eq. FDX1 reactions: $n = 2$).

4.2.6.1 Cu but not Ele inhibits lipoylation *in vitro*

To assess a possible inhibition of lipoyl synthesis by Ele or Cu in a cell-free and hence less complex context as compared to *in vivo* conditions, the lipoylation assay described above was employed. CuCl₂ or Ele were titrated in reactions containing FDX1 as an electron donor, and reactions were quenched at different time points. Since Ele had to be dissolved in DMSO, control reactions containing up to 4% v/v DMSO were performed, yet did not affect formation of the LIAS products (Figure 34). Cu abrogated 6-thiooctanoyl and lipoyl formation at 2 mM concentration, corresponding to a 14- and 58-fold excess over FDX1 and LIAS, respectively. Loss of the reddish colour of the reaction mixture indicated Cu-mediated disruption of Fe/S clusters (addressed in detail in chapter 4.2.6.3). In contrast, Ele did not interfere with lipoylation at any time point and up to the highest tested concentration of 4 mM, which corresponds to a 28- and 114-fold excess over FDX1 and LIAS, respectively. In contrast to a previous report (Tsvetkov *et al.*, 2019),

the results support that Ele alone does not interfere with FDX1 function, whereas Cu constitutes an inhibitor of lipoylation.

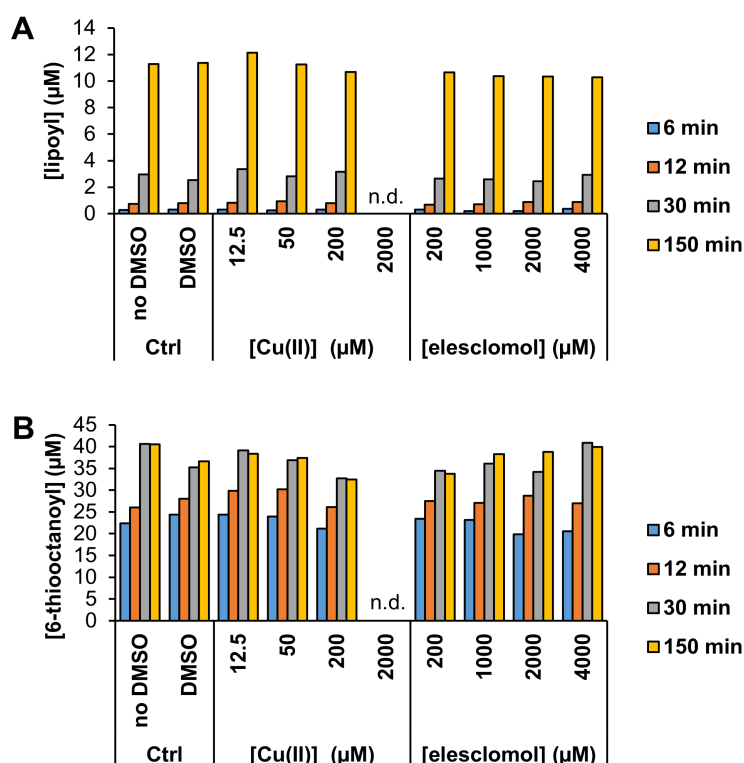


Figure 34: Cu but not Ele inhibits lipoyl synthesis *in vitro*. Formation of 6-thiooctanoyl (A) and lipoyl (B) peptide by LIAS from an octanoyl substrate. Samples included 0.5 mM peptide substrate, 1 mM SAM, 35 μM LIAS, 2 mM NADPH, 20 μM FDXR, 140 μM FDX1 and optionally CuCl₂ or Ele as indicated. Reactions contained 1% v/v DMSO, except controls lacking DMSO (no DMSO), 2 mM Ele reactions (2% v/v), 4 mM Ele reactions (4% v/v) and DMSO controls (4% v/v). n.d., not detected.

4.2.6.2 The Ele:Cu complex inhibits lipoylation *in vitro*

Next, the question was raised whether an Ele:Cu complex would interfere with lipoylation. In lipoylation reactions, Ele:Cu was titrated in an 1.5:1 ratio and incubated for at least 5 min before the addition of proteins, to ensure that all Cu in solution was chelated by Ele. Furthermore, a titration of Cu in presence of 1 mM Ele was done for comparison with the Cu only titration. As observed before, Ele alone did not affect formation of LIAS products (Figure 35A-B). This is in accordance with a wealth of data indicating that Ele can only impart its toxic effect in presence of Cu or other metals (Hasinoff *et al.*, 2014; Modica-Napolitano *et al.*, 2019; Nagai *et al.*, 2012). Cu alone severely affected lipoyl formation in a dose-dependent manner, whereas 6-thiooctanoyl formation showed a less pronounced decrease in comparison. Titrating Ele:Cu at a 1.5:1 ratio also inhibited lipoylation, albeit slightly less pronounced than with Cu only. A similar effect could be ob-

served when titrating Cu to reactions containing 1 mM Ele. It appeared that Ele:Cu complex formation attenuated Cu inhibition of lipoylation. The stability constant $K_{\text{Ele:Cu(II)}} = 10^{24.2}$ L/mol determines Ele:Cu to be highly stable (Yadav *et al.*, 2013). The virtually quantitative formation of the Ele:Cu complex may indicate both Cu and Ele:Cu to inhibit lipoyl formation, yet Cu alone being the more potent inhibitor. A similar behaviour had been observed for the superoxide dismutase activity in presence of Cu versus Ele:Cu (Hasinoff *et al.*, 2014). Alternatively or in addition, Cu might be released from the stable Ele:Cu complex through associative replacement, which might allow for Cu-mediated inhibition, even if the Ele:Cu complex itself is not inhibiting (Yadav *et al.*, 2013).

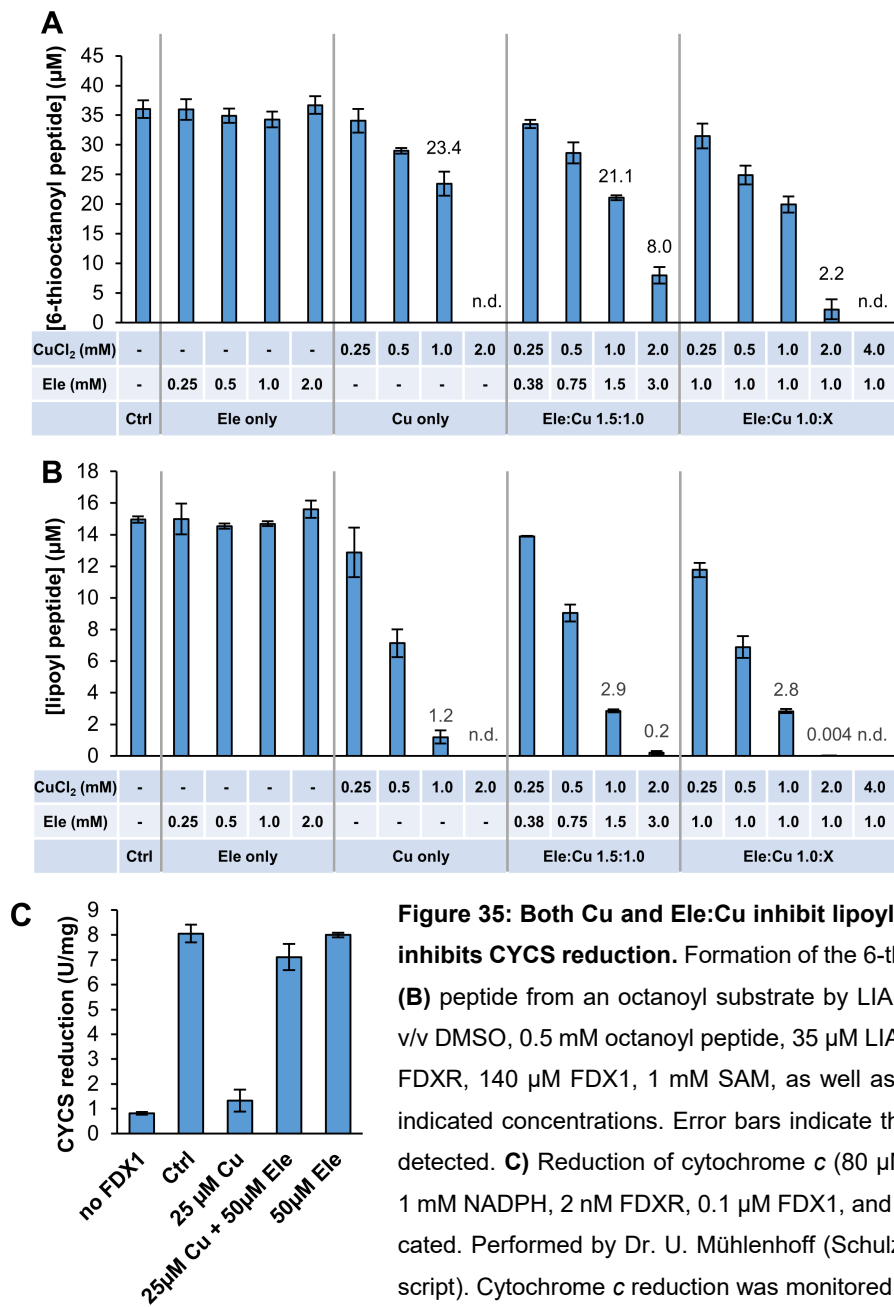


Figure 35: Both Cu and Ele:Cu inhibit lipoyl synthesis, but only Cu inhibits CYCS reduction. Formation of the 6-thiooctanoyl (A) and lipoyl (B) peptide from an octanoyl substrate by LIAS. Samples included 2% v/v DMSO, 0.5 mM octanoyl peptide, 35 μM LIAS, 2 mM NADPH, 20 μM FDXR, 140 μM FDX1, 1 mM SAM, as well as CuCl₂ and/or Ele at the indicated concentrations. Error bars indicate the SEM ($n = 2$). n.d., not detected. C) Reduction of cytochrome *c* (80 μM) in samples containing 1 mM NADPH, 2 nM FDXR, 0.1 μM FDX1, and CuCl₂ and/or Ele as indicated. Performed by Dr. U. Mühlenhoff (Schulz *et al.*, submitted manuscript). Cytochrome *c* reduction was monitored at 550 nm for 60 s. Error bars indicate the SEM ($n \geq 3$ except for 50 μM Ele reactions: $n = 2$).

To address the effect of Ele/Cu specifically on FDX1 function, FDX1-dependent cytochrome *c* (CYCS) reduction was analysed. The assay employed an ETC consisting of NADPH, FDXR and FDX1, monitoring NADPH consumption. Robust activity in presence of FDX1 was almost completely abolished upon addition of a 250-fold excess of Cu over FDX1, in line with the inhibitory effect of Cu seen for lipoyl synthesis (Figure 35C). Addition of a 2-fold excess of Ele over Cu almost completely recovered CYCS reduction. The results suggest that Cu, but not Ele or Ele:Cu, interferes with FDX1 function. Regarding Ele:Cu, this is in contrast to lipoyl formation, where a 14- and 57-fold excess of Ele:Cu over FDX1 and LIAS, respectively, led to almost complete abrogation of lipoyl synthesis (Figure 35B). It is tempting to speculate that Ele:Cu may be specifically inhibiting LIAS.

4.2.6.3 Chelation of Cu by Ele protects Fe/S clusters from destruction

Experiments in the previous chapters showed that both Cu and Ele:Cu inhibit lipoyl formation. However, the underlying mechanism(s) of Cu and Ele:Cu-mediated inhibition were not entirely clear. In living organisms, Cu-mediated disruption of Fe/S clusters, in particular of solvent-accessible [4Fe-4S] clusters, has been reported as the main cause of Cu toxicity (Solioz, 2018). Hence, the effect of Cu and Ele:Cu on the Fe/S cluster integrity of human FDXs and LIAS was investigated by CD spectroscopy.

140 μM FDX1 (equivalent to the concentration in lipoylation assays) was titrated with CuCl_2 under anaerobic conditions, and spectra were recorded after 2 min incubation. Cu addition led to a concentration-dependent decrease of the CD signal, suggesting degradation of the [2Fe-2S] cluster (Figure 36A). The spectrum recorded in presence of 250 μM CuCl_2 remained stable for at least 30 min (Appendix Figure 70), indicating that the observed Cu-induced Fe/S cluster degradation occurred quickly, and the equilibrium was reached before the start of each CD measurement. In contrast, titration of up to 10.7 eq. Ele had no effect on the FDX1 CD spectrum. Importantly, the presence of Ele even prevented Fe/S cluster degradation (Figure 36B). Whereas 750 μM Cu led to complete destruction of the FDX1 Fe/S cluster, almost no effect was observed in presence of additional 1.5 mM Ele, most likely due to chelation of Cu by Ele, forming a stable 1:1 complex (Vo *et al.*, 2014). FDX2 titrations showed a similar Cu-dependent Fe/S cluster disruption that could be completely prevented by Ele addition (Figure 36C-D). In the absence of Ele, a lower concentration of Cu (500 μM) sufficed for complete Fe/S cluster destruction, indicating FDX2 to be slightly more susceptible to Cu-induced disruption than FDX1. Similarly, Cu titration in the CYCS reduction assay showed FDX2 to be slightly more sensitive to inhibition (Figure 36H).

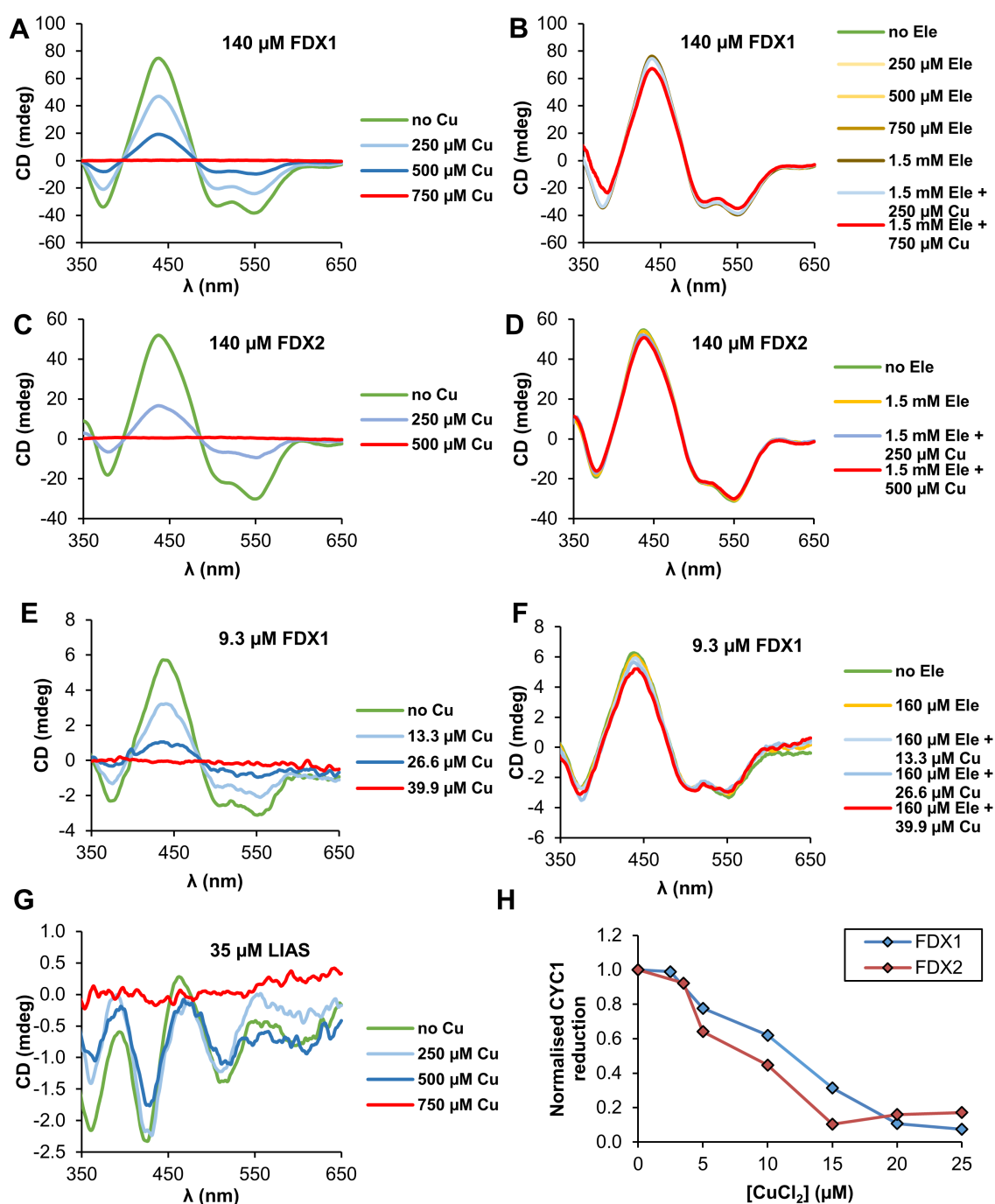


Figure 36: FDXs are more sensitive to Cu-mediated Fe/S cluster disruption than LIAS, and cluster disruption is prevented by Ele. **A-G)** Samples containing FDX1, FDX2 or LIAS were titrated under anaerobic conditions with increasing concentrations of CuCl_2 and/or Ele, as indicated. CD spectra of the Fe/S proteins were recorded after each titration step. Excess of Ele prevented Fe/S cluster destruction on FDX1 and 2, likely by formation of the highly stable Ele:Cu complex. Due to the weak CD signal of holo-LIAS and the high absorption of Ele, Ele titrations in presence of LIAS did not yield interpretable data. **H)** Reduction of cytochrome c (80 μM) in samples containing 1 mM NADPH, 2 nM FDXR, 0.1 μM FDX, and CuCl_2 as indicated. Performed by Dr. U. Mühlenhoff. Reduction was monitored at 550 nm for 60 s and normalised to reactions lacking CuCl_2 .

The Cu concentrations needed for inhibition of CYCS reduction were much lower than those inhibiting lipoyl synthesis (Figure 35A-B) and for destroying [2Fe-2S] clusters of FDXs (Figure 36A-D). However, it was observed that a lower FDX1 concentration (9.3 vs. 140 μ M) also required lower Cu amounts for Fe/S cluster destruction, which again could be prevented by Ele supplementation (Figure 36E-F). For 140 μ M FDX1, a 50% decrease of the CD signal at 439 nm needed approximately 2.4 eq. Cu, whereas 1.7 eq. were required for 9.3 μ M FDX1. Hence, the ratio of Cu to FDX seems to be more decisive for Fe/S cluster stability than the absolute concentration of Cu. This finding may be of importance regarding the relevance of these experiments to the physiological situation, since the employed protein and Cu concentrations by far surpass those present in human cells (Linder, 1991).

Upon titration of LIAS with Cu, a high excess of Cu could be applied before the LIAS clusters were completely destroyed (Figure 36G, 21.4 eq. for LIAS compared to up to 5.4 eq. for FDXs), indicating at least one of the two [4Fe-4S] clusters being relatively stable. However, at the concentrations of FDX1 and LIAS employed in the lipoylation assay (140 and 35 μ M, respectively), both proteins Fe/S clusters are completely disrupted at 750 μ M Cu. This suggests that both proteins are affected by Cu-mediated Fe/S cluster disruption upon Cu titration in the lipoylation assay (Figure 35A-B). The higher total protein concentration and an additional 0.5 mM peptide substrate in lipoylation reactions leading to a decreased concentration of free Cu likely explain why product formation is completely abrogated only at concentrations slightly higher than 750 μ M Cu.

Altogether, the data from Ele/Cu titrations in lipoylation, CYCS reduction and Fe/S cluster stability experiments indicate Cu alone but not Ele to exert a toxic effect on Fe/S proteins which is not limited to FDX1. This is in line with Cu sensitivity being observed for a multitude of Fe/S enzymes (Bulut *et al.*, 2020; Chillappagari *et al.*, 2010; Fung *et al.*, 2013; Macomber & Imlay, 2009; Solioz, 2018). Chelation of toxic Cu by Ele, forming Ele:Cu, prevented both disruption of Fe/S clusters and inhibition of FDX1 function. Hence, the observed inhibition of lipoylation by Ele:Cu may be conferred by a distinct mechanism which remains to be further investigated.

5 Discussion

5.1 *De novo* [2Fe-2S] cluster formation on ISCU2

A major aim of this work was to achieve a molecular understanding of ISCU2 persulfidation in *de novo* [2Fe-2S] cluster biosynthesis. Biochemical, structural and spectroscopic analyses have enabled the detailed characterisation of consecutive stages leading to persulfidation. Decisive progress was made in particular by the characterisation of a persulfide-bound (Fe-NIAUX)₂ complex in a high resolution cryo-EM structure. The implications of these findings regarding the molecular mechanism of physiological ISCU2 persulfidation will be discussed in chapters 5.1.1 to 5.1.4. Studies from this work further enabled identification of specific protein ligands required for the coordination of the mature ISCU2-bound [2Fe-2S] cluster. The biosynthetic steps proceeding persulfide formation will be discussed in chapters 5.1.5 to 5.1.7.

5.1.1 The order of assembly of the (Fe-NIAUX)₂ complex

An important question regarding the mechanism of ISCU2 persulfidation is in which order the required components of the core ISC machinery are assembled under physiological conditions. Structural studies in this and previous works show that in the (NIAUX)₂ complex, the three factors NFS1, ISCU2 and FXN all make contact to each other (Figure 19) (Fox *et al.*, 2019). Pull-down experiments performed with human and yeast proteins have shown FXN to bind a pre-formed (NIAU)₂ complex, but not (NIA)₂ or ISCU2 individually (Manicki *et al.*, 2014; Schmucker *et al.*, 2011). This is in line with dissociation constants reported for the interactions (NIA)₂–ISCU2 (1.7 μ M), (NIA)₂–FXN (26.2 μ M) and (NIAU)₂–FXN (3.0 μ M) (Cai *et al.*, 2018b). The same study also reported FXN and ISCU2 not to interact on their own. aSEC experiments from this work indicate Fe-independent formation of a stable (NIAU)₂ complex which binds FXN sub-stoichiometrically (Appendix Figure 59). NMR studies further support a high affinity of mouse ISCU to (NIA)₂, whereas FXN shows medium affinity to a pre-formed (NIAU)₂ complex (Gervason *et al.*, 2019). Overall, this suggests an assembly in the order (NIA)₂, (NIAU)₂ and then (NIAUX)₂.

At which point does Fe(II) enter the biosynthetic complex? Experiments in this work showed ISCU2 persulfidation to be metal-dependent, and furthermore verified Fe(II) but not Zn(II) being required for physiologically relevant Fe/S cluster assembly (chapter 4.1.3). The results are in agreement with similar studies performed with mouse ISCU (Gervason *et al.*, 2019). Spectroscopic studies show free ISCU2 to readily bind Fe(II) at its assembly site (chapters 4.1.2 and 4.1.7) (Gervason *et al.*, 2019). Hence, ISCU2 preloaded with Fe(II) may enter the (NIA)₂ complex. However, cryo-EM structures

of (Fe-NIAUX)₂ obtained in this work exhibit Fe bound at the ISCU2 assembly site, even though Fe was (for technical reasons) added after formation of the (NIAUX)₂ complex. This result indicates that Fe can also enter ISCU2 after (NIAUX)₂ formation and is in line with the ISCU2 assembly site being solvent accessible in (NIAU)₂ and (NIAUX)₂. A strongly negatively charged region of FXN has previously been proposed to potentially facilitate Fe-delivery to the ISCU2 site (Stemmler *et al.*, 2010). Cryo-EM structures of (NIAUX)₂ (Figure 19) (Fox *et al.*, 2019) do not support this hypothesis, as they consistently show the negatively charged FXN region located distal from the ISCU2 Fe binding site. Overall, it appears that ISCU2 can in principle coordinate Fe both before and after binding to (NIA)₂. However, different affinities of Fe(II) to ISCU2, (NIAU)₂ and (NIAUX)₂ may dictate at which point Fe enters the reaction cycle. An interesting yet unresolved question is how Zn coordination is avoided, since this metal interferes with Fe/S cluster synthesis (Figure 55) (Gervason *et al.*, 2019).

5.1.2 Fe coordination by ISCU2 at different stages of [2Fe-2S] cluster formation

5.1.2.1 Free ISCU2 coordinates Fe via residues Cys69, Asp71, Cys95 and His137

CD spectroscopy of ISCU2 variants anaerobically reconstituted with 2 eq. Fe(II) showed Cys69, Asp71 and Cys95 but not Cys138 to be essential for Fe ligation (chapter 4.1.2). The H137A variant led to a diminished signal with altered spectral features, indicating that His137 may be part of the native coordination sphere but not strictly essential *in vitro*. Another study published during the time of this work reported overall similar results upon reconstitution of mutant mouse ISCU proteins with 1 eq. Fe(II) (Gervason *et al.*, 2019). The CD signal in presence of mouse ISCU H137A was almost completely abolished, indicating a low affinity of the variant to Fe(II). The study further reported that as-purified ISCU WT and C138S but not the variants C69S, D71A, C95A and H137A bound Zn. In addition, an NMR solution structure of mouse ISCU, structurally conserved to human ISCU2, shows tetrahedral Zn coordination by Cys69, Asp71, Cys95 and His137 (to be published, pdb code: 1WFZ). Analyses of human and mouse Fe-ISCU by zero-field Mössbauer spectroscopy (chapter 4.1.7) (Gervason *et al.*, 2019) yielded similar results, suggesting Fe(II) being bound by four ligands, thereof 1 – 2 Cys residues and 2 – 3 N/O ligands. The high concentration and purity of Fe-ISCU2 reconstituted in this work enabled its unprecedented analysis by applied-field Mössbauer spectroscopy. Recorded spectra show similarity to those of a previously reported Fe(II) species ligated by two Cys and one His residue and water (Bill *et al.*, 1989). In conclusion, the data strongly support that free ISCU2 tetrahedrally coordinates Fe(II) via its assembly site residues Cys69, Asp71, Cys95 and His137.

5.1.2.2 An equilibrium between distinct Fe coordination states present in the core ISC complex is modulated by FXN binding

Whereas Mössbauer spectroscopy showed only one Fe species being present in free ISCU2, two distinct Fe-ISCU2 species were detected in both the (Fe-NIAU)₂ and (Fe-NIAUX)₂ complexes (Figure 37). The tetrahedral Fe(II) species observed for free ISCU2 also constituted the major fraction of ISCU2-bound Fe (around 71%, species 1) in the (Fe-NIAU)₂ complex, exhibiting almost identical Mössbauer parameters (Table 15). This may indicate Fe coordination by ISCU2 Cys69, Asp71, Cys95 and His137 in (Fe-NIAU)₂. However, the cryo-EM structure of (Fe-NIAU)₂ (in presence of cysteine) showed metal ligation by Cys381^{NFS1} instead of Cys69^{ISCU2} (chapter 4.1.5). A crystal structure of (Zn-NIAU)₂ (obtained in absence of cysteine) showed coordination of Zn via ISCU2 Asp71, Cys95 and His137 as well as NFS1 Cys381 (Boniecki *et al.*, 2017). The replacement of one Cys ligand by another is not detectable by Mössbauer spectroscopy, assuming the coordination geometry remains unchanged. It is therefore conceivable that Cys69^{ISCU2} is replaced by Cys381^{NFS1} upon binding of free ISCU2 to (NIA)₂. Whether Cys69^{ISCU2} is fully replaced, or if an equilibrium between the binding of both Cys residues exists, remains to be investigated.

Mössbauer spectroscopy of (Fe-NIAU)₂ also revealed a second, minor species, constituting approximately 29% of ISCU2-bound Fe. This species 2 is also present in persulfidated and non-persulfidated (Fe-NIAUX)₂ and exhibits ISCU2 Asp71, Cys95 and Cys138 as Fe-ligands (see also chapter 4.1.7). Notably, cryo-EM structures (Figure 19) (Fox *et al.*, 2019) show Asp71 acting as a bidentate ligand via its carboxylate moiety, in contrast to species 1 featuring Asp71 as a monodentate ligand. Mössbauer parameters are in line with an octahedral coordination of Fe(II) in species 2 via 1 – 2 cysteine and 4 – 5 N/O ligands. In support of this, the metal coordination geometry of persulfidated (Fe-NIAUX)₂ can be best fitted with an octahedron, followed by five-fold ligation via a trigonal bipyramid (Figure 38). The former constitutes the most common coordination geometry for Fe(II) (Bauer & Knölker, 2008). The implied octahedral coordination of species 2 would presumably be completed by two water molecules. Water ligands could not be resolved in the 3D structure of persulfidated (Fe-NIAUX)₂.

(Fe-NIAU)₂ exhibits a dynamic equilibrium between two different Fe binding modes, with approximately 71% species 1 and 29% species 2. Binding of FXN increases the proportion of species 2 to 63% (chapter 4.1.7). As FXN was found to bind to the (NIA)₂ complex less stably than ISCU2 (Figure 59), the equilibrium observed in (Fe-NIAUX)₂ samples may reflect the dynamic association and dissociation of FXN. The 37% of species 1 observed in Mössbauer analysis of (Fe-NIAUX) may therefore reflect a portion of the ISC assembly complex lacking FXN. Cryo-EM structures of (M-NIAUX)₂ only exhibit metal

coordination that corresponds to species 2 (Figure 19) (Fox *et al.*, 2019), as particles lacking FXN are not considered for structure solving.

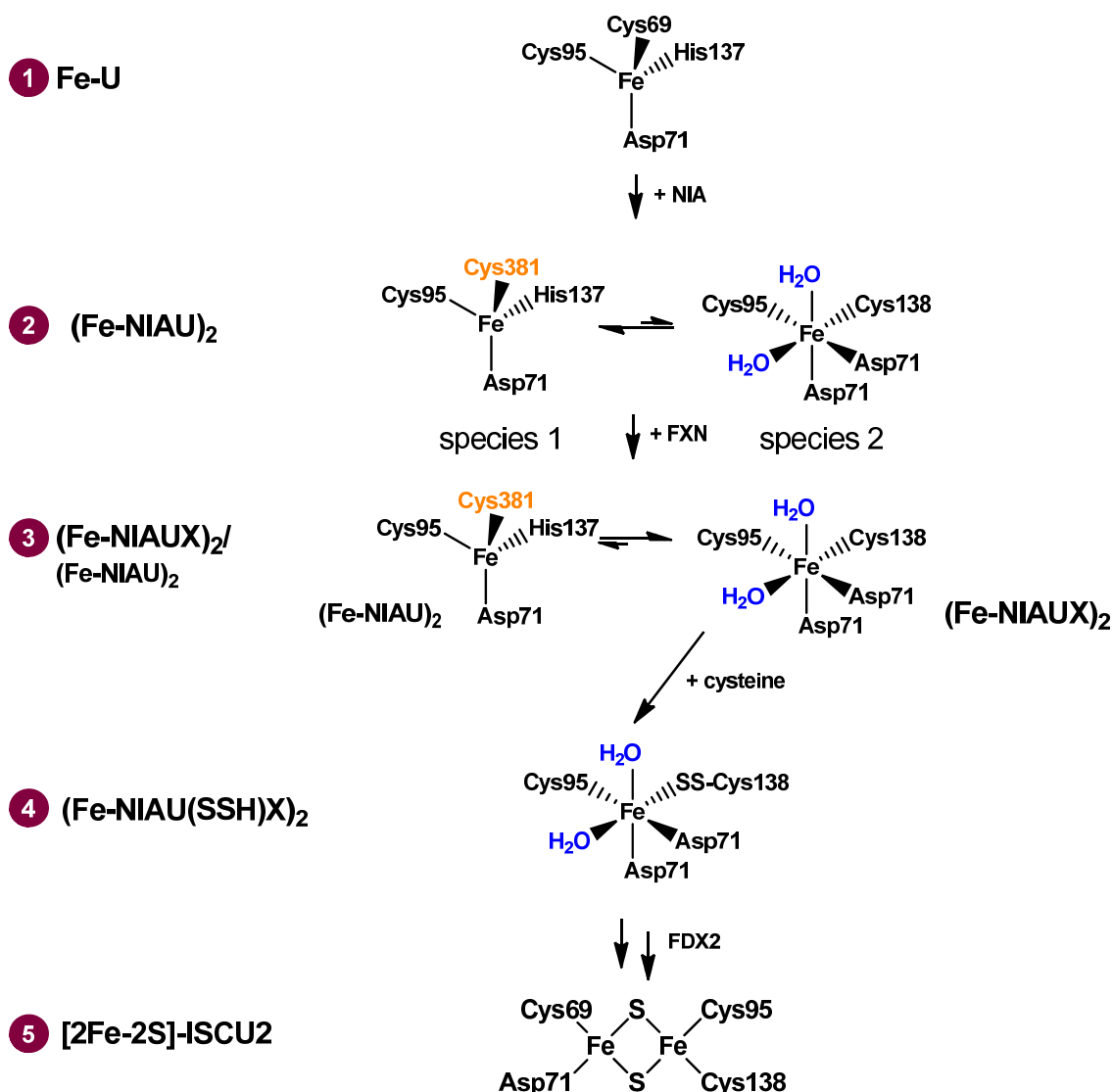


Figure 37: Model of Fe coordination by ISCU2 at consecutive stages of *de novo* [2Fe-2S] cluster biosynthesis. Protein ligands are colored black (ISCU2) and orange (NFS1) and water ligands blue. **1)** Free ISCU2 (U) tetrahedrally coordinates Fe(II) via its residues Cys69, Asp71, Cys95 and His137. **2)** Binding of Fe-ISCU2 to (NIA)₂ induces an equilibrium of two distinct binding modes within the (Fe-NIAU)₂ complex. The preferred state (species 1) is similar to Fe coordination in free ISCU2 (**1**), but Cys69^{ISCU2} is likely replaced by Cys381^{NFS1}. The minor state (species 2) exhibits ISCU2 Asp71, Cys95 and Cys138 as protein Fe-ligands. Asp71 functions as bidentate ligand and the octahedral coordination sphere is completed by water ligands. **3)** Dynamic binding of FXN to (Fe-NIAU)₂ shifts the equilibrium towards species 2. **4)** Persulfidation of ISCU2 in presence of cysteine requires the Asp71, Cys95 and Cys138 coordination mode (species 2) favored in the (Fe-NIAUX)₂ complex. A persulfide is transferred from Cys381^{NFS1} to Cys138^{ISCU2}. Subsequently, Cys138-SSH coordinates Fe(II) via its terminal sulfhydryl moiety. **5)** FDX2-dependent reduction of the persulfide to inorganic sulfide and dimerization of two [1Fe-1S]-bound ISCU2 molecules enables [2Fe-2S] cluster formation (discussed in chapter 5.1.6). The Fe/S cluster is coordinated by Cys69, Cys95, Cys138 and probably Asp71 of one ISCU2 molecule (discussed in chapter 5.1.7).

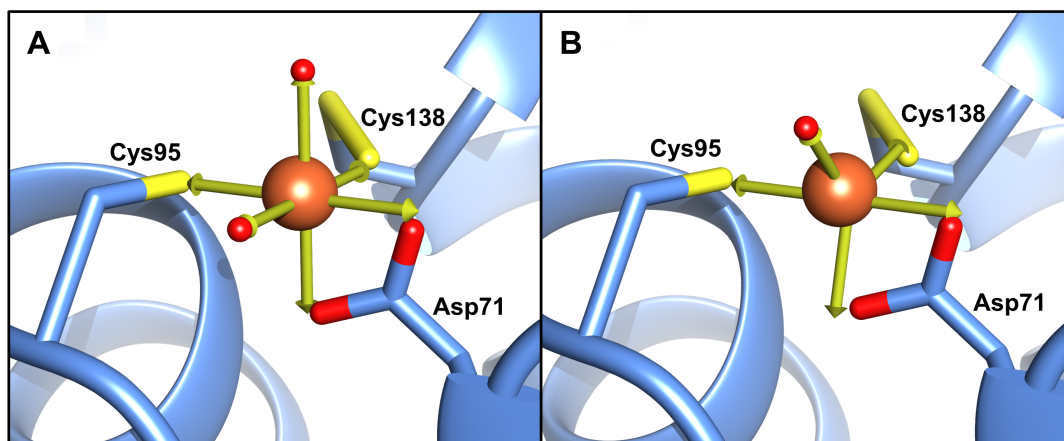


Figure 38: Modelled coordination geometries of Fe in (Fe-NIAU(SSH)X)₂. Idealized Fe coordination geometries at the ISCU2 (blue) assembly site are visualized by yellow arrows and positions of water ligands (small red spheres) were modelled using UCSF Chimera version 1.12. Fe is depicted as an orange sphere. **A)** Fitting of an octahedral metal coordination (UCSF Chimera) yields a root-mean-square deviation (RMSD) of 0.295 Å for the deviation of ISCU2 ligands from idealized ligand positions. **B)** Fitting of trigonal bipyramidal coordination yields an RMSD of 0.303 Å.

Species 2 is most likely stabilized by FXN interaction with ISCU2, leading to removal of Cys69^{ISCU2} and His137^{ISCU2} from the ISCU2 assembly site as supported by cryo-EM (Figure 19) (Fox *et al.*, 2019). Biochemical studies from this work support a specific interaction of Cys69^{ISCU2} with Gln148^{FXN}, most likely via hydrogen bonding (chapter 4.1.7). In contrast, Asn151^{FXN} located in vicinity of Cys69^{ISCU2} (Figure 19) is not important for Fe/S cluster synthesis. *In vitro* experiments further support the insertion of His137^{ISCU2} into a hydrophobic pocket of FXN (formed by residues including Trp155^{FXN} and Arg165^{FXN}) being essential for ISCU2 persulfidation.

Persulfidation of (Fe-NIAUX)₂ further increases the proportion of species 2 from 63% to 88%, as observed by Mössbauer spectroscopy. Cryo-EM of (Fe-NIAUX)₂ in presence of cysteine yielded approximately 75% (Fe-NIAU(SSH)X)₂ particles and 25% (Fe-NIAU)₂ particles. (Fe-NIAU(SSH)X)₂ exhibited Fe coordination as in species 2, with Asp71, Cys95 and the terminal sulfur of Cys138-SSH functioning as ligands. This is well in line with Fe-dependent persulfidation of ISCU2 *in vitro* requiring Asp71, Cys95 and Cys138, but not Cys69 and His137 (chapter 4.1.3). In conclusion, structural, spectroscopic and biochemical data strongly suggest Fe coordination as in species 2 being essential for persulfidation of ISCU2 Cys138.

5.1.3 The molecular mechanism of Fe-dependent persulfidation of ISCU2 Cys138

5.1.3.1 Conformational states of the persulfide-transferring NFS1 Cys381-loop are modulated by its interaction with Fe-ISCU2 and FXN

Conformational rearrangement of the flexible loop harbouring the catalytic residue Cys381^{NFS1} is a prerequisite for sulfur transfer from the NFS1 PLP site to Cys138^{ISCU2}. Crystal structures of metal-free (NIAU)₂ exhibit a partially resolved Cys381^{NFS1}-loop facing either the PLP site of NFS1 (Freibert *et al.*, 2021) or being positioned halfway between the PLP site and the ISCU2 assembly site (Boniecki *et al.*, 2017). In contrast, structures of metal (M)-bound (M-NIAU)₂ exhibit a fully resolved loop ligating the respective ISCU2-bound Fe or Zn ion via Cys381^{NFS1} (Figure 19) (Boniecki *et al.*, 2017). It is tempting to speculate that metal binding by ISCU2 modulates the Cys381^{NFS1}-loop in favour of a “sulfur-donating” conformation, with Cys381^{NFS1} ligating the metal centre. However, this conformation is not observed anymore upon binding of FXN to (NIAU)₂. (Zn-NIAUX)₂ was reported to exhibit the Cys381-loop in an intermediate conformation halfway between the NFS1 PLP site and ISCU2 (Fox *et al.*, 2019). The conformation was proposed to be stabilised by hydrophobic interaction of Trp155^{FXN} with Leu386^{NFS1} and potentially hydrogen bonding between Asn146^{FXN} and Ala384^{NFS1}. In the persulfidated (Fe-NIAUX)₂ complex (Figure 19), the Cys381^{NFS1}-loop could not be resolved as of now, which may reflect dynamic movement of the loop in presence of cysteine. The same result had been obtained in a previous, independent cryo-EM analysis of persulfidated (Fe-NIAUX)₂ (done in collaboration with R. Steinhilper and Dr. B. Murphy, not shown).

In summary, structural studies indicate distinct preferred Cys381^{NFS1}-loop conformations in different metal-bound core ISC complexes. In (M-NIAU)₂, the loop faces ISCU2, Cys381^{NFS1} participating in metal ligation, whereas (M-NIAUX)₂ exhibits an “intermediate” conformation of the loop potentially stabilised by contacts to FXN. In presence of cysteine, (Fe-NIAUX)₂ shows high structural flexibility of the Cys381-loop, which may facilitate efficient sulfur transfer from the NFS1-PLP site via Cys381^{NFS1} to Cys138^{ISCU2}. Overall, structural data suggest binding of Fe-ISCU2, FXN and likely cysteine to (NIA)₂ to modulate Cys381^{NFS1}-loop conformations.

5.1.4 The mechanism of persulfide transfer from NFS1 Cys381 to ISCU2 Cys138

The structural, spectroscopic and biochemical data obtained in this work provide valuable insights regarding the molecular mechanism of persulfide transfer from Cys381^{NFS1} to Cys138^{ISCU2} (Figure 39), as discussed in this chapter. As reasoned in chapter 5.1.1, the (Fe-NIAUX)₂ complex enabling ISCU2 persulfidation is likely assembled in the order (NIA)₂, (Fe-NIAU)₂, (Fe-NIAUX)₂, assuming that ISCU2 enters the complex with pre-

bound Fe. Binding of ISCU2 or FXN to (NIA)₂ is not essential for cysteine-dependent persulfidation of Cys381^{NFS1}, as shown in this work (Figure 18) and in line with earlier studies (Parent *et al.*, 2015; Patra & Barondeau, 2019). Under physiological conditions, (NIA)₂ may hence be persulfidated before binding of partner proteins. Upon binding of Fe-ISCU2, Cys381-SSH^{NFS1} may then participate in Fe coordination (Figure 39, stage 2). This is supported by (M-NIAU)₂ structures showing Cys381^{NFS1} coordinating the ISCU2-bound metal (Figure 19) (Boniecki *et al.*, 2017). Limited resolution of the cryo-EM structure of (Fe-NIAU)₂ in presence of cysteine has so far precluded identification of the Cys381^{NFS1}-bound persulfide.

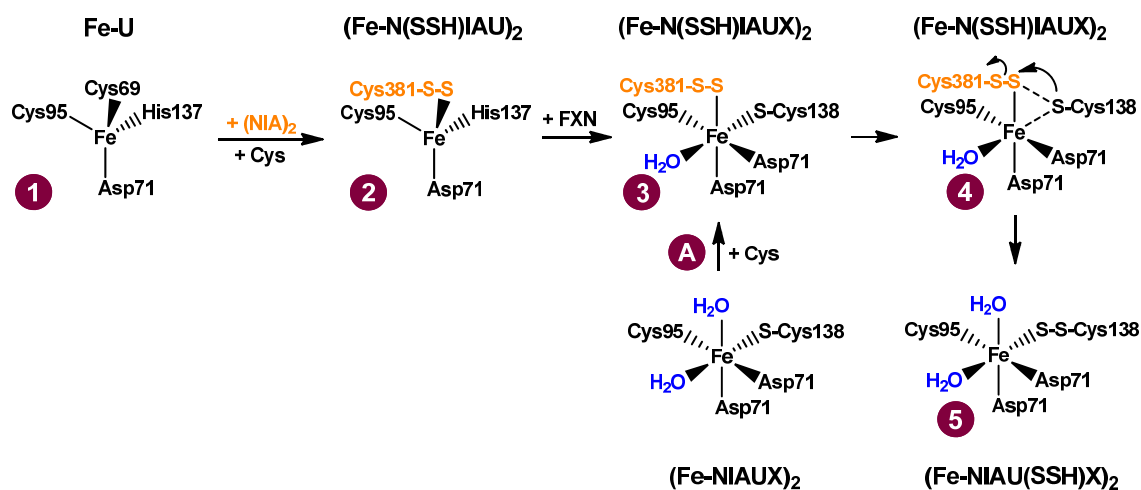


Figure 39: Proposed mechanism(s) of persulfide transfer from Cys381-SSH^{NFS1} to Cys138^{ISCU2}. Protein ligands are colored in black (ISCU2) and orange (NFS1) and water ligands in blue. **1)** ISCU2 (U) tetrahedrally coordinates Fe(II) via four of its assembly site residues. **2)** Cys381^{NFS1} of (NIA)₂ is persulfidated in presence of cysteine (Cys). Upon binding of Fe-U to (NIA)₂, Cys69^{ISCU2} is replaced as Fe-ligand by Cys381-SSH^{NFS1}. **3)** Binding of FXN induces a conformational change at the assembly site, leading to octahedral Fe coordination with Asp71^{ISCU2} acting as bidentate ligand. His137^{ISCU2} is replaced as Fe-ligand by Cys138^{ISCU2}, bringing the Cys138^{ISCU2} sulfur in close proximity (below 4 Å) to the Cys381-SSH^{NFS1} persulfide sulfur. **4)** Donation of electron density of the persulfide sulfur to Fe(II) facilitates nucleophilic attack by the Cys138^{ISCU2} thiol moiety under concomitant weakening of the Cys138-SH^{ISCU2}-coordinative bond to Fe. Cys381^{NFS1} is released from the assembly site, yielding Fe coordinated by Cys138-SSH^{ISCU2} **(5)**. An alternative route to persulfide transfer may occur when the (Fe-NIAUX)₂ complex is formed before persulfidation of (NIA)₂ in presence of cysteine (**Step A**). The octahedral complex would be formed and subsequently one water ligand be replaced by Cys381-SSH^{NFS1} **(3)**.

Direct persulfide transfer to ISCU2 in the absence of FXN with the sulfur atoms of Cys138^{ISCU2} and Cys381^{NFS1} being more than 6 Å apart (Figure 6A) and at opposite sides of the central Fe atom appears unlikely. Binding of FXN was shown to facilitate persulfide transfer (chapter 4.1.3) (Parent *et al.*, 2015) and change the preferred geometry of the metal site from tetrahedral (species 1) to octahedral (species 2) coordination (Figure 37).

Swinging of His137^{ISCU2} away from the assembly site via interaction with FXN provides access for persulfidation of Cys138^{ISCU2}. Furthermore, the change to an octahedral Fe coordination (see chapter 5.1.2.2) could potentially enable Fe ligation of the terminal sulfur of Cys381-SSH^{NFS1} at a distance of around 3.3 Å from the Cys138^{ISCU2} sulfur (Figure 39, stage 2; details in Figure 40). This proximity may be sufficient for direct transfer, considering the S–S bond length of a persulfide of 2.0 Å (Bailey *et al.*, 2014). Donation of electron density from the terminal sulfur of Cys381-SSH^{NFS1} to Fe may activate the persulfide for nucleophilic attack by cysteine.

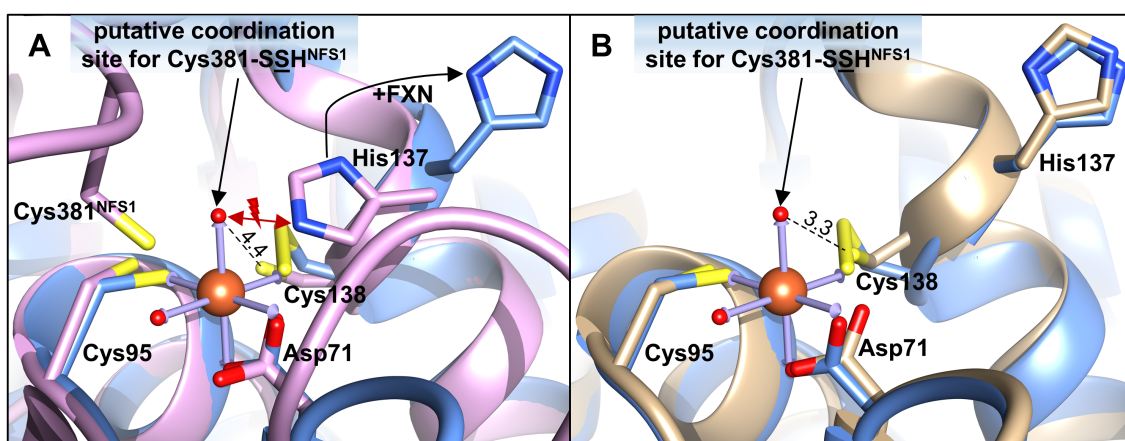


Figure 40: Fe coordination by the terminal sulfur of Cys381-SSH^{NFS1} in persulfidated (Fe-N(SSH)IAUX)₂ may facilitate direct persulfide transfer to Cys138^{ISCU2}. The region of Fe coordination in persulfidated (Fe-NIAU(SSH)X)₂ (blue) is overlaid with corresponding regions of structures of (Zn-NIAU)₂ (**A**, pdb code: 5WLW, magenta) and (Zn-NIAUX)₂ (**B**, 6NZU, beige). The bound metal is depicted only for (Fe-NIAU(SSH)X)₂. The idealized coordination geometry of Fe (orange sphere) is depicted by arrows, with water ligands (small red spheres) modelled at vacant coordination sites. The vacant site on top represents the putative coordination site for the terminal sulfur of Cys381-SSH. Distances are given in Å. **A**) (Zn-NIAU)₂ exhibits Cys138^{ISCU2} Sy 4.4 Å and His137^{ISCU2} Nε2 2.2 Å distance from the putative coordination site. In absence of FXN, His137^{ISCU2} sterically hinders positioning of Cys381^{NFS1} in proximity of Cys138^{ISCU2} (indicated by red arrows). **B**) (Zn-NIAUX)₂ exhibits Cys138^{ISCU2} Sy 3.3 Å distance from the putative Cys381-SSH coordination site, and His137^{ISCU2} is located distal from the assembly site. Binding of FXN to (M-NIAU)₂ thereby provides access for Cys381-SSH^{NFS1} to the putative coordination site by folding His137^{ISCU2} away from and moving Cys138^{ISCU2} closer to the coordination site. A distance of 3.3 Å between Cys381-SSH^{NFS1} and Cys138^{ISCU2} would likely allow for direct persulfide transfer.

The mechanism described above assumes persulfidation of Cys381^{NFS1} in (Fe-NIAU)₂ to happen before FXN enters the complex. If, in contrast, Cys381^{NFS1} is persulfidated after (Fe-NIAUX)₂ assembly, the octahedral Fe site (species 2) would be formed before Cys381-SSH^{NFS1} enters the assembly site (Figure 39, Step A). The Cys381^{NFS1}-bound persulfide may then directly enter the octahedral Fe site. High structural flexibility of the

Cys381^{NFS1}-loop in (Fe-NIAUX)₂ in presence of cysteine may enable fast persulfide shuttling from the NFS1 PLP site to Cys138^{ISCU2}. Which route to ISCU2 the persulfide sulfur takes under physiological conditions may depend on whether Fe and cysteine enter the (NIAU)₂ complex before or after binding of FXN. The biochemical, spectroscopic and structural results obtained in this work suggest some flexibility in these mechanisms.

The discussed mechanisms assume a direct persulfide transfer from Cys381^{NFS1} to Cys138^{ISCU2}. Persulfidation experiments done in this work showed that Cys69^{ISCU2} is not participating in persulfide transfer, however, a rapid sulfur relay from Cys381^{NFS1} via Cys95^{ISCU2} to Cys138^{ISCU2} could not be excluded, as temporal resolution was limited to a reaction time of approximately 10 s (chapters 4.1.3 and 4.1.4). Cys95 exhibits low conformational flexibility and its sulfhydryl moiety points away from the site of the NFS1 Cys381-loop (Figure 40). With a CSS bond angle of around 103° (Snyder & Carlsen, 1977), Cys381-SSH^{NFS1} would likely be similarly positioned for persulfide transfer to Cys95^{ISCU2} as compared to Cys138^{ISCU2}, if the transfer proceeds via the Fe site. This may indicate that a sulfur relay via Cys95^{ISCU2} is not necessary.

In vitro studies have consistently shown residual ISCU2 persulfidation to occur even in absence of FXN (Figure 17C) (Gervason *et al.*, 2019; Parent *et al.*, 2015). However, this observation has not yet been mechanistically explained. Mössbauer analyses show that tetrahedrally coordinated Fe (species 1), most likely not allowing for persulfide transfer to Cys138^{ISCU2}, predominates in (Fe-NIAU)₂ (Figure 37). Species 1 is in equilibrium with octahedrally coordinated Fe (species 2, ca. 29% of (Fe-NIAU)₂), the latter being capable of ISCU2 persulfidation. The transient formation of species 2 may hence explain the observed residual slow rates of Cys138^{ISCU2} persulfidation in the absence of FXN. Since FXN binding shifts the equilibrium from species 1 to 2, this readily explains the stimulatory function of FXN for sulfur transfer.

5.1.5 A proposed molecular mechanism of persulfide reduction

Formation of a [2Fe-2S] cluster on ISCU2 necessitates the reduction of the Cys138-bound persulfide (S⁰) to inorganic sulfide (S²⁻). This and previous works showed the electron donor FDX2 to be essential for efficient *de novo* synthesis of [2Fe-2S] clusters (Figure 33) (Gervason *et al.*, 2019; Schulz *et al.*, submitted manuscript; Sheftel *et al.*, 2010; Webert *et al.*, 2014). One study also reported FDX2 to specifically reduce the ISCU2- but not the NFS1-bound persulfide (Gervason *et al.*, 2019). FDX2-mediated Cys138-SSH^{ISCU2} reduction was furthermore shown to require Fe(II)-bound ISCU2 but was not possible in presence of Zn(II) or in absence of metal. The Fe(II) bound in persulfidated ISCU2 is completely converted to Fe(III) in the final [2Fe-2S]²⁺ cluster (chapter 4.1.7). It hence appears likely that sulfide formation is enabled by one electron delivered

from FDX2, whereas the other one is supplied by the Fe(II) ion coordinated by the persulfide.

Persulfides (Figure 41, **1**) exhibit a significantly lower pK_a (~6.2) compared to thiols (~7.6) (Park *et al.*, 2015), and thus exist mainly in their deprotonated anionic form (**2**) at the alkaline conditions (pH ~8) in the mitochondrial matrix (Llopis *et al.*, 1998; Santo-Domingo & Demaurex, 2012). The more electrophilic internal sulfur atom (**3**) may be the preferred target for initial single-electron persulfide reduction (**4**) and would lead to formation of a highly reactive anionic radical species (**5**) which yields inorganic sulfide (**6**) upon receiving a second electron. A presumably short-lived nature of the radical anion intermediate may avoid undesired side reactions. It is therefore conceivable that the first electron may be delivered by FDX2, and the second reduction step may occur spontaneously via oxidation of Fe(II), driven by the high reactivity of the radical intermediate.

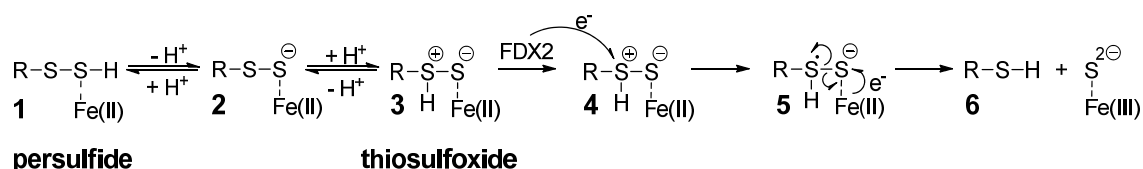


Figure 41: Mechanism proposed for the reduction of the Fe(II)-coordinated persulfide of ISCU2 Cys138. Persulfides (**1**) exhibit a pK_a of around 6.2, and therefore predominantly exist in their deprotonated form (**2**) at physiological pH (Park *et al.*, 2015). They can undergo tautomerization, forming thiosulfoxides with an electrophilic singlet sulfur (**3**) (Ono *et al.*, 2014). Supply of a single electron by FDX2 (**4**) would presumably lead to formation of an unstable anionic radical species (**5**). Supply of the second electron via oxidation of Fe(II) to Fe(III) may enable rapid formation of sulfide-coordinating Fe(III) (**5**). Dashed lines indicate coordinate bonds.

5.1.6 Assembly of a [2Fe-2S] cluster from persulfidated Fe-ISCU2 *in vivo*

Multiple studies have shown that FDX2-mediated persulfide reduction on ISCU2 is essential for [2Fe-2S] cluster maturation (Figure 33) (Gervason *et al.*, 2019; Webert *et al.*, 2014). Nevertheless, the mechanistic steps following ISCU2 persulfidation in *de novo* [2Fe-2S] cluster formation have not been well understood. A recent advance was made by a study showing the N-terminal Tyr35 of ISCU2 to enable [2Fe-2S] cluster formation by facilitating dimerization of two ISCU2 molecules from separate core ISC complexes (Freibert *et al.*, 2021). Whereas Y35K and Y35D variants of ISCU2 did not enable [2Fe-2S] cluster synthesis in enzymatic reconstitutions individually, combination of both variants in one reaction rescued the synthesis defect. This indicated that Lys–Asp salt bridge formation in ISCU2 could replace the role of hydrophobic Tyr35 side chain interaction in ISCU2 WT to enable dimerization. Importantly, exchange of Tyr35 does not affect ISCU2

persulfidation and subsequent FDX2-mediated persulfide reduction *in vitro* as observed by a gel-shift assay (Figure 64) (Freibert *et al.*, 2021).

In an attempt to identify a potential “reduced persulfide” intermediate (possibly representing either **5** or **6** in Figure 41), an enzymatic [2Fe-2S] cluster reconstitution done in presence of ISCU2 Y35D (allowing persulfide formation and reduction, but not cluster formation) was analysed by Mössbauer spectroscopy in this work (chapter 4.1.7). ISCU2-bound Fe exhibited parameters similar to species 2 in (Fe-NIAUX)₂ (Figure 23 and Table 15). The lack of a distinct species indicates a “reduced persulfide” intermediate not being easily distinguishable by Mössbauer spectroscopy or not being present in the sample due to its potential instability. Sample preparation limited the temporal resolution of persulfide reduction to ~2 min reaction of time. As discussed in the previous chapter, single electron transfer from FDX2 to Cys138-SSH^{ISCU2} and immediate supply of a second electron from Fe(II) may induce rapid sulfide formation. Impaired dimerization in the ISCU2 Y35D variant may then lead to release of sulfide into solution. It is conceivable that dimerization under physiological conditions may occur before (or simultaneous with) electron transfer from FDX2 to prevent loss of sulfide.

ISCU2 dimerization occurs between two molecules bound to separate core ISC complexes (Freibert *et al.*, 2021). *In vitro* persulfidation experiments support that both Fe-ISCU2 units bound to a heterodimeric core ISC complex are persulfidated in presence of cysteine (chapter 4.1.3). This indicates each of two dimerizing ISCU2 molecules binding one Fe and one persulfide/sulfide. It is hence conceivable that a [2Fe-2S] cluster bridged between two ISCU2 units may (transiently) form. IscU dimers binding either one or two [2Fe-2S] clusters have been reported for IscU from various organisms, however, bridged coordination of a [2Fe-2S] cluster by WT ISCU has not been convincingly shown (Agar *et al.*, 2000a; Agar *et al.*, 2000b; Bonomi *et al.*, 2011; Dzul *et al.*, 2017; Kunichika *et al.*, 2021; Mansy *et al.*, 2002; Shimomura *et al.*, 2008; Webert *et al.*, 2014; Wu *et al.*, 2002a). For an easier understanding, numbering of IscU residues from different organisms will be done according to the sequence of human ISCU2 in the following. Bridged [2Fe-2S] cluster ligation by a *E. coli* IscU dimer via residues Cys95 and Cys138 has been proposed based on CD-spectroscopic analysis of chemically reconstituted IscU mutant proteins (Bonomi *et al.*, 2011). However, no variant of the conserved Asp71 was analysed. Furthermore, IscU C69A was not regarded as ligand despite significantly decreased and shifted spectral features. In this work, a (weak) CD spectrum of chemically reconstituted human ISCU2 C69S could be assigned to a not physiologically relevant multimeric holo-ISCU2 species (chapter 4.1.11). It is hence possible, that *E. coli* IscU coordinates a [2Fe-2S] cluster via its three conserved cysteine residues and Asp71 of one monomer, as suggested here.

In this work, Cys69, Cys95 and Cys138 of one ISCU2 molecule were found to be essential cluster ligands (chapter 4.1.11), with either His137 or, more likely, Asp71 constituting the fourth ligand (chapter 4.1.7, see also chapter 5.1.7 for a detailed discussion of the ligands). This is in line with cluster coordination in a holo-monomer. Alternatively, an ISCU2 dimer may asymmetrically coordinate the cluster via Cys69, Cys95, Cys138 and possibly Asp71 of one ISCU2 molecule, the second molecule contributing either Asp71 or no cluster ligand. It is tempting to speculate that upon [2Fe-2S] cluster formation on an ISCU2 dimer *in vivo*, the newly formed cluster may be immediately transferred to one unit of the dimer (Figure 42).

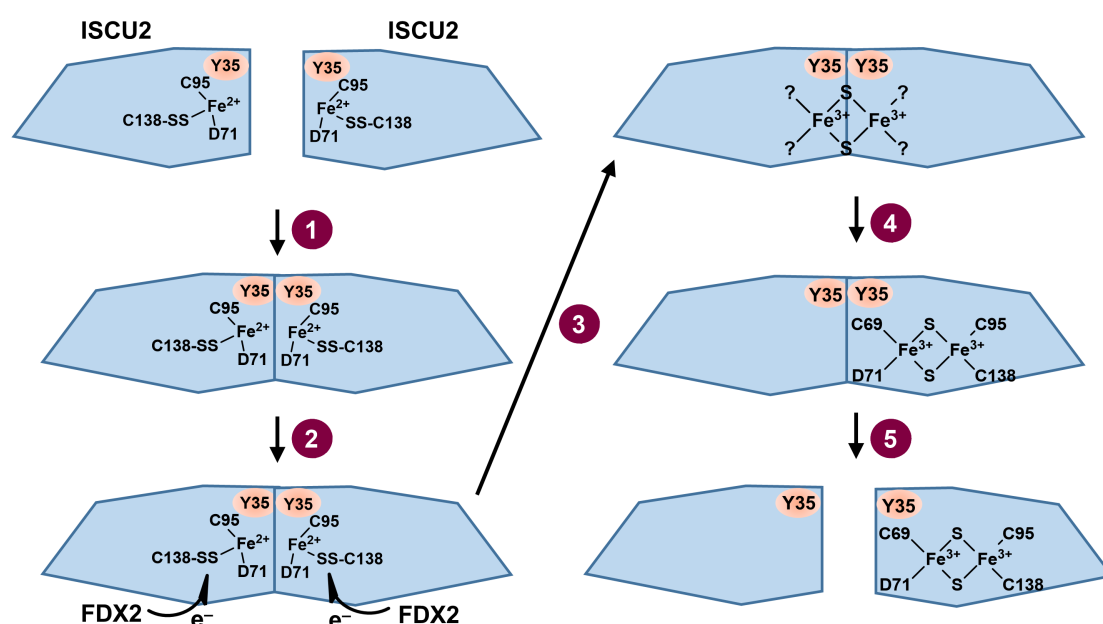


Figure 42: Model of [2Fe-2S]-ISCU2 formation from persulfidated monomeric Fe-ISCU2. 1) Two units of persulfidated Fe-ISCU2 dimerize mediated by π -stacking their N-terminal Tyr35 residues (Freibert *et al.*, 2021). 2) Each persulfide (S^0) moiety is reduced to S^{2-} by receiving one electron from FDX2 and the other from Fe(II). It cannot be excluded that persulfide reduction occurs already before ISCU2 dimerization, however, this may increase the propensity of sulfide loss. 3) The newly formed [2Fe-2S] cluster may be transiently coordinated in a bridged dimeric fashion. The ligands of such a species are presently unknown. 4) The cluster is transferred to one ISCU2 molecule of the dimer. One Fe ion of the cluster is coordinated by Cys95 and Cys138, the other one by Cys69 and presumably Asp71 (see next chapter for details). 5) The asymmetric holo-dimer dissociates, forming one apo- and one holo-monomer. The apo-monomer is available for another round of *de novo* [2Fe-2S] cluster synthesis. The cluster of the holo-monomer is transferred to GLRX5 via the ATP-dependent HSC20/HSPA9 chaperone system. Whether dissociation of the asymmetric ISCU2 holo-dimer occurs spontaneously or is induced by chaperones remains to be investigated.

Fe and cysteine titrations in enzymatic reconstitutions of mouse ISCU indicated formation of approximately one [2Fe-2S] cluster per ISCU monomer, and native MS of holo-ISCU supported the presence of holo-monomers but not -dimers (Gervason *et al.*, 2019).

Upon enzymatic reconstitution of ISCU2 done in this work, exclusively monomeric [2Fe-2S]-ISCU2 was observed by aSEC-MALS (Appendix Figure 65C-D). This indicates holo-dimers formed under physiological conditions being rather labile, potentially dissociating into one holo- and one apo-monomer. It remains to be elucidated if *in vivo* the dimer dissociates before or after interaction with the HSC20/HSPA9 chaperone system, which enables [2Fe-2S] cluster transfer to GLRX5 (chapter 1.3.2). Titrations of Fe and cysteine were reported to yield around 90% enzymatically reconstituted mouse ISCU at 2 eq. Fe and cysteine (eq. over total ISCU concentration) (Gervason *et al.*, 2019). This indicates that at least *in vitro* the holo-dimer can dissociate, enabling the released apo-ISCU to re-enter the biosynthetic complex for another round of [2Fe-2S] cluster synthesis.

5.1.7 Asymmetric [2Fe-2S] cluster ligation by ISCU2

So far, 3D structures of [2Fe-2S] cluster-bound IscU from three thermophilic organisms including bacteria and archaea have been published (Kunichika *et al.*, 2021; Marinoni *et al.*, 2012; Shimomura *et al.*, 2008). Strikingly, all structures show the three conserved Cys residues of one IscU monomer to participate in cluster coordination (Table 16), as suggested for human ISCU2 in this work based on *in vitro* reconstitutions (chapter 4.1.11). The three Cys residues may fulfil a conserved function as [2Fe-2S] cluster ligands. In all published structures, one Fe ion is coordinated by residues Cys95 and Cys138. The second Fe ion is ligated by Cys69, and in the only structure of WT IscU (Kunichika *et al.*, 2021) also by Asp71. Structures obtained with Asp to Ala variants of IscU exhibit ligation with either His (Shimomura *et al.*, 2008), Cys from a second IscU molecule (Kunichika *et al.*, 2021), or the Cys of the catalytic NFS1-loop (Marinoni *et al.*, 2012). Mössbauer spectroscopy of [2Fe-2S]-ISCU2 in this and a previous work supported cluster coordination by three Cys residues and one N/O ligand (chapter 4.1.7) (Gervason *et al.*, 2019), indicating either Asp71 or His137 to constitute the fourth cluster ligand. As exchange of Asp71 but not His137 leads to a significant change in the CD spectrum of chemically reconstituted [2Fe-2S]-ISCU2 (chapter 4.1.11), Asp71 appears to be the more likely candidate. In agreement, the structurally conserved *Methanotherix thermoacetophila* IscU exhibits [2Fe-2S] cluster ligation by three Cys residues and Asp71 (Figure 43). Exchange of the conserved Asp71 to Ala has repeatedly been reported to lead to an overall more stable cluster binding, inhibiting the physiologically crucial ability of IscU to transfer its cluster (Mansy *et al.*, 2002; Marinoni *et al.*, 2012; Shimomura *et al.*, 2007; Wu *et al.*, 2002a; Wu *et al.*, 2002b). Accordingly, upon IMAC purification in this work, only the D71A variant of ISCU2 exhibited a reddish-orange colour and a CD spectrum indicating [2Fe-2S] cluster binding without prior reconstitution (Figure 15).

Table 16: Overview of cluster-ligating residues in published crystal structures of [2Fe-2S]-IscU. The only structure of WT IscU is highlighted in **bold**. For each structure, residues ligating the same Fe ion are marked in the same color (orange or blue boxes). Numbering is according to the IscU sequence of the respective organism, and numbering of the equivalent ISCU2 residues is given on the right. The table is assembled from data of the following publications: Kunichika *et al.*, 2021; Marinoni *et al.*, 2012; Shimomura *et al.*, 2008.

Organism	<i>Aquifex aeolicus</i>	<i>Archaeoglobus fulgidus</i>	<i>Methanothrix thermoacetophila</i>				Equivalent ISCU2 residue
Pdb code	2Z7E	4EB5	7C8M	7C8N	7CNV	7C8O	
Variant	D38A	D35A	WT	H106A	H106C	D40A/H106A	
Structure	$([2Fe2S]IscU_{D38A})(IscU_{D38A})_2$	$([2Fe2S](IscS-IscU_{D35A}))_2$	$([2Fe2S]IscU)_2$	$([2Fe2S]IscU_{H106A})_2$	$([2Fe2S]IscU_{H106C})_2$	$[2Fe2S](IscU_{D40A/H106A})_2$	
Coordinating residues (molecule 1)	Cys36	Cys33	Cys38	Cys38	Cys38	Cys38	Cys69
			Asp40	Asp40	Asp40		Asp71
	Cys63	Cys58	Cys63	Cys63	Cys63	Cys63	Cys95
	His106						His137
	Cys107	Cys102	Cys107	Cys107	Cys107	Cys107	Cys138
Coordinating residues (molecule 2)		Cys321 ^{NFS1}				Cys63	

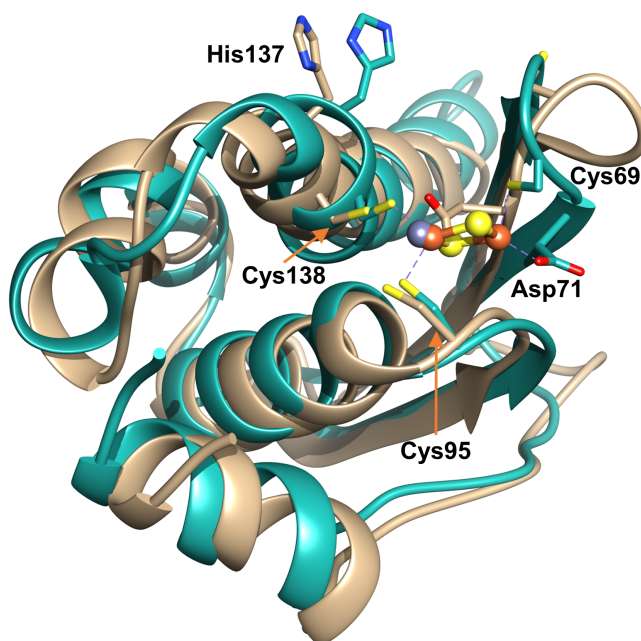


Figure 43: Structural similarity between human Zn-ISCU2 and archaeal [2Fe-2S]-IscU. Overlay of [2Fe-2S] cluster-bound *M. thermoacetophila* IscU (pdb code: 7C8M, green) and Zn-bound human ISCU2 (pdb code: 6NZU, beige). Numbering of residues is according to human ISCU2. Positioning of ISCU2 Cys95 and Cys138 is similar to *Mt* IscU, whereas Cys69 and Asp71 are positioned on a flexible loop. Zn is depicted as grey sphere and the [2Fe-2S] cluster as coloured spheres/sticks.

Coordination of one Fe ion of the [2Fe-2S] cluster via Cys69 and Asp71 located on a flexible loop may enable accessibility/lability of the cluster, facilitating chaperone-mediated transfer to GLRX5. Replacement of the Cys69-Asp71 loop by one molecule GLRX5 may enable transient formation of a [2Fe-2S] cluster-bridged GLRX5-ISCU2 heterodimer. Subsequent displacement of ISCU2 by a second GLRX5 molecule would then enable formation of the [2Fe-2S] cluster-bridged GLRX5 homodimer functioning in Fe/S protein biogenesis. As of now, the physiological relevance of this stepwise process remains to be verified.

5.1.8 Outlook

Biochemical, structural and spectroscopic studies in this work have provided detailed insights into the process of *de novo* [2Fe-2S] cluster assembly and in particular ISCU2 persulfidation in a physiologically relevant context. A high resolution cryo-EM structure of an intermediate of Fe/S cluster biogenesis showed (Fe-NIAUX)₂ with persulfidated Cys138^{ISCU2} ligating the ISCU2-bound Fe via its persulfide moiety. Whereas Cys138^{ISCU2} was also identified in biochemical studies as the terminal persulfide acceptor, sulfur relay via Cys95^{ISCU2} on the second or sub-second time scale could not completely be ruled out, due to technical limitations. The employed iodoTMT-based assay may be combined with a quench-flow approach in future experiments, which would potentially enable millisecond reaction times (Bingaman *et al.*, 2017). It would be crucial for such a setup to ensure that temporal resolution is not limited by the quenching step. If persulfidation of ISCU2 Cys95 is not detectable on the second to millisecond timescale, this would in all likelihood exclude a function as intermediate sulfur acceptor.

Efficient ISCU2 persulfidation requires binding of FXN to (Fe-NIAU)₂. However, if (Fe-NIAU)₂ interacts with cysteine before FXN binding, a species exhibiting persulfidated Cys381^{NFS1} coordinating Fe at the ISCU2 assembly site may be formed (see Figure 39). Electron density at the assembly site in the cryo-EM structure of (Fe-NIAU)₂ obtained in presence of cysteine (Figure 20) may be in line with the presence of Cys381-SSH^{NFS1}-Fe, but limited resolution at the Fe site has precluded a conclusive answer. As the (Fe-NIAU)₂ structure obtained in this work represented only 25% of cryo-EM particles from the respective sample, resolution improvements should be possible. Obtaining and comparing higher resolution cryo-EM structures of (Fe-NIAU)₂ in presence and absence of cysteine may increase the chances of identifying a Cys381-SSH^{NFS1}-Fe species. Improved structural data may also enable a better refinement of His137^{ISCU2} and the Cys69^{ISCU2}-loop, possibly allowing for the resolution of distinct conformations. Weak electron densities of these structural elements had implied flexibility in the absence of FXN, supported by Mössbauer spectroscopy.

The biosynthetic steps following ISCU2 persulfidation, namely persulfide reduction and [2Fe-2S] cluster maturation, are not fully understood on a molecular level, despite recent progress (Freibert *et al.*, 2021; Gervason *et al.*, 2019). A “reduced persulfide” intermediate formed via electron transfer from FDX2 may be short-lived (chapter 5.1.5). Sample preparation using a rapid freeze-quench method with subsequent spectroscopic analysis (Krebs *et al.*, 2005), e.g., by Mössbauer spectroscopy, may enable further characterisation of persulfide reduction.

Binding of FXN and FDX2 to (NIAU)₂ has been reported to occur at opposite sides of ISCU2 based on experiments with yeast and *C. thermophilum* proteins (Boniecki *et al.*, 2017) (chapter 1.3.1.1). In contrast, a recent study reported overlapping binding sites for both proteins in yeast (Uzarska *et al.*, 2022). A high-resolution structure of a mammalian FDX2-bound core ISC complex has not yet been published and would provide valuable insights into FDX2 function. It has recently been shown that dimerization of ISCU2 molecules from two separate core ISC complexes is required for [2Fe-2S] cluster maturation (Freibert *et al.*, 2021). This raises the question whether FDX2 reduces the ISCU2-bound persulfide before or after ISCU2 dimerization. The published data also imply that a dimer of two heterodimeric core ISC units may be transiently formed. Such a complex may be detected by cryo-EM analysis of enzymatic reconstitutions of [2Fe-2S]-ISCU2. As the dimer may constitute a short-lived intermediate, crosslinking may increase the chances of capturing such a species.

5.2 FDX1-dependent function of LIAS in human lipoyl biosynthesis

5.2.1 *In vitro* reconstitution of human lipoyl synthesis reveals similarities to bacterial catalysis

Despite the molecular mechanism of lipoyl biosynthesis having been extensively characterised, the physiological electron donor for human LIAS has remained unknown (Lanz *et al.*, 2014; McCarthy & Booker, 2017; McCarthy *et al.*, 2019). Studies in human cell culture indicated that both FDX1 and FDX2 are required for lipoyl synthesis (Appendix Figure 48). *FDX2* knock-down severely diminishes the assembly of [4Fe-4S] clusters vital for LIAS catalysis. Whether FDX2 may also assist the radical SAM reaction mechanism of LIAS can therefore not be assessed *in vivo*. To unequivocally identify the physiological electron donor of human LIAS, a suitable *in vitro* lipoylation assay was developed in this work. LIAS catalysis could be initiated with electrons supplied by the artificial inorganic reductant DT as done before in bacterial lipoylation assays (McCarthy & Booker, 2018). Remarkably, product yields were 2-fold higher using a physiological ETC comprising NADPH, FDXR and FDX1 (Figure 31). Omitting FDX1 or replacing it with

FDX2 dramatically diminished product formation. FDX1 could thereby be identified as the physiological electron donor for human LIAS. The weaker efficiency of DT could be rescued in presence of the [4Fe-4S] cluster donor NFU1, possibly suggesting DT to partially destroy LIAS-bound [4Fe-4S] clusters which are regenerated in presence of excess [4Fe-4S]-cluster-containing NFU1. Replacing DT with a physiological ETC might therefore improve the generally low reaction rate/turnover of lipoyl synthesis *in vitro* also in setups with non-human proteins, in particular when handling lipoyl synthases with labile Fe/S clusters.

Assays from this work showed lipoyl formation to progress significantly slower than formation of the 6-thiooctanoyl intermediate, indicating the second sulfur-insertion step to be rate-limiting (Figure 29C). Depending on the reaction conditions, up to 0.5 eq. lipoyl and additionally around 1 eq. 6-thiooctanoyl over LIAS were obtained, consistently more than 1 eq. total products, in reactions lacking an Fe/S cluster donor regenerating the sulfur-donating auxiliary cluster of LIAS. During lipoyl synthesis, the octanoyl substrate stays bound to LIAS until it is fully processed to a mature lipoyl product (Figure 11). When synthesizing 0.5 eq. lipoyl, 0.5 eq. LIAS exhibit a degraded auxiliary cluster lacking two sulfur atoms. Therefore, half of the additionally synthesized 1 eq. 6-thiooctanoyl intermediate would have to be synthesized from LIAS with a degraded auxiliary cluster in such reactions. Apparently, after one turnover, at least the first step of a second turnover is possible, leading to the incorporation of at least three sulfur atoms into octanoyl substrates. Hence, one auxiliary cluster of LIAS might support the formation of two lipoyl molecules by donating all four sulfur atoms, which has been previously proposed for *E. coli* LipA based on *in vitro* lipoylation experiments using ³⁴S-labelling (McCarthy & Booker, 2017). The second sulfur-insertion step being rate-limiting as well as total products exceeding 1 eq. over LIAS in absence of Fe/S cluster donors has also been reported for *E. coli* LipA (Lanz *et al.*, 2014), showing mechanistic similarities between human and bacterial lipoyl biosynthesis. This also underlines the potential of the *in vitro* assay to dissect mechanistic details of lipoylation in humans.

5.2.2 Potential Fe/S cluster donors for LIAS

The auxiliary cluster of LIAS being sacrificed to enable lipoyl synthesis requires its regeneration by dedicated Fe/S cluster donors. BOLA3 and in particular NFU1 seemed likely candidates for this function in humans, based on previous research. However, neither homodimeric [4Fe-4S]-NFU1 nor a heterodimeric [2Fe-2S]-BOLA3-GLRX5 complex led to increased turnover or rate of lipoylation reactions in presence of the physiological electron donor FDX1. This does not necessarily exclude a function of these complexes in LIAS regeneration. In reactions lacking Fe/S cluster donors, a maximum of around

0.5 eq. lipoyl over LIAS was formed at the longest reaction time (150 min). If addition of Fe/S cluster donors does not accelerate the reaction rate, multiple turnovers cannot be observed. The overall slow rate of lipoyl formation may indicate that another protein factor is required for efficient catalysis. Addition of NFU1 increased lipoyl formation 2.1-fold in DT-containing reactions, indicating that NFU1 may in principle be capable to transfer [4Fe-4S] clusters to LIAS (see previous chapter). However, it cannot be distinguished whether the auxiliary and/or catalytic cluster are targeted, as both could be subject to DT-mediated destruction.

Mutations of *NFU1* in humans as well as NFU1 depletion in human cell culture were reported to lead to decreased activities of lipoyl-dependent enzymes, due to impaired lipoyl production by LIAS (Navarro-Sastre *et al.*, 2011). Lipoyl-production is enabled by Nfu1 in yeast (Melber *et al.*, 2016; Navarro-Sastre *et al.*, 2011; Uzarska *et al.*, 2016), the homologs NFU4 and NFU5 in plants (Przybyla-Toscano *et al.*, 2022; Uzarska *et al.*, 2018) and possibly by Nfu2 and Nfu3 in *Trypanosoma brucei* (Benz *et al.*, 2016). Furthermore, *E. coli* NfuA serves as [4Fe-4S] cluster donor for LipA, enabling multiple turnovers of lipoyl synthesis (McCarthy & Booker, 2017; McCarthy *et al.*, 2019). Both human and bacterial NFU1 coordinate a [4Fe-4S] cluster as a bridged homodimer via two conserved Cys residues of the C-terminal domain of each monomer (Cai *et al.*, 2016; Py *et al.*, 2012). In conclusion, this supports a conserved function of NFU1 as an Fe/S cluster donor for human LIAS.

Genetic studies in yeast supported a function of Bol1 and Bol3 in lipoyl synthesis that is at least partially overlapping but distinct from Nfu1 (Melber *et al.*, 2016; Uzarska *et al.*, 2016). In human patients, mutation of *BOLA3* was reported to diminish lipoyl production, whereas *BOLA1* mutation was not reported in this context (Baker *et al.*, 2014; Cameron *et al.*, 2011). This may suggest BOLA3 to fulfil a distinct function in human lipoylation that is not redundant with BOLA1. *In vitro*, both BOLA1 and BOLA3 can form homodimeric [2Fe-2S] cluster-bridged complexes as well as heterodimeric [2Fe-2S] cluster-bridged complexes with GLRX5 (Jia *et al.*, 2020; Melber *et al.*, 2016; Nasta *et al.*, 2017; Sen *et al.*, 2021; Uzarska *et al.*, 2016; Wachnowsky *et al.*, 2019). However, the physiological function of these complexes remains to be identified. Lipoylation assays done in this work indicated full degradation of the LIAS auxiliary cluster throughout lipoyl synthesis (see previous chapter), which may favour its regeneration via a [4Fe-4S] rather than [2Fe-2S] cluster donor. *In vitro* binding studies showing interaction between NFU1 and BOLA3 (Uzarska *et al.*, 2016) may suggest that a (transient) NFU1-BOLA3 complex is required for [4Fe-4S] cluster delivery to LIAS.

ISCA1/2 and IBA57 are required for the synthesis of [4Fe-4S] clusters from [2Fe-2S] cluster precursors delivered by GLRX5. It is conceivable that at least one of the proteins

ISCA1/2 and IBA57 might be part of a complex donating Fe/S clusters to LIAS (and possibly other recipient proteins). Based on NMR studies, formation of an NFU1-ISCA1 [4Fe-4S] cluster-bridged complex representing a potential [4Fe-4S] cluster donor was reported (Saudino *et al.*, 2022; Suraci *et al.*, 2021).

In vitro lipoylation experiments with *E. coli* LipA showed that not only [4Fe-4S]-NfuA but also [4Fe-4S]-IscU allowed multiple enzymatic turnovers (McCarthy & Booker, 2017). Since human ISCU2 is not directly involved in mitochondrial [4Fe-4S] cluster targeting *in vivo* (Lill & Freibert, 2020) and furthermore was shown in this and previous works to bind a [2Fe-2S] but not [4Fe-4S] cluster as the physiologically relevant species (chapters 4.1.8 and 4.1.11) (Gervason *et al.*, 2019), it most likely does not represent a bona fide cluster donor for LIAS.

In summary, [4Fe-4S]-bound NFU1 appears to be an essential Fe/S cluster donor for LIAS. However, additional factors possibly interacting with NFU1, e.g., BOLA3 or ISCA1, may be required to form complexes facilitating cluster transfer (Figure 44). Furthermore, insertion of the catalytic and auxiliary cluster into LIAS might require different targeting complexes.

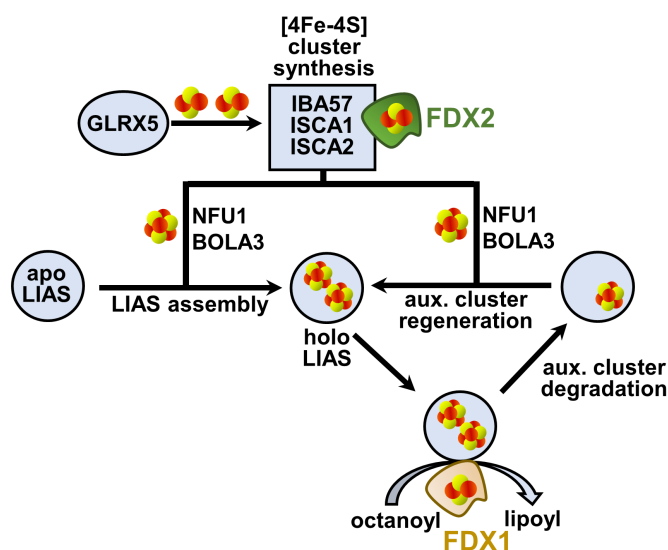


Figure 44: Candidate Fe/S cluster donors for LIAS. GLRX5 delivers [2Fe-2S] precursors for the assembly of [4Fe-4S] clusters by ISCA1, ISCA2, IBA57 and FDX2. Two [4Fe-4S] clusters are inserted into apo-LIAS to enable enzymatic function. Upon FDX1-dependent lipoyl formation by LIAS, its auxiliary (aux.) cluster is degraded and has to be regenerated. Human NFU1 and BOLA3 have been reported as essential for lipoylation *in vivo*, and may assist both [4Fe-4S] cluster insertion and regeneration. BOLA3 and ISCA1 were shown to interact with [4Fe-4S]-NFU1, and these interactions may be required for [4Fe-4S] cluster delivery.

5.2.3 Lipoyl biosynthesis is inhibited by Cu and the Ele:Cu complex

The mitochondria targeting Cu ionophore and anticancer agent Ele has been proposed to inhibit the function of FDX1 in Fe/S protein biogenesis (Tsvetkov *et al.*, 2019). This

explanation can be refuted based on experiments from this and previous works showing FDX2, but not FDX1 participating in Fe/S protein biogenesis (Figure 33) (Schulz *et al.*, submitted manuscript; Sheftel *et al.*, 2010; Webert *et al.*, 2014). Recently, it was shown that Ele interferes with protein lipoylation *in vivo* (Schulz *et al.*, submitted manuscript; Tsvetkov *et al.*, 2022), and the underlying mechanism was further investigated in this work.

Cu alone interfered with both FDX1 function and lipoyl synthesis (Figure 35). Several mechanisms of action have been assigned to general Cu toxicity, including formation of reactive oxygen species, thiol depletion and Fe/S cluster destruction, with recent research suggesting replacement of Fe in Fe/S clusters being the predominant cause of toxicity (Chillappagari *et al.*, 2010; Solioz, 2018). Hydratases with their solvent exposed [4Fe-4S] clusters are prone to disruption, the accessibility of the cluster being a major determinant of this mechanism (Macomber & Imlay, 2009). Furthermore, FDXs as well as mitochondrial [4Fe-4S] cluster assembly have been proposed as target of Cu toxicity (Brancaccio *et al.*, 2017; Vallieres *et al.*, 2017). In agreement, Cu titrations done in this work showed that Fe/S clusters of FDX1 and FDX2 as well as the solvent-exposed clusters of LIAS were destroyed by excess Cu. Destruction was prevented by addition of Ele. Formation of the highly stable Ele:Cu complex (Yadav *et al.*, 2013) probably inhibits Cu-mediated Fe/S cluster disruption. Consequently, Cu likely has to be released from the Ele:Cu complex to enable Fe/S cluster disruption *in vivo*.

It was shown in this work that Ele alone imparts no effect on Fe/S cluster integrity, FDX function or lipoylation *in vitro*, in line with results from *in vivo* studies (Tsvetkov *et al.*, 2022; Tsvetkov *et al.*, 2019). In contrast, the Ele:Cu complex inhibited lipoylation, but not FDX function. Ele has been shown to selectively shuttle Cu to mitochondria, inducing mitochondrial dysfunction (Nagai *et al.*, 2012; Tsvetkov *et al.*, 2019). It is possible that the Ele:Cu complex entering mitochondria might specifically inhibit lipoyl synthesis in a mechanism distinct from Cu-mediated Fe/S cluster destruction.

Ele levels in human cells have been reported to stay low throughout Ele treatment, whereas Cu levels increased to up to 1000-fold over Ele levels within 6 h (Nagai *et al.*, 2012). This and further research (Tsvetkov *et al.*, 2022; Tsvetkov *et al.*, 2019) indicates accumulated Cu, but not the Ele:Cu complex itself being the predominant mediator of toxicity. Ele, but not Ele:Cu, is a substrate of the p-glycoprotein pump, likely enabling Ele efflux from cells after Cu release (Munteanu *et al.*, 2006; Nagai *et al.*, 2012). The accumulated Cu likely leads to disruption of Fe/S clusters, with FDXs, hydratases and LIAS representing potential targets. As LIAS exhibits two solvent-exposed Fe/S clusters and relies on function of both FDX2 and FDX1 for maturation and catalysis, respectively, lipoylation appears to be a likely physiological target of Cu. In agreement, recent studies

find decreased levels of Fe/S proteins, in particular LIAS, based on immunoblotting of Ele-treated cells (Schulz *et al.*, submitted manuscript; Tsvetkov *et al.*, 2022). Furthermore, Tsvetkov *et al.* proposed an additional pathway of Ele-induced toxicity mediated by Cu binding to the lipoyl cofactor of PDH and KGDH, inducing protein aggregation. Overall, multiple mechanisms of Ele-mediated toxicity may affect mitochondria, however, lipoylation appears to be the key marker.

5.2.4 Structure prediction of a catalytically active LIAS-GCSH-FDX1 complex

Anaerobic crystallization of LIAS was attempted in this work, but not successful. To nevertheless enhance the structural understanding of lipoyl synthesis, LIAS was modelled in a catalytic heterotrimeric complex with the physiological octanoyl substrate carrier GCSH (Figure 11) and the electron donor FDX1 using Google Colab, a software based on AlphaFold (Jumper *et al.*, 2021; Varadi *et al.*, 2022).

Predicted folds of GCSH and FDX1 are almost identical to published crystal structures of bovine GCSH (pdb code: 3KLR) and human FDX1 (3P1M), excluding the disordered N- and C-terminal regions. Apart from the N-terminus, the predicted fold of LIAS and positioning of its Fe/S cluster-coordinating residues is similar to published crystal structures of *Mycobacterium tuberculosis* and *Thermosynechococcus elongatus* LipA (pdb codes: 5EXJ, 5EXK, 5U0O, 5U0P) (Harmer *et al.*, 2014; McLaughlin *et al.*, 2016). Similarity is highest to a crystallographic snapshot of lipoyl synthesis showing *Mt* LipA with a 6-thiooctanoyl intermediate bound at the auxiliary cluster site (Figure 45A).

Intriguingly, the predicted LIAS-GCSH-FDX1 complex exhibits GCSH and FDX1 suitably positioned to fulfill their respective functions (Figure 45B). GCSH Lys104 functioning as octanoyl carrier is inserted into the substrate binding tunnel of LIAS, resembling positioning of the 6-thiooctanoyllysyl intermediate as observed in *Mt* LipA catalysis (the respective Lys ϵ -amino moieties of both structures being displaced by 1.9 Å) (McLaughlin *et al.*, 2016). FDX1 binds to LIAS via its cluster-coordinating loop C and helix F. Both segments have been reported to interact with FDXR, CYP11A1 and CYP11B2 (Brixius-Anderko & Scott, 2021; Muller *et al.*, 2001; Strushkevich *et al.*, 2011). The FDX1-bound Fe/S cluster is located above a tunnel giving access to the catalytic cluster site of LIAS (Figure 45C). The distance between the Fe-atoms of the FDX1 and LIAS clusters predicted to be 16.2 Å may allow for direct electron transfer (Chiliza *et al.*, 2020). For both *Mt* and *Te* LipA, crystal structures exhibiting the same tunnel have been published (pdb codes: 5EXK and 5U0P), yet other structures of the same two proteins show the tunnel entrance being blocked by rearrangement of residues of the catalytic cluster-coordinating loop (pdb codes: 5EXJ and 5U0O). It is tempting to speculate that this might represent a means of regulating electron flow to the catalytic cluster of lipoyl synthase.

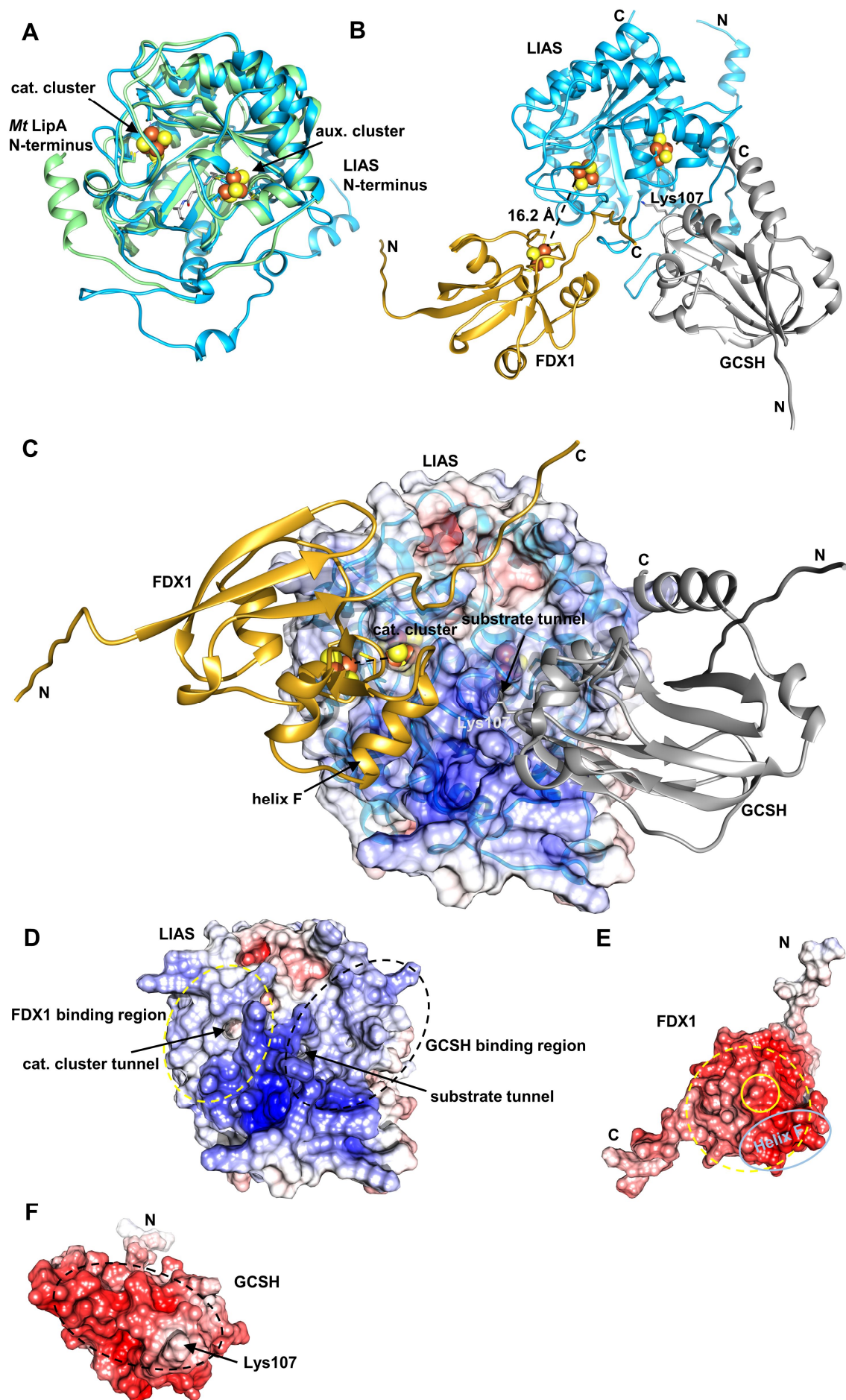


Figure 45: Predicted structure of the trimeric LIAS-GCSH-FDX1 complex. Structures were predicted with Google Colab (https://colab.research.google.com/github/sokrypton/ColabFold/blob/main/beta/AlphaFold2_advanced.ipynb) and the top-scoring prediction is displayed. **A)** Overlay of the predicted LIAS structure (blue, residues: 29-372) with *Mt* LipA (pdb code: 5EXK, green). The *Mt* LipA catalytic (cat.) and auxiliary (aux.) cluster Fe (orange) and S (yellow) atoms are displayed as spheres and the bound 6-thiooctanoyllysyl moiety as grey sticks. **B-C)** Predicted LIAS-GCSH-FDX1 complex (residues: LIAS, 29-372; GCSH, 41-173; FDX1, 54-184). Fe/S cluster-coordinating residues and GCSH Lys107 are shown as sticks. Positions of Fe/S clusters are modelled based on crystal structures of FDX1 (3P1M) and *Mt* LipA (5EXK). LIAS, blue; GCSH, grey; FDX1, gold. The electrostatic surface potential is mapped onto the semi-transparent surface of LIAS in **(C)**. **D-E)** Electrostatic surfaces mapped onto LIAS **(D)**, FDX1 **(E)** and GCSH **(F)**. LIAS-FDX1 and LIAS-GCSH interacting regions are encircled by yellow and black dashed lines, respectively. The locations of the FDX1-bound [2Fe-2S] cluster and helix F are encircled by yellow and light blue solid lines, respectively. Surface potentials were calculated using the APBS server (<https://server.poissonboltzmann.org>). Negative charges are colored in red, positive charges in blue. The color bar covers the range from -10 kT/e to +10 kT/e.

In the predicted trimeric complex, LIAS-binding regions of both GCSH and FDX1 are strongly negatively charged and contact positively charged regions of LIAS, indicating electrostatic interactions to be crucial for protein binding (Figure 45D-F). The region between both aforementioned tunnels of LIAS exhibits the most positive surface potential of the protein.

Removal of the FDX2 C-terminus was shown in this work to enable lipoylation to some extent (14.2% of FDX1 reactions, Figure 32E). As this may suggest the FDX2 C-terminus to interfere with LIAS interaction, it is interesting to note that the FDX1 C-terminus makes slight contact to LIAS in the predicted structure. Modelling the trimeric complex with FDX2 WT or the $\Delta C12$ variant instead of FDX1 did not yield any physiologically relevant quaternary structure, in line with only FDX1 serving as a redox partner of LIAS. Modelling a dimeric LIAS-FDX1 complex predicted binding of FDX1 at the GCSH site of the trimeric LIAS-GCSH-FDX1 complex in all five top-scoring models. This may indicate that presence of GCSH facilitates correct positioning of FDX1 for electron transfer. In summary, the predicted structure of the LIAS-GCSH-FDX1 complex is in line with the experimental data from this work and may support future investigation of the biosynthetic mechanism of lipoyl formation.

5.3 Functions and specificity of the human ferredoxins

5.3.1 FDX1 and FDX2 support different mitochondrial pathways

In vitro experiments done in this work identified FDX1 but not FDX2 to supply electrons for LIAS-catalysed lipoyl formation, showcasing a high specificity of LIAS for its redox

partner. FDX1 (also termed adrenodoxin), but not FDX2, is furthermore known for shuttling electrons to seven mitochondrial CYP enzymes participating in adrenal steroid hormone biosynthesis as well as bile acid and vitamin A and D metabolism (Ewen *et al.*, 2012; Johnson *et al.*, 2017; Omura, 2006; Sheftel *et al.*, 2010). In addition, human cell culture and yeast complementation studies (Schulz *et al.*, submitted manuscript) revealed that FDX1 is the preferred electron donor for the biosynthesis of heme *a*, a co-factor needed for activity of the respiratory chain complex IV (cytochrome *c* oxidase (COX)). FDX1 most likely is the redox partner of COX15, a monooxygenase catalysing the last step of heme *a* synthesis (Swenson *et al.*, 2020). Heme *a* synthesis has been previously proposed to require FDX2 (Sheftel *et al.*, 2010). However, the recent studies showed that despite FDX2 functioning to a limited extent in heme *a* biosynthesis, FDX1 is the preferred electron donor. Altogether, this shows FDX1 to be remarkably versatile regarding its redox partners and involvement in different pathways (Figure 46). Moreover, each FDX appears to be highly specific for a given pathway.

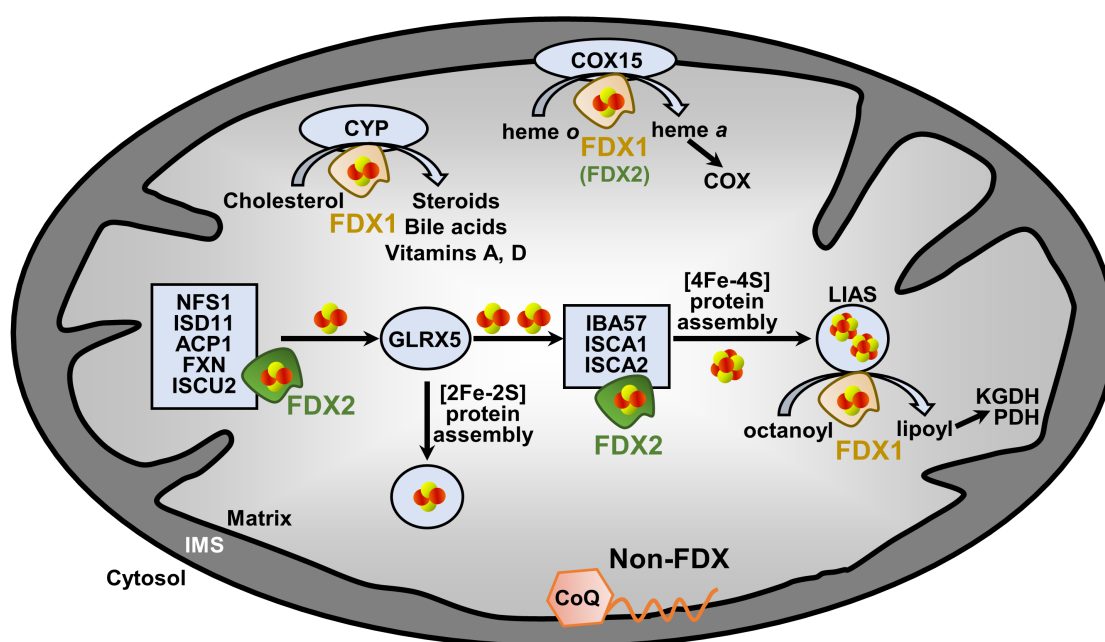


Figure 46: Overview of the differential FDX1 and FDX2 functions. FDX1 delivers electrons to LIAS, COX15 and seven mitochondrial CYPs. It thereby supports lipoyl, heme *a* and steroid biosynthesis and furthermore bile acid as well as vitamin A and D metabolism. However, FDX1 does not support Fe/S protein biogenesis. FDX2 enables formation of [2Fe-2S] and [4Fe-4S] clusters in this pathway at two different steps. Furthermore, FDX2 exhibits a redundant function in heme *a* synthesis. Neither of the two FDXs supports coenzyme Q (CoQ) biosynthesis. The electron donor for this pathway in humans remains to be identified (Schulz *et al.*, submitted manuscript).

FDX2 on the other hand predominantly functions in Fe/S protein biogenesis. Within Fe/S protein biogenesis, two assembly complexes specifically require FDX2. The core ISC

assembly machinery requires electrons for *de novo* [2Fe-2S] cluster synthesis, biochemical and structural data implying FDX2 interaction with the scaffold protein ISCU2 and/or the desulfurase NFS1 (Boniecki *et al.*, 2017; Weibert *et al.*, 2014). Additionally, reductive fusion of [2Fe-2S] to [4Fe-4S] clusters dependent on ISCA1/2 and IBA57 requires electron flow from FDX2 (Jain *et al.*, 2020; Weiler *et al.*, 2020).

Two studies proposed a redundant function of FDX1 in Fe/S protein biogenesis. One study reported FDX1 depletion to affect Fe/S proteins (Shi *et al.*, 2012), contradicting a previous study (Sheftel *et al.*, 2010). Possibly, this difference may be attributed to indirect effects of decreased lipoyl and heme *a* synthesis. Recent studies showed that even *FDX1* deletion does not affect Fe/S protein levels (Figure 48) and activities (Schulz *et al.*, submitted manuscript).

FDX1 was also reported to enable [2Fe-2S] cluster formation on ISCU2 *in vitro*, albeit less efficiently than FDX2 (Cai *et al.*, 2017). Notably, FDXs had been reduced with DT and the reductant was removed by dialysis prior to use. In contrast, this and previous works employing a physiological ETC with catalytic amounts of FDXR observed only FDX2 to support [2Fe-2S] cluster formation, even when using excess FDX1 (Figure 33) (Weibert *et al.*, 2014).

In summary, the two human FDXs fulfill highly distinct functions. In agreement, transcriptomics data show that both *FDX1* and *FDX2* genes are expressed in all analysed human cell types and tissues, with usually higher *FDX2* levels and extremely high *FDX1* levels in the steroid producing adrenal gland (Figure 47A). However, unexpectedly, FDX1 protein was detected by immunoblotting only in the steroid-producing organs testis, placenta and the adrenal gland with the associated kidney (Figure 47B and Sheftel *et al.*, 2010). This may indicate minimal FDX1 levels below the immunoblotting detection threshold being sufficient to support the synthesis of the lipoyl cofactor required in virtually all tissues.

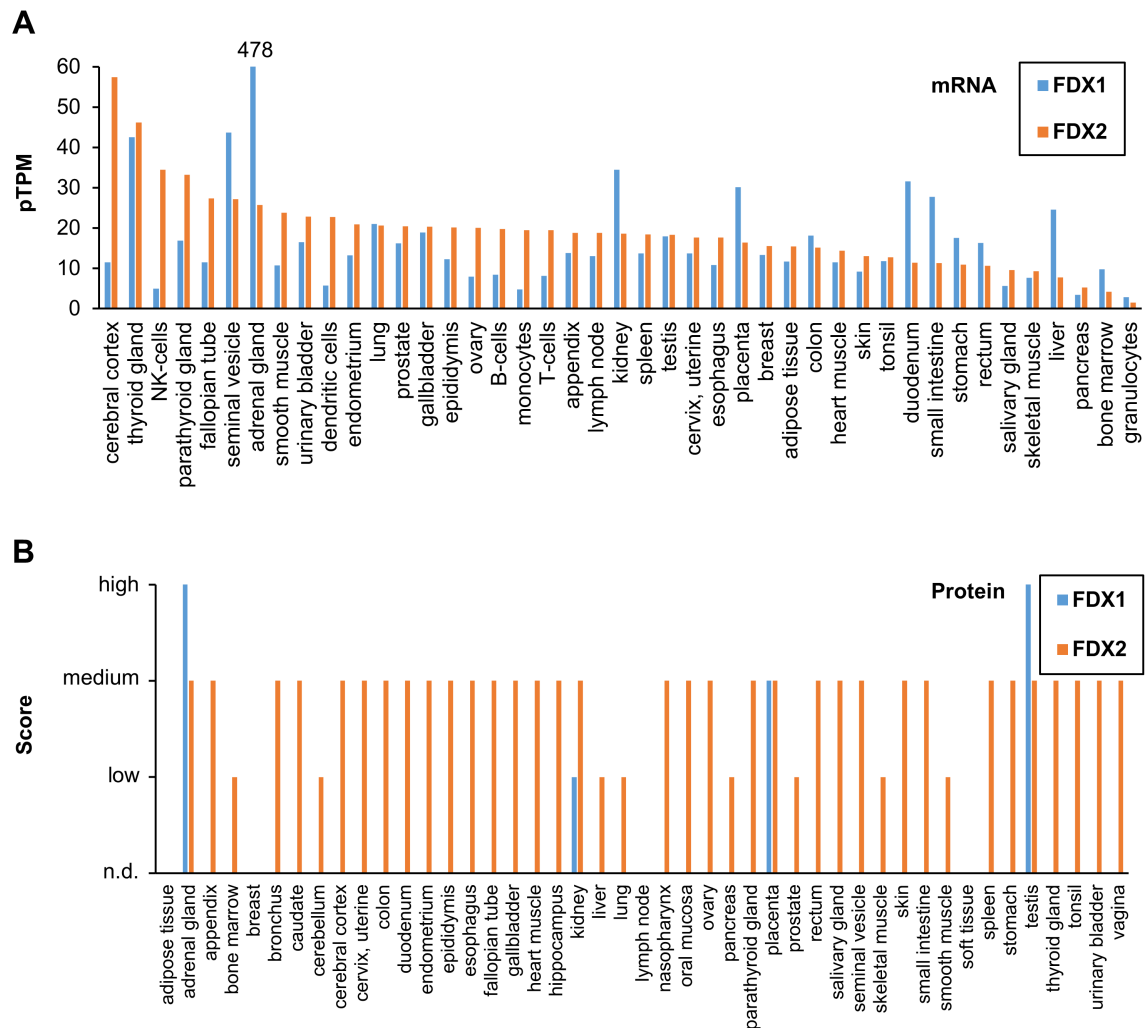


Figure 47: Tissue-specific protein and mRNA levels for human mitochondrial FDX1 and FDX2. A) Quantitative analysis of *FDX1* and *FDX2* mRNA levels represented in protein-coding transcripts per million (pTPM) across 43 tissues/cell types. **B)** Semi-quantitative analysis of FDX1 and FDX2 protein levels across 45 tissues by immunoblot analysis. Credit: Human Protein Atlas (Uhlen *et al.*, 2015); <https://www.proteinatlas.org/ENSG00000137714-FDX1/tissue> (A), <https://www.proteinatlas.org/ENSG00000267673-FDX2/tissue> (B), release 01.10.2020).

5.3.2 Electrostatic and specific intermolecular interactions are key determinants of human FDX specificity

As discussed above, human FDXs fulfil highly distinct and specific functions in mitochondria. Given the high structural similarity of FDX1 and 2 (Figure 12), a critical question was how this specificity may be achieved. Formation of electron transfer complexes typically requires two steps: An encounter complex is established mainly relying on electrostatic complementation, followed by formation of an electron-transferring stereospecific

complex supported by specific intermolecular contacts (see also chapter 1.5). An important determinant of electron transfer is furthermore the redox potential, with electrons flowing from the protein with lower to that with higher potential (Chiliza *et al.*, 2020).

FDX2 exhibits a lower redox potential (−342 mV) than FDX1 (−267 mV) (Sheftel *et al.*, 2010), which may contribute to the inability of FDX1 to participate in Fe/S protein biogenesis. Conversely, the inability of FDX2 to support LIAS, CYP and COX15 reduction cannot be explained by the redox potentials of human FDXs.

FDX1 and FDX2 show remarkably different electrostatic surfaces (Appendix Figure 69) possibly reflecting their differential functions. The depicted FDX1-type FDXs (FDX1 and *Bt* Adx) as well as fungal *Sp* Etp1^{fd} and *Sc* Yah1 exhibit a significantly stronger negative charge around the Fe/S cluster site than FDX2 and *E. coli* Fdx. Fungal Yah1 and Etp1^{fd} are needed for both Fe/S protein biogenesis and heme *a* synthesis, but have also been shown to enable CYP catalysis, despite not possessing endogenous mitochondrial CYPs (Schiffler *et al.*, 2004; Webert, 2011). The less negatively charged FDX2 and *Ec* Fdx exhibit a limited and thus more specific functionality. *E. coli* lacks CYPs (Jenkins & Waterman, 1994; Wittstock & Halkier, 2000) and heme *a* (Svensson *et al.*, 1993) and employs flavodoxin for lipoyl synthesis by LipA (Cicchillo *et al.*, 2004), hence Fdx function is likely limited to Fe/S protein biogenesis (Braymer *et al.*, 2020). Therefore, the stronger negative charge around the redox centers of FDX1-type and fungal FDXs might relate to their more diverse functionality. In a study of bacterial Fdx-CYP interactions, Fdxs interacting with a greater number of CYP partners were reported to exhibit a more negatively charged surface around their redox site (Zhang *et al.*, 2018).

Crystal structures of FDX1 in complex with FDXR, CYP11A1 and CYP11B2 as well as the modelled LIAS-GCSH-FDX1 trimer all show FDX1 interacting with redox partners via the cluster-coordinating loop C and the strongly negatively charged helix F (Brixius-Anderko & Scott, 2021; Muller *et al.*, 2001; Strushkevich *et al.*, 2011). Nevertheless, the crystal structures show that only two FDX1 residues (Asp132 and Asp136) interact with all of the partner proteins FDXR, CYP11A1 and CYP11B2 (Table 17) (Brixius-Anderko & Scott, 2021). Whilst loop C and helix F seemingly represent a conserved interaction region, their molecular interaction modes appear to differ depending on the redox partner.

The R135E variant of FDX2 enabling cortisol formation by CYP11B1 indicates the corresponding FDX1 residue Glu133 to be crucial for FDX1–CYP11B1 interaction (Webert, 2011). In accordance, all interacting CYP11B2 residues in the FDX1–CYP11B2 complex are also conserved in CYP11B1 (Brixius-Anderko & Scott, 2021). FDX1 Glu133 is strictly conserved in FDX1-type but not in FDX2-type FDXs, fitting its requirement for CYP interaction. Lipoylation assays with FDX2 variants done in this work did not correlate with

the results from cortisol formation. Here, variant Δ C12 but not R135E enabled highest lipoyl production, which may suggest the FDX2 C-terminus being a mediator of FDX specificity by interfering with LIAS interaction. Together, the data may indicate differing specific intermolecular interactions of FDX1–CYP11B1 compared to FDX1–LIAS.

Table 17: Intermolecular interactions of FDX1 with its redox partners. Interacting residues of helix F and the Fe/S cluster-coordinating loop C are listed for human FDX1–CYP11A1 (pdb code: 3N9Y) and FDX1–CYP11B2 (7M8I) as well as bovine FDX1–FDXR (1E6E). Only few of the FDX1 residues of helix F and loop C form similar interaction modes with different partner proteins.

Structural element	FDX1 residue	CYP11A1		CYP11B2		FDXR	
Loop C	Ala105	Lys109	H-bond				
	Cys106					Asn60	H-bond
	Glu107					Asn63	H-bond
	Leu110			Arg454	H-bond		
	Ala111	Glu422	H-bond				
	Ser113					Thr377	H-bond
Helix F	Asp132	Lys339	salt bridge	Arg432	salt bridge	Arg244	H-bond
	Glu133	Lys339	H-bond	Arg366	salt bridge		
	Asp136	Lys343	salt bridge	Arg366	salt bridge	Arg211	salt bridge
				Lys370	salt bridge		
				Arg432	salt bridge		
	Asp139			Phe438	H-bond	Arg240	salt bridge
	Leu140	Trp418	H-bond	Gln101	H-bond		
	Ala141			Asn437	H-bond		

Complementation studies in yeast indicated the conserved FDX2 C-terminus being crucial for Fe/S protein biogenesis, in good agreement with the fact that FDX2-type but not FDX1-type FDXs exhibit conservation of the 12 C-terminal residues (Webert, 2011). It has been shown that FDX2 can interact with NFS1 and, in its reduced state, also ISCU2 *in vitro* (Cai *et al.*, 2017; Kim *et al.*, 2013; Webert *et al.*, 2014; Yan *et al.*, 2013). Involvement of helix F in both protein interactions has been inferred from NMR data (Kim *et al.*, 2013; Webert *et al.*, 2014). It is tempting to speculate that furthermore the flexible FDX2 C-terminus is making contact to NFS1 and/or ISCU2.

In summary, electrostatic interactions, specific intermolecular interactions involving loop C and helix F, and the FDX2 C-terminus likely represent key features establishing differential specificities of human FDXs. Even though FDX1 seems to have a largely conserved interaction site with its various electron acceptors, specific intermolecular interactions appear to differ between redox partners. Whether the higher redox potential of FDX1 compared to FDX2 contributes to the inability of the former in supporting Fe/S protein biogenesis remains to be investigated.

5.3.3 Outlook

The *in vitro* lipoylation assay with exclusively human proteins established in this work enabled identification of FDX1 as the physiological electron donor, initiating the radical SAM-based reaction mechanism of LIAS. However, identification of Fe/S cluster donors regenerating the auxiliary LIAS cluster was hindered by limited lipoylation turnover *in vitro*. Prediction of catalytic complexes including LIAS, GCSH and FDX1 using AlphaFold suggested that presence of GCSH may be required for efficient LIAS-FDX1 interaction. Replacement of the employed octanoyl peptide substrate with octanoyl-GCSH in lipoylation assays may therefore enable improved turnover and possibly allow investigation of this interesting biochemical reaction in a more physiological fashion. In turn, this may enable the identification of potential regenerating Fe/S cluster donors ensuring multiple turnovers of human LIAS. [4Fe-4S]-NFX1 alone or in combination with BOLA3 and/or ISCA proteins appear to be suitable candidates. Furthermore, a LIAS species with only one [4Fe-4S] cluster bound could enable elucidation whether the same or different Fe/S cluster donors are required for insertion of the catalytic and auxiliary cluster, respectively. It should hence be assessed if such a species can be biochemically reconstituted. Finally, identifying the binding sites of Fe/S cluster donors would provide valuable insight into LIAS assembly and regeneration.

Subjecting FDX2 variants to the lipoylation assay revealed the FDX2 C-terminus to possibly mediate FDX2 specificity by interfering with LIAS interaction. Whereas structural modelling predicts FDX1 to bind LIAS via loop C and helix F (as in other FDX1 complexes), specific molecular interactions between both proteins remain to be identified. This could be achieved by subjecting interaction site variants of LIAS and FDX1 to the lipoylation assay. Furthermore, obtaining 3D structures of LIAS and ideally the LIAS-GCSH-FDX1 complex could provide valuable insight. Since anaerobic crystallization of LIAS was not successful in this work, cryo-EM may be employed as an alternate approach to solve the LIAS-GCSH-FDX1 structure. The small size of the trimeric complex (68 kDa) is close to the cryo-EM detection limit (Liu *et al.*, 2019). Hence, fusion of a nanobody-binding tag (Wu & Rapoport, 2021) to the LIAS C-terminus (which was predicted to be distant from the FDX1 and GCSH binding sites) may enable improved resolution. Structural and mutational analyses may also validate whether opening and closing of the catalytic cluster tunnel of LIAS represents a mechanism of regulating electron flow from FDX1. Lastly, characterising the interaction of LIAS with Ele:Cu might reveal how the metal-complex interferes with LIAS catalysis.

6 Literature

- Adam AC, Bornhövd C, Prokisch H, Neupert W, Hell K (2006) The Nfs1 interacting protein Isd11 has an essential role in Fe/S cluster biogenesis in mitochondria. *EMBO J* 25: 174-183
- Adinolfi S, Iannuzzi C, Prischi F, Pastore C, Iametti S, Martin SR, Bonomi F, Pastore A (2009) Bacterial frataxin CyaY is the gatekeeper of iron-sulfur cluster formation catalyzed by IscS. *Nat Struct Mol Biol* 16: 390-396
- Afonine PV, Poon BK, Read RJ, Sobolev OV, Terwilliger TC, Urzhumtsev A, Adams PD (2018) Real-space refinement in PHENIX for cryo-EM and crystallography. *Acta Crystallogr D Struct Biol* 74: 531-544
- Agar JN, Krebs C, Frazzon J, Huynh BH, Dean DR, Johnson MK (2000a) IscU as a scaffold for iron-sulfur cluster biosynthesis: sequential assembly of [2Fe-2S] and [4Fe-4S] clusters in IscU. *Biochemistry* 39: 7856-7862
- Agar JN, Zheng L, Cash VL, Dean DR, Johnson MK (2000b) Role of the IscU protein in iron-sulfur cluster biosynthesis: IscS-mediated assembly of a [Fe₂S₂] cluster in IscU. *J Am Chem Soc* 122: 2136-2137
- Al-Hassnan ZN, Al-Dosary M, Alfadhel M, Fageih EA, Alsagob M, Kenana R, Almass R, Al-Harazi OS, Al-Hindi H, Malibari OI *et al.* (2015) ISCA2 mutation causes infantile neurodegenerative mitochondrial disorder. *J Med Genet* 52: 186-194
- Alaimo JT, Besse A, Alston CL, Pang K, Appadurai V, Samanta M, Smpokou P, McFarland R, Taylor RW, Bonnen PE (2018) Loss-of-function mutations in ISCA2 disrupt 4Fe-4S cluster machinery and cause a fatal leukodystrophy with hyperglycinemia and mtDNA depletion. *Hum Mutat* 39: 537-549
- Alfadhel M, Nashabat M, Alrifai MT, Alshaalan H, Al Mutairi F, Al-Shahrani SA, Plecko B, Almass R, Alsagob M, Almutairi FB *et al.* (2018) Further delineation of the phenotypic spectrum of ISCA2 defect: A report of ten new cases. *Eur J Paediatr Neurol* 22: 46-55
- Anderson CP, Shen M, Eisenstein RS, Leibold EA (2012) Mammalian iron metabolism and its control by iron regulatory proteins. *Biochim Biophys Acta* 1823: 1468-1483
- Andreini C, Banci L, Rosato A (2016) Exploiting Bacterial Operons To Illuminate Human Iron-Sulfur Proteins. *J Proteome Res* 15: 1308-1322
- Andreini C, Rosato A, Banci L (2017) The Relationship between Environmental Dioxygen and Iron-Sulfur Proteins Explored at the Genome Level. *PLoS One* 12: e0171279
- Atkinson JT, Campbell I, Bennett GN, Silberg JJ (2016) Cellular Assays for Ferredoxins: A Strategy for Understanding Electron Flow through Protein Carriers That Link Metabolic Pathways. *Biochemistry* 55: 7047-7064
- Bailey TS, Zakharov LN, Pluth MD (2014) Understanding hydrogen sulfide storage: probing conditions for sulfide release from hydrodisulfides. *J Am Chem Soc* 136: 10573-10576
- Baker PR, 2nd, Friederich MW, Swanson MA, Shaikh T, Bhattacharya K, Scharer GH, Aicher J, Creadon-Swindell G, Geiger E, MacLean KN *et al.* (2014) Variant non ketotic hyperglycinemia is caused by mutations in LIAS, BOLA3 and the novel gene GLRX5. *Brain* 137: 366-379

- Banci L, Brancaccio D, Ciofi-Baffoni S, Del Conte R, Gadepalli R, Mikolajczyk M, Neri S, Piccioli M, Winkelmann J (2014) [2Fe-2S] cluster transfer in iron-sulfur protein biogenesis. *Proc Natl Acad Sci U S A* 111: 6203-6208
- Barros MH, Carlson CG, Glerum DM, Tzagoloff A (2001) Involvement of mitochondrial ferredoxin and Cox15p in hydroxylation of heme O. *FEBS Lett* 492: 133-138
- Barros MH, Nobrega FG, Tzagoloff A (2002) Mitochondrial ferredoxin is required for heme A synthesis in *Saccharomyces cerevisiae*. *J Biol Chem* 277: 9997-10002
- Bauer I, Knölker H-J (2008) Iron Complexes in Organic Chemistry. In *Iron Catalysis in Organic Chemistry* Plietker B (ed.) pp 1-27 WILEY-VCH Weinheim
- Behshad E, Bollinger JM, Jr. (2009) Kinetic analysis of cysteine desulfurase CD0387 from *Synechocystis* sp. PCC 6803: formation of the persulfide intermediate. *Biochemistry* 48: 12014-12023
- Beilschmidt LK, Puccio HM (2014) Mammalian Fe-S cluster biogenesis and its implication in disease. *Biochimie* 100: 48-60
- Beinert H, Holm RH, Münck E (1997) Iron-sulfur clusters: nature's modular, multipurpose structures. *Science* 277: 653-659
- Bencze KZ, Yoon T, Millan-Pacheco C, Bradley PB, Pastor N, Cowan JA, Stemmler TL (2007) Human frataxin: iron and ferrochelatase binding surface. *Chem Commun (Camb)* 14: 1798-1800
- Benz C, Kovarova J, Kralova-Hromadova I, Pierik AJ, Lukes J (2016) Roles of the Nfu Fe-S targeting factors in the trypanosome mitochondrion. *Int J Parasitol* 46: 641-651
- Bertini I, Donaire A, Feinberg BA, Luchinat C, Piccioli M, Yuan H (1995) Solution structure of the oxidized 2[4Fe-4S] ferredoxin from *Clostridium pasteurianum*. *Eur J Biochem* 232: 192-205
- Bian S, Cowan JA (1999) Protein-bound iron-sulfur centers. Form, function, and assembly. *Coordination Chemistry Reviews* 190-192: 1049-1066
- Bill E, Haas C, Ding XQ, Maret W, Winkler H, Trautwein AX, Zeppezauer M (1989) Fe(II)-substituted horse liver alcohol dehydrogenase, a model for non-heme iron enzymes. Various states of iron-dioxygen interaction investigated by Mossbauer and EPR spectroscopy. *Eur J Biochem* 180: 111-121
- Bingaman JL, Messina KJ, Bevilacqua PC (2017) Probing fast ribozyme reactions under biological conditions with rapid quench-flow kinetics. *Methods* 120: 125-134
- Blahut M, Sanchez E, Fisher CE, Outten FW (2020) Fe-S cluster biogenesis by the bacterial Suf pathway. *Biochim Biophys Acta Mol Cell Res* 1867: 118829
- Blahut M, Wise CE, Bruno MR, Dong G, Makris TM, Frantom PA, Dunkle JA, Outten FW (2019) Direct observation of intermediates in the SufS cysteine desulfurase reaction reveals functional roles of conserved active-site residues. *J Biol Chem* 294: 12444-12458
- Boniecki MT, Freibert SA, Muhlenhoff U, Lill R, Cygler M (2017) Structure and functional dynamics of the mitochondrial Fe/S cluster synthesis complex. *Nat Commun* 8: 1287
- Bonomi F, Iametti S, Morleo A, Ta D, Vickery LE (2011) Facilitated transfer of IscU-[2Fe2S] clusters by chaperone-mediated ligand exchange. *Biochemistry* 50: 9641-9650

- Booker SJ, Cicchillo RM, Grove TL (2007) Self-sacrifice in radical S-adenosylmethionine proteins. *Curr Opin Chem Biol* 11: 543-552
- Brancaccio D, Gallo A, Mikolajczyk M, Zovo K, Palumaa P, Novellino E, Piccioli M, Ciofi-Baffoni S, Banci L (2014) Formation of [4Fe-4S] clusters in the mitochondrial iron-sulfur cluster assembly machinery. *J Am Chem Soc* 136: 16240-16250
- Brancaccio D, Gallo A, Piccioli M, Novellino E, Ciofi-Baffoni S, Banci L (2017) [4Fe-4S] Cluster Assembly in Mitochondria and Its Impairment by Copper. *J Am Chem Soc* 139: 719-730
- Braymer JJ, Freibert SA, Rakwalska-Bange M, Lill R (2020) Mechanistic concepts of iron-sulfur protein biogenesis in Biology. *Biochim Biophys Acta Mol Cell Res* 1868: 118863
- Bridwell-Rabb J, Fox NG, Tsai CL, Winn AM, Barondeau DP (2014) Human Frataxin Activates Fe-S Cluster Biosynthesis by Facilitating Sulfur Transfer Chemistry. *Biochemistry* 53: 4904-4913
- Bridwell-Rabb J, Winn AM, Barondeau DP (2011) Structure-function analysis of Friedreich's ataxia mutants reveals determinants of frataxin binding and activation of the Fe-S assembly complex. *Biochemistry* 50: 7265-7274
- Brixius-Anderko S, Scott EE (2021) Structural and functional insights into aldosterone synthase interaction with its redox partner protein adrenodoxin. *J Biol Chem* 296: 100794
- Brown A, Rathore S, Kimanius D, Aibara S, Bai XC, Rorbach J, Amunts A, Ramakrishnan V (2017) Structures of the human mitochondrial ribosome in native states of assembly. *Nat Struct Mol Biol* 24: 866-869
- Brown EN, Friemann R, Karlsson A, Parales JV, Couture MM, Eltis LD, Ramaswamy S (2008) Determining Rieske cluster reduction potentials. *J Biol Inorg Chem* 13: 1301-1313
- Bryant P, Kriek M, Wood RJ, Roach PL (2006) The activity of a thermostable lipoyl synthase from *Sulfolobus solfataricus* with a synthetic octanoyl substrate. *Anal Biochem* 351: 44-49
- Bulut H, Valjakka J, Yuksel B, Yilmazer B, Turunen O, Binay B (2020) Effect of Metal Ions on the Activity of Ten NAD-Dependent Formate Dehydrogenases. *Protein J* 39: 519-530
- Bych K, Kerscher S, Netz DJ, Pierik AJ, Zwicker K, Huynen MA, Lill R, Brandt U, Balk J (2008) The iron-sulphur protein Ind1 is required for effective complex I assembly. *Embo J* 27: 1736-1746
- Cai K, Frederick RO, Dashti H, Markley JL (2018a) Architectural Features of Human Mitochondrial Cysteine Desulfurase Complexes from Crosslinking Mass Spectrometry and Small-Angle X-Ray Scattering. *Structure* 26: 1127-1136 e1124
- Cai K, Frederick RO, Tonelli M, Markley JL (2018b) Interactions of iron-bound frataxin with ISCU and ferredoxin on the cysteine desulfurase complex leading to Fe-S cluster assembly. *J Inorg Biochem* 183: 107-116
- Cai K, Liu G, Frederick RO, Xiao R, Montelione GT, Markley JL (2016) Structural/Functional Properties of Human NFU1, an Intermediate [4Fe-4S] Carrier in Human Mitochondrial Iron-Sulfur Cluster Biogenesis. *Structure* 24: 2080-2091

Cai K, Tonelli M, Frederick RO, Markley JL (2017) Human Mitochondrial Ferredoxin 1 (FDX1) and Ferredoxin 2 (FDX2) Both Bind Cysteine Desulfurase and Donate Electrons for Iron-Sulfur Cluster Biosynthesis. *Biochemistry* 56: 487-499

Calvo SE, Tucker EJ, Compton AG, Kirby DM, Crawford G, Burt NP, Rivas M, Guiducci C, Bruno DL, Goldberger OA *et al.* (2010) High-throughput, pooled sequencing identifies mutations in NUBPL and FOXRED1 in human complex I deficiency. *Nat Genet* 42: 851-858

Cameron JM, Janer A, Levandovskiy V, Mackay N, Rouault TA, Tong WH, Ogilvie I, Shoubridge EA, Robinson BH (2011) Mutations in iron-sulfur cluster scaffold genes NFU1 and BOLA3 cause a fatal deficiency of multiple respiratory chain and 2-oxoacid dehydrogenase enzymes. *Am J Hum Genet* 89: 486-495

Campbell IJ, Bennett GN, Silberg JJ (2019) Evolutionary Relationships Between Low Potential Ferredoxin and Flavodoxin Electron Carriers. *Frontiers in Energy Research* 7

Chiliza ZE, Martinez-Oyanedel J, Syed K (2020) An overview of the factors playing a role in cytochrome P450 monooxygenase and ferredoxin interactions. *Biophys Rev* 12: 1217-1222

Chillappagari S, Seubert A, Trip H, Kuipers OP, Marahiel MA, Miethke M (2010) Copper stress affects iron homeostasis by destabilizing iron-sulfur cluster formation in *Bacillus subtilis*. *J Bacteriol* 192: 2512-2524

Christ S, Leichert LI, Willms A, Lill R, Muhlenhoff U (2016) Defects in Mitochondrial Iron-Sulfur Cluster Assembly Induce Cysteine S-Polythiolation on Iron-Sulfur Apoproteins. *Antioxid Redox Signal* 25: 28-40

Cicchillo RM, Iwig DF, Jones AD, Nesbitt NM, Baleanu-Gogonea C, Souder MG, Tu L, Booker SJ (2004) Lipoyl synthase requires two equivalents of S-adenosyl-L-methionine to synthesize one equivalent of lipoic acid. *Biochemistry* 43: 6378-6386

Ciesielski SJ, Schilke BA, Osipiuk J, Bigelow L, Mulligan R, Majewska J, Joachimiak A, Marszalek J, Craig EA, Dutkiewicz R (2012) Interaction of J-protein co-chaperone Jac1 with Fe-S scaffold Isu is indispensable in vivo and conserved in evolution. *J Mol Biol* 417: 1-12

Coghlan VM, Vickery LE (1991) Site-specific mutations in human ferredoxin that affect binding to ferredoxin reductase and cytochrome P450_{scc}. *J Biol Chem* 266: 18606-18612

Cook A, Giunti P (2017) Friedreich's ataxia: clinical features, pathogenesis and management. *Br Med Bull* 124: 19-30

Cook JD, Kondapalli KC, Rawat S, Childs WC, Murugesan Y, Dancis A, Stemmler TL (2010) Molecular details of the yeast frataxin-Isu1 interaction during mitochondrial Fe-S cluster assembly. *Biochemistry* 49: 8756-8765

Cory SA, Van Vranken JG, Brignole EJ, Patra S, Winge DR, Drennan CL, Rutter J, Barondeau DP (2017) Structure of human Fe-S assembly subcomplex reveals unexpected cysteine desulfurase architecture and acyl-ACP-ISD11 interactions. *Proc Natl Acad Sci U S A* 114: E5325-E5334

Cronan JE (2016) Assembly of Lipoic Acid on Its Cognate Enzymes: an Extraordinary and Essential Biosynthetic Pathway. *Microbiol Mol Biol Rev* 80: 429-450

Dong G, Cao L, Ryde U (2018) Insight into the reaction mechanism of lipoyl synthase: a QM/MM study. *J Biol Inorg Chem* 23: 221-229

- Douglas P, Kriek M, Bryant P, Roach PL (2006) Lipoyl synthase inserts sulfur atoms into an octanoyl substrate in a stepwise manner. *Angew Chem Int Ed Engl* 45: 5197-5199
- Ducker GS, Rabinowitz JD (2017) One-Carbon Metabolism in Health and Disease. *Cell Metab* 25: 27-42
- Dutkiewicz R, Nowak M (2018) Molecular chaperones involved in mitochondrial iron-sulfur protein biogenesis. *J Biol Inorg Chem* 23: 569-579
- Dutkiewicz R, Schilke B, Cheng S, Knieszner H, Craig EA, Marszalek J (2004) Sequence-specific interaction between mitochondrial Fe-S scaffold protein Isu and Hsp70 Ssq1 is essential for their *in vivo* function. *J Biol Chem* 279: 29167-29174
- Dzul SP, Rocha AG, Rawat S, Kandedegara A, Kusowski A, Pain J, Murari A, Pain D, Dancis A, Stemmler TL (2017) In vitro characterization of a novel Isu homologue from *Drosophila melanogaster* for de novo FeS-cluster formation. *Metallomics* 9: 48-60
- Eck RV, Dayhoff MO (1966) Evolution of the structure of ferredoxin based on living relics of primitive amino acid sequences. *Science* 152: 363-366
- Einsle O, Rees DC (2020) Structural Enzymology of Nitrogenase Enzymes. *Chem Rev* 120: 4969-5004
- Ellinghaus TL, Marcellino T, Srinivasan V, Lill R, Kuhlbrandt W (2021) Conformational changes in the yeast mitochondrial ABC transporter Atm1 during the transport cycle. *Sci Adv* 7: eabk2392
- Emsley P, Lohkamp B, Scott WG, Cowtan K (2010) Features and development of Coot. *Acta Crystallogr D Biol Crystallogr* 66: 486-501
- Ewen KM, Ringle M, Bernhardt R (2012) Adrenodoxin--a versatile ferredoxin. *IUBMB Life* 64: 506-512
- Fox NG, Das D, Chakrabarti M, Lindahl PA, Barondeau DP (2015) Frataxin Accelerates [2Fe-2S] Cluster Formation on the Human Fe-S Assembly Complex. *Biochemistry* 54: 3880-3889
- Fox NG, Martelli A, Nabhan JF, Janz J, Borkowska O, Bulawa C, Yue WW (2018) Zinc(II) binding on human wild-type ISCU and Met140 variants modulates NFS1 desulfurase activity. *Biochimie* 152: 211-218
- Fox NG, Yu X, Feng X, Bailey HJ, Martelli A, Nabhan JF, Strain-Damerell C, Bulawa C, Yue WW, Han S (2019) Structure of the human frataxin-bound iron-sulfur cluster assembly complex provides insight into its activation mechanism. *Nat Commun* 10: 2210
- Frazier AE, Thorburn DR, Compton AG (2019) Mitochondrial energy generation disorders: genes, mechanisms, and clues to pathology. *J Biol Chem* 294: 5386-5395
- Freibert SA, Boniecki MT, Stumpfig C, Schulz V, Krapoth N, Winge DR, Muhlenhoff U, Stehling O, Cygler M, Lill R (2021) N-terminal tyrosine of ISCU2 triggers [2Fe-2S] cluster synthesis by ISCU2 dimerization. *Nat Commun* 12: 6902
- Freibert SA, Goldberg AV, Hacker C, Molik S, Dean P, Williams TA, Nakjang S, Long S, Sendra K, Bill E *et al.* (2017) Evolutionary conservation and in vitro reconstitution of microsporidian iron-sulfur cluster biosynthesis. *Nat Commun* 8: 13932

- Freibert SA, Weiler BD, Bill E, Pierik AJ, Muhlenhoff U, Lill R (2018) Biochemical Reconstitution and Spectroscopic Analysis of Iron-Sulfur Proteins. *Methods Enzymol* 599: 197-226
- Frey PA, Hegeman AD, Ruzicka FJ (2008) The Radical SAM Superfamily. *Crit Rev Biochem Mol Biol* 43: 63-88
- Fugate CJ, Jarrett JT (2012) Biotin synthase: insights into radical-mediated carbon-sulfur bond formation. *Biochim Biophys Acta* 1824: 1213-1222
- Fujiwara K, Motokawa Y (1983) Mechanism of the glycine cleavage reaction. Steady state kinetic studies of the P-protein-catalyzed reaction. *J Biol Chem* 258: 8156-8162
- Fung DK, Lau WY, Chan WT, Yan A (2013) Copper efflux is induced during anaerobic amino acid limitation in Escherichia coli to protect iron-sulfur cluster enzymes and biogenesis. *J Bacteriol* 195: 4556-4568
- Fuss JO, Tsai CL, Ishida JP, Tainer JA (2015) Emerging critical roles of Fe-S clusters in DNA replication and repair. *Biochim Biophys Acta* 1853: 1253-1271
- Garcia-Serres R, Clemancey M, Latour JM, Blondin G (2018) Contribution of Mossbauer spectroscopy to the investigation of Fe/S biogenesis. *J Biol Inorg Chem* 23: 635-644
- Gelling C, Dawes IW, Richhardt N, Lill R, Mühlenhoff U (2008) Mitochondrial Iba57p is required for Fe/S cluster formation on aconitase and activation of radical SAM enzymes. *Mol Cell Biol* 28: 1851-1861
- Gervason S, Larkem D, Mansour AB, Botzanowski T, Muller CS, Pecqueur L, Le Pavec G, Delaunay-Moisan A, Brun O, Agramunt J *et al.* (2019) Physiologically relevant reconstitution of iron-sulfur cluster biosynthesis uncovers persulfide-processing functions of ferredoxin-2 and frataxin. *Nat Commun* 10: 3566
- Goldman AD, Kacar B (2021) Cofactors are Remnants of Life's Origin and Early Evolution. *J Mol Evol* 89: 127-133
- Gourdoupis S, Nasta V, Calderone V, Ciofi-Baffoni S, Banci L (2018) IBA57 Recruits ISCA2 to Form a [2Fe-2S] Cluster-Mediated Complex. *J Am Chem Soc* 140: 14401-14412
- Gunnlaugsson H (2016) Spreadsheet based analysis of Mössbauer spectra. *Hyperfine Interactions* 237: 79
- Guthrie LM, Soma S, Yuan S, Silva A, Zulkifli M, Snively TC, Greene HF, Nunez E, Lynch B, De Ville C *et al.* (2020) Elesclomol alleviates Menkes pathology and mortality by escorting Cu to cuproenzymes in mice. *Science* 368: 620-625
- Hanke G, Mulo P (2013) Plant type ferredoxins and ferredoxin-dependent metabolism. *Plant, cell & environment* 36: 1071-1084
- Harmer JE, Hiscox MJ, Dinis PC, Fox SJ, Iliopoulos A, Hussey JE, Sandy J, Van Beek FT, Essex JW, Roach PL (2014) Structures of lipoyl synthase reveal a compact active site for controlling sequential sulfur insertion reactions. *Biochem J* 464: 123-133
- Hasinoff BB, Yadav AA, Patel D, Wu X (2014) The cytotoxicity of the anticancer drug elesclomol is due to oxidative stress indirectly mediated through its complex with Cu(II). *J Inorg Biochem* 137: 22-30

Hermes FA, Cronan JE (2013) The role of the *Saccharomyces cerevisiae* lipoate protein ligase homologue, Lip3, in lipoic acid synthesis. *Yeast* 30: 415-427

Hildenbeutel M, Hegg EL, Stephan K, Gruschke S, Meunier B, Ott M (2014) Assembly factors monitor sequential hemylation of cytochrome b to regulate mitochondrial translation. *J Cell Biol* 205: 511-524

Hiltunen JK, Autio KJ, Schonauer MS, Kursu VA, Dieckmann CL, Kastaniotis AJ (2010) Mitochondrial fatty acid synthesis and respiration. *Biochim Biophys Acta* 1797: 1195-1202

Hiruma Y, Hass MA, Kikui Y, Liu WM, Olmez B, Skinner SP, Blok A, Kloosterman A, Koteishi H, Lohr F *et al.* (2013) The structure of the cytochrome p450cam-putidaredoxin complex determined by paramagnetic NMR spectroscopy and crystallography. *J Mol Biol* 425: 4353-4365

Iannuzzi C, Adrover M, Puglisi R, Yan R, Temussi PA, Pastore A (2014) The role of zinc in the stability of the marginally stable IscU scaffold protein. *Protein Sci* 23: 1208-1219

Jain A, Singh A, Maio N, Rouault TA (2020) Assembly of the [4Fe-4S] cluster of NFU1 requires the coordinated donation of two [2Fe-2S] clusters from the scaffold proteins, ISCU2 and ISCA1. *Hum Mol Genet* 29: 3165-3182

Jenkins CM, Waterman MR (1994) Flavodoxin and NADPH-flavodoxin reductase from *Escherichia coli* support bovine cytochrome P450c17 hydroxylase activities. *J Biol Chem* 269: 27401-27408

Jeoung JH, Martins BM, Dobbek H (2020) Double-Cubane [8Fe9S] Clusters: A Novel Nitrogenase-Related Cofactor in Biology. *Chembiochem* 21: 1710-1716

Jia M, Sen S, Wachnowsky C, Fidai I, Cowan JA, Wysocki VH (2020) Characterization of [2Fe-2S]-Cluster-Bridged Protein Complexes and Reaction Intermediates by use of Native Mass Spectrometric Methods. *Angew Chem Int Ed Engl* 59: 6724-6728

Johnson DC, Dean DR, Smith AD, Johnson MK (2005) Structure, function and formation of biological iron-sulfur clusters. *Ann Rev Biochem* 74: 247-281

Johnson KM, Phan TTN, Albertolle ME, Guengerich FP (2017) Human mitochondrial cytochrome P450 27C1 is localized in skin and preferentially desaturates trans-retinol to 3,4-dehydroretinol. *J Biol Chem* 292: 13672-13687

Joseph AP, Lagerstedt I, Jakobi A, Burnley T, Patwardhan A, Topf M, Winn M (2020) Comparing Cryo-EM Reconstructions and Validating Atomic Model Fit Using Difference Maps. *J Chem Inf Model* 60: 2552-2560

Jumper J, Evans R, Pritzel A, Green T, Figurnov M, Ronneberger O, Tunyasuvunakool K, Bates R, Zidek A, Potapenko A *et al.* (2021) Highly accurate protein structure prediction with AlphaFold. *Nature* 596: 583-589

Kaiser JT, Clausen T, Bourenkow GP, Bartunik HD, Steinbacher S, Huber R (2000) Crystal structure of a NifS-like protein from *Thermotoga maritima*: Implications for iron-sulfur cluster assembly. *J Mol Biol* 297: 451-464

Kamyshny A, Jr., Ekelchik I, Gun J, Lev O (2006) Method for the determination of inorganic polysulfide distribution in aquatic systems. *Anal Chem* 78: 2631-2639

Kastaniotis AJ, Autio KJ, Keratar JM, Monteuuis G, Makela AM, Nair RR, Pietikainen LP, Shvetsova A, Chen Z, Hiltunen JK (2017) Mitochondrial fatty acid synthesis, fatty acids and mitochondrial physiology. *Biochim Biophys Acta Mol Cell Biol Lipids* 1862: 39-48

Kelly SM, Price NC (2000) The use of circular dichroism in the investigation of protein structure and function. *Curr Protein Pept Sci* 1: 349-384

Kikuchi G, Motokawa Y, Yoshida T, Hiraga K (2008) Glycine cleavage system: reaction mechanism, physiological significance, and hyperglycinemia. *Proc Jpn Acad Ser B Phys Biol Sci* 84: 246-263

Kim HJ, Khalimonchuk O, Smith PM, Winge DR (2012) Structure, function, and assembly of heme centers in mitochondrial respiratory complexes. *Biochim Biophys Acta* 1823: 1604-1616

Kim JH, Frederick RO, Reinen NM, Troupis AT, Markley JL (2013) [2Fe-2S]-Ferredoxin binds directly to cysteine desulfurase and supplies an electron for iron-sulfur cluster assembly but is displaced by the scaffold protein or bacterial frataxin. *J Am Chem Soc* 135: 8117-8120

Kimura S, Suzuki T (2015) Iron-sulfur proteins responsible for RNA modifications. *Biochim Biophys Acta* 1853: 1272-1283

Kirshner JR, He S, Balasubramanyam V, Kepros J, Yang CY, Zhang M, Du Z, Barsoum J, Bertin J (2008) Elesclomol induces cancer cell apoptosis through oxidative stress. *Mol Cancer Ther* 7: 2319-2327

Konz T, Montes-Bayon M, Sanz-Medel A (2014) Incorporation of (57)Fe-isotopically enriched in apoferritin: formation and characterization of isotopically enriched Fe nanoparticles for metabolic studies. *Analyst* 139: 5451-5459

Krebs C, Price JC, Baldwin J, Saleh L, Green MT, Bollinger JM, Jr. (2005) Rapid freeze-quench 57Fe Mossbauer spectroscopy: monitoring changes of an iron-containing active site during a biochemical reaction. *Inorg Chem* 44: 742-757

Kunichika K, Nakamura R, Fujishiro T, Takahashi Y (2021) The Structure of the Dimeric State of IscU Harboring Two Adjacent [2Fe-2S] Clusters Provides Mechanistic Insights into Cluster Conversion to [4Fe-4S]. *Biochemistry* 60: 1569-1572

Laemmli UK (1970) Cleavage of structural proteins during the assembly of the head of bacteriophage T4. *Nature* 227: 680-685

Lanz ND, Pandelia ME, Kakar ES, Lee KH, Krebs C, Booker SJ (2014) Evidence for a catalytically and kinetically competent enzyme-substrate cross-linked intermediate in catalysis by lipoyl synthase. *Biochemistry* 53: 4557-4572

Lee YH, Ikegami T, Standley DM, Sakurai K, Hase T, Goto Y (2011) Binding energetics of ferredoxin-NADP⁺ reductase with ferredoxin and its relation to function. *ChemBiochem* 12: 2062-2070

Li J, Saxena S, Pain D, Dancis A (2001) Adrenodoxin reductase homolog (Arh1p) of yeast mitochondria required for iron homeostasis. *J Biol Chem* 276: 1503-1509

Li Y, Liu PP, Ni X (2019) Molecular Evolution and Functional Analysis of Rubredoxin-Like Proteins in Plants. *Biomed Res Int* 2019: 2932585

Lill R (2009) Function and biogenesis iron-sulphur proteins. *Nature* 460: 831-838

- Lill R, Freibert SA (2020) Mechanisms of Mitochondrial Iron-Sulfur Protein Biogenesis. *Annu Rev Biochem* 89: 471-499
- Linder M (1991) *Biochemistry of Copper*. Springer Science+Business Media New York
- Liu J, Oganessian N, Shin DH, Jancarik J, Yokota H, Kim R, Kim SH (2005) Structural characterization of an iron-sulfur cluster assembly protein IscU in a zinc-bound form. *Proteins* 59: 875-881
- Liu Y, Huynh DT, Yeates TO (2019) A 3.8 Å resolution cryo-EM structure of a small protein bound to an imaging scaffold. *Nat Commun* 10: 1864
- Llopis J, McCaffery JM, Miyawaki A, Farquhar MG, Tsien RY (1998) Measurement of cytosolic, mitochondrial, and Golgi pH in single living cells with green fluorescent proteins. *Proc Natl Acad Sci U S A* 95: 6803-6808
- Lloyd SJ, Lauble H, Prasad GS, Stout CD (1999) The mechanism of aconitase: 1.8 Å resolution crystal structure of the S642A: citrate complex. *Protein Sci* 8: 2655-2662
- Long H, Chang CH, King PW, Ghirardi ML, Kim K (2008) Brownian dynamics and molecular dynamics study of the association between hydrogenase and ferredoxin from *Chlamydomonas reinhardtii*. *Biophys J* 95: 3753-3766
- Lossos A, Stumpfig C, Stevanin G, Gaussen M, Zimmerman BE, Mundwiler E, Asulin M, Chamma L, Sheffer R, Misk A *et al.* (2015) Fe/S protein assembly gene IBA57 mutation causes hereditary spastic paraplegia. *Neurology* 84: 659-667
- Macomber L, Imlay JA (2009) The iron-sulfur clusters of dehydratases are primary intracellular targets of copper toxicity. *Proc Natl Acad Sci U S A* 106: 8344-8349
- Manicki M, Majewska J, Ciesielski S, Schilke B, Blenska A, Kominek J, Marszalek J, Craig EA, Dutkiewicz R (2014) Overlapping binding sites of the frataxin homologue assembly factor and the heat shock protein 70 transfer factor on the Isu iron-sulfur cluster scaffold protein. *J Biol Chem* 289: 30268-30278
- Mansy SS, Wu G, Surerus KK, Cowan JA (2002) Iron-sulfur cluster biosynthesis. *Thermatoga maritima* IscU is a structured iron-sulfur cluster assembly protein. *J Biol Chem* 277: 21397-21404
- Marinoni EN, de Oliveira JS, Nicolet Y, Raulfs EC, Amara P, Dean DR, Fontecilla-Camps JC (2012) (IscS-IscU)₂ complex structures provide insights into Fe₂S₂ biogenesis and transfer. *Angew Chem Int Ed Engl* 51: 5439-5442
- Marquet A, Bui BT, Florentin D (2001) Biosynthesis of biotin and lipoic acid. *Vitam Horm* 61: 51-101
- Martinez-Julvez M, Medina M, Velazquez-Campoy A (2009) Binding thermodynamics of ferredoxin:NADP⁺ reductase: two different protein substrates and one energetics. *Biophys J* 96: 4966-4975
- Masud AJ, Kastaniotis AJ, Rahman MT, Autio KJ, Hiltunen JK (2019) Mitochondrial acyl carrier protein (ACP) at the interface of metabolic state sensing and mitochondrial function. *Biochim Biophys Acta Mol Cell Res* 1866: 118540
- Mayr JA, Feichtinger RG, Tort F, Ribes A, Sperl W (2014) Lipoic acid biosynthesis defects. *J Inherit Metab Dis* 37: 553-563

- McCarthy EL, Booker SJ (2017) Destruction and reformation of an iron-sulfur cluster during catalysis by lipoyl synthase. *Science* 358: 373-377
- McCarthy EL, Booker SJ (2018) Biochemical Approaches for Understanding Iron-Sulfur Cluster Regeneration in *Escherichia coli* Lipoyl Synthase During Catalysis. *Methods Enzymol* 606: 217-239
- McCarthy EL, Rankin AN, Dill ZR, Booker SJ (2019) The A-type domain in *Escherichia coli* NfuA is required for regenerating the auxiliary [4Fe-4S] cluster in *Escherichia coli* lipoyl synthase. *J Biol Chem* 294: 1609-1617
- McLaughlin MI, Lanz ND, Goldman PJ, Lee KH, Booker SJ, Drennan CL (2016) Crystallographic snapshots of sulfur insertion by lipoyl synthase. *Proc Natl Acad Sci U S A* 113: 9446-9450
- McLaughlin MP, Retegan M, Bill E, Payne TM, Shafaat HS, Pena S, Sudhamsu J, Ensign AA, Crane BR, Neese F *et al.* (2012) Azurin as a protein scaffold for a low-coordinate nonheme iron site with a small-molecule binding pocket. *J Am Chem Soc* 134: 19746-19757
- Melber A, Na U, Vashisht A, Weiler BD, Lill R, Wohlschlegel JA, Winge DR (2016) Role of Nfu1 and Bol3 in iron-sulfur cluster transfer to mitochondrial clients. *Elife* 5: e15991
- Mettert EL, Kiley PJ (2015) How Is Fe-S Cluster Formation Regulated? *Annu Rev Microbiol* 69: 505-526
- Meyer J (2008) Iron-sulfur protein folds, iron-sulfur chemistry, and evolution. *J Biol Inorg Chem* 13: 157-170
- Miethke M, Pierik AJ, Peuckert F, Seubert A, Marahiel MA (2011) Identification and characterization of a novel-type ferric siderophore reductase from a gram-positive extremophile. *J Biol Chem* 286: 2245-2260
- Modica-Napolitano JS, Bharath LP, Hanlon AJ, Hurley LD (2019) The Anticancer Agent Elesclomol Has Direct Effects on Mitochondrial Bioenergetic Function in Isolated Mammalian Mitochondria. *Biomolecules* 9: 298
- Morikawa T, Yasuno R, Wada H (2001) Do mammalian cells synthesize lipoic acid? Identification of a mouse cDNA encoding a lipoic acid synthase located in mitochondria. *FEBS Lett* 498: 16-21
- Mühlenhoff U, Richter N, Pines O, Pierik AJ, Lill R (2011) Specialized function of yeast Isa1 and Isa2 proteins in the maturation of mitochondrial [4Fe-4S] proteins. *J Biol Chem* 286: 41205-41216
- Muller JJ, Lapko A, Bourenkov G, Ruckpaul K, Heinemann U (2001) Adrenodoxin reductase - adrenodoxin complex structure suggests electron transfer path in steroid biosynthesis. *J Biol Chem* 276: 2786-2789
- Munteanu E, Verdier M, Grandjean-Forestier F, Stenger C, Jayat-Vignoles C, Huet S, Robert J, Ratinaud MH (2006) Mitochondrial localization and activity of P-glycoprotein in doxorubicin-resistant K562 cells. *Biochem Pharmacol* 71: 1162-1174

- Nagai M, Vo NH, Shin Ogawa L, Chimmanamada D, Inoue T, Chu J, Beaudette-Zlatanova BC, Lu R, Blackman RK, Barsoum J *et al.* (2012) The oncology drug elesclomol selectively transports copper to the mitochondria to induce oxidative stress in cancer cells. *Free Radic Biol Med* 52: 2142-2150
- Nasta V, Giachetti A, Ciofi-Baffoni S, Banci L (2017) Structural insights into the molecular function of human [2Fe-2S] BOLA1-GRX5 and [2Fe-2S] BOLA3-GRX5 complexes. *Biochim Biophys Acta Gen Subj* 1861: 2119-2131
- Navarro-Sastre A, Tort F, Stehling O, Uzarska MA, Arranz JA, Del Toro M, Labayru MT, Landa J, Font A, Garcia-Villoria J *et al.* (2011) A fatal mitochondrial disease is associated with defective NFU1 function in the maturation of a subset of mitochondrial Fe-S proteins. *Am J Hum Genet* 89: 656-667
- Netz DJ, Stith CM, Stumpfig M, Kopf G, Vogel D, Genau HM, Stodola JL, Lill R, Burgers PM, Pierik AJ (2012) Eukaryotic DNA polymerases require an iron-sulfur cluster for the formation of active complexes. *Nat Chem Biol* 8: 125-132
- Omura T (2006) Mitochondrial P450s. *Chem Biol Interact* 163: 86-93
- Ono K, Akaike T, Sawa T, Kumagai Y, Wink DA, Tantillo DJ, Hobbs AJ, Nagy P, Xian M, Lin J *et al.* (2014) Redox chemistry and chemical biology of H₂S, hydropersulfides, and derived species: implications of their possible biological activity and utility. *Free Radic Biol Med* 77: 82-94
- Ozeir M, Mühlenhoff U, Webert H, Lill R, Fontecave M, Pierrel F (2011) Coenzyme Q biosynthesis: Coq6 is required for the C5-hydroxylation reaction and substrate analogs rescue Coq6 deficiency. *Chem Biol* 18: 1134-1142
- Parent A, Elduque X, Cornu D, Belot L, Le Caer JP, Grandas A, Toledano MB, D'Autréaux B (2015) Mammalian frataxin directly enhances sulfur transfer of NFS1 persulfide to both ISCU and free thiols. *Nat Commun* 6: 5686
- Park CM, Weerasinghe L, Day JJ, Fukuto JM, Xian M (2015) Persulfides: current knowledge and challenges in chemistry and chemical biology. *Mol Biosyst* 11: 1775-1785
- Patra S, Barondeau DP (2019) Mechanism of activation of the human cysteine desulfurase complex by frataxin. *Proc Natl Acad Sci U S A* 116: 19421-19430
- Percudani R, Peracchi A (2009) The B6 database: a tool for the description and classification of vitamin B6-dependent enzymatic activities and of the corresponding protein families. *BMC Bioinformatics* 10: 273
- Pettersen EF, Goddard TD, Huang CC, Couch GS, Greenblatt DM, Meng EC, Ferrin TE (2004) UCSF Chimera--a visualization system for exploratory research and analysis. *J Comput Chem* 25: 1605-1612
- Pierella Karlusich JJ, Lodeyro AF, Carrillo N (2014) The long goodbye: the rise and fall of flavodoxin during plant evolution. *J Exp Bot* 65: 5161-5178
- Pierrel F, Hamelin O, Douki T, Kieffer-Jaquinod S, Muhlenhoff U, Ozeir M, Lill R, Fontecave M (2010) Involvement of mitochondrial ferredoxin and para-aminobenzoic acid in yeast coenzyme Q biosynthesis. *Chem Biol* 17: 449-459

- Pritts JD, Hursey MS, Michalek JL, Batelu S, Stemmler TL, Michel SLJ (2020) Unraveling the RNA Binding Properties of the Iron-Sulfur Zinc Finger Protein CPSF30. *Biochemistry* 59: 970-982
- Przybyla-Toscano J, Maclean AE, Franceschetti M, Liebsch D, Vignols F, Keech O, Rouhier N, Balk J (2022) Protein lipoylation in mitochondria requires Fe-S cluster assembly factors NFU4 and NFU5. *Plant Physiol* 188: 997-1013
- Przybyla-Toscano J, Roland M, Gaymard F, Couturier J, Rouhier N (2018) Roles and maturation of iron-sulfur proteins in plastids. *J Biol Inorg Chem* 23: 545-566
- Punjani A, Rubinstein JL, Fleet DJ, Brubaker MA (2017) cryoSPARC: algorithms for rapid unsupervised cryo-EM structure determination. *Nat Methods* 14: 290-296
- Py B, Gerez C, Angelini S, Planel R, Vinella D, Loiseau L, Talla E, Brochier-Armanet C, Garcia Serres R, Latour JM *et al.* (2012) Molecular organization, biochemical function, cellular role and evolution of NfuA, an atypical Fe-S carrier. *Mol Microbiol* 86: 155-171
- Rahman S, Mayr JA (2016) Disorders of Oxidative Phosphorylation. In: *Inborn Metabolic Diseases: Diagnosis and Treatment*, Saudubray J.-M., Baumgartner M.R., Walter J. (eds.) pp 223-242 Springer Berlin Heidelberg
- Ramelot TA, Cort JR, Goldsmith-Fischman S, Kornhaber GJ, Xiao R, Shastry R, Acton TB, Honig B, Montelione GT, Kennedy MA (2004) Solution NMR structure of the iron-sulfur cluster assembly protein U (IscU) with zinc bound at the active site. *J Mol Biol* 344: 567-583
- Raran-Kurussi S, Cherry S, Zhang D, Waugh DS (2017) Removal of Affinity Tags with TEV Protease. *Methods Mol Biol* 1586: 221-230
- Reed LJ (2001) A trail of research from lipoic acid to alpha-keto acid dehydrogenase complexes. *J Biol Chem* 276: 38329-38336
- Rohou A, Grigorieff N (2015) CTFFIND4: Fast and accurate defocus estimation from electron micrographs. *J Struct Biol* 192: 216-221
- Rupnik K, Lee CC, Hu Y, Ribbe MW, Hales BJ (2011) [4Fe4S]₂⁺ clusters exhibit ground-state paramagnetism. *J Am Chem Soc* 133: 6871-6873
- Santo-Domingo J, Demareux N (2012) Perspectives on: SGP symposium on mitochondrial physiology and medicine: the renaissance of mitochondrial pH. *J Gen Physiol* 139: 415-423
- Santos R, Lefevre S, Sliwa D, Seguin A, Camadro JM, Lesuisse E (2010) Friedreich ataxia: molecular mechanisms, redox considerations, and therapeutic opportunities. *Antioxid Redox Signal* 13: 651-690
- Saudino G, Ciofi-Baffoni S, Banci L (2022) Protein-Interaction Affinity Gradient Drives [4Fe-4S] Cluster Insertion in Human Lipoyl Synthase. *J Am Chem Soc* 144: 5713-5717
- Schagger H (2006) Tricine-SDS-PAGE. *Nat Protoc* 1: 16-22
- Schiffler B, Bureik M, Reinle W, Muller EC, Hannemann F, Bernhardt R (2004) The adrenodoxin-like ferredoxin of *Schizosaccharomyces pombe* mitochondria. *J Inorg Biochem* 98: 1229-1237

- Schmucker S, Martelli A, Colin F, Page A, Wattenhofer-Donze M, Reutenauer L, Puccio H (2011) Mammalian frataxin: an essential function for cellular viability through an interaction with a preformed ISCU/NFS1/ISD11 iron-sulfur assembly complex. *PLoS One* 6: e16199
- Schneider G, Kack H, Lindqvist Y (2000) The manifold of vitamin B6 dependent enzymes. *Structure* 8: R1-6
- Schonauer MS, Kastaniotis AJ, Kursu VA, Hiltunen JK, Dieckmann CL (2009) Lipoic acid synthesis and attachment in yeast mitochondria. *J Biol Chem* 284: 23234-23242
- Schünemann V, Winkler H (2000) Structure and dynamics of biomolecules studied by Mössbauer spectroscopy. *Reports on Progress in Physics* 63: 263-353
- Sen S, Hendricks AL, Cowan JA (2021) Cluster exchange reactivity of [2Fe-2S]-bridged heterodimeric BOLA1-GLRX5. *FEBS J* 288: 920-929
- Shaag A, Saada A, Berger I, Mandel H, Joseph A, Feigenbaum A, Elpeleg ON (1999) Molecular basis of lipoamide dehydrogenase deficiency in Ashkenazi Jews. *Am J Med Genet* 82: 177-182
- Sheftel AD, Stehling O, Pierik AJ, Elsasser HP, Muhlenhoff U, Weibert H, Hobler A, Hannemann F, Bernhardt R, Lill R (2010) Humans possess two mitochondrial ferredoxins, Fdx1 and Fdx2, with distinct roles in steroidogenesis, heme, and Fe/S cluster biosynthesis. *Proc Natl Acad Sci U S A* 107: 11775-11780
- Sheftel AD, Stehling O, Pierik AJ, Netz DJ, Kerscher S, Elsässer HP, Wittig I, Balk J, Brandt U, Lill R (2009) Human ind1, an iron-sulfur cluster assembly factor for respiratory complex I. *Mol Cell Biol* 29: 6059-6073
- Shi Y, Ghosh M, Kovtunovich G, Crooks DR, Rouault TA (2012) Both human ferredoxins 1 and 2 and ferredoxin reductase are important for iron-sulfur cluster biogenesis. *Biochim Biophys Acta* 1823: 484-492
- Shimomura Y, Kamikubo H, Nishi Y, Masako T, Kataoka M, Kobayashi Y, Fukuyama K, Takahashi Y (2007) Characterization and crystallization of an IscU-type scaffold protein with bound [2Fe-2S] cluster from the hyperthermophile, aquifex aeolicus. *J Biochem* 142: 577-586
- Shimomura Y, Wada K, Fukuyama K, Takahashi Y (2008) The asymmetric trimeric architecture of [2Fe-2S] IscU: implications for its scaffolding during iron-sulfur cluster biosynthesis. *J Mol Biol* 383: 133-143
- Snyder JP, Carlsen L (1977) Lone pair-lone pair interactions in unsymmetrical systems: RSSR vs. RSOR. *J Am Chem Soc* 99: 2931-2942
- Soliz M (2018) Copper Toxicity. In *Copper and Bacteria* pp 11-19 Springer Cham
- Solomonson A, DeBerardinis RJ (2018) Lipoic acid metabolism and mitochondrial redox regulation. *J Biol Chem* 293: 7522-7530
- Soreze Y, Boutron A, Habarou F, Barnerias C, Nonnenmacher L, Delpech H, Mamoune A, Chretien D, Hubert L, Bole-Feysot C *et al.* (2013) Mutations in human lipoyltransferase gene LIPT1 cause a Leigh disease with secondary deficiency for pyruvate and alpha-ketoglutarate dehydrogenase. *Orphanet J Rare Dis* 8: 192
- Sousa FL, Thiergart T, Landan G, Nelson-Sathi S, Pereira IA, Allen JF, Lane N, Martin WF (2013) Early bioenergetic evolution. *Philos Trans R Soc Lond B Biol Sci* 368: 20130088

- Stehling O, Wilbrecht C, Lill R (2014) Mitochondrial iron–sulfur protein biogenesis and human disease. *Biochimie* 100: 61-77
- Stemmler TL, Lesuisse E, Pain D, Dancis A (2010) Frataxin and mitochondrial FeS cluster biogenesis. *J Biol Chem* 285: 26737-26743
- Strushkevich N, MacKenzie F, Cherkesova T, Grabovec I, Usanov S, Park HW (2011) Structural basis for pregnenolone biosynthesis by the mitochondrial monooxygenase system. *Proc Natl Acad Sci U S A* 108: 10139-10143
- Studier FW, Rosenberg AH, Dunn JJ, Dubendorff JW (1990) Use of T7 RNA polymerase to direct expression of cloned genes. *Methods Enzymol* 185: 60-89
- Suraci D, Saudino G, Nasta V, Ciofi-Baffoni S, Banci L (2021) ISCA1 Orchestrates ISCA2 and NFU1 in the Maturation of Human Mitochondrial [4Fe-4S] Proteins. *J Mol Biol* 433: 166924
- Svensson B, Lubben M, Hederstedt L (1993) Bacillus subtilis CtaA and CtaB function in haem A biosynthesis. *Mol Microbiol* 10: 193-201
- Swenson SA, Moore CM, Marcero JR, Medlock AE, Reddi AR, Khalimonchuk O (2020) From Synthesis to Utilization: The Ins and Outs of Mitochondrial Heme. *Cells* 9: 579
- Tada K, Kure S (2005) Nonketotic hyperglycinemia: Pathophysiological studies. *Proceedings of The Japan Academy Series B-physical and Biological Sciences - PROC JPN ACAD B* 81: 411-417
- Tao L, Stich TA, Fugate CJ, Jarrett JT, Britt RD (2018) EPR-Derived Structure of a Paramagnetic Intermediate Generated by Biotin Synthase BioB. *J Am Chem Soc* 140: 12947-12963
- Toldo I, Nosadini M, Boscardin C, Talenti G, Manara R, Lamantea E, Legati A, Ghezzi D, Perilongo G, Sartori S (2018) Neonatal mitochondrial leukoencephalopathy with brain and spinal involvement and high lactate: expanding the phenotype of ISCA2 gene mutations. *Metab Brain Dis* 33: 805-812
- Tong WH, Jameson GN, Huynh BH, Rouault TA (2003) Subcellular compartmentalization of human Nfu, an iron-sulfur cluster scaffold protein, and its ability to assemble a [4Fe-4S] cluster. *Proc Natl Acad Sci U S A* 100: 9762-9767
- Torraco A, Stehling O, Stumpf C, Rosser R, De Rasmio D, Fiermonte G, Verrigni D, Rizza T, Voza A, Di Nottia M *et al.* (2018) ISCA1 Mutation In A Patient With Infantile-Onset Leukodystrophy Causes Defects In Mitochondrial [4Fe-4S] Proteins. *Hum Mol Genet* 27: 2739-2754
- Tort F, Ferrer-Cortes X, Thio M, Navarro-Sastre A, Matalonga L, Quintana E, Bujan N, Arias A, Garcia-Villoria J, Acquaviva C *et al.* (2014) Mutations in the lipoyltransferase LIPT1 gene cause a fatal disease associated with a specific lipoylation defect of the 2-ketoacid dehydrogenase complexes. *Hum Mol Genet* 23: 1907-1915
- Tran QM, Rothery RA, Maklashina E, Cecchini G, Weiner JH (2006) The quinone binding site in Escherichia coli succinate dehydrogenase is required for electron transfer to the heme b. *J Biol Chem* 281: 32310-32317
- Tsai CL, Barondeau DP (2010) Human frataxin is an allosteric switch that activates the Fe-S cluster biosynthetic complex. *Biochemistry* 49: 9132-9139

- Tsuda-Sakurai K, Miura M (2019) The hidden nature of protein translational control by diphthamide: the secrets under the leather. *J Biochem* 165: 1-8
- Tsvetkov P, Coy S, Petrova B, Dreishpoon M, Verma A, Abdusamad M, Rossen J, Joesch-Cohen L, Humeidi R, Spangler RD *et al.* (2022) Copper induces cell death by targeting lipoylated TCA cycle proteins. *Science* 375: 1254-1261
- Tsvetkov P, Detappe A, Cai K, Keys HR, Brune Z, Ying W, Thiru P, Reidy M, Kugener G, Rossen J *et al.* (2019) Mitochondrial metabolism promotes adaptation to proteotoxic stress. *Nat Chem Biol* 15: 681-689
- Tucker NP, D'Autreaux B, Yousafzai FK, Fairhurst SA, Spiro S, Dixon R (2008) Analysis of the nitric oxide-sensing non-heme iron center in the NorR regulatory protein. *J Biol Chem* 283: 908-918
- Uhlen M, Fagerberg L, Hallstrom BM, Lindskog C, Oksvold P, Mardinoglu A, Sivertsson A, Kampf C, Sjostedt E, Asplund A *et al.* (2015) Proteomics. Tissue-based map of the human proteome. *Science* 347: 1260419
- Uzarska MA, Grochowina I, Soldek J, Jelen M, Schilke B, Marszalek J, Craig EA, Dutkiewicz R (2022) During FeS cluster biogenesis, ferredoxin and frataxin use overlapping binding sites on yeast cysteine desulfurase Nfs1. *J Biol Chem* 298: 101570
- Uzarska MA, Nasta V, Weiler BD, Spantgar F, Ciofi-Baffoni S, Saviello MR, Gonnelli L, Muhlenhoff U, Banci L, Lill R (2016) Mitochondrial Bol1 and Bol3 function as assembly factors for specific iron-sulfur proteins. *Elife* 5: e16673
- Uzarska MA, Przybyla-Toscano J, Spantgar F, Zannini F, Lill R, Muhlenhoff U, Rouhier N (2018) Conserved functions of Arabidopsis mitochondrial late-acting maturation factors in the trafficking of ironsulfur clusters. *Biochim Biophys Acta Mol Cell Res* 1865: 1250-1259
- Vallieres C, Holland SL, Avery SV (2017) Mitochondrial Ferredoxin Determines Vulnerability of Cells to Copper Excess. *Cell Chem Biol* 24: 1228-1237 e1223
- Van Vranken JG, Jeong MY, Wei P, Chen YC, Gygi SP, Winge DR, Rutter J (2016) The mitochondrial acyl carrier protein (ACP) coordinates mitochondrial fatty acid synthesis with iron sulfur cluster biogenesis. *Elife* 5: e17828
- Varadi M, Anyango S, Deshpande M, Nair S, Natassia C, Yordanova G, Yuan D, Stroe O, Wood G, Laydon A *et al.* (2022) AlphaFold Protein Structure Database: massively expanding the structural coverage of protein-sequence space with high-accuracy models. *Nucleic Acids Res* 50: D439-D444
- Vaubel RA, Isaya G (2013) Iron-sulfur cluster synthesis, iron homeostasis and oxidative stress in Friedreich ataxia. *Mol Cell Neurosci* 55: 50-61
- Venkateswara Rao P, Holm RH (2004) Synthetic analogues of the active sites of iron-sulfur proteins. *Chem Rev* 104: 527-559
- Vo NH, Xia Z, Hanko J, Yun T, Bloom S, Shen J, Koya K, Sun L, Chen S (2014) Synthesis, crystallographic characterization and electrochemical property of a copper(II) complex of the anticancer agent elesclomol. *J Inorg Biochem* 130: 69-73

- Wachnowsky C, Rao B, Sen S, Fries B, Howard CJ, Ottesen JJ, Cowan JA (2019) Reconstitution, characterization, and [2Fe-2S] cluster exchange reactivity of a holo human BOLA3 homodimer. *J Biol Inorg Chem* 24: 1035-1045
- Webert H (2011) Strukturelle und funktionelle Charakterisierung von Komponenten der eukaryotischen Eisen-Schwefel-Cluster-Biogenese-Maschinerie.
- Webert H, Freibert SA, Gallo A, Heidenreich T, Linne U, Amlacher S, Hurt E, Mühlenhoff U, Banci L, Lill R (2014) Functional reconstitution of mitochondrial Fe/S cluster synthesis on Isu1 reveals the involvement of ferredoxin. *Nat Commun* 5: 5013
- Weiler BD, Bruck MC, Kothe I, Bill E, Lill R, Mühlenhoff U (2020) Mitochondrial [4Fe-4S] protein assembly involves reductive [2Fe-2S] cluster fusion on ISCA1-ISCA2 by electron flow from ferredoxin FDX2. *Proc Natl Acad Sci U S A* 117: 20555-20565
- Wiedemann N, Urzica E, Guiard B, Müller H, Lohaus C, Meyer HE, Ryan MT, Meisinger C, Mühlenhoff U, Lill R *et al.* (2006) Essential role of Isd11 in mitochondrial iron-sulfur cluster synthesis on Isu scaffold proteins. *Embo J* 25: 184-195
- Willems P, Wanschers BF, Esseling J, Szklarczyk R, Kudla U, Duarte I, Forkink M, Nootboom M, Swarts H, Gloerich J *et al.* (2013) BOLA1 is an aerobic protein that prevents mitochondrial morphology changes induced by glutathione depletion. *Antioxid Redox Signal* 18: 129-138
- Wirth C, Brandt U, Hunte C, Zickermann V (2016) Structure and function of mitochondrial complex I. *Biochim Biophys Acta* 1857: 902-914
- Wittstock U, Halkier BA (2000) Cytochrome P450 CYP79A2 from *Arabidopsis thaliana* L. Catalyzes the conversion of L-phenylalanine to phenylacetaldoxime in the biosynthesis of benzylglucosinolate. *J Biol Chem* 275: 14659-14666
- Wu G, Mansy SS, Wu Sp SP, Surerus KK, Foster MW, Cowan JA (2002a) Characterization of an Iron-Sulfur Cluster Assembly Protein (ISU1) from *Schizosaccharomyces pombe*. *Biochemistry* 41: 5024-5032
- Wu SP, Wu G, Surerus KK, Cowan JA (2002b) Iron-sulfur cluster biosynthesis. Kinetic analysis of [2Fe-2S] cluster transfer from holo ISU to apo Fd: role of redox chemistry and a conserved aspartate. *Biochemistry* 41: 8876-8885
- Wu X, Rapoport TA (2021) Cryo-EM structure determination of small proteins by nanobody-binding scaffolds (Legobodies). *Proc Natl Acad Sci U S A* 118: e2115001118
- Xu X, Reinle W, Hannemann F, Konarev PV, Svergun DI, Bernhardt R, Ubbink M (2008) Dynamics in a pure encounter complex of two proteins studied by solution scattering and paramagnetic NMR spectroscopy. *J Am Chem Soc* 130: 6395-6403
- Yadav AA, Patel D, Wu X, Hasinoff BB (2013) Molecular mechanisms of the biological activity of the anticancer drug elesclomol and its complexes with Cu(II), Ni(II) and Pt(II). *J Inorg Biochem* 126: 1-6
- Yan R, Konarev PV, Iannuzzi C, Adinolfi S, Roche B, Kelly G, Simon L, Martin SR, Py B, Barras F *et al.* (2013) Ferredoxin competes with bacterial frataxin in binding to the desulfurase IscS. *J Biol Chem* 288: 24777-24787

- Yoon T, Cowan JA (2003) Iron-sulfur cluster biosynthesis. Characterization of frataxin as an iron donor for assembly of [2Fe-2S] clusters in ISU-type proteins. *J Am Chem Soc* 125: 6078-6084
- Yoshida T, Kikuchi G (1972) Comparative study on major pathways of glycine and serine catabolism in vertebrate livers. *J Biochem* 72: 1503-1516
- Yoshida T, Kikuchi G (1973) Major pathways of serine and glycine catabolism in various organs of the rat and cock. *J Biochem* 73: 1013-1022
- Yun CH, Crofts AR, Gennis RB (1991) Assignment of the histidine axial ligands to the cytochrome bH and cytochrome bL components of the bc1 complex from *Rhodobacter sphaeroides* by site-directed mutagenesis. *Biochemistry* 30: 6747-6754
- Zhang W, Du L, Li F, Zhang X, Qu Z, Han L, Li Z, Sun J, Qi F, Yao Q *et al.* (2018) Mechanistic Insights into Interactions between Bacterial Class I P450 Enzymes and Redox Partners. *ACS Catalysis* 8: 9992-10003
- Zheng L, Dean DR (1994) Catalytic formation of a nitrogenase iron-sulfur cluster. *J Biol Chem* 269: 18723-18726
- Zheng SQ, Palovcak E, Armache JP, Verba KA, Cheng Y, Agard DA (2017) MotionCor2: anisotropic correction of beam-induced motion for improved cryo-electron microscopy. *Nat Methods* 14: 331-332
- Zhu J, Vinothkumar KR, Hirst J (2016) Structure of mammalian respiratory complex I. *Nature* 536: 354-358
- Zimorski V, Ku C, Martin WF, Gould SB (2014) Endosymbiotic theory for organelle origins. *Curr Opin Microbiol* 22: 38-48
- Zivanov J, Nakane T, Forsberg BO, Kimanius D, Hagen WJ, Lindahl E, Scheres SH (2018) New tools for automated high-resolution cryo-EM structure determination in RELION-3. *Elife* 7: e42166

7 Appendix

7.1 Figures

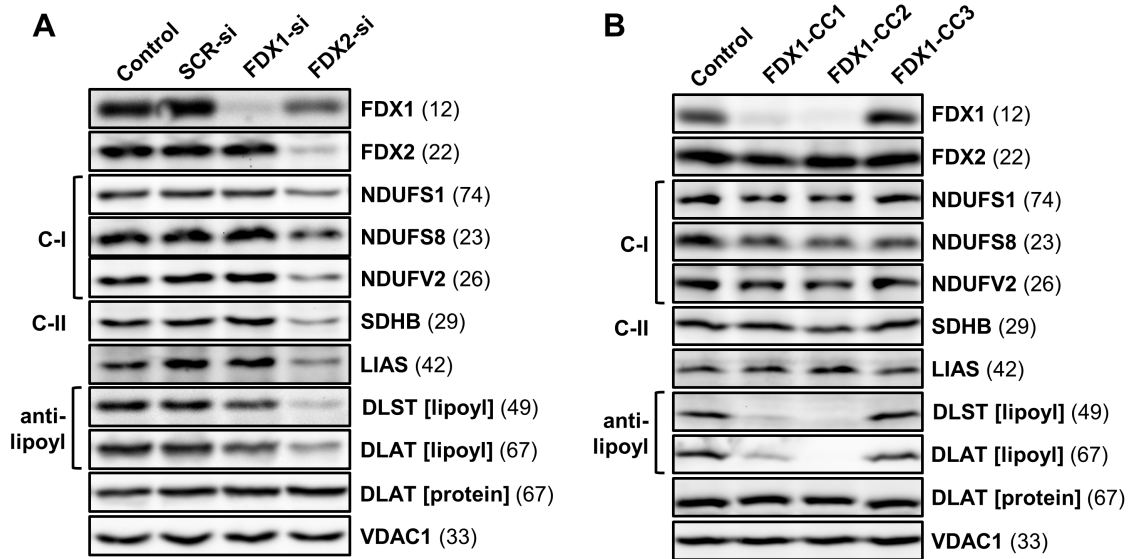


Figure 48: Function of both FDX2 and FDX1 is required for lipoyl synthesis. A) In an RNAi depletion approach, HEK293 cells were transfected without (control) or with scrambled (SCR) non-targeting siRNA, or with pools of *FDX1*- or *FDX2*-directed siRNAs (si). *FDX2* depletion led to decreased levels of the Fe/S proteins *FDX1*, subunits of respiratory chain complexes I (C-I) and II (C-II) as well as *LIAS*, in line with the crucial function of *FDX2* in Fe/S protein biogenesis. As a consequence of impaired *LIAS* maturation, lipoyl levels of *DLST* and *DLAT*, the lipoyl-binding subunits of *KGDH* and *PDH*, respectively, were decreased. Depletion of *FDX1* did not affect Fe/S protein levels but led to a slight decrease of *DLST* and *DLAT* lipoyl levels. **B)** As RNAi-mediated depletion of *FDX1* might not have revealed the full phenotypical consequences, CRISPR-Cas9-based deletion was performed subsequently. HEK293 cells were transfected with the empty plasmid PX459 (control) or with plasmids containing three different *FDX1*-directed gRNAs (CC1 to CC3). CC2 led to virtually complete *FDX1* deletion, whereas no significant effect was observed with CC3. Fe/S protein levels of *FDX2*, subunits of respiratory chain complexes I and II as well as *LIAS* were hardly affected, in line with *FDX1* not participating in Fe/S protein biogenesis (Schulz *et al.*, submitted manuscript; Sheftel *et al.*, 2010; Webert *et al.*, 2014). This was further supported by enzyme activities of aconitase and complex II not significantly being affected by *FDX1* deletion (not shown). Despite *LIAS* protein levels not being diminished, lipoyl levels of *DLST* and *DLAT* were decreased dramatically. In contrast, *DLAT* protein levels were not affected. Overall, the experiments show lipoylation to depend on both *FDX2* and *FDX1*. Whereas the requirement of *FDX2* is explained by its role in Fe/S cluster assembly of *LIAS*, *FDX1* appears to fulfil a different function. The *in vitro* studies in this work have revealed *FDX1* to function as electron donor for the catalytic cluster of *LIAS* to enable the radical SAM reaction mechanism. Observed molecular masses (kDa) of the proteins are given in parentheses. Experiments were performed by Dr. S. Basu and Dr. O. Stehling (Schulz *et al.*, submitted manuscript).

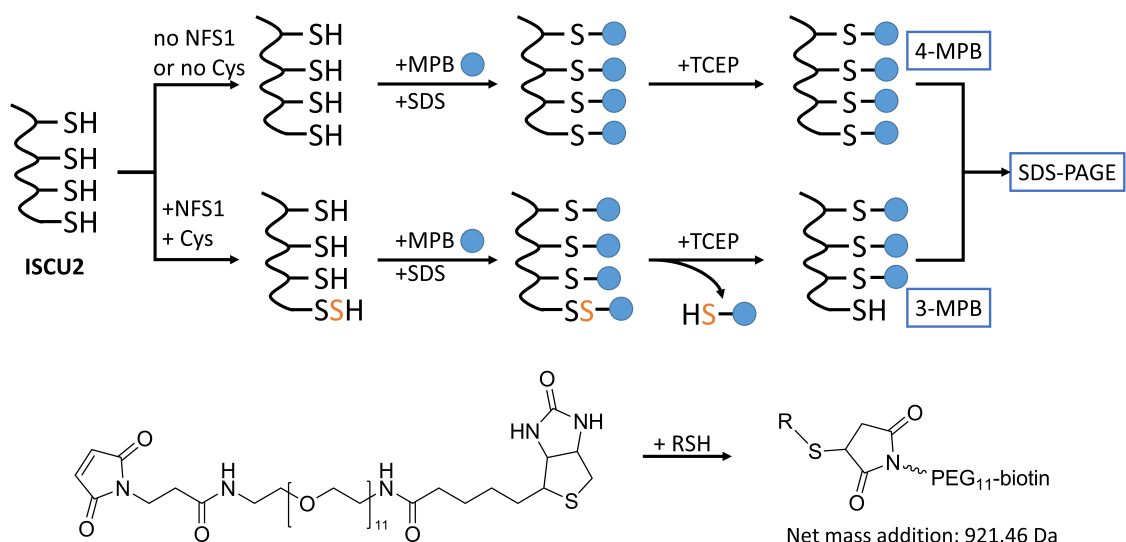


Figure 49: Schematic outline of the MPB-based ISCU2 persulfidation assay. ISCU2 containing four Cys residues (-SH) is incubated with excess NIA, FXN, Fe(II) (to ensure all ISCU2 is bound in an (Fe-NIAUX)₂ complex) and ascorbate (to maintain Fe as Fe(II)). Addition of free cysteine induces persulfide formation on Cys381^{NFS1} by the cysteine desulfurase complex (NIA)₂ under concomitant release of alanine (not shown). Cys381^{NFS1} then transfers the persulfide sulfur to a Cys residue on ISCU2. The reaction is quenched by adding maleimide-polyethyleneglycol₁₁-biotin (MPB), labelling all thiols including persulfides, leading to a net mass addition of 921.46 Da per molecule MPB. Addition of SDS denatures all proteins, ensuring that the physiological reaction is stopped and that also otherwise sterically hindered Cys residues will be labelled completely. Subsequently, all persulfides are cleaved using SDS-PAGE sample buffer containing the reductant TCEP, leading to a loss of the persulfide-bound MPB molecules. Control reactions omitting either (NIA)₂ or cysteine prevent persulfide formation, yielding fully MPB-labelled ISCU2. The mass shift induced by the different number of MPB labels of persulfidated and non-persulfidated ISCU2 can be visualised by SDS-PAGE.

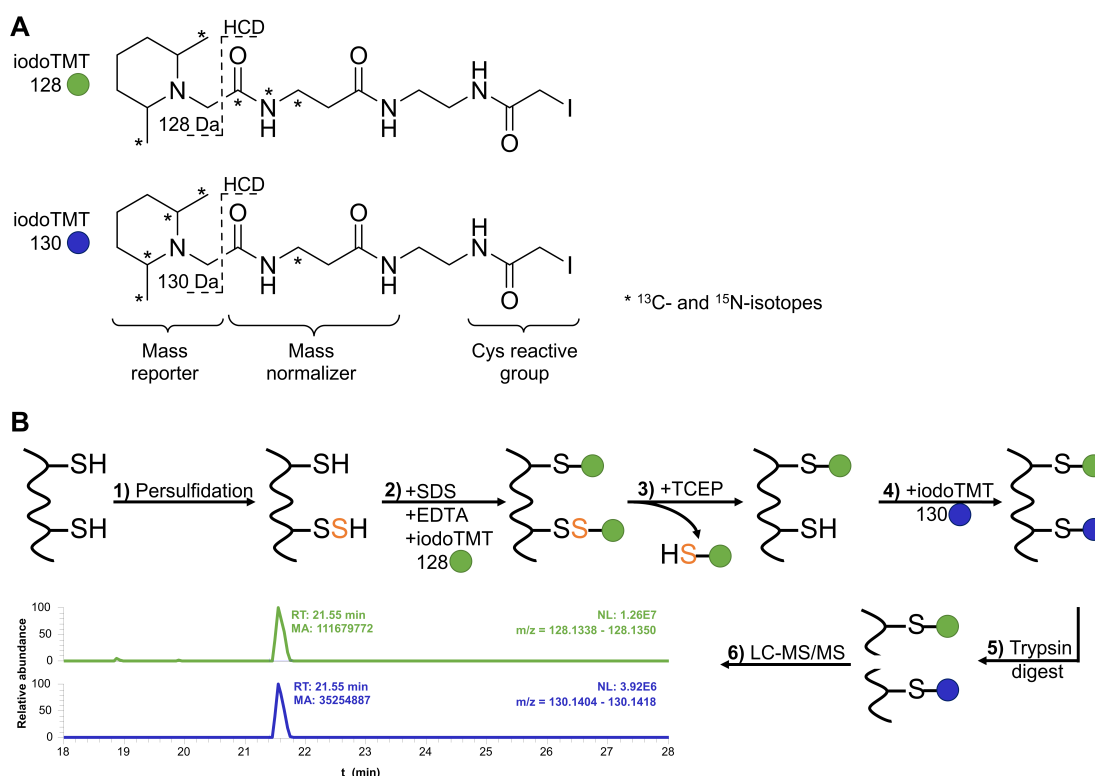


Figure 50: Schematic outline of the iodoTMT-based persulfidation assay. **A)** The iodoTMT sixplex kit (Thermo Fisher) includes six labels of identical structure but with differing distribution of ^{13}C - and ^{15}N -isotopes, named iodoTMT 126, 127, 128, 129, 130 and 131, according to the MW of their mass reporter moiety. Labels form a covalent C-S bond with thiols via the cysteine reactive group. Depicted are iodoTMT 128 and 130 as examples. **B)** **Step 1:** ISCU2 Cys residues were persulfidated by the cysteine desulfurase NFS1 in presence of free cysteine. **Step 2:** Persulfidated samples were labelled with, e.g., iodoTMT 128. Label stocks containing SDS and EDTA facilitated simultaneous labelling and rapid denaturation of the proteins to avoid a prolonged persulfidation reaction. Excess label was quenched by adding excess cysteine. **Step 3:** Persulfides were reductively cleaved *in situ* using TCEP. **Step 4:** Cleaved samples were subjected to a second labelling step (e.g., iodoTMT 130), and excess label was quenched with cysteine. **Step 5:** Labelled proteins were cleaved by on-bead trypsin digest and resulting peptides enriched according to the manufacturer's protocol. **Step 6:** NanoHPLC-MS² enables separation of peptides and fragmentation of iodoTMT molecules by higher energy collisional dissociation or collision-induced dissociation (HCD or CID, indicated by dashed lines). IodoTMT molecules were fragmented by CID, and signals of mass reporter fragments were integrated to calculate the percentage of persulfidation for each Cys-containing peptide.

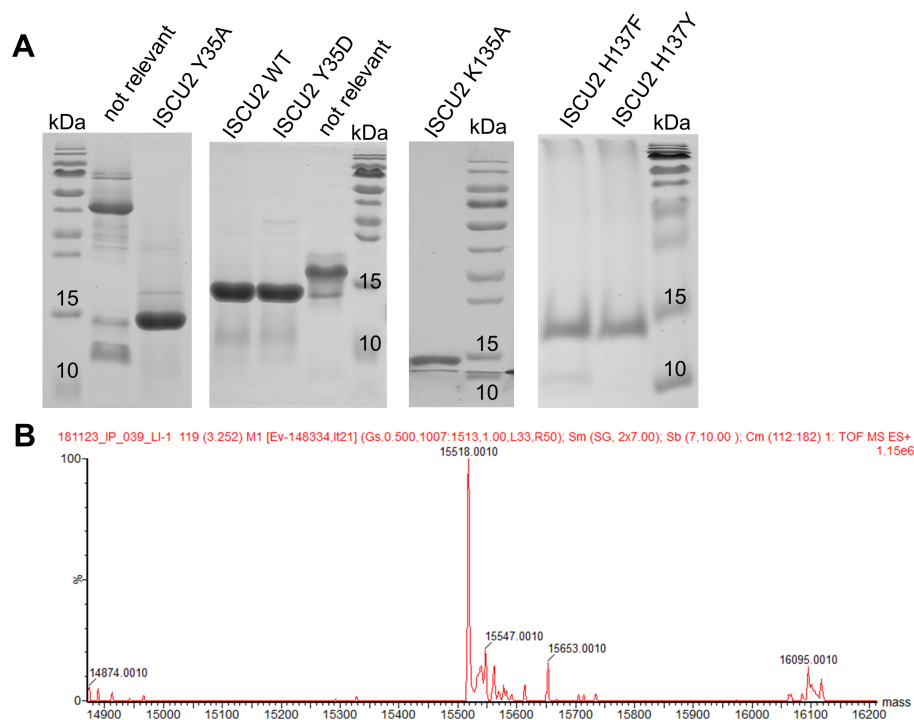
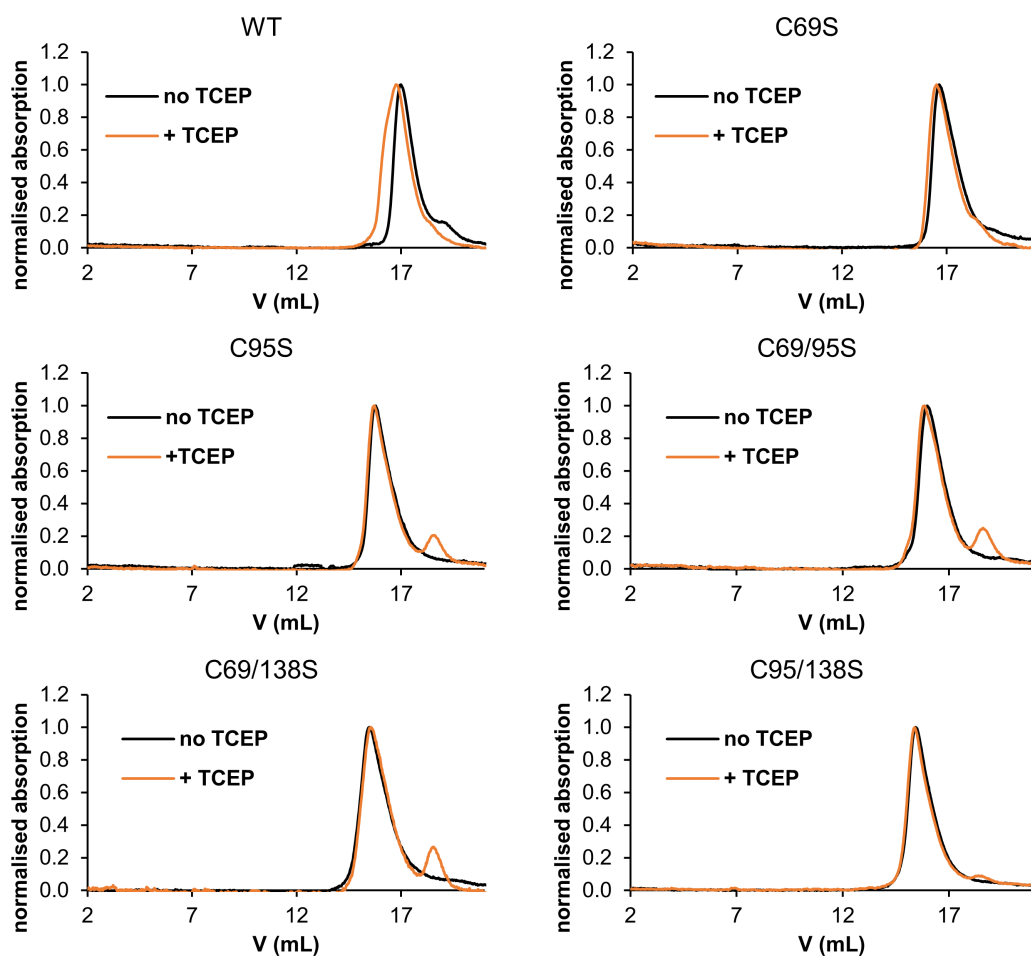


Figure 51: Biochemical characterization of ISCU2 WT and mutant proteins. A) SDS-PAGE indicates high purity of anaerobically purified ISCU2 variants. **B)** Intact protein MS of anaerobically purified ISCU2 WT shows signals at 15,518 and 15,547 Da which likely correspond to $[\text{ISCU2}+\text{H}]^+$ and $[\text{ISCU2}+\text{Na}]^+$ species of the full length protein with the N-terminal Met cleaved (theoretical masses: $[\text{ISCU2}+\text{H}]^+$: 15,522.87 Da; $[\text{ISCU2}+\text{Na}]^+$: 15,544.85 Da).



	MW (kDa)	
	no TCEP	+ TCEP
WT	15.9	17.5
C69S	18.7	19.8
C95S	27.8	28.7
C69/95S	25.3	27.1
C69/138S	31.7	30.6
C95/138S	32.4	33.3

Figure 52: aSEC of ISCU2 variants using a Superdex 200 10/300 GL column monitoring the absorption at 280 nm. Proteins were analysed with a mobile phase containing either no or 5 mM TCEP. Chromatograms were normalised to the major peak for each run. The calculated MW (from column calibration with an LMW kit) is given in the table (bottom). The minor peaks at 18.8 mL elution volume observed for ISCU2 C95S, C69/95S and C69/138S in presence of TCEP correspond to a calculated MW of 6.9 kDa, indicating either an impurity or possibly a truncated ISCU2 species.

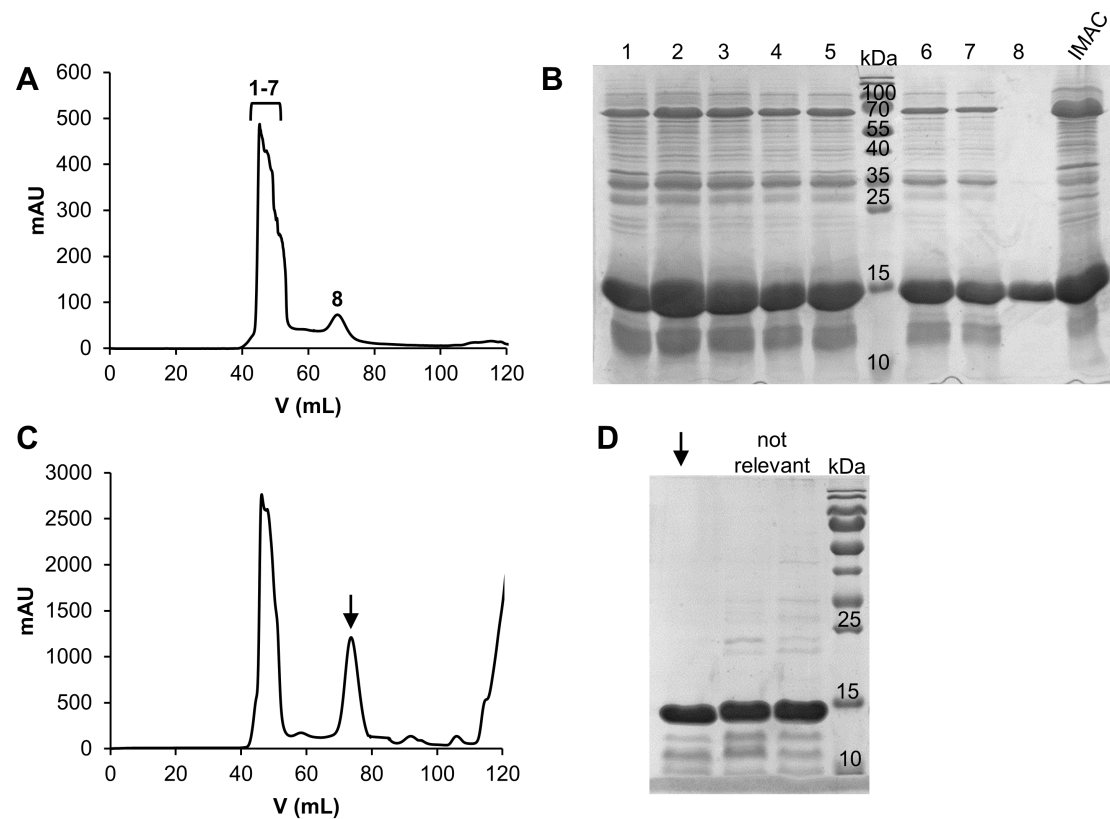


Figure 53: Purification of ISCU2 D71A. **A)** Chromatogram depicting absorbance at 280 nm from SEC of ISCU2 D71A after the standard purification procedure. **B)** SDS-PAGE of SEC fractions labelled in **(A)** plus IMAC-purified ISCU2 D71A (before SEC, right lane). **C)** Chromatogram depicting absorbance at 280 nm from SEC of ISCU2 D71A after the optimized purification procedure. High absorbance at 120 mL elution volume likely corresponds to ATP added before SEC. **D)** SDS-PAGE of the 74 mL peak marked by an arrow as in **(C)**. The two middle lanes do not depict ISCU2 D71A.

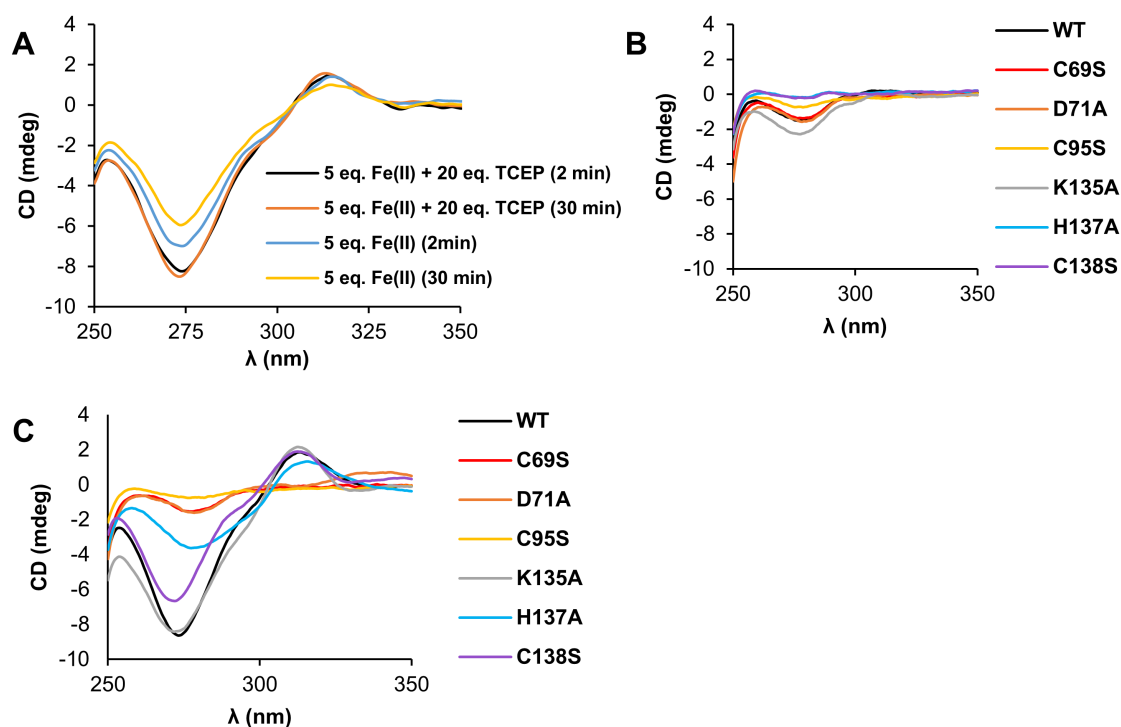


Figure 54: Anaerobic CD-spectroscopic analysis of ISCU2 Fe binding. **A)** 100 μ M ISCU2 WT was incubated with Fe(II) in presence or absence of TCEP. TCEP ensured robust signals for Fe-ISCU2, likely counteracting disulfide formation over time. **B-C)** CD spectra of 100 μ M ISCU2 WT and mutant proteins in presence of 2 mM TCEP were recorded before (**B**) and after (**C**) addition of 2 eq. Fe(II).

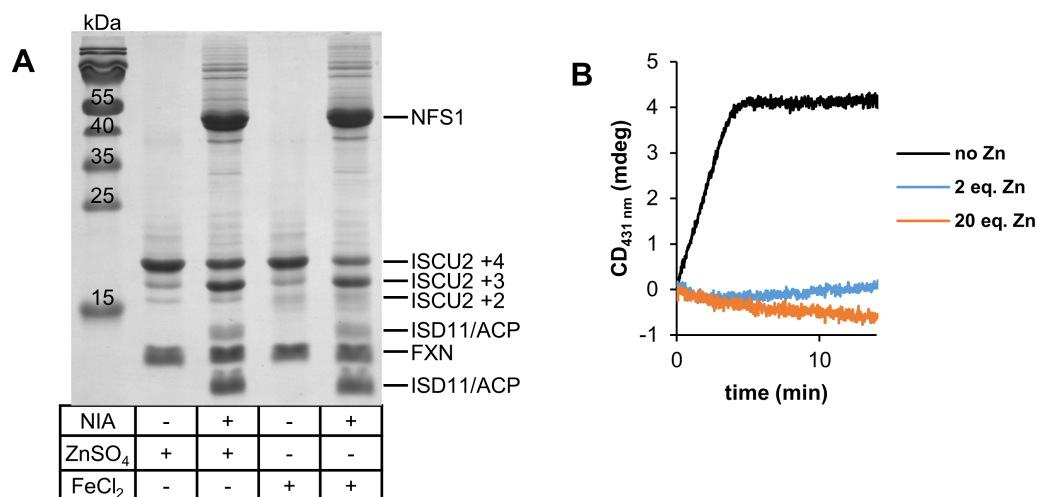


Figure 55: The role of Zn in *de novo* Fe/S cluster formation on ISCU2. **A)** MPB-based persulfidation assay of ISCU2. Reactions contained 20 μ M ISCU2, equimolar amounts of NIA and FXN as well as 80 μ M of either ZnSO₄ or FeCl₂ and ascorbate. Persulfidation was initiated with 500 μ M cysteine and quenched after 2 min with MPB. Samples were denatured with SDS and treated with TCEP before SDS-PAGE. **B)** Enzymatic reconstitution of ISCU2 monitored via the CD signal of the formed [2Fe-2S] cluster at 431 nm. Reactions included 30 μ M ISCU2, 4 μ M NIA, FXN and FDX2 and 0.3 μ M FDXR as well as 0.3 mM FeCl₂ and cluster synthesis was initiated by addition of 0.5 mM cysteine. Reactions were titrated with ZnSO₄ (eq. over ISCU2), which led to formation of precipitates in presence of 20 eq. but not 2 eq. Zn.

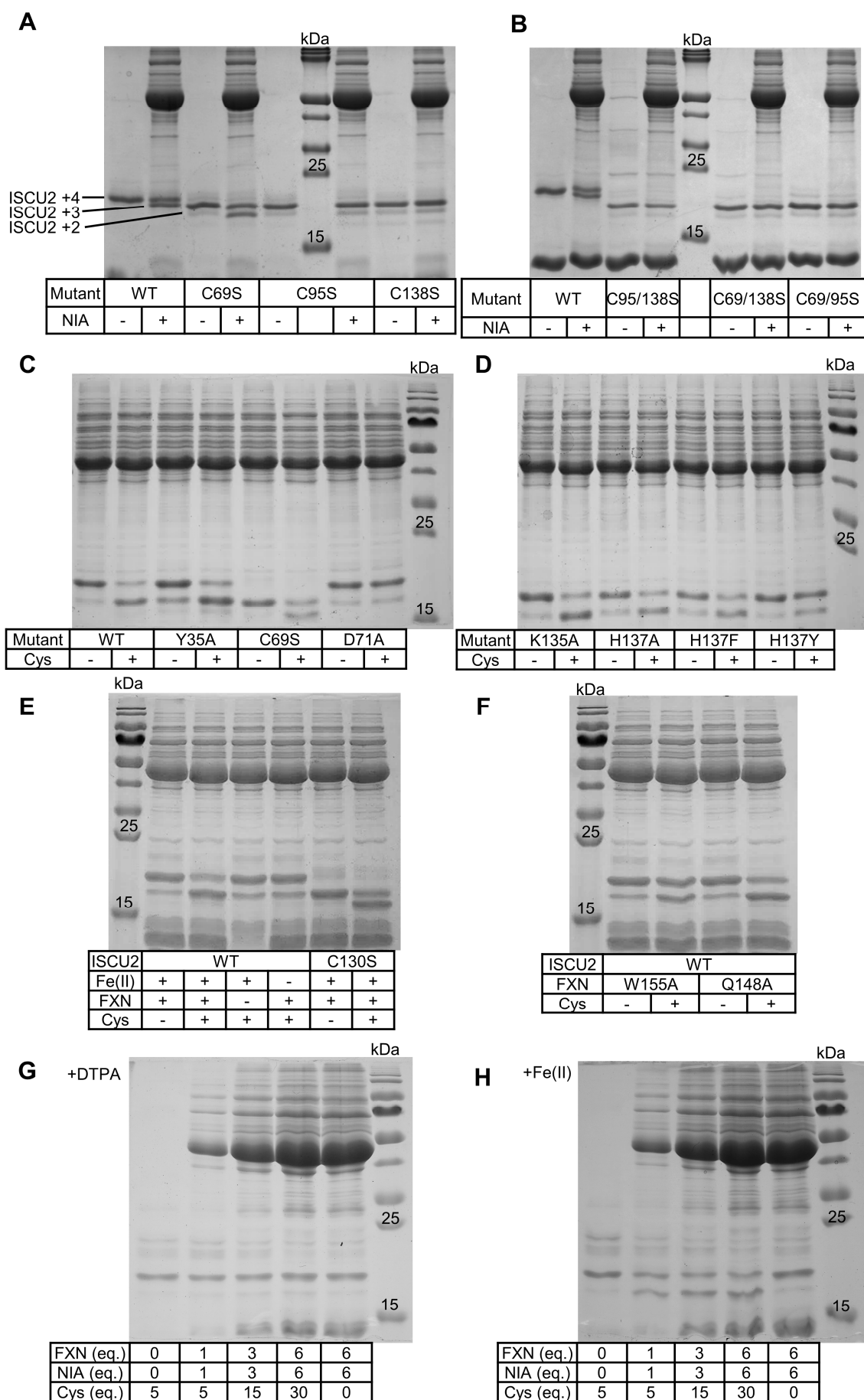


Figure 56: SDS-PAGE analysis of MPB-based ISCU2 persulfidation assays. Standard reactions contained ISCU2, FXN, (NIA)₂, ascorbate and Fe(II). 10 s reactions initiated by cysteine addition were quenched with MPB and SDS. Negative controls were performed by omitting either (NIA)₂ or cysteine. **A-D)** Persulfidation assays of ISCU2 variants. The non-persulfidated species is labelled with four molecules MPB (ISCU2 +4) in the WT protein exhibiting four Cys residues. Upon exchange of one or two Cys residues, ISCU2 +3 and ISCU2 +2, respectively, represent the non-persulfidated species. Gels in **(C)** and **(D)** show samples from the same experiment. **E-F)** Persulfidation assay of ISCU2 and FXN variants. In addition, reactions containing ISCU2 WT and lacking either FXN or Fe(II)/ascorbate were performed **(E)**, the latter containing 1 mM DTPA. **G-H)** Persulfidation assay with ISCU2 WT in presence or absence of Fe(II). Reactions contained either 1 mM DTPA (left panel) or 100 μ M of each Fe(II) and ascorbate. NIA, FXN and cysteine were titrated (eq. indicating equivalents over ISCU2) to assess the influence of different reaction compositions on persulfidation yield in 10 s reactions. A slight but not dramatic increase in ISCU2 persulfidation can be seen in Fe(II) reactions, as well as a subtle increase in DTPA reactions (representing background persulfidation). It was concluded that the usually employed 1:2 ratio of ISCU2 to NIA was suitable for efficient persulfidation reactions.

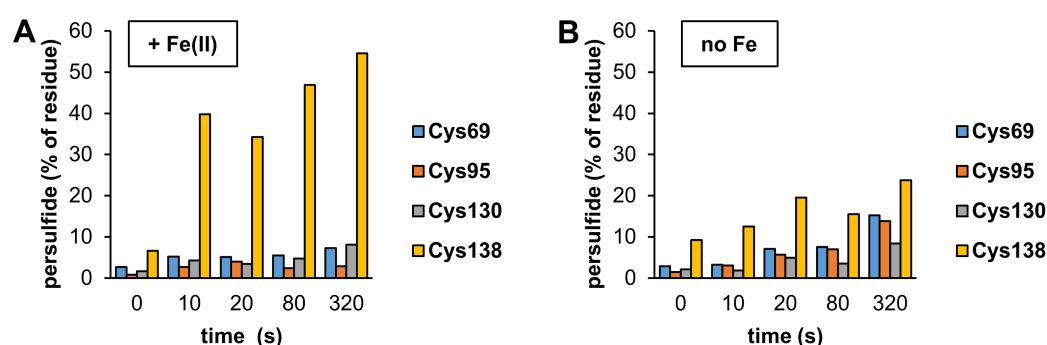


Figure 57: Efficient persulfidation of ISCU2 Cys138 requires Fe(II). Persulfidation of ISCU2 Cys residues was analysed by a iodoTMT-based labelling approach. Reactions contained 20 μ M ISCU2, NIA and FXN and either 100 μ M **(A)** or no **(B)** FeCl₂. Persulfidation was initiated with 400 μ M cysteine and reactions were quenched at the indicated reaction time points with 1.5 mM (2.2 eq. over initial total thiol concentration) iodoTMT 128 (dissolved in methanol). After 1 min, SDS was added to 1% w/v concentration. Excess label was quenched with 1.7 mM cysteine, and persulfides were reductively cleaved with 2 mM TCEP. 3 mM iodoTMT 130 or 131 (dissolved in methanol) were used for the second labelling step and excess label was quenched with 6 mM cysteine. Samples were subjected to trypsin digestion and persulfide content of Cys-containing peptides was quantified via HPLC-MS².

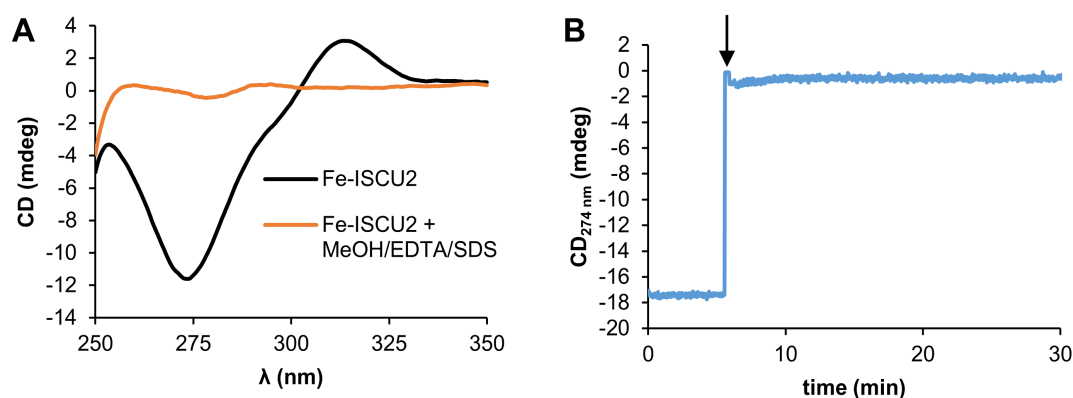


Figure 58: A quench mixture used in iodoTMT-based persulfidation assays leads to rapid removal of Fe from Fe-ISCU2. 100 μM ISCU2, 200 μM FeCl_2 and 2 mM TCEP were mixed under anaerobic conditions to a final volume of 300 μL in a cuvette which was tightly sealed with a rubber plug. The CD spectrum of Fe-ISCU2 was recorded (**A**, black curve). Subsequently, the CD signal at 274 nm was recorded in a time course (**B**). After 5.5 min (marked by arrow in **B**), the CD spectrometer was opened and 300 μL of a quench mixture as used in iodoTMT-based persulfidation assays (Figure 18) containing 50% v/v methanol, 10 mM EDTA and 10% w/v SDS was injected into the cuvette as fast as possible. The CD spectrometer was closed again 10 s after the injection (the shortest possible time), at which time point the Fe-ISCU2 CD signal had almost completely vanished. After completion of the time course, a CD spectrum was recorded, confirming loss of Fe from ISCU2 (**A**, orange curve). The experiment indicates that application of the quench mix as done in the iodoTMT-based analysis of Fe-dependent ISCU2 persulfidation (Figure 18) leads to the rapid release of Fe from Fe-ISCU2, abolishing persulfidation. High concentrations of methanol and SDS likely induce fast protein denaturation. As the 10 s time point represents the technical limitation of the experiment, loss of Fe may proceed even faster.

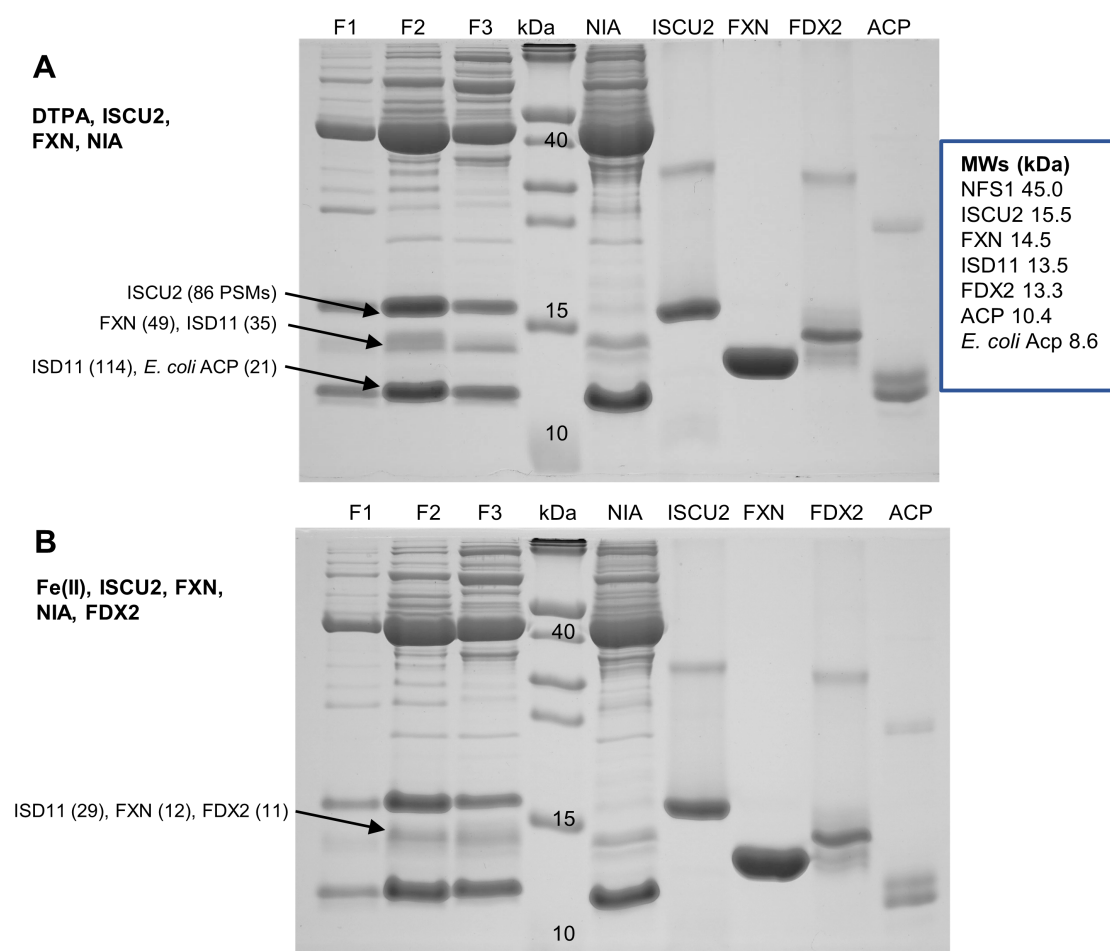
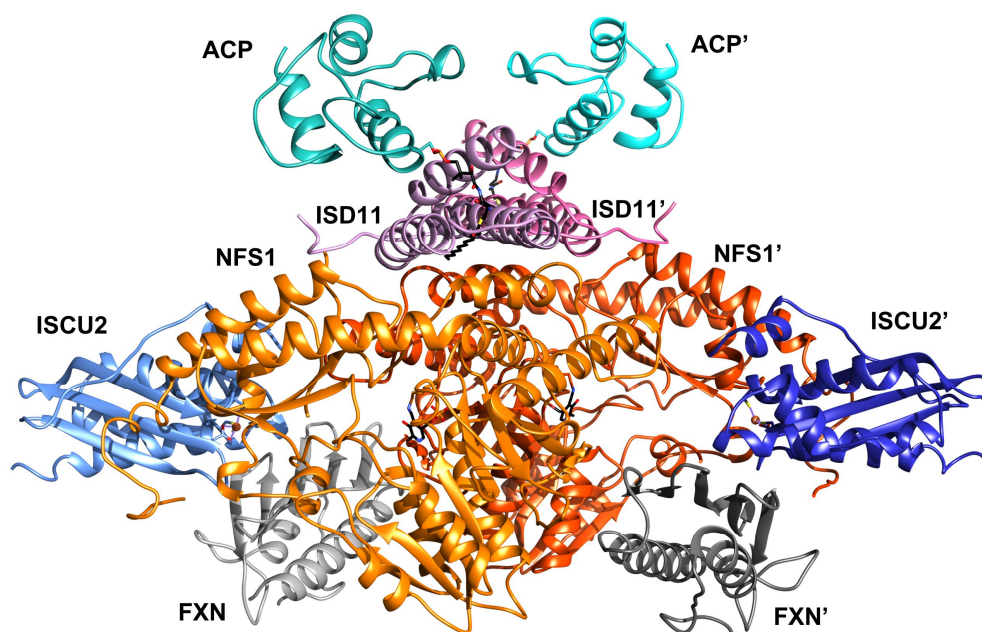


Figure 59: ISCU2 binds more stably to the core ISC complex than FXN and FDX2. 100 μ M of each NIA, ISCU2 and FXN were incubated with either 1 mM DTPA (**A**) or 500 μ M FeCl_2 , 500 μ M ascorbate and 100 μ M FDX2 (**B**) in standard SEC buffer and incubated at room temperature for 10 min. Samples were passed through a Superdex 200 increase 10/300 GL column, and fractions (F1 – F3) collected from the observed HMW peak were subjected to tricine SDS-PAGE. Individual purified proteins were also run (lanes right of the marker) to facilitate protein identification. Bands marked by arrows were analysed by qualitative MS. Peptide spectrum matches (PSM) are given in brackets for the detected proteins. This revealed ISD11 to produce two distinct bands upon SDS-PAGE separation (**A**). ACP generally shows low coverage upon qualitative MS analysis and only *E. coli* ACP peptides were detected. Bands for ISD11, FXN and FDX2 ran at similar height on the gel. The experiment reveals stable stoichiometric binding of ISCU2 to NIA independent of the presence of Fe(II). In contrast, only low amounts of both FXN and FDX2 could be detected, indicating less stable binding to NIA.

A



B

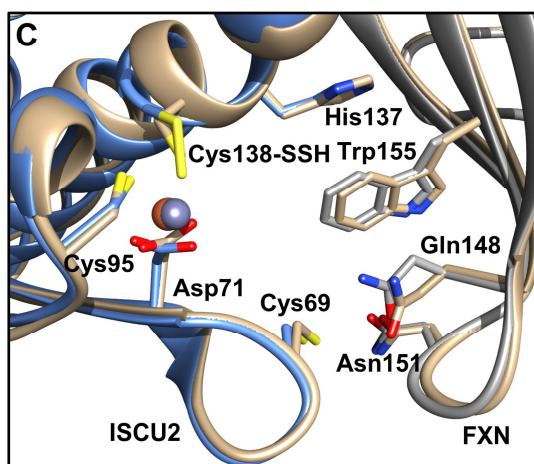
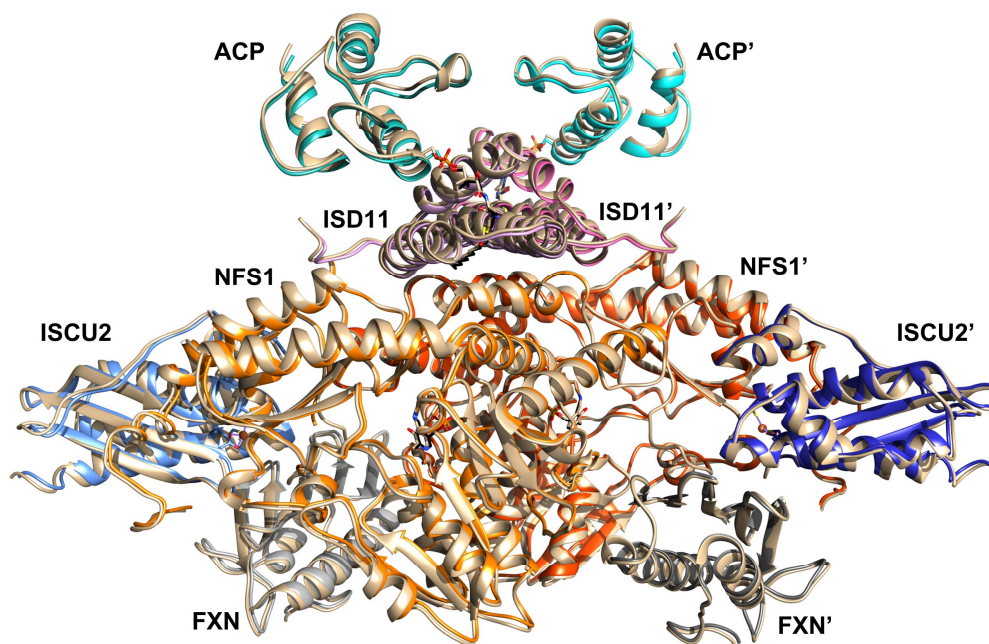


Figure 60: The structure of persulfidated (Fe-NIAU(SSH)X)₂ is similar to non-persulfidated (Zn-NIAUX)₂. **A)** Structure of (Fe-NIAU(SSH)X)₂ at 2.4 Å resolution, viewing the ISD11-ACP binding site from the side. The structure is fully resolved except residues 378 – 386 of the flexible catalytic loop of NFS1. NFS1-bound PLP and the ACP-bound fatty acyl phosphopantetheinyl moiety are depicted as black sticks. **B)** Overlay with the published structure of non-persulfidated (Zn-NIAUX)₂ (pdb code: 6NZU) at the same orientation. Colouring of (Fe-NIAUX)₂ as in **(A)**, (Zn-NIAUX)₂ is coloured beige. **C)** Zoom into the ISCU2-FXN interaction site of the overlay shown in **B**. Fe is represented as orange sphere and Zn as grey sphere. Done in collaboration with R. Steinhilper and Dr. B. Murphy.

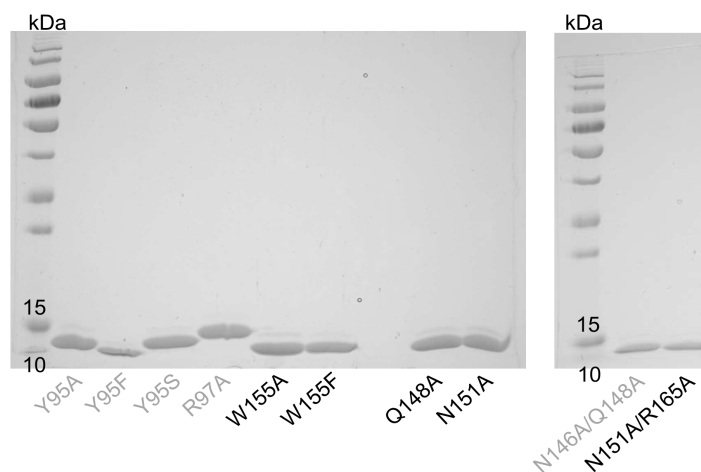


Figure 61: SDS-PAGE of purified FXN mutant proteins. Variants labelled in grey were not used for experiments shown in this work. Jointly prepared with Nils Krapoth.

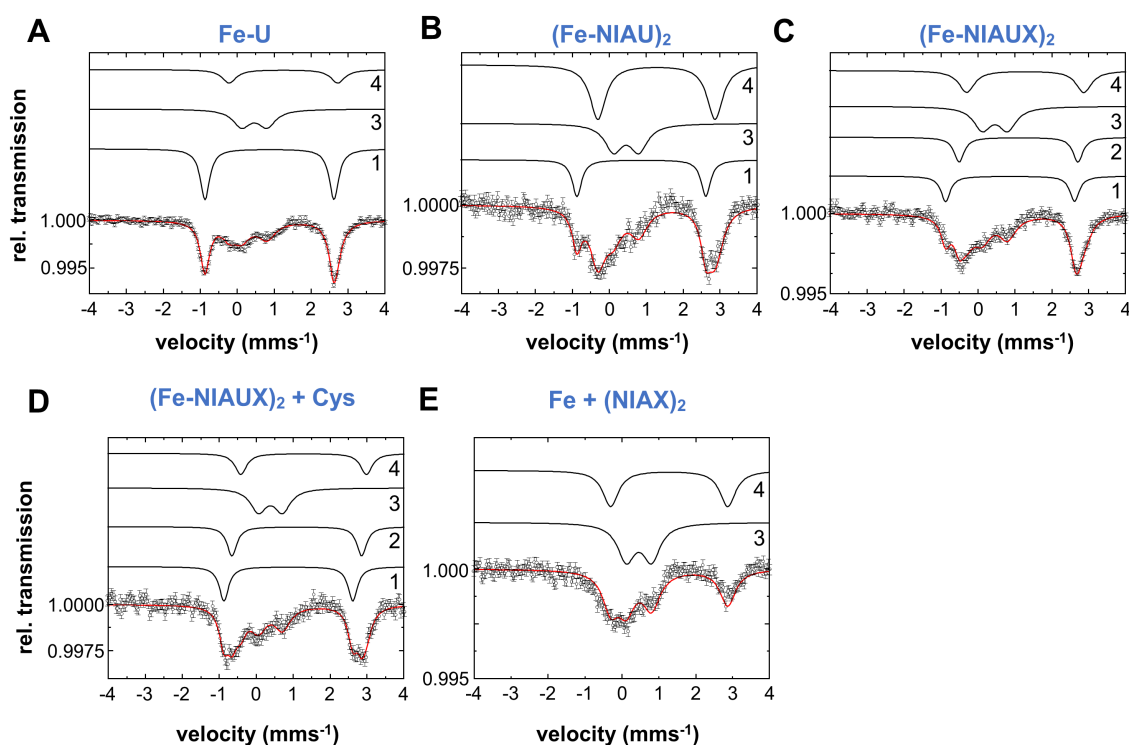


Figure 62: Mössbauer spectroscopic analysis of intermediates of [2Fe-2S] cluster synthesis. Mössbauer spectra of different core ISC sub-complexes reconstituted with 1.5 eq. ^{57}Fe -enriched FAC over ISCU2. **Cys** indicates 1.5 eq. cysteine over ISCU2 added as last component. U: ISCU2; X: FXN; F: FDX2. Proteins were present in a ratio NIA:U:X of 1:1:2. Each spectrum was recorded at 77 K and 0 T. The red line displays the best fit of the data using the components shown as black lines. Error bars indicate the SD. Done in collaboration with J. Oltmanns and Dr. V. Schünemann.

Table 18: Final μM concentration of the components of Mössbauer samples shown in Figure 62. Samples were buffer exchanged into 50 mM Tris, 150 mM NaCl, 2 mM TCEP, 5% w/v glycerol, pH 8.0 using ZebaSpin 7K columns immediately before flash freezing.

Compound (μM)	Fe-U	(Fe-NIAU) ₂	(Fe-NIAUX) ₂	(Fe-NIAUX) ₂ + Cys	Fe + (NIAUX) ₂
TCEP	2000	2000	2000	-	2000
ISCU WT	350	350	350	350	-
ascorbate	5250	5250	5250	5250	5250
^{57}Fe (FAC)	525	525	525	525	525
NIA	-	350	350	350	350
FXN	-	-	700	700	700
cysteine	-	-	-	350	-

Table 19: Mössbauer parameters of the individual components numbered in Figure 62. Isomer shift (δ), quadruple splitting (ΔE_Q) and line width (Γ) are given in mm s^{-1} . A^2 , surface area. ISCU2-specific components 1 and 2 exhibit parameters similar to those of the respective $(\text{NH}_4)_2^{57}\text{Fe}(\text{SO}_4)_2$ reconstituted samples (Table 15). A difference is evident for $(\text{Fe-NIAU})_2$, exhibiting 27% component 2 in $(\text{NH}_4)_2^{57}\text{Fe}(\text{SO}_4)_2$ reconstituted $(\text{Fe-NIAU})_2$, but lacking component 2 here. However, the $(\text{Fe-NIAU})_2$ spectrum here could also be fitted with 15% component 1 and 10% component 2, with no significant difference in quality between the two fits. Overlap with the dominant component 4 complicates precise quantification of component 2 in the $(\text{Fe-NIAU})_2$ spectrum. Components 3 and 4 exhibit a high line width, indicating unspecific Fe binding. Their presence in the $\text{Fe}+(\text{NIA})_2$ sample shows these species to be independent of ISCU2.

	Component 1				Component 2				Component 3				Component 4			
	δ	ΔE_Q	Γ	A^2 (%)	δ	ΔE_Q	Γ	A^2 (%)	δ	ΔE_Q	Γ	A^2 (%)	δ	ΔE_Q	Γ	A^2 (%)
Fe-U	0.87	3.49	0.31	49					0.46	0.68	0.57	31	1.25	2.94	0.46	20
(Fe-NIAU)₂	0.87	3.49	0.31	21					0.46	0.68	0.57	28	1.28	3.18	0.51	51
(Fe-NIAUX)₂	0.87	3.49	0.31	19	1.10	3.22	0.33	21	0.46	0.68	0.57	32	1.28	3.18	0.51	28
(Fe-NIAUX)₂ + Cys	0.87	3.49	0.31	25	1.15	3.53	0.34	30	0.46	0.68	0.57	28	1.32	2.94	0.51	17
Fe + (NIA)₂									0.46	0.68	0.57	53	1.28	3.18	0.51	47

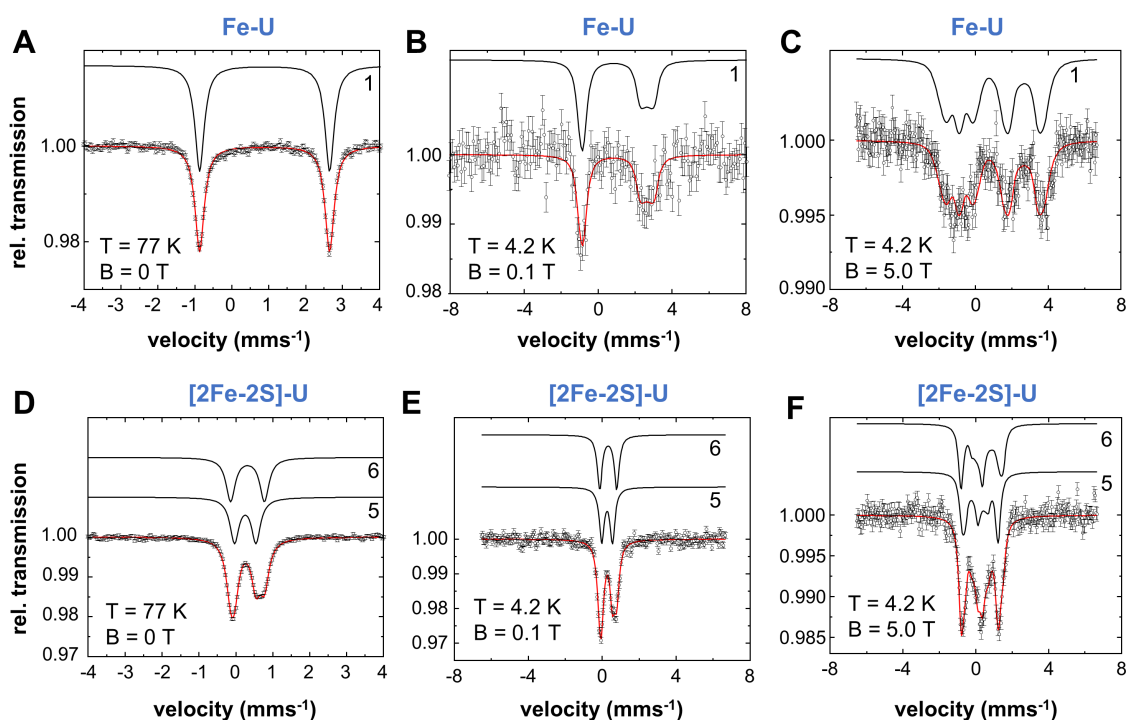


Figure 63: Mössbauer spectra of Fe-ISCU2 and [2Fe-2S]-ISCU2 recorded at varying magnetic field. Spectra of the same samples shown in Figure 23A and G, recorded at the indicated temperatures and field strengths. Components present in Fe-ISCU2 (**A-C**) and [2Fe-2S]-ISCU2 (**D-F**) could be fitted with the same respective parameter sets (given in Table 20) at different applied fields (except for the line width of Fe-ISCU2). The red line displays the best fit of the data using the components shown as black lines. Error bars indicate the SD. Fe-U spectra exhibit similarity to those reported for Fe(II)-substituted horse liver alcohol dehydrogenase ligating Fe via two Cys and one His residue and water (Bill *et al.*, 1989). [2Fe-2S]-U spectra are highly similar to those reported for mouse [2Fe-2S]-U (Gervason *et al.*, 2019). Done in collaboration with J. Oltmanns and Dr. V. Schünemann.

Table 20: Mössbauer parameters of the individual components numbered in Figure 63. δ , isomer shift; ΔE_Q , quadruple splitting; Γ , line width; η , asymmetry parameter; D and E, zero-field splitting parameters; A, hyperfine coupling tensor; A^2 , surface area.

	Fe-U	[2Fe-2S]-U	
	Component 1	Component 5	Component 6
δ (mms ⁻¹)	0.89	0.26	0.32
ΔE_Q (mms ⁻¹)	3.52	0.58	0.92
Γ (mms ⁻¹)	0.3*	0.29	0.30
D (cm ⁻¹)	-8		
E/D	0.20		
η	0.0		
$A_{x,y,z}$ (T)	-21.5 -16.6 -4.5		
A^2 (%)	100	50	50

* $\Gamma = 0.5$ mms⁻¹ for B = 0.1 T and B = 5 T

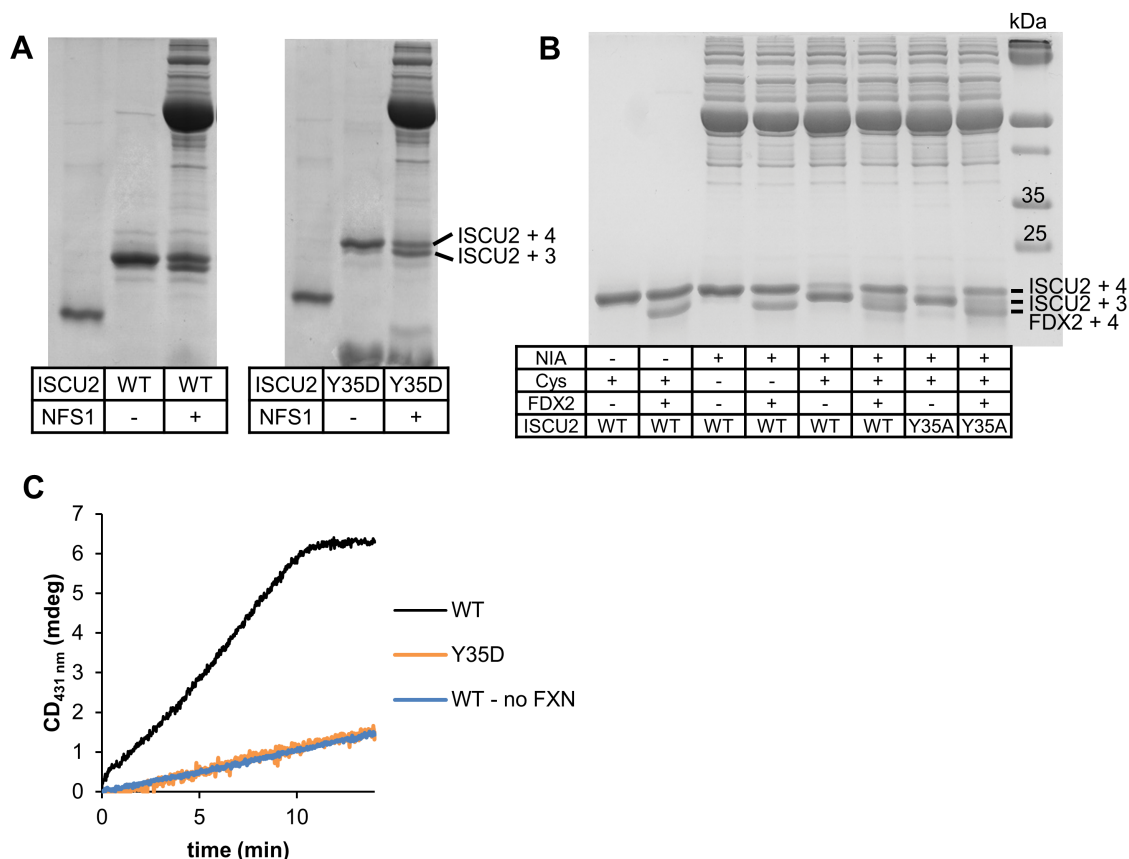


Figure 64: Persulfide transfer, persulfide reduction and Fe/S cluster formation of ISCU2 Tyr35 mutant proteins. A-B) MPB-based detection of *in vitro* persulfidation of ISCU2 WT and Tyr35 variants. **A)** Both ISCU2 WT and Y35D are persulfidated to similar degrees *in vitro* after 10 s reaction time in presence of cysteine. **B)** *In vitro* persulfide formation and reduction of ISCU2 WT and Y35A. Samples lacking FDX2 represent standard persulfidation reactions. In other reactions, FDX2, FDXR and NADPH were added after cysteine-mediated ISCU2 persulfidation. For both ISCU2 WT and Y35A, a shift from the persulfidated ISCU2 +3 species (lanes 5 and 7 from the left) back to the non-persulfidated ISCU2 +4 species (lanes 6 and 8) indicates a major portion of persulfide being reductively cleaved. **C)** Time course of the enzymatic reconstitution of a [2Fe-2S] cluster on ISCU2 WT and variant Y35D. Exchange of Tyr35 leads to abrogation of cluster synthesis. Performed by Dr. S.-A. Freibert (Freibert *et al.*, 2021). Experimental results from **A-C** indicate ISCU2 Tyr35 variants to enable persulfidation and persulfide reduction, but not [2Fe-2S] cluster formation. This makes them a promising candidate to trap a potential “reduced persulfide” intermediate state in *de novo* Fe/S cluster synthesis.

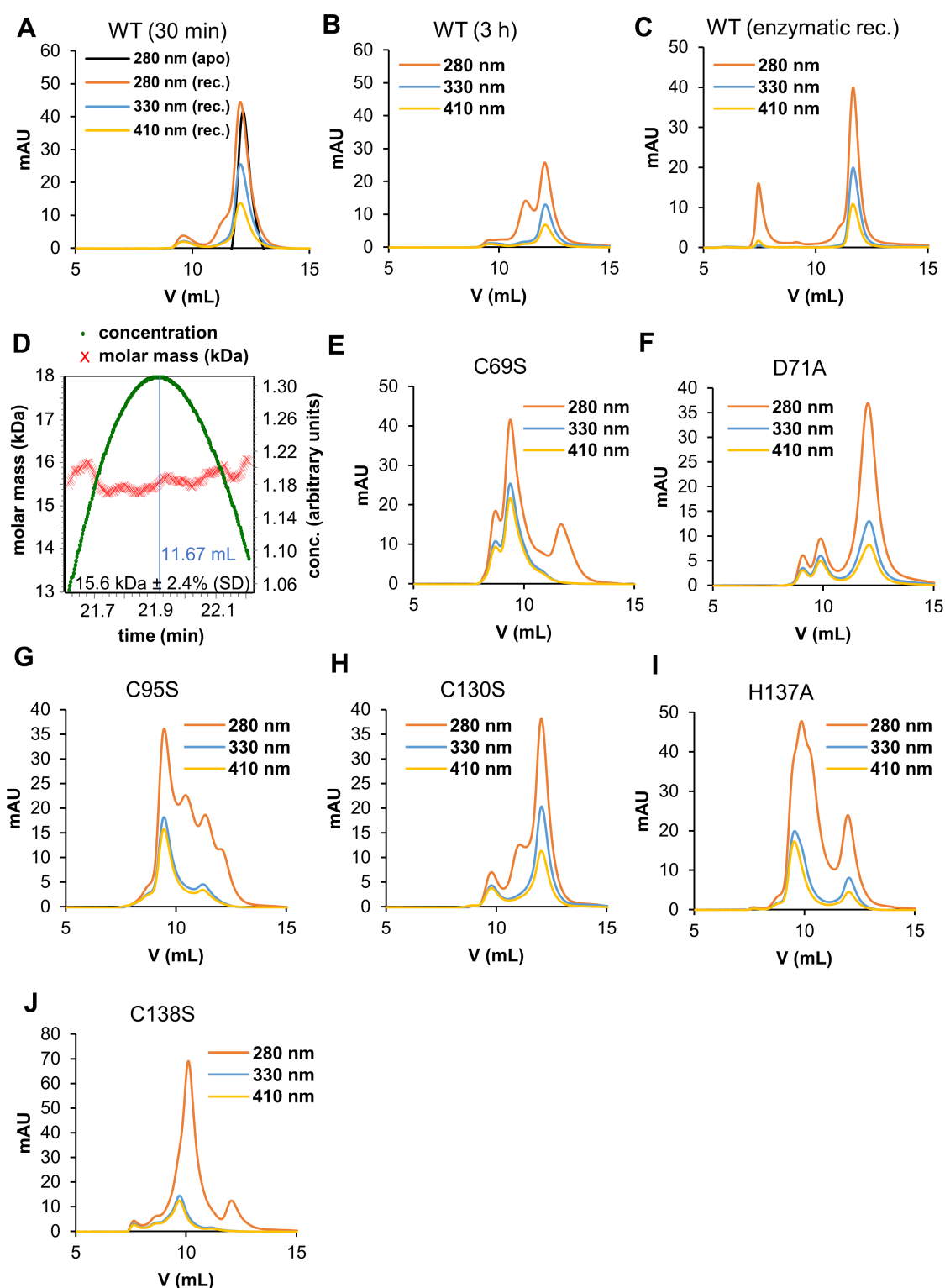


Figure 65: aSEC and aSEC-MALS analyses of reconstituted ISCU2 WT and mutant proteins. A) Overlay of chromatograms from aSEC runs of chemically reconstituted (30 min reconstitution time) and apo-ISCU2 WT. **B)** Chromatograms from aSEC of chemically reconstituted ISCU2 WT (3 h reconstitution time). **C)** Chromatograms from aSEC of enzymatically reconstituted ISCU2 WT. The molar mass of the major peak at 11.7 mL representing holo-ISCU2 was determined by SEC-MALS (**D**) to be 15.6 kDa. **E-J)** Chromatograms from aSEC runs of chemically reconstituted ISCU2 variants (30 min reconstitution time). Colours: Black (apo-protein, visualized at 280 nm), orange (reconstituted protein visualized at 280 nm), blue, yellow (Fe/S cluster of reconstituted protein visualized at 330 and 410 nm, respectively).

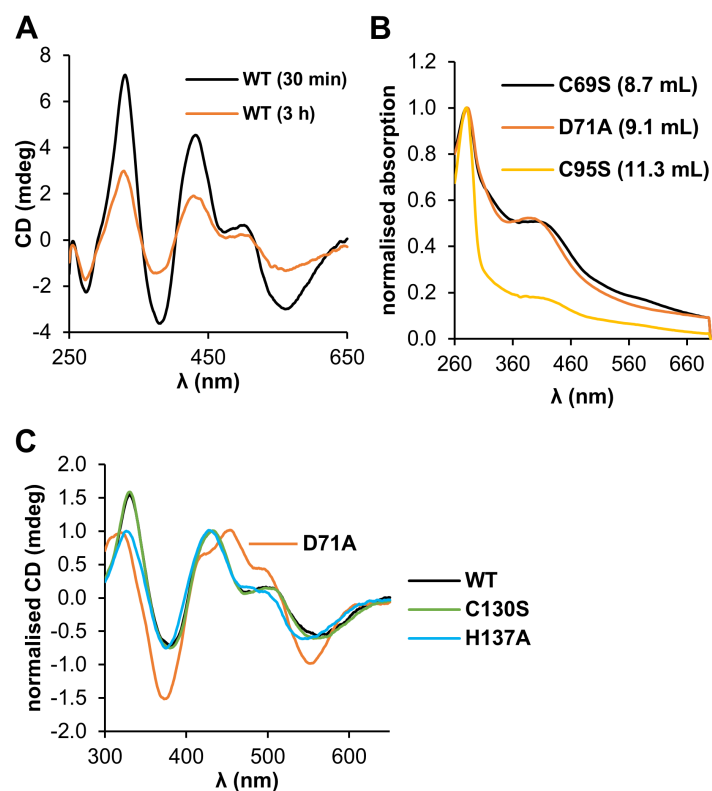


Figure 66: UV/Vis and CD spectra from chemical reconstitutions of ISCU2 WT and mutant proteins.

A) CD spectra of chemically reconstituted ISCU2 WT at the indicated reconstitution times. **B)** DAD-recorded UV/Vis spectra from aSEC (Figure 65) of chemically reconstituted ISCU2 variants at the indicated elution volumes normalised to the absorption at 280 nm. **C)** CD spectra of chemically reconstituted ISCU2 WT and variants normalised to the major peak in the range 400 – 500 nm.

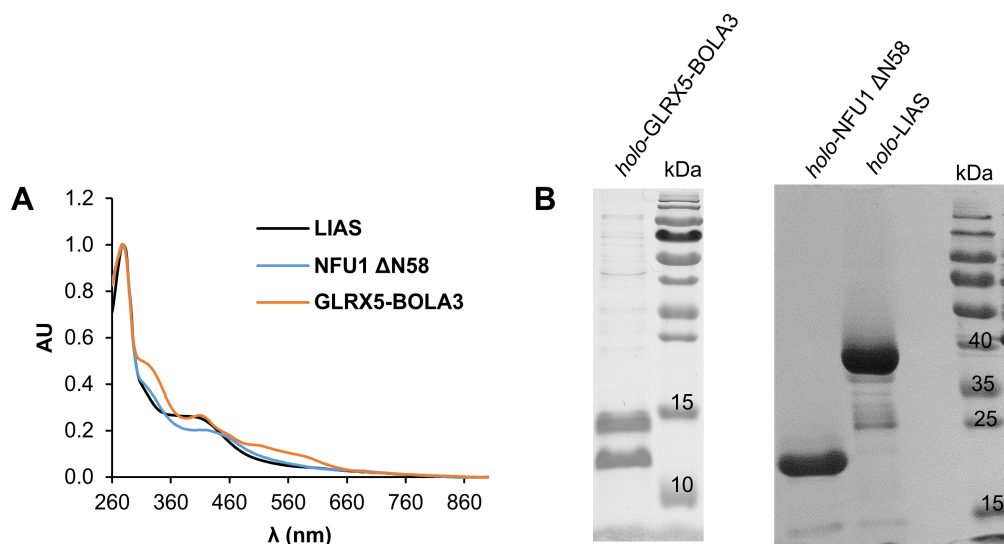


Figure 67: Chemical reconstitution of LIAS, NFU1 and GLRX5-BOLA3. UV/Vis spectra (**A**) and SDS-PAGE (**B**) of the indicated chemically reconstituted proteins. BOLA3 (11.1 kDa), GLRX5 (15.8 kDa), LIAS (40.2 kDa), NFU1 Δ N58 (21.8 kDa).

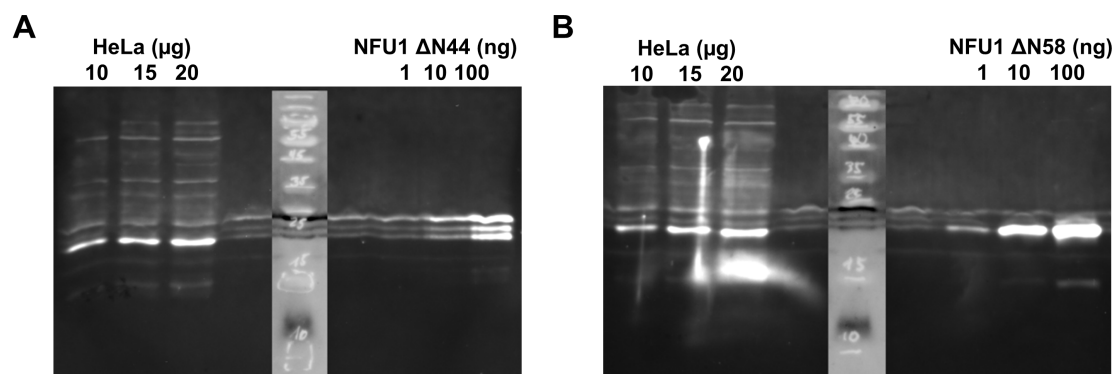


Figure 68: Western blot of N-terminally truncated NFU1 constructs. Sizes of purified NFU1 Δ N44 (**A**) and NFU1 Δ N58 (**B**) were compared with NFU1 from HeLa cell extracts using an NFU1-specific antibody. Amounts of HeLa cell extract (total protein) and NFU1 are indicated. Blots indicated NFU1 Δ N58 to be the physiologically relevant construct. NFU1 Δ N44 (23.5 kDa), NFU1 Δ N58 (21.8 kDa).

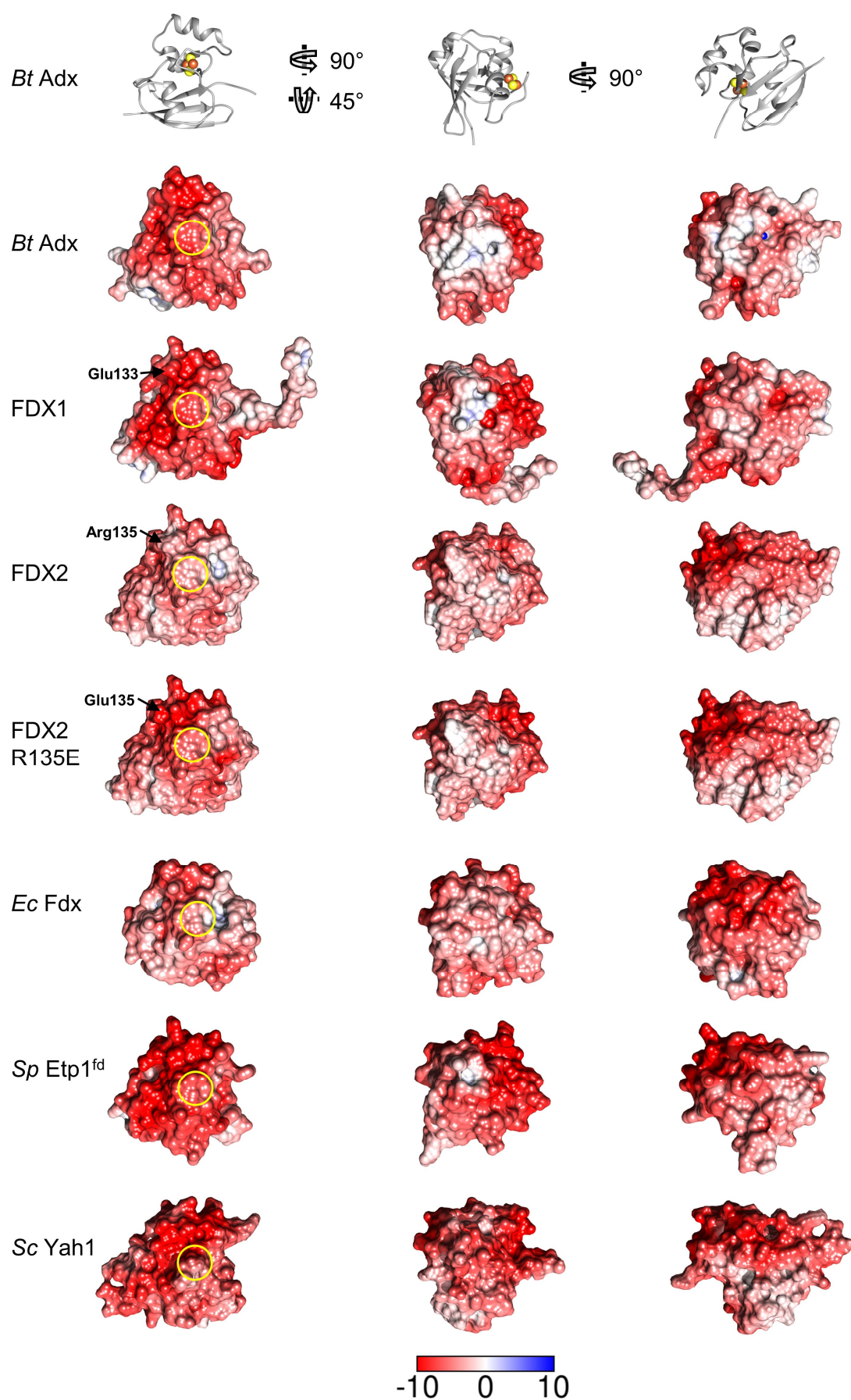


Figure 69: Electrostatic surface potential of various FDXs. The electrostatic surface potentials were calculated by the APBS server (<https://server.poissonboltzmann.org>), and mapped to the indicated FDX

surfaces. Negative charges are presented in red, positive charges in blue. The color bar covers the range from -10 kT/e to +10 kT/e. Depicted are *Bt* Adx (pdb code: 1CJE, 63 – 169), FDX1 (3P1M, residues 65 – 184), FDX2 (2Y5C, 69 – 174), *Ec* Fdx (1I7H, 2 – 110), *Sp* Etp^{td} (2WLB, 518 – 603) and *Sc* Yah1 (2MJD, 58 – 160). All proteins are shown in three different orientations, as defined on top by the ribbon presentation of *Bt* Adx (grey). In the left column the position of the Fe/S cluster binding site is marked by yellow circles. For *Sc* Yah1, the NMR structure was employed, as no crystal structure was available. The C-terminal residues are only shown for FDX1. The structure of FDX2 R135E variant was modelled using UCSF Chimera version 1.12 (Pettersen *et al.*, 2004). The exchanged residue is indicated by an arrow.

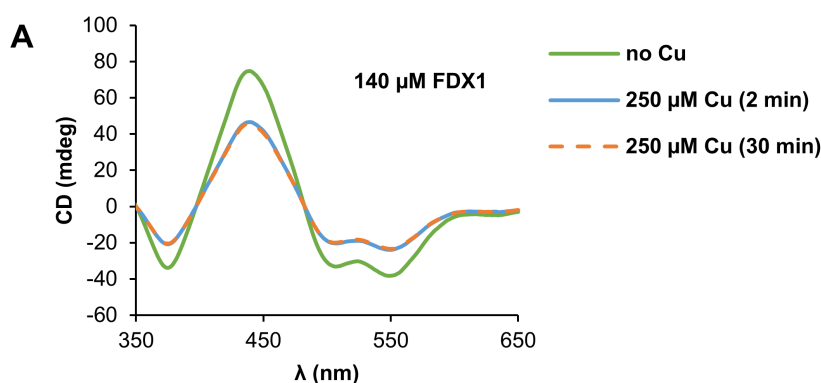


Figure 70: Stability of [2Fe-2S]-FDX1 in presence of Cu. CD spectra of 140 μ M FDX1 recorded at different incubation times after addition of 250 μ M CuCl_2 . Spectral features are virtually identical 2 and 30 min after Cu addition.

7.2 Abbreviations

5'-dA \cdot	5'-Deoxyadenosyl radical
5'-dAH	5'-Deoxyadenosine
ACP, A	Acyl carrier protein
AEC	Anion exchange chromatography
Arh1	Adrenodoxin reductase homolog 1
aSEC	Analytical size exclusion chromatography
ATP	Adenosine triphosphate
AU	Absorption units
BCKDH	Branched-chain α -ketoacid dehydrogenase
Cas9	CRISPR-associated endonuclease 9
CD	Circular dichroism
CIA	Cytosolic Fe/S cluster assembly
CID	Collision-induced dissociation
CoA	Coenzyme A
CoQ	Coenzyme Q
COX	Cytochrome <i>c</i> oxidase
COX10	Heme <i>o</i> synthase

COX15	Heme <i>a</i> synthase
CRISPR	Clustered regularly interspaced short palindromic repeats
CTF	Contrast transfer function
CV	Column volume
CYCS	Cytochrome <i>c</i>
CYP	Cytochrome P450
CYP11A1	11 α -Hydroxylase
CYP11B1	11 β -Hydroxylase
DAD	Diode array detector
dd	Double distilled
DLAT	Dihydrolipoamide acetyltransferase
DLD	Dihydrolipoamide dehydrogenase
DMSO	Dimethyl sulfoxide
DT	Dithionite
DTPA	Diethylenetriaminepentaacetic acid
DTT	Dithiothreitol
EDTA	Ethylenediaminetetraacetic acid
Ele	Elesclomol
ETC	Electron transfer chain
EXAFS	Extended X-ray absorption fine structure
FAC	Ferric ammonium citrate
FDX, F	Ferredoxin
FDXR	Ferredoxin reductase
Fe/S	Iron-sulfur
FPLC	Fast protein liquid chromatography
FRDA	Friedreich's Ataxia
FXN, X	Frataxin
G6P	Glucose-6-phosphate
GCS	Glycine cleavage system
GCSH	H protein of the glycine cleavage system
GLRX5	Glutaredoxin 5
GSH	Glutathione, reduced
HEPES	4-(2-Hydroxyethyl)-1-piperazineethanesulfonic acid
HiPIP	High potential Fe/S protein
HMW	High molecular weight
HPLC	High-performance liquid chromatography
HS	High-spin
IMAC	Immobilised metal affinity chromatography
iodoTMT	Iodoacetyl tandem mass tag
IPTG	Isopropyl β -D-thiogalactopyranoside
IRP1	Iron regulatory protein 1

ISC	Fe/S cluster assembly
ISCU2, U	Fe/S cluster assembly enzyme
ISD11, I	LYR motif-containing protein 4
KADH	α -Ketoadipate dehydrogenase
KGDH	α -Ketoglutarate dehydrogenase
LB	Lysogeny broth
LIAS	Lipoyl synthase
LMW	Low molecular weight
LpIA	Lipoyl-protein ligase
LYRM	Leu-Tyr-Arg motif
M	Metal
MA	Mass area
MALS	Multi-angle light scattering
ME	β -Mercaptoethanol
MoCo	Molybdenum cofactor
MPB	Maleimide polyethylenglycol ₁₁ biotin
MS	Mass spectrometry
mtFAS II	Mitochondrial fatty acid synthesis system II
MTHF	5,10-Methylenetetrahydrofolate
NADPH	Nicotinamide adenine dinucleotide phosphate, reduced
NFS1, N	Cysteine desulfurase
NIF	Nitrogen fixation
NMR	Nuclear magnetic resonance
OD	Optical density
ORF	Open reading frame
PCR	Polymerase chain reaction
PDH	Pyruvate dehydrogenase
PLP	Pyridoxal-phosphate
RMSD	Root-mean-square deviation
SAH	S-Adenosyl homocysteine
SAHN	S-Adenosyl homocysteine nucleosidase
SAM	S-Adenosyl methionine
SAXS	Small-angle X-ray scattering
SDS-PAGE	Sodium dodecyl sulfate polyacrylamide gel electrophoresis
SEC	Size exclusion chromatography
SOB	Super optimal broth
SSH	Persulfide
SUF	Sulfur mobilization
TB	Terrific broth
TCA	Tricarboxylic acid
TCEP	Tris(2-carboxyethyl)phosphine

TEMED	Tetramethylethylenediamine
TPP	Thiamine pyrophosphate
Tris	Tris(hydroxymethyl)aminomethane
WT	Wild-type
XANES	X-ray absorption near edge structure
XAS	X-ray absorption spectroscopy
Yah1	Yeast adrenodoxin homolog 1

8 Verzeichnis der akademischen Lehrenden

Meine akademischen Lehrenden in Marburg waren die Damen und Herren: Aigner, Auel, Bange, Dehnen, Einhäuser-Treyer, Essen, Galland, Geyer, Gottfried, Graumann, Hampp, Harbrecht, Hilt, von Hänisch, Koert, Linne, Meggers, Pilgrim, Reinhard, Roling, Schween, Seubert, Sundermeyer, Tallarek, Vazquez, Waidner, Wilmsmeyer, von Zezschwitz.

9 Danksagung

Zuallererst möchte ich meinem Doktorvater Prof. Dr. Roland Lill meinen tiefsten Dank für das entgegengebrachte Vertrauen sowie die herausfordernde und gleichzeitig interessante, vielseitige und relevante wissenschaftliche Arbeit, die er mir ermöglicht hat, ausdrücken. Für die stete Unterstützung sowie zahlreiche Diskussionen und Gespräche wissenschaftlicher Art und darüber hinaus bin ich besonders dankbar.

Weiterhin danke ich dem Korreferenten für die freundliche Übernahme des Zweitgutachtens. Allen ehemaligen und gegenwärtigen Mitarbeitern der AG Lill und des Instituts für Zytobiologie möchte für die große Kollegialität und die schöne Zeit zusammen danken. Man könnte sich wirklich keinen besseren Ort für eine Doktorarbeit wünschen! Ganz besonderer Dank geht an Dr. Sven-Andreas Freibert, für Rat und Hilfe bei zahlreichen Experimenten, das Initiieren fruchtbarer Kollaborationen, unzählige Diskussionen wissenschaftlicher und anderer Art, sowie seinen unumstößlichen Optimismus. Prof. Dr. Ulrich Mühlenhoff danke ich für die Unterstützung und viele unbezahlbaren Ratschläge bei der Laborarbeit, sowie seine Fähigkeit, die Dinge beim Namen zu nennen. Danke auch an Dr. Oliver Stehling für die gute Zusammenarbeit beim Manuskript schreiben. Nils Krapoth möchte ich für die produktive gemeinsame Arbeit an der ISCU2-FXN-Interaktion danken. Martin Stümpfig danke ich für die Unterstützung und seinen Humor im Labor, sowie dafür, dass er die treibende Kraft der Wildtypes war. Vielen Dank an alle Mitglieder der Wildtypes für die gemeinsame musikalische Ekstase und an meine Sitznachbarn Steffi, Juri und Thomas für die schöne Zeit!

Ralf Steinhilper und Dr. Bonnie Murphy gebührt mein Dank für die fruchtbare Zusammenarbeit bei der Analyse von cryo-EM-Proben. Jonathan Oltmanns und Prof. Dr. Volker Schünemann danke ich für die gute Zusammenarbeit bei der Analyse von Mössbauer-Proben, und Jonathan zudem für das Korrekturlesen und die produktiven wissenschaftlichen Diskussionen. Mein Dank geht weiterhin an Dr. Timothy Stemmler und Tiara Hinton für die Kollaboration bei der Analyse von XAS-Proben. Prof. Dr. Squire Booker und Dr. Douglas Warui danke ich für die Zusammenarbeit bei Lipoylsyntheseassays. Den Mitarbeitern der Abteilung Massenspektrometrie, insbesondere Dr. Uwe Linne und Jan Bamberger, danke ich für die Messung verschiedenster Proben.

Besonders schätze ich auch die mit meinen Freunden abseits des Labors verbrachte Zeit. Ein großer Dank an Niki, Luc, Christoph, Niklas, Josi, Nikolai, Christian, Carsten, Jules, Moritz und alle anderen! Meiner Familie möchte ich ganz besonderen Dank ausdrücken, für die fortwährende Unterstützung in allen Formen und Lebenslagen, ohne die das Durchführen dieser Arbeit gar nicht möglich gewesen wäre. Vielen Dank an euch! Und nicht zuletzt allerliebsten Dank an Karen für das Korrekturlesen und vor allem die gemeinsame Zeit, die ohne sie nur halb so schön wäre! ♥